Advancements in volumetric PIV measurements

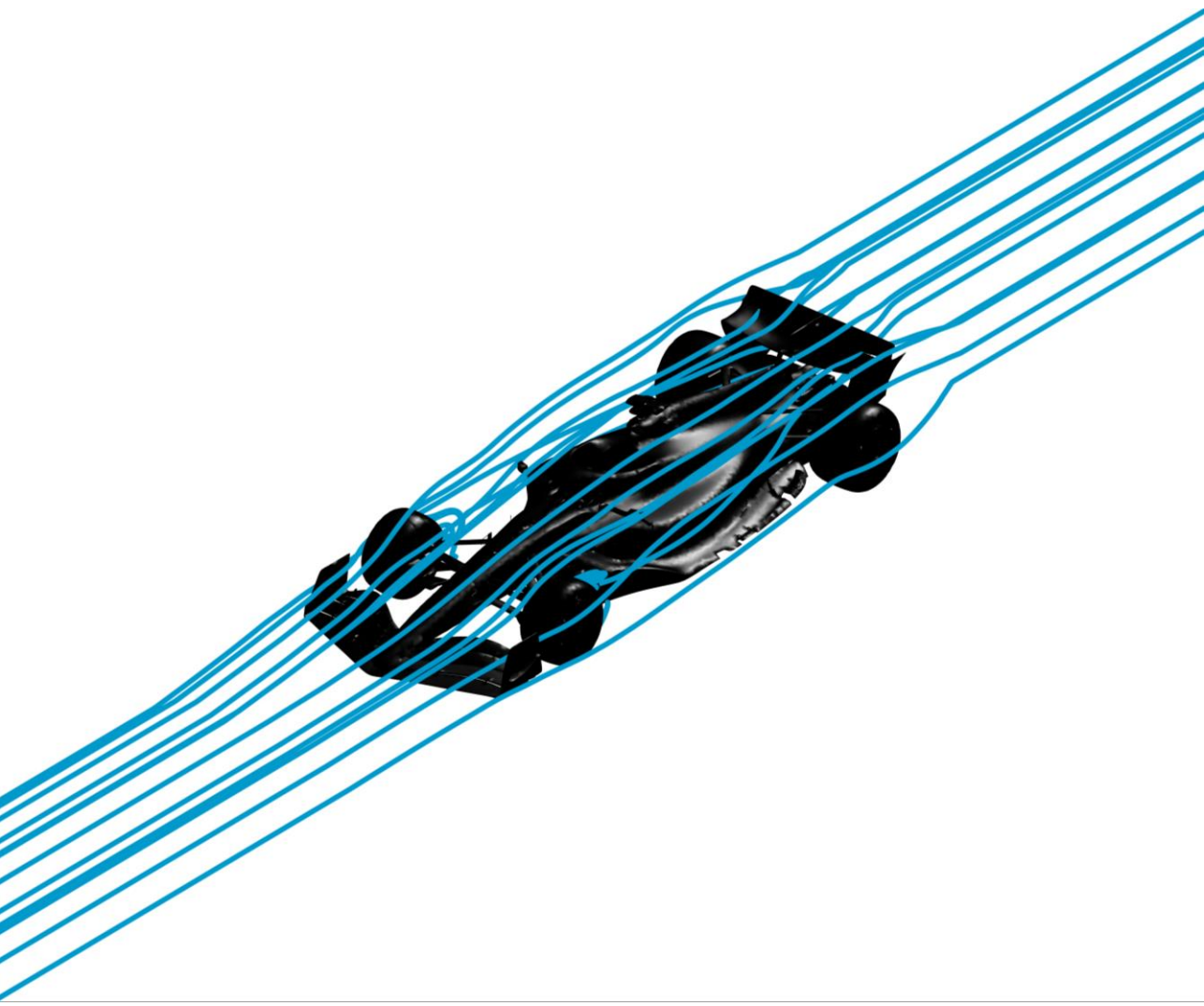

Adrián Grille Guerra

Propositions

accompanying the dissertation

Advancements in volumetric PIV measurements

by

Adrián GRILLE GUERRA

1. Volumetric PIV experiments in air may be scaled *ad libitum* using helium-filled soap bubbles as tracers. (*chapter 3*)
2. No image preprocessing method can successfully eliminate the contribution of light reflections to the overall intensity, and thus, image masking is the way to go. (*chapter 4*)
3. Multi-exposure recording strategies will democratize volumetric PIV by enabling high-quality measurements using low-repetition rate cameras. (*chapter 5*)
4. Modal analysis allows for a high-resolution representation of instantaneous turbulent flows. (*chapter 6*)
5. Talent may come from anywhere, and as such, societies will advance by welcoming it.
6. Electric mobility is superior, but will not triumph solely by imposition.
7. The academic future of a PhD candidate as a postdoctoral researcher under temporary contracts is a disappointing outlier in nowadays job market.
8. The so-called artificial intelligence is currently the greatest threat to critical thinking, surpassing the traditional role of religion in this regard.
9. Investing resources in defence only accelerates the fall of that civilization.
10. After confirming the degeneration of democracy into tyranny, already postulated by Plato (IV BC), it is time to explore alternative forms of government.

These propositions are regarded as opposable and defendable, and have been approved as such by the promotors prof. dr. F. Scarano and dr. A. Sciacchitano.

Advancements in volumetric PIV measurements

Advancements in volumetric PIV measurements

Dissertation

for the purpose of obtaining the degree of doctor
at Delft University of Technology
by the authority of the Rector Magnificus,
Prof. dr. ir. H. Bijl,
chair of the Board for Doctorates
to be defended publicly on
Wednesday, 24 June 2026, 10:00

by

Adrian GRILLE GUERRA

This dissertation has been approved by the promotors.

Composition of the doctoral committee:

Rector Magnificus,	chairperson
Prof. dr. F. Scarano,	Delft University of Technology, *promotor*
Dr. A. Sciacchitano,	Delft University of Technology, *promotor*
Independent members:	
Prof. dr. ir. J. Westerweel	Delft University of Technology
Prof. dr. S. Discetti	Universidad Carlos III de Madrid, Spain
Dr. M.A. Mendez	von Karman Institute for Fluid Dynamics, Belgium
Dr. rer. nat. D. Schanz	German Aerospace Center, Germany
Dr. E. Saredi	Alpine F1 Team, United Kingdom
Prof. dr. M. Kotsonis	Delft University of Technology, *reserve member*

Keywords: Quantitative flow visualization, particle image velocimetry, aerodynamics

Printed by: Koninklijke Rijnja

Cover by: A. Grille Guerra and L. Leston Cambeiro. Front: streamlines around a F1 car. Back: streamlines around a cow.

ISBN 978-94-6384-957-9

An electronic copy of this dissertation is available at
https://repository.tudelft.nl/.

To my daughter Manuela

Contents

Summary

Particle Image Velocimetry (PIV) constitutes the state-of-the-art for quantitative flow diagnostics. Its volumetric variant is nowadays also well established, able to provide a full description of the three-dimensional flow field. Despite the maturity of the technique, the use of volumetric PIV in industrial facilities is seldom considered, due to the challenges associated with the high Reynolds numbers, the presence of complex wind tunnel models in the domain of interest or the long distances with respect to the PIV instrumentation. In an attempt to aid the dissemination of volumetric PIV in industrial large-scale facilities and promote its use for engineering design and validation of flow simulations, four elements of the PIV working principle are critically reviewed in this dissertation, namely: the scalability of tracer particles for experiments in air flows; image preprocessing to deal with complex light reflections; the recording strategy and particle tracking algorithm; and data reduction techniques that exploit the modal decomposition of the velocity field.

The scalability of experiments using PIV relies upon several parameters: primarily the tracers scattering cross section and their concentration, the power and distribution of illumination; and the imagers sensor size and their amount. Given their larger cross section, helium-filled soap bubbles (HFSB) allow measurements in air flows over a significantly larger domain compared to traditional oil or water droplets. Controlling their diameter translates into scalability of the experiment. In chapter 3, a technique is presented to extend the control of HFSB diameter by geometrical variations of the generator. A theoretical model predicts the bubble size and production rate, which is verified experimentally by high-speed shadow visualization. The overall range of HFSB produced in a stable regime can be varied from approximately 150 µm, targeting experiments in research facilities at high spatial resolution, to a few millimetres, sufficient for large-scale measurements in industrial facilities as well as full-scale on-site experiments. Imaging by light scattering of such tracers is also investigated, in view of controversies in the literature on whether diffraction or geometrical imaging dominate the imaging regime. For large-scale volumetric applications, it is shown that varying the bubble diameter allows increasing both the measurement domain as well as the working distance of the imagers at 10 m and beyond.

Measuring the velocity field around a complex object by volumetric PIV is hindered by shadow formation (illumination), camera occlusion (imaging) and light reflections from the object surface. The former have been recently dealt with by multiplying illumination and imaging directions (redundancy) and by the integration of ray-tracing techniques to include the effect of visual blockage caused by the object. Instead, the problem of light reflections blinding regions of the images has not been afforded yet. The latter pertains to interactions between illumination and imaging through the object surface and it poses additional challenges to ghost particle formation, particle detection and tracking in general, increasing the computational cost and reducing the accuracy of the measured

velocity field. In chapter 4, a method is proposed to effectively detect such regions, and measures to modify the particle triangulation algorithm are devised. The viability of this novel approach is examined by application to two experiments of increasing complexity. The first case is the flow around a stationary wall-mounted cube as imaged with a redundant number of cameras. The second experiment tackles an elite runner sprinting across the measurement region obtained with the Ring-of-Fire technique. A considerable reduction of ghost particles (false positives) is attained, while the formation of voids (false negatives) is also minimized. The overall result of the method maximizes the measurement region around and in proximity of the object of interest.

Multiple-exposure (ME) recording is a variant of PIV whereby more than two samples of the particle position are obtained to overcome some limitations of single-exposure dual-frame recordings, such as accelerometry, pressure from instantaneous PIV data, or to further extend the dynamic velocity range. Compared to time-resolved systems, ME lowers system requirements in terms of laser power and camera frame rate, thus making it more suitable for applications involving a redundant number of cameras and higher flow velocities. In chapter 5, the reliability and accuracy of volumetric particle tracking in ME recordings comprising up to 5 exposures with one or two frames is first scrutinized on a synthetic particle field motion based on a Taylor-Green vortex lattice, yielding viable results. The measurement accuracy in terms of dynamic velocity and acceleration ranges is reported, as a function of particle image density, number of pulses and timing sequence. Besides, ME recordings are simulated from a time-resolved experiment around a wall-mounted cube, which yield equivalence between ME and time-resolved conditions. A demonstration of volumetric ME for accelerometry and pressure from PIV is also included, with experiments in the turbulent wake of a circular cylinder.

Modal decomposition of PIV measurements is a common approach to reduce data complexity and aid interpretability. In chapter 6, a method to reconstruct the dense velocity field from relatively sparse particle tracks, as obtained for instance from volumetric ME recordings, is introduced. The goal is to provide a representation of the 3D flow field on a Cartesian grid, for inspection of derived flow quantities, at high spatial resolution. The approach leverages the properties of proper orthogonal decomposition (POD) and it iteratively reconstructs the detailed spatial modes from a first, coarse estimation thereof. The initially coarse Cartesian representation of the velocity field is obtained by local data averaging, where POD is applied. The spatial resolution of the POD modes is enhanced by reprojecting them onto the sparse particles velocity to iteratively improve the reconstruction of the temporal coefficients. Finally, the enhanced velocity field is represented at high-resolution with a reduced order model using the dominant POD modes. Experiments in the wake of a cylinder at Re_D = 27,000 are used to assess the suitability of the method to resolve the turbulent Kármán-Benard wake. The approach is benchmarked against traditional as well as state-of-the-art reconstruction methods, illustrating the capability of enhancing the spatial resolution of sparse velocity data.

Samenvatting

Particle Image Velocimetry (PIV) is de meest geavanceerde techniek voor kwantitatieve stroomdiagnostiek. De volumetrische variant is inmiddels ook goed ingeburgerd en biedt een volledige beschrijving van het driedimensionale stromingsveld. Ondanks de volwassenheid van de techniek wordt het gebruik van volumetrische PIV in industriële installaties zelden overwogen, vanwege de uitdagingen die gepaard gaan met hoge Reynoldsgetallen, de aanwezigheid van complexe windtunnelmodellen in het onderzoeksgebied of de grote afstanden tot de PIV-instrumentatie. Om de verspreiding van volumetrische PIV in grootschalige industriële installaties te bevorderen en het gebruik ervan voor technisch ontwerp en validatie van stromingssimulaties te stimuleren, worden in dit proefschrift vier elementen van het werkingsprincipe van PIV kritisch besproken, namelijk: de schaalbaarheid van tracerdeeltjes voor experimenten in luchtstromen; beeldvoorverwerking om complexe lichtreflecties te verwerken; de opnamestrategie en het deeltjesvolgalgoritme; en datareductietechnieken die gebruikmaken van de modale decompositie van het snelheidsveld.

De schaalbaarheid van experimenten met PIV is afhankelijk van verschillende parameters: voornamelijk de verstrooiingsdoorsnede en concentratie van de tracers, het vermogen en de verdeling van de belichting; en de grootte en het aantal sensoren van de beeldvormers. Door hun grotere doorsnede maken met helium gevulde zeepbellen (HFSB) metingen in luchtstromen over een aanzienlijk groter gebied mogelijk in vergelijking met traditionele olie- of waterdruppels. Het beheersen van hun diameter vertaalt zich in schaalbaarheid van het experiment. In hoofdstuk 3 wordt een techniek gepresenteerd om de controle over de HFSB-diameter uit te breiden door geometrische variaties van de generator. Een theoretisch model voorspelt de belgrootte en de productiesnelheid, wat experimenteel wordt geverifieerd door middel van hogesnelheidsschaduwvisualisatie. Het totale bereik van de in een stabiel regime geproduceerde HFSB kan worden gevarieerd van ongeveer 150 µm, gericht op experimenten in onderzoeksfaciliteiten met een hoge ruimtelijke resolutie, tot enkele millimeters, voldoende voor grootschalige metingen in industriële faciliteiten en grootschalige experimenten op locatie. Ook beeldvorming door lichtverstrooiing van dergelijke tracers wordt onderzocht, gezien de controverses in de literatuur over de vraag of diffractie of geometrische beeldvorming het beeldvormingsregime domineert. Voor grootschalige volumetrische toepassingen wordt aangetoond dat variatie van de bubbeldiameter het mogelijk maakt om zowel het meetgebied als de werkafstand van de beeldvormers te vergroten tot 10 m en verder.

Het meten van het snelheidsveld rond een complex object met behulp van volumetrische PIV wordt bemoeilijkt door schaduwvorming (verlichting), camera-occlusie (beeldvorming) en lichtreflecties van het objectoppervlak. De eerste problemen zijn recentelijk aangepakt door de verlichtings- en beeldvormingsrichtingen te vermenigvuldigen (redundantie) en door raytracing-technieken te integreren om het effect van

visuele blokkering door het object mee te nemen. Het probleem van lichtreflecties die delen van de beelden verblinden, is echter nog niet aangepakt. Dit laatste probleem betreft interacties tussen verlichting en beeldvorming door het objectoppervlak en vormt extra uitdagingen voor de vorming van spookdeeltjes, de detectie en het volgen van deeltjes in het algemeen, waardoor de rekenkosten toenemen en de nauwkeurigheid van het gemeten snelheidsveld afneemt. In hoofdstuk 4 wordt een methode voorgesteld om dergelijke gebieden effectief te detecteren, en worden maatregelen bedacht om het deeltjestriangulatiealgoritme aan te passen. De haalbaarheid van deze nieuwe aanpak wordt onderzocht door toepassing op twee experimenten met toenemende complexiteit. Het eerste geval betreft de stroming rond een stationaire, aan de muur bevestigde kubus, zoals vastgelegd met een redundant aantal camera's. Het tweede experiment betreft een topatleet die sprint over het meetgebied dat is verkregen met de Ring-of-Fire-techniek. Een aanzienlijke vermindering van spookdeeltjes (valse positieven) wordt bereikt, terwijl de vorming van lege ruimtes (valse negatieven) ook wordt geminimaliseerd. Het algehele resultaat van de methode is het maximaliseren van het meetgebied rond en in de nabijheid van het object van interesse.

Multiple-exposure (ME) is een variant van PIV waarbij meer dan twee metingen van de deeltjespositie worden verkregen om enkele beperkingen van enkelvoudige belichting met twee frames te ondervangen, zoals accelerometrie, druk uit momentane PIV-gegevens, of om het dynamische snelheidsbereik verder uit te breiden. In vergelijking met tijdresolutiesystemen verlaagt ME de systeemvereisten wat betreft laservermogen en camerabeeldsnelheid, waardoor het geschikter is voor toepassingen met een redundant aantal camera's en hogere stroomsnelheden. In hoofdstuk 5 wordt de betrouwbaarheid en nauwkeurigheid van volumetrische deeltjesvolging in ME-opnames met maximaal 5 belichtingen van één of twee frames eerst onderzocht op een synthetische deeltjesveldbeweging gebaseerd op een Taylor-Green-vortexrooster, wat bruikbare resultaten oplevert. De meetnauwkeurigheid in termen van dynamische snelheids- en acceleratiebereiken wordt gerapporteerd als functie van de deeltjesbeelddichtheid, het aantal pulsen en de timingsequentie. Bovendien worden ME-opnames gesimuleerd op basis van een tijdresolutie-experiment rond een aan de muur bevestigde kubus, wat equivalentie oplevert tussen ME- en tijdresolutie-omstandigheden. Ook is een demonstratie van volumetrische ME voor accelerometrie en drukmetingen met PIV opgenomen, met experimenten in het turbulente zog van een cirkelvormige cilinder.

Modale decompositie van PIV-metingen is een veelgebruikte methode om de complexiteit van data te verminderen en de interpreteerbaarheid te verbeteren. In hoofdstuk 6 wordt een methode geïntroduceerd om het dichte snelheidsveld te reconstrueren uit relatief schaarse deeltjessporen, zoals bijvoorbeeld verkregen uit volumetrische ME-opnames. Het doel is om een representatie van het 3D-stromingsveld op een cartesiaans rooster te bieden, voor inspectie van afgeleide stromingsgrootheden, met een hoge ruimtelijke resolutie. De methode maakt gebruik van de eigenschappen van proper orthogonal decomposition (POD) en reconstrueert iteratief de gedetailleerde ruimtelijke modi vanuit een eerste, grove schatting daarvan. De aanvankelijk grove cartesiaanse representatie van het snelheidsveld wordt verkregen door lokale data-middeling, waarbij POD wordt toegepast. De ruimtelijke resolutie van de POD-modi wordt verbeterd door ze te herprojecteren op de schaarse deeltjessnelheid om de reconstructie van de temporele

coëfficiënten iteratief te verbeteren. Ten slotte wordt het verbeterde snelheidsveld met een gereduceerde orde weergegeven met behulp van de dominante POD-modi. Experimenten in het zog van een cilinder bij Re_D = 27.000 worden gebruikt om de geschiktheid van de methode te beoordelen voor het oplossen van het turbulente Kármán-Benard-zog. De aanpak wordt vergeleken met traditionele en state-of-the-art reconstructiemethoden, waarmee de mogelijkheid wordt aangetoond om de ruimtelijke resolutie van schaarse snelheidsgegevens te verbeteren.

1 Introduction

While the behaviour of fluid flows is well characterized by the Navier-Stokes equations (Navier, 1823; Stokes, 1845), the vast range of spatio-temporal scales associated with turbulent flows at high Reynolds number, $Re = \frac{LU}{\nu}$, where L and U are characteristic length and velocity scales respectively and ν is the kinematic viscosity of the fluid, pose a challenging engineering scenario. In the design of wind turbines ($Re \sim 10^4 - 10^7$), ground transport vehicles ($Re \sim 10^6 - 10^7$) or commercial aircraft ($Re \sim 10^6 - 10^8$), the state-of-the-art for aerodynamic development is to employ a combination of numerical simulations, i.e., computational fluid dynamics (CFD), and experiments. But why such a multidisciplinary approach?

The prohibitive computational demands of high-fidelity simulations resolving all scales of turbulence, i.e., direct numerical simulations (DNS), with the number of floating point operations required scaling as a power of the Reynolds number (since the range of length scales follows $Re^{3/4}$, the number of grid points scales as $Re^{9/4}$; apart from the temporal discretization), mean that lower-fidelity models have to be used instead. The most common approach, which is expected to still constitute the main development tool for industrial applications for the next few decades (Xiao & Cinnella, 2019), is to solve the Reynolds-averaged Navier-Stokes equations (RANS), where the full spectrum of turbulence is modelled. Since this comes at the cost of accuracy in the estimation of the flow properties, results are typically validated with the use of experiments.

For the external aerodynamics around solid objects (airfoils, bluff bodies, etc.), CFD results provide insight into the variables of interest, namely flow velocity and pressure, in the whole simulated domain, from which other related quantities (vorticity, skin friction, etc.) are readily available. A primary objective of aerodynamic investigations is the evaluation of forces acting on the body of interest (namely lift and drag), which can be obtained via integration of other flow properties. In the context of experimental simulations, the most common approach for inferring aerodynamic loads is the use of wind tunnels, where (usually scaled) models are subject to constant flow conditions and mounted on force balances to extract loads and moments acting on the body, as illustrated in figure 1.1(left) for an aircraft model inside an industrial wind tunnel facility.

While the aerodynamic forces provide an indication of the overall performance and efficiency of the object of interest, design optimization without an understanding of

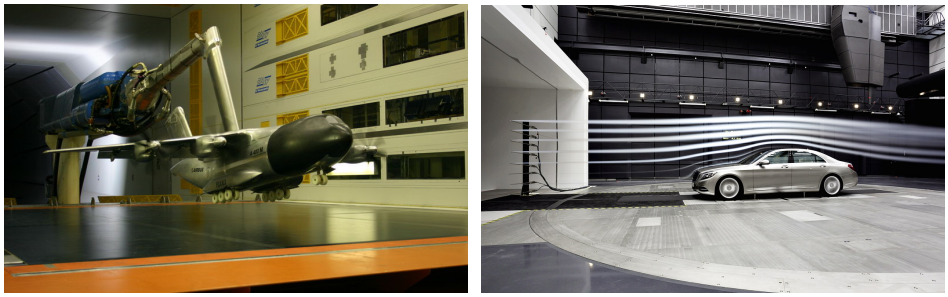

Figure 1.1: Experimental simulations inside wind tunnel facilities. Airbus *A400 M* scaled model inside the DNW LLF wind tunnel, mounted on a force balance (left) and smoke visualization around a Mercedes passenger car (right).

the underlying flow mechanisms is challenging. For that reason, a variety of flow measurement techniques exist that can measure various properties of the flow field to complement the integral forces. These range from rudimentary qualitative flow visualization methods, such as smoke lines, as illustrated in figure 1.1(right) for a passenger ground vehicle, to quantitative techniques that can measure point-wise information (pressure taps and probes, hot-wires, etc.) or for instance surface flow properties (infrared thermography, pressure sensitive paint, etc.).

Experimental simulations in wind tunnels do suffer from scaling effects, as the achievable Reynolds number is typically limited by the size and maximum speed of the facility. Also, other corrections are necessary to account for the presence of walls bounding the flow. Alternatively, on-site full-scale measurements can be used to eliminate any source of modelling, incorporating flow measurement tools into the test object. Examples of these are shown in figure 1.2 for a race car, which has been fitted with tufts on the suction side of the rear wing for inspection of possible flow separation (figure 1.2-left). Surface flow topology may also be inferred from oil-flow visualization (figure 1.2-middle), applied in the front suspension arms and lateral region of the car. The vehicle is also fitted with a pressure rake incorporating Kiel probes for the estimation of total pressure in the front tyre wake region (figure 1.2-right). On-site measurements may provide valuable information for verification of the final design, but the cost and challenges of manufacturing and testing full-scale models typically exclude these from the design optimization phase, making wind tunnels the preferred option instead.

A popular quantitative flow measurement technique in fluid mechanics research is particle image velocimetry (PIV, Adrian and Westerweel, 2011; Raffel *et al.*, 2018), a non-intrusive, optical-based method that can provide the velocity distribution in a fluid flow by measuring the displacement of tracer particles dispersed in it. While originally developed at research facilities of moderate size and velocities, PIV has now been used in several industrial facilities in its planar (or stereoscopic) configuration (Cardano *et al.*, 2008; Jenkins *et al.*, 2009; Raffel *et al.*, 2004, among others). Combining micron-sized aerosol tracer particles, dual-cavity Nd:YAG lasers to create a thin light sheet and double-frame scientific cameras, measurement planes of roughly 1 m^2 can be achieved. While obtaining information on the three components of the velocity field from a

Figure 1.2: Flow measurement devices for on-site full-scale testing of a race car. Left: tufts fitted on the rear wing. Middle: oil-flow visualization of the front suspension arms. Right: pressure rake on the front tyre wake.

stereoscopic PIV arrangement may provide valuable insight into the flow dynamics and serve for CFD validation purposes, most industrial designs are highly three-dimensional, and therefore a full understanding of the volumetric flow field would be beneficial.

Inspection of the time-averaged (not instantaneous) 3D flow field may be achieved by scanning the domain of interest with various PIV planes, as illustrated in figure 1.3 for measurements in the wake of a car. This requires traversing systems, careful adjustment of camera and laser optics, and involves long measurement times. Scanning-PIV systems are now popular in automotive wind tunnels, by making use of robotic manipulation for the cameras and laser head, together with remote adjustment of lens aperture, focus and Scheimpflug condition (Michaux *et al.*, 2018; Senft & Gillan, 2019).

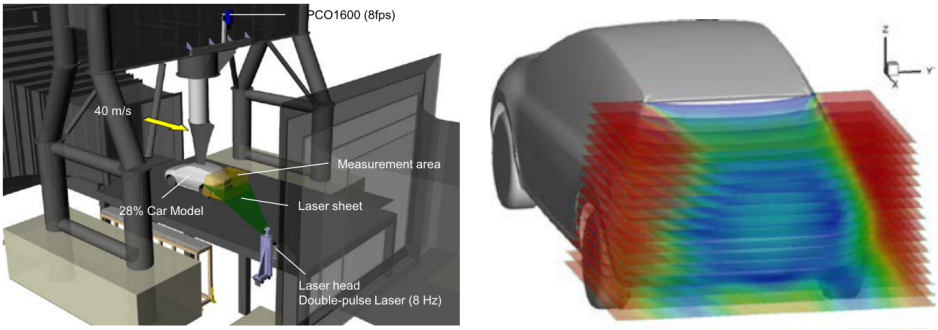

Figure 1.3: Experimental setup (left) and visualization of the 3D flow field (right) in the wake of a passenger car, measured using a scanning-PIV approach. Figures adapted from Nakagawa *et al.* (2015).

The volumetric velocity field may also be tackled via the latest advancements in 3D particle tracking (Schröder & Schanz, 2023), whereby various directions of imaging are combined to triangulate and track the position of tracers inside an illuminated measurement volume. Volumetric PIV may provide insight into the instantaneous 3D velocity field, or alternatively, a time-averaged solution may be constructed from ensemble-averaging of the particle trajectories accumulated during a recording. But can volumetric PIV provide a full description of high Reynolds number turbulent flows inside an industrial wind tunnel facility?

Taking the example of the Large Low-speed Facility (LLF, see figure 1.1-left) at the German-Dutch Wind Tunnels (DNW), with characteristic scales in the order of $L \sim 1$ m and $U \sim 100$ m/s ($Re \sim 10^6 - 10^7$), the combination of size and speed pose a wildly different scenario compared to most research facilities. Attempting to perform a volumetric PIV measurement that captures the full range of spatio-temporal scales of the flow (from the characteristic scales to the Kolmogorov ones) is unfeasible, both in terms of tracers' light scattering capabilities, camera resolution and frame rate, and also illumination power. Fortunately, this type of measurement is unnecessary in the context of industrial aerodynamics. Designing a measurement system capable of capturing the complete range of spatio-temporal scales in high Reynolds number turbulent flows is the experimental analogy of DNS, with the added complexity of the experimental environment.

Unlike low-fidelity CFD simulations, where the modelling of turbulence impacts the overall calculation of the 3D velocity field, a volumetric PIV system can be designed to capture the large spatio-temporal scales of the flow only (the most energetic ones), without introducing any further modelling apart from the wind tunnel environment. This alleviates the requirements in terms of spatial resolution (and therefore the number of pixels in the cameras) and temporal marching (frame rate). Furthermore, tracer particles may also be produced in lower concentrations and can be chosen for improved light scattering capabilities at the cost of tracing fidelity, while still being sufficient to capture the dominant turbulent fluctuations. While the instantaneous resolution might be limited to the dominant scales only, a high-resolution representation of the flow statistics may be obtained via ensemble averaging from long recordings. Contrary to simulations, where boundary conditions are typically imposed both in the far-field and on the object's surface, a PIV experiment can capture only a portion of the entire flow field, thus limiting the size of the measurement domain.

1.1. Outline

With the final goal of promoting the dissemination of volumetric PIV capabilities in industrial wind tunnel facilities, this dissertation tackles some of the challenges that prevent the use of such systems. These can provide a representation of the 3D velocity field around complex objects at sufficient resolution for interpretation of the dominant flow mechanisms. This may help the engineering design process by complementing the information on the integral forces and for CFD validation. The key elements of PIV are reviewed in detail in chapter 2, starting from a historical evolution of the technique, from planar measurements towards volumetric capabilities at different scales. This provides the context for the research activities included in the dissertation, which tackle four different aspects of the PIV measurement process. A sketch of the typical volumetric PIV measurement chain is given in figure 1.4, which includes activities performed before the experiments, others conducted during the experimental campaign, and also data processing steps done after the measurements. While some activities are not further elaborated in the document (in gray in figure 1.4), those covered are briefly discussed in the following.

The first of them is the choice of tracer particles for volumetric PIV. The use of

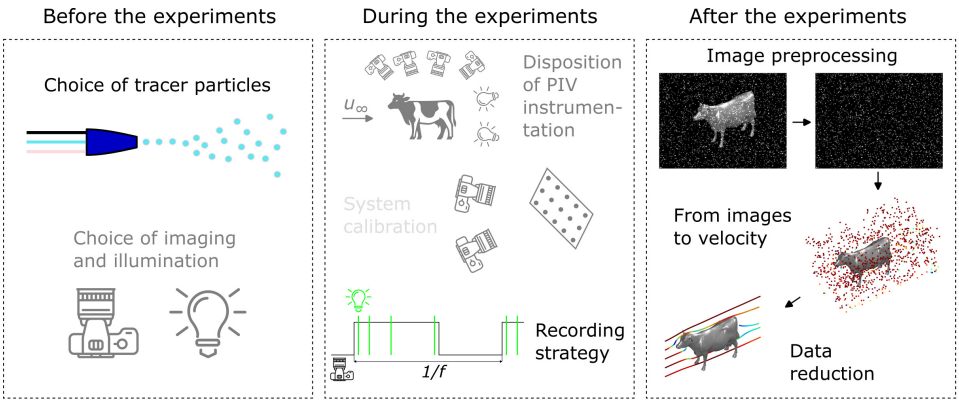

Figure 1.4: Schematic representation of the typical volumetric PIV measurement chain. In colour, the research activities covered in this dissertation: the choice of tracer particles for volumetric PIV in air (chapter 3), image preprocessing to mitigate light reflections (chapter 4), alternative recording strategies and image evaluation algorithms (chapter 5), and data reduction techniques (chapter 6).

volumetric illumination (either laser- or LED-based) results in lower energy densities than for conventional planar PIV systems, in turn requiring larger tracers for improved light scattering efficiency. For air flows, this requirement has been fulfilled by the recent development of neutrally buoyant helium-filled soap bubbles (HFSB, Scarano *et al.*, 2015), in the sub-millimetre range. In chapter 3, the scalability of HFSB is further explored to justify their suitability for a wide range of applications. An HFSB generator family is proposed that can produce tracers ranging from 100 µm, targeting experiments in research facilities at higher spatial resolution, up to the millimetre range, sufficient for large-scale industrial wind tunnels and even on-site full-scale measurements.

The second challenge arises from the illumination of tracer particles in close proximity to the wind tunnel models. Light impinges on the model and reflects back to the cameras, causing a superposition of intensity in the sensor from reflections and particle images. Areas of light reflections can lead to the appearance of spurious particle trajectories in the domain of interest, thus corrupting the resulting velocity field. In chapter 4, the nature of light reflections in volumetric PIV recordings is reviewed, and a method is proposed, as an image preprocessing step, to isolate the regions of the images affected by reflections such that these do not affect the particle tracking steps.

The subsequent step of the measurement chain is the evaluation of particle images for triangulation and tracking in the 3D domain. The state-of-the-art particle tracking algorithm, the so-called Shake-the-Box algorithm (STB, Schanz *et al.*, 2016), makes use of high-speed illumination and imaging to exploit the temporal information and simplify the matching exercise, thus allowing for higher particle concentration and resolution. For industrial applications, the multiplication of light sources and imagers required to robustly achieve optical access around the wind tunnel model depicts a

complex scenario to maintain the high-speed requirements. Instead, alternative timing approaches and evaluation methods are explored in chapter 5 to simplify the hardware involved, without compromising the accuracy and resolution of the system.

The scattered particle trajectories obtained from the analysis of the particle images are typically reduced onto a Cartesian grid for the evaluation of related flow properties (vorticity, pressure from PIV, etc.). Several methods have been proposed to enhance the spatial resolution of the resulting gridded velocity field by imposing the constitutive equations of fluid motion on top of the measured trajectories. Alternatively, a new method is proposed in chapter 6 that exploits the statistical information obtained from long recordings of volumetric PIV data to extract the dominant modes of the dynamical turbulent flow at high resolution. These modes help the interpretation of the flow mechanisms and allow for constructing reduced-order models to represent the instantaneous flow field at a resolution beyond the one measured.

Finally, overall conclusions for the research activities included in this dissertation are given in chapter 7. These are complemented by a discussion on possible lines of future research, highlighting the remaining challenges preventing the growth of volumetric PIV systems at industrial wind tunnels.

References

Adrian, R. J., & Westerweel, J. (2011). *Particle Image Velocimetry*. Cambridge University Press. https://books.google.nl/books?id=jbDl2-yHbooC

Cardano, D., Carlino, G., & Cogotti, A. (2008). PIV in the Car Industry: State-of-the-Art and Future Perspectives. In *Particle image velocimetry. topics in applied physics* (pp. 363–376, Vol. 112). Springer, Berlin, Heidelberg. https://doi.org/10.1007/978-3-540-73528-1_19

Jenkins, L. N., Yao, C.-s., Bartram, S. M., Harris, J., Allan, B., Wong, O., & Mace, W. D. (2009). Development of a Large Field-of-View PIV System for Rotorcraft Testing in the 14- x 22-Foot Subsonic Tunnel. *American Helicopter Society 65th Annual Forum, Grapevine, Texas, May 27-29, 2009*, 1–22.

Michaux, F., Mattern, P., & Kallweit, S. (2018). RoboPIV: How robotics enable PIV on a large industrial scale. *Measurement Science and Technology*, *29*(7). https://doi.org/10.1088/1361-6501/aab5c1

Nakagawa, M., Michaux, F., Kallweit, S., & Maeda, K. (2015). Unsteady flow measurements in the wake behind a wind-tunnel car model by using high-speed planar PIV. *11th International Symposium on Particle Image Velocimetry*.

Navier, C. L. M. H. (1823). Mémoire sur les lois du Mouvement des Fluids.

Raffel, M., Richard, H., Ehrenfried, K., Van der Wall, B., Burley, C., Beaumier, P., McAlister, K., & Pengel, K. (2004). Recording and evaluation methods of PIV investigations on a helicopter rotor model. *Experiments in Fluids*, *36*(1), 146–156. https://doi.org/10.1007/s00348-003-0689-7

Raffel, M., Willert, C. E., Scarano, F., Kähler, C. J., Wereley, S. T., & Kompenhans, J. (2018). *Particle Image Velocimetry: A Practical Guide*. Springer International Publishing. https://doi.org/10.1007/978-3-319-68852-7

Scarano, F., Ghaemi, S., Caridi, G. C. A., Bosbach, J., Dierksheide, U., & Sciacchitano, A. (2015). On the use of helium-filled soap bubbles for large-scale tomographic PIV in wind tunnel experiments. *Experiments in Fluids*, *56*(2). https://doi.org/10.1007/s00348-015-1909-7

Schanz, D., Gesemann, S., & Schröder, A. (2016). Shake-The-Box: Lagrangian particle tracking at high particle image densities. *Experiments in Fluids*, *57*(5), 70. https://doi.org/10.1007/s00348-016-2157-1

Schröder, A., & Schanz, D. (2023). 3D Lagrangian Particle Tracking in Fluid Mechanics. *Annual Review of Fluid Mechanics*, *55*(1), 511–540. https://doi.org/10.1146/annurev-fluid-031822-041721

Senft, V., & Gillan, M. A. (2019). Recent advances and test processes in automotive and motorsports aerodynamic development. *Proceedings of the Institution of Mechanical Engineers, Part C: Journal of Mechanical Engineering Science*, *233*(23-24), 7573–7589. https://doi.org/10.1177/0954406219875770

Stokes, G. G. (1845). On the theories of the internal friction of fluids in motion.

Xiao, H., & Cinnella, P. (2019). Quantification of model uncertainty in RANS simulations: A review. *Progress in Aerospace Sciences*, *108*(September 2018), 1–31. https://doi.org/10.1016/j.paerosci.2018.10.001

2

Particle image velocimetry

This chapter provides an overview of particle image velocimetry (PIV), focusing on the topics that will be further elaborated throughout the dissertation. First, a short historical evolution is included in section 2.1 to give context to the work and highlight past and existing bottlenecks in the development of the technique.

After that, the chapter is split into four core elements of PIV, which later constitute the main research activities included in the dissertation. Section 2.2 covers the choice of tracer particles as a means of enabling measurements at different scales. In section 2.3, the appearance and relevance of light reflections affecting the measurements are discussed, highlighting the challenges associated with volumetric PIV experiments. The working principles of PIV evaluation algorithms, i.e., going from particle images to velocity, are reviewed in section 2.4. The focus is on the timing strategy applied to illuminators and imagers, to obtain high-quality velocity information while relaxing the hardware requirements. Finally, section 2.5 provides an overview of existing data reduction algorithms that exploit the full potential of PIV recordings.

The chapter ends in section 2.6 by presenting the specific research objectives of the PhD dissertation.

2.1. Historical evolution

Particle image velocimetry (PIV) is a quantitative flow measurement technique based on the imaging of tracer particles carried by the flow. It first appeared in the 1980s (Adrian, 1984) as a low seeding density alternative when compared to the existing laser speckle velocimetry approach (Meynart, 1983). Initial efforts relied on the recording of two illumination pulses onto a photographic film, which introduces a directional ambiguity that needed to be solved using techniques such as image shifting (Adrian, 1986). The popularity of PIV for experimental research in fluid mechanics rose rapidly with the use of digital cameras (Westerweel, 1993; C. E. Willert & Gharib, 1991), and especially since the development of double-frame imagers and dual-cavity pulsed lasers, simplifying the recording and image evaluation steps.

The layout of a typical PIV experimental set-up inside a wind tunnel is illustrated in figure 2.1, as reproduced from the book of Raffel *et al.* (2018). The flow is seeded upstream of the domain of interest, and the particles are illuminated by a laser light sheet, shaped from the original laser beam using a combination of optical elements. The light scattered by the tracers is imaged onto the camera. Using two illumination pulses imaged onto two different frames, separated by a certain time delay, the result is a two-dimensional representation of the instantaneous flow field in a plane. The most common approach to obtain velocity vectors from the recorded images is the use of a cross-correlation algorithm between the two frames inside small interrogation windows (containing approximately ten particle images each).

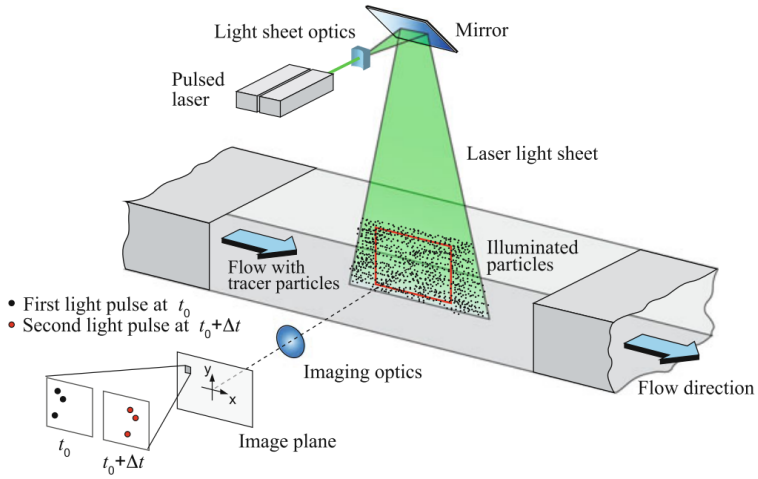

Figure 2.1: Schematic of a planar, two-component PIV set-up. Reproduced from Raffel *et al.* (2018).

Adding a second camera to the set-up, viewing the illuminated plane at a different angle, allows measuring the out-of-plane velocity component as well, in the so-called stereoscopic arrangement (C. Willert, 1997). Aside from initial efforts on particle tracking (pairing of individual particles) inside illuminated volumes (Maas *et al.*, 1993; Malik

et al., 1993; Nishino *et al.*, 1989), only successful for very low seeding densities, a major breakthrough in the development of the technique was the introduction of tomographic PIV by Elsinga *et al.* (2006). Combining multiple cameras (typically three to six), volumetric reconstruction algorithms such as MART (Herman & Lent, 1976) and 3D cross-correlation for image evaluation, the three components of the flow inside a volume became available. A typical tomographic PIV set-up is illustrated in figure 2.2, comprising four cameras.

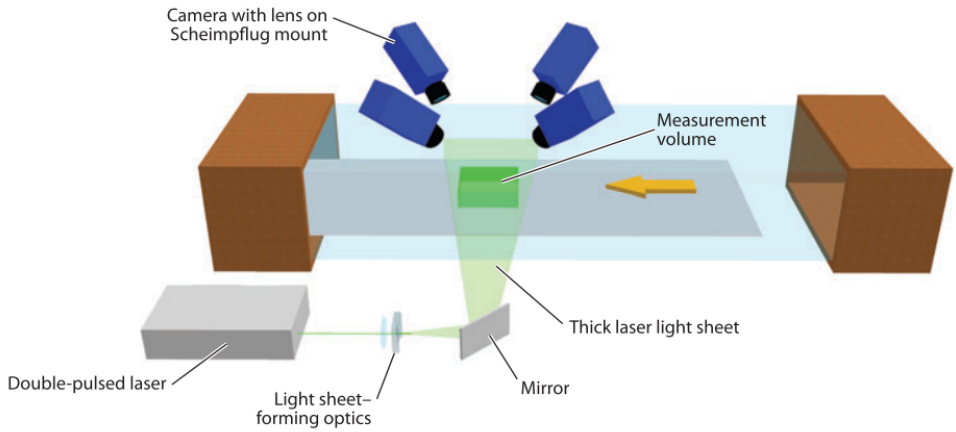

Figure 2.2: Schematic of a tomographic PIV set-up. Reproduced from Westerweel *et al.* (2013).

The lower energy density from expanding the laser beam into a volume, together with the smaller lens aperture necessary to maintain focus along the depth direction, meant a rapid decrease in the detectability of the tracers. Practically, this limited the measurement volume size to at most a few centimetres in the depth direction (Scarano & Poelma, 2009; A. Schröder *et al.*, 2008). With the use of distributed LED arrays for volumetric illumination and the development of tracer particles with higher light scattering capabilities, experiments in air flows can nowadays exceed the cubic meter scale (A. Schröder *et al.*, 2022). From the image processing perspective, the tomographic approach has been superseded by more efficient particle tracking methods now capable of dealing with high seeding densities, as will be further elaborated in section 2.4.

The high complexity of volumetric PIV set-ups, requiring optical access from multiple directions (tomographic aperture) and an accurate calibration, prevents the dissemination of the technique inside large-scale wind tunnel facilities, where the problematic is exacerbated by the long distances between illuminators, imagers, and the domain of interest. A possible solution to overcome these limitations has been the recent introduction of robotic volumetric PIV (Jux *et al.*, 2018), consisting of the manipulation of a compact 3D velocimeter mounted on a robotic arm. The so-called coaxial volumetric velocimeter (CVV, Schneiders *et al.*, 2018), illustrated in figure 2.3(left), comprises four cameras with a small tomographic angle between them, and a coaxial illumination

arrangement via expansion of a laser beam reaching the velocimeter's head through an optical fibre.

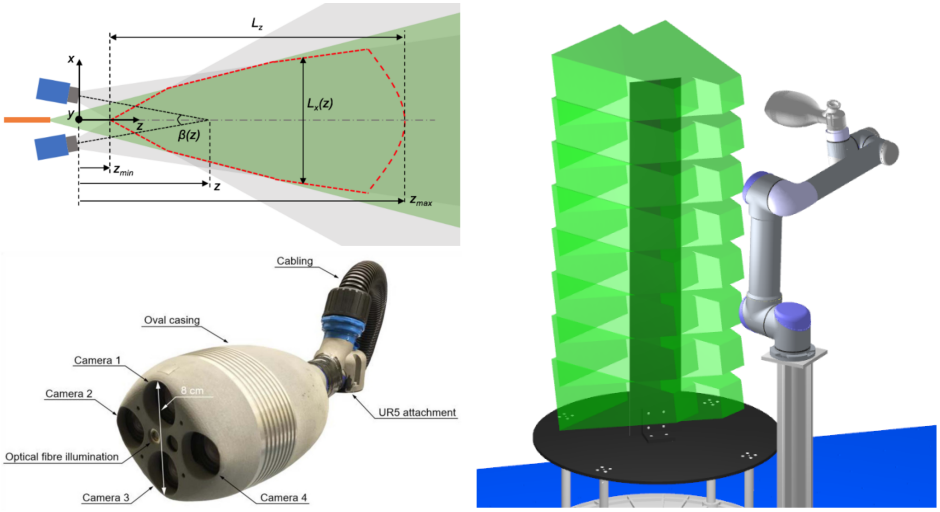

Figure 2.3: Schematic of the coaxial volumetric velocimeter (CVV), reproduced from Schneiders *et al.* (2018) (top-left) and picture of the *MiniShaker Aero* CVV from LaVision GmbH, reproduced from Jux *et al.* (2020) (bottom-left). Illustration of the working principle of robotic volumetric PIV, reproduced from Mitrotta *et al.* (2022) (right).

The intersection of the cameras' field of view and the illuminated cone returns a measurement volume of approximately 30 litres. A statistical representation of the flow on a larger domain can be easily achieved by scanning the volume with the CVV. Up to several hundred independent views were combined by Jux *et al.* (2018) to measure the flow around a full-scale cyclist, reaching a volume of two cubic meters. The working principle of robotic volumetric PIV is sketched in figure 2.3(right), reproduced from the work of Mitrotta *et al.* (2022), who used this approach to measure the flow around a plate with a span exceeding one meter. Despite the suitability of robotic volumetric PIV for measuring the flow around complex objects, certain limitations pose a challenge for a wider range of applications. For instance, the small tomographic aperture of the cameras produces an increased uncertainty in the particle positioning in the depth direction, which propagates into the velocity estimation (Schneiders *et al.*, 2018). Similarly, the coaxial arrangement between imaging and illumination makes the system prone to severe light reflections (Porcar Galan *et al.*, 2024). For industrial wind tunnels, the aerodynamic intrusiveness of the device, combined with the time-consuming scanning procedure make it challenging to justify its use when targeting large measurement volumes.

2.2. Tracer particles

After the introduction of tomographic PIV (Elsinga *et al.*, 2006), many volumetric experiments were realised both in air and water flows (Scarano, 2013). Yet, the domain that could be covered remained in the order of 10^1 – 10^2 cm^3, mostly due to the unfavourable scaling of the volume size and the particle detectability. For air flows, the setup typically involved expanding a Nd:YAG laser beam to illuminate a thicker plane. Concurrently, the imaging system needed to encompass such a thickness within its focal depth. Using the typical seeding tracers of 1 µm diameter, experiments rarely exceeded a volume thickness of 1 cm (Atkinson *et al.*, 2011; Humble *et al.*, 2009, among others). This restriction is partly relaxed in water flow experiments, where neutrally buoyant tracers of larger size can be employed. For example, 10 µm hollow glass spheres were frequently employed (van Hout *et al.*, 2022), 15 µm Rhodamine B particles (Tokgoz *et al.*, 2020) or most frequently 56 µm polyamide particles (Percin & van Oudheusden, 2015; Scarano & Poelma, 2009; A. Schröder *et al.*, 2011) have also been employed for measurement volumes exceeding 100 cm^3. Upscaled field experiments adopted solutions such as snow-flakes as natural tracers (Wei *et al.*, 2021), however, with limited control of their concentration and tracing fidelity.

A major leap forward in terms of upscaling was introduced by developing large neutrally buoyant tracers techniques based on helium-filled soap bubbles (HFSB) as PIV tracers (Bosbach *et al.*, 2009). Early applications of HFSB in aerodynamics were made for flow visualization (Hale *et al.*, 1971) and the low production rate of bubble generators (typically below 1000 bubbles/s, http://www. sageaction.com) discouraged their application for PIV measurements in wind tunnels. Furthermore, the work from Kerho and Bragg (1994) indicated that HFSB in the millimetre range were unsuited for the study of aerodynamic flows. Later, at the German Aerospace Centre (DLR) a miniature generator was developed, capable of producing 230 µm HFSB at a rate of 200,000 bubbles/s (Bosbach *et al.*, 2009). A sketch of this type of generator, together with a shadow visualisation of the bubble production process, is given in figure 2.4. The aerodynamic behaviour of sub-millimetre HFSB tracers were again evaluated and compared to conventional fog droplets, yielding a Stokes response time in the order of 10 to 30 µs (Faleiros *et al.*, 2018), thus proving the suitability of HFSB for low-speed aerodynamics experiments.

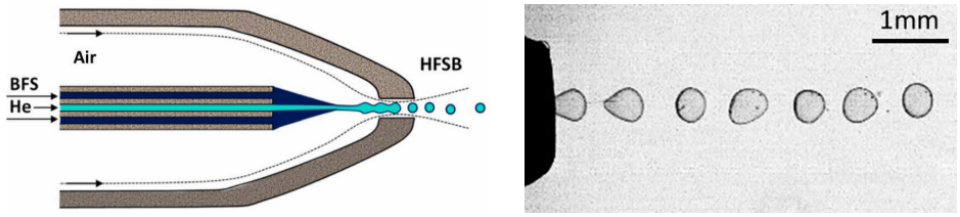

Figure 2.4: Schematic representation of the cross-section of a HFSB generator (left) and shadow visualisation of the bubble production process (right). Images reproduced from Faleiros *et al.* (2018).

An early HFSB seeding system for wind tunnels involved the accumulation and

rapid release of bubbles inside a piston-cylinder device, operating a single or very few generators (Caridi *et al.*, 2016). Coupling a generator with a piston-cylinder system to accumulate the tracers, Scarano *et al.* (2015) introduced HFSB at a higher rate in a wind tunnel within a volume of approximately 5 litres. However, this approach required large ducts for transport and dispersion, disturbing the free stream uniformity and turbulence intensity. The latter piston-cylinder system was superseded by systems featuring arrays of tens (Gibeau *et al.*, 2020) or hundreds of generators (Scarano *et al.*, 2022). Using a 204-generators seeder, van der Hoek *et al.* (2022) measured the wake of a scaled horizontal-axis wind turbine over a volume of 280 litres. At the Netherlands Aerospace Laboratories (NLR), an array of 3x3 m^2 comprising 400 generators was operated to measure the velocity field around a tilt-rotor model aircraft over 0.7 m^3 (Faleiros, 2021). Finally, the use of HFSB for indoor ventilation (Bluyssen *et al.*, 2021; Kühn *et al.*, 2011) and on-site aerodynamics (Spoelstra *et al.*, 2019) has sparked interest in further upscaling of experiments.

The scattered light of HFSB has been reported to largely exceed that of conventional micron-size PIV tracers, namely 10^4 – 10^5 times (Caridi, 2018). This corresponds with a scaling of the particle image peak intensity with the square of the particle diameter, in agreement with Mie theory of scattering, and an imaging regime governed by diffraction. The above is in contrast with the literature, where such scaling has been long questioned. Just to cite the two most popular books on PIV (Adrian & Westerweel, 2011; Raffel *et al.*, 2018), it is conjectured that beyond a given tracer size (assumed around 100 µm), the increase in scattered light would not increase the particle image peak intensity and therefore not improve the particle detectability (Adrian, 1991). Instead, the excellent light scattering capabilities of HFSB have enabled PIV measurements around large objects, as for instance the experiments of the flow around a tiltrotor aircraft model inside the LLF of DNW, shown in figure 2.5.

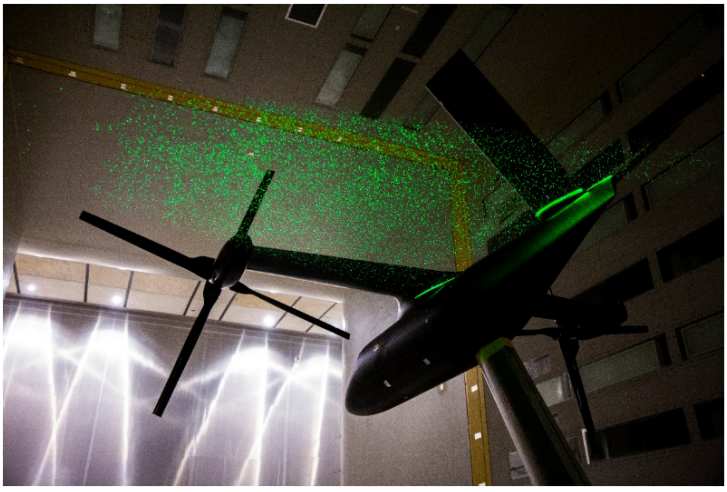

Figure 2.5: PIV measurements around a tiltrotor aircraft model using HFSB as tracers, inside the LLF of DNW. Image reproduced from Faleiros (2021).

From an experimental perspective, the difference in scattering power justifies the large difference in the size (reference length scale from the reported measurement volume) of experiments conducted with conventional PIV tracers in air (figure 2.6 grey cluster) and those making use of HFSB (pink cluster). Overall, the measurement size is found to correlate linearly with the particle tracer diameter, which is demonstrated in chapter 3.

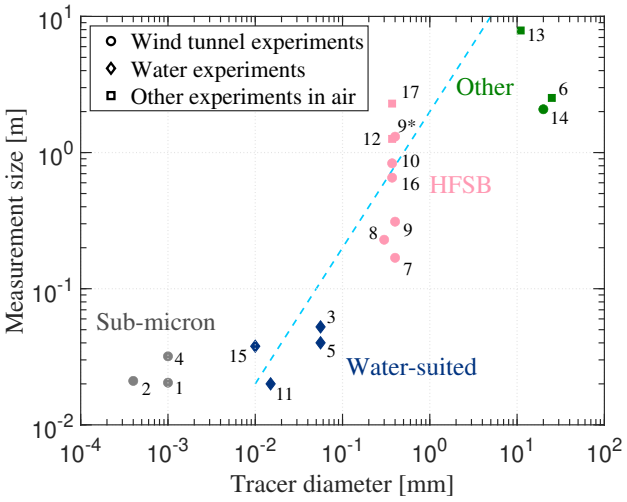

Figure 2.6: Measurement size of PIV experiments versus tracer diameter. Experiments are sorted according to the year of publication. 1 Elsinga *et al.* (2006), 2 Humble *et al.* (2009), 3 Scarano and Poelma (2009), 4 Atkinson *et al.* (2011), 5 A. Schröder *et al.* (2011), 6 Rosi *et al.* (2014), 7 Scarano *et al.* (2015), 8 Caridi *et al.* (2016), 9* Jux *et al.* (2018), 10 Schanz *et al.* (2019), 11 Tokgoz *et al.* (2020), 12 Godbersen *et al.* (2021), 13 Wei *et al.* (2021), 14 Hou *et al.* (2021), 15 van Hout *et al.* (2022), 16 van der Hoek *et al.* (2022), 17 A. Schröder *et al.* (2022). * The total measurement volume combines several views from robotic volumetric PIV.

Despite the interest in experiment upscaling or downscaling (see for instance the work from Barros *et al.*, 2021), the survey of most experiments performed in the past decade shows that HFSB tracers have been used in a relatively narrow range of diameters, namely between 0.3 – 0.6 mm as allowed by the fine control of the relative helium-air flow rates, as discussed in the seminal study by Faleiros *et al.* (2019). Beyond a specific range of *bubbling* production, the generator was reported to either interrupt production or to enter some irregular regimes with a much broader range of sizes and less controlled neutral buoyancy condition. The above work concluded that for a given generator, a max-min ratio (MMR) of bubble diameters not exceeding 1.5 could be practically achieved. The work included in this dissertation revises the main hypothesis of constant generator geometry, in the attempt to significantly extend the MMR for the benefit of measurement upscaling (or downscaling). By doing so, one responds to

experimental needs on two sides: at first, smaller tracers enable volumetric experiments at medium-scale (approximately 1 liter) of fundamental problems (e.g. jets, boundary layers, wakes); secondly, larger tracers will extend further the range of large-scale PIV (several cubic metres) for full-scale on-site applications. Examples of the latter were made in the automotive sector (Hüttig *et al.*, 2023) and for sport aerodynamics (Jux *et al.*, 2018).

2.3. Light reflections

While 3D LPT (A. Schröder & Schanz, 2023) represents the state-of-the-art for volumetric velocimetry techniques, the study of the flow around complex objects remains little explored due to inherent limitations of optical access. The literature abounds with experiments conducted in the bulk of flows like for free jets (Huhn *et al.*, 2018; Violato & Scarano, 2011), near and far wakes (Friedhoff *et al.*, 2021; Scarano *et al.*, 2022) or wall-bounded flows (Bross *et al.*, 2023; A. Schröder *et al.*, 2008), to mention a few. Exceptions have been achieved using index of refraction matching techniques (Bai & Katz, 2014; A. Schröder *et al.*, 2020) or traversing and re-orienting the PIV system, for instance employing robotic 3D PIV (Jux *et al.*, 2018; Schneiders *et al.*, 2018). For moving targets, such as rotors (D. Schröder *et al.*, 2023; Wolf *et al.*, 2024) or animals (Bomphrey *et al.*, 2012; Flammang *et al.*, 2011; Usherwood *et al.*, 2020) the complexity is further increased, and the measurement domains are most commonly limited to the objects' wakes, after these have left the illuminated/imaged region. Volumetric PIV measurements in the vicinity of objects may enable further understanding of fluid-structure interactions and associated loads (Mertens *et al.*, 2023), therefore enriching the current capabilities of such systems. An overview of 3D PIV experiments is listed in table 2.1, based on the presence of objects in the measurement domain, to provide a comprehensive overview of the state-of-the-art.

The problem of optical blockage has been recently addressed by Hysa *et al.* (2024), who considered both the topics of constrained illumination (shadows) and camera occlusion. Volumetric measurements were conducted around a ship model doubling the illumination direction and with a set of 7 imaging cameras, in excess of the standard 4-camera system used for 3D PIV. In this work, the multiplication imaging paradox became clear: the more cameras are added the more occlusions erode the measurement volume. The proposed solution was partitioning the system into camera sub groups and recombining the results afterwards. An elegant solution to the paradox has been offered by Wieneke and Rockstroh (2024), who incorporate the object information into the optical model (ray tracing) used for particle detection. With this technique, the formation of camera sub-groups is not necessary and a monolithic system comprises the whole set of cameras. Controlling the object position in the measurement domain is paramount in the above approach and techniques to mark and verify position and shape have been discussed and demonstrated in the study of Hendriksen *et al.* (2024) leading to the so-called object-aware Lagrangian particle tracking (OA-LPT). As a result, to date, the problems of shadow formation and optical blockage can be considered as solved.

Another source of optical interference arises from light reflections at the objects'

surface. Similar to the previous case of domain erosion due to imaging blockage (Hysa *et al.*, 2024), light reflections also introduce a paradox: when illumination and imaging directions are multiplied, the regions blinded by excessive illumination progressively erode the measurement domain. In this case, modelling the mechanism producing blinded regions is of formidable complexity as it requires a precise combination of object detection, ray tracing from illumination to imager and modelling reflective/diffusive light-surface interactions.

Bulk flow investigations		Object in view	
Research group	Research topic	Research group	Research topic
Flammang *et al.* (2011)	Freely swimming fish wake	Jux *et al.* (2018)	Full-scale cylist model, using robotic 3D PIV
Bomphrey *et al.* (2012)	Desert locust wakes	A. Schröder *et al.* (2020)	Wall-mounted cube, using refractive index matching
Usherwood *et al.* (2020)	Free flying gliding raptor wake	Mertens *et al.* (2023)	Flexible wing, moving the 3D PIV system around the object
Friedhoff *et al.* (2021)	Ducted propeller wake	Hysa *et al.* (2024)	Ship model, partitioning a redundant 3D PIV system
Scarano *et al.* (2022)	Cylinder wake	Hendriksen *et al.* (2024)	Various static objects, using OA-LPT
D. Schröder *et al.* (2023)	Tip vortex evolution		
Wolf *et al.* (2024)	Free flying quadcopter wake		

Table 2.1: List of volumetric PIV experiments with and without the presence of objects in the measurement domain.

The problem of light reflections in PIV has been extensively investigated, mostly for planar PIV systems, where the reflection features a bright stripe produced by the laser sheet against the surface. Examples of this are given in figure 2.7, for a cavity flow experiment (left) and a flapping wing (right). A gamut of best-practice approaches is available from the literature: Kähler *et al.* (2006) advise to direct the illumination surface-parallel when possible. When the latter is not possible, Paterna *et al.* (2013) propose to treat the object surface with light absorbing paint or employing the principle of fluorescence (Depardon *et al.*, 2005). Many other studies have focused on image pre-processing in order to separate the light intensity from the particles and that due to background, surface reflections or even ambient light. Adrian and Westerweel (2011) offer a wide discussion of the subject, with most popular choices exploiting the differences between the dot-like particle signal and the broader intensity distribution of the background. Subtraction of pixel minimum intensity in the time domain is also proven an effective method, and Sciacchitano and Scarano (2014) have proposed a frequency

domain high-pass filter that eliminates slowly-moving signals from time-resolved image recordings. The use of masking (i.e. total cancellation of the overexposed region) approaches, although robust, is only considered for extreme situations (Masullo & Theunissen, 2017), since it involves the loss of velocity information and introduces data gaps.

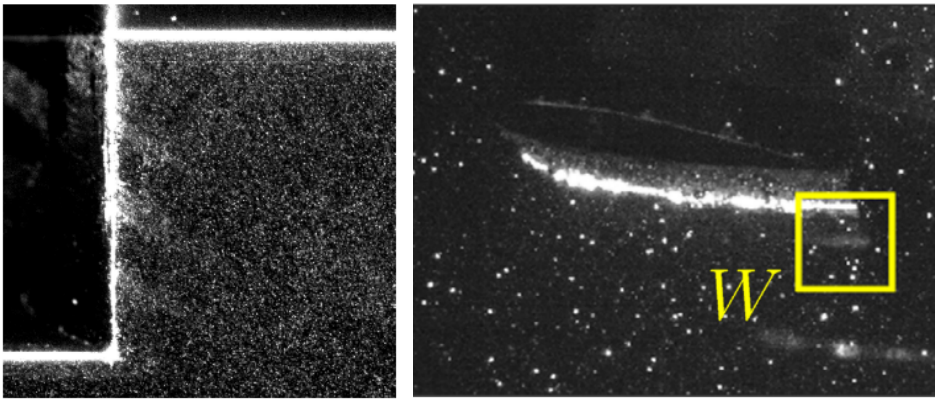

Figure 2.7: Images of light reflections in planar PIV experiments. Cavity flow measurements (left), reproduced from Adatrao and Sciacchitano (2019), and flapping wing investigation (right), adapted from Mendez *et al.* (2017).

The specific treatment of light reflections in 3D PIV measurements has barely been discussed in the literature and most recipes are based on the best practice gained from planar PIV. Topologically, the most prominent change is the shift from reflection lines arising from the impingement of a laser sheet on the surface, to more diffuse reflection regions due to the distributed illumination. However, in 3D measurements, regions of high-intensity negatively affect particle triangulation because in the imaging bundle corresponding to the overexposed image the detection algorithms produces a multitude of false positives (a.k.a. ghost particles, Elsinga *et al.*, 2011), thus locally corrupting the measurement and the particle tracking analysis. Examples of light reflections in volumetric PIV experiments are given in figure 2.8, both for a robotic volumetric PIV situation (left), where the coaxial arrangement of laser illumination and imaging causes severe reflections in the camera, and also a high tomographic aperture experiment using LED-based illumination (right).

2.4. Tracers motion analysis

Several PIV processing algorithms exist that provide velocity information from the particle images, and the choice is heavily dependent on the hardware and recording mode considered in the experiment. An overview of existing recording strategies can be found in Adrian and Westerweel (2011), and a schematic representation is reproduced in figure 2.9. When illuminating the particles with a continuous light source, their motion produces small *streaks* in the camera frame (Zhang *et al.*, 2024). The direction and

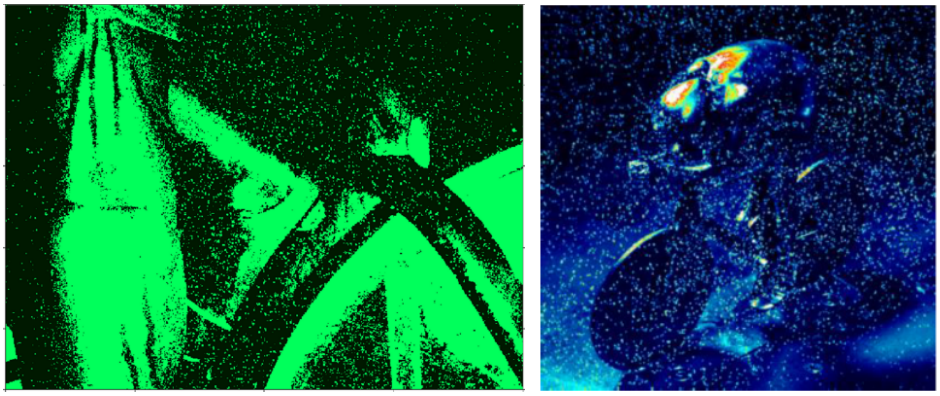

Figure 2.8: Images of light reflections in volumetric PIV experiments. Robotic 3D PIV measurements around a full-scale cyclist (left), reproduced from Jux *et al.* (2018), and object-aware LPT measurements around a scaled cylist model (right), reproduced from Hendriksen *et al.* (2024).

magnitude of the fluid's velocity can be estimated from the orientation and length of the streaks. However, this does not reveal the sign of motion, which may be retrieved by pulse coding approaches (Agüí & Jiménez, 1987) combining *dots* (short illumination pulses) and *streaks* (long illumination pulses).

The use of pulsed light sources, such as pulsed lasers, avoids the motion blur of the particle images. Placing two illumination pulses in a frame (or photographic film) transforms the problem into identifying the particle images belonging to the same physical tracer, and still suffers from directional ambiguity (Adrian, 1986). The use of more pulses with time delays that are not equal is a possible solution (Grant & Liu, 1990).

Using instead double-frame cameras entirely solves the directional ambiguity issue. In the so-called double-frame single-exposure recording mode, by far the most popular one in PIV, one illumination pulse is placed in each of the two frames. For low seeding densities, particle tracking algorithms may be used that pair individual tracers, although the most common is the use of robust statistical evaluation methods based on cross-correlation between the two frames, working on images containing higher levels of particle images. An extension of the double-frame approach is the use of single-exposure multi-frame recordings, given the use of high-speed cameras and illuminators.

2.4.1. Volumetric measurements

Regarding volumetric approaches, tomographic PIV (Elsinga *et al.*, 2006) adopted the common single-exposure double-frame strategy. The additional processing step with respect to planar experiments, i.e., the volumetric reconstruction, set the limit for the achievable seeding density, typically expressed as particles-per-pixel (ppp), around ppp = 0.05, which dictates the spatial resolution of the measured velocity field. Later,

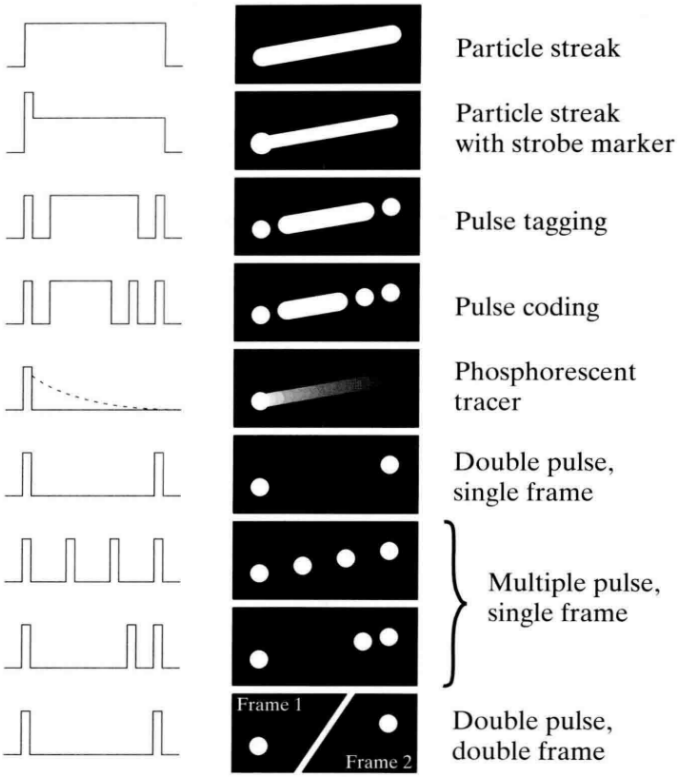

Figure 2.9: Schematic representation of recording strategies for PIV. Reproduced from Adrian and Westerweel (2011).

comparable ppp levels could be successfully reconstructed with the iterative particle reconstruction algorithm (IPR, Wieneke, 2013), a much more efficient approach both in terms of memory requirements and computational processing time. A schematic representation of the IPR algorithm is given in figure 2.10, reproduced from Jahn *et al.* (2021), who proposed a series of advancements to the method that allow for a further increase in the attainable ppp levels, now in the order of ppp ~ 0.1. The IPR method iteratively triangulates particle images in the 3D space to mitigate the reconstruction of spurious particles (ghosts). The outcome is a cloud of scattered particles, compared to a full gridded intensity distribution (in voxel space) produced by tomographic reconstruction.

Shifting from intensity distributions to scattered particles implies a change in the PIV processing algorithm from 3D cross-correlation approaches to particle tracking methods (3D particle tracking velocimetry, 3D-PTV). In this regard, a major breakthrough was the introduction of the so-called Shake-the-Box method (STB, Schanz *et al.*, 2016), a 3D-PTV algorithm (or Lagrangian particle tracking, LPT) capable of dealing with high seeding densities in the order of ppp ~ 0.2, as recently surveyed by A. Schröder and

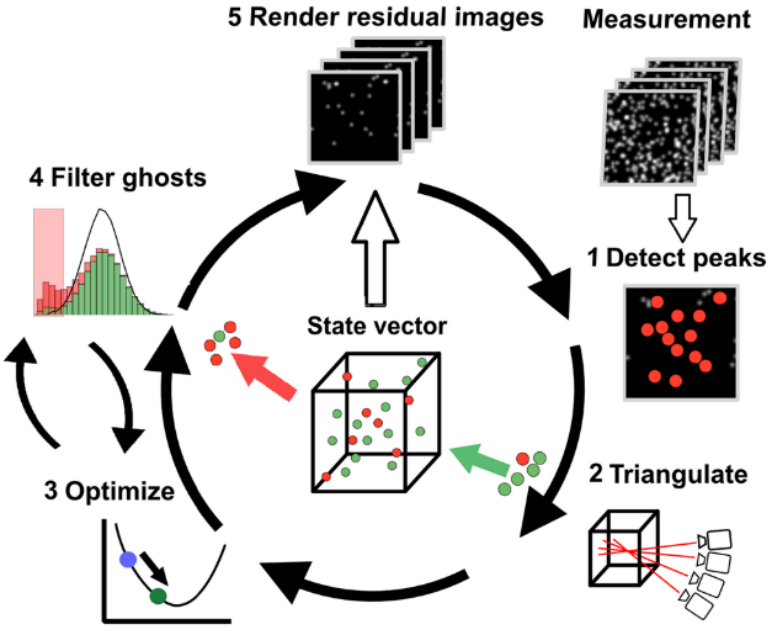

Figure 2.10: Schematic representation of the IPR algorithm. Reproduced from Jahn *et al.* (2021).

Schanz (2023). A schematic representation of the algorithm is given in figure 2.11. STB employs the multi-frame single-exposure recording strategy, thus requiring the use of high-speed imagers and illumination. Particle trajectories are initialized over a few frames from the particle clouds obtained from IPR. Then, these trajectories are extrapolated onto the next frame. The predicted particle locations are corrected for them to match the intensity distribution in the images. Finally, tracked particles are subtracted from the images, effectively reducing the ppp level, simplifying the particle reconstruction step with IPR.

The main caveat of STB is the need for high-speed hardware to finely describe the tracers' motion along their trajectories. The latter requires a small time separation Δt_0 and a fine displacement, compared to the inter-particle distance. The corresponding system requires a relatively high repetition rate, $f = 1/\Delta t_0$, as illustrated in figure 2.12(a). The multi-frame strategy may revert to the more typical double-frame mode for certain applications. For instance, in high-speed flow (e.g. in the compressible regime), otherwise requiring systems repetition rate in the order of 100kHz, unless dedicated burst illumination and imagers are adopted (Beresh *et al.*, 2015; Thurow *et al.*, 2013). For volumetric applications, dual-frame recording has been largely practiced in aerodynamic flows (Saredi *et al.*, 2020), where the measurement conditions (flow velocity, optical magnification, seeding density) do not allow time-resolved recording (Novara *et al.*, 2023; Novara *et al.*, 2016). Figure 2.12(b) illustrates the timing diagram

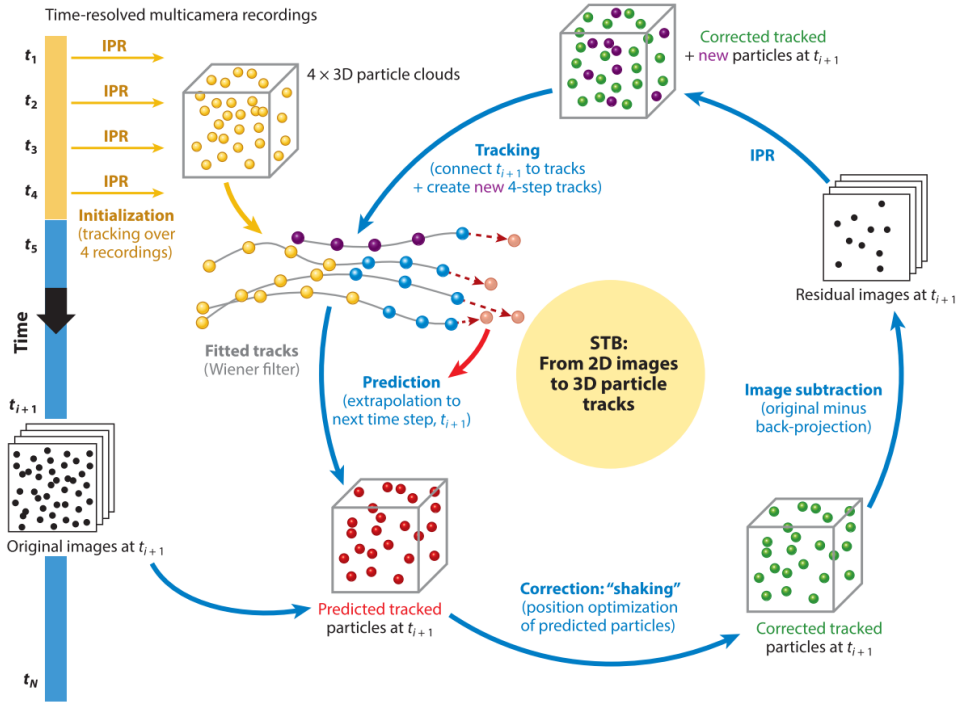

Figure 2.11: Schematic representation of the STB algorithm. Reproduced from A. Schröder and Schanz (2023).

of illumination and image acquisition for the dual-frame recording mode, featuring light pulses around the transition between the two frames. Volumetric measurements around complex objects require multiple, redundant views for volume coverage (Hysa *et al.*, 2024). The latter problem has been largely simplified by the introduction of object-aware particle reconstruction and tracking (Wieneke & Rockstroh, 2024) along with the necessary object registration techniques (Hendriksen *et al.*, 2024). As a result the number of cameras in an experiment has upscaled from the typical set of 4 used in tomographic PIV (Elsinga *et al.*, 2006) to 8 or 12 (Hendriksen *et al.*, 2024). In the latter conditions, it may be argued that the adoption of low repetition rate systems is a more viable option, compared to kilohertz rate imagers, based on data rate, data requirement for statistical convergence and overall system specifications and complexity.

2.4.2. Multi-exposure recording strategies

Despite the versatility of the double-frame recording technique, velocity measurements based on only two pulses suffer from an intrinsic compromise between the random and truncation error (Boillot & Prasad, 1996), in turn limiting the measurement dynamic velocity range (DVR, Adrian, 1997). Varying the time separation also affects measurement robustness in PTV (particle pairing success rate) as well as the

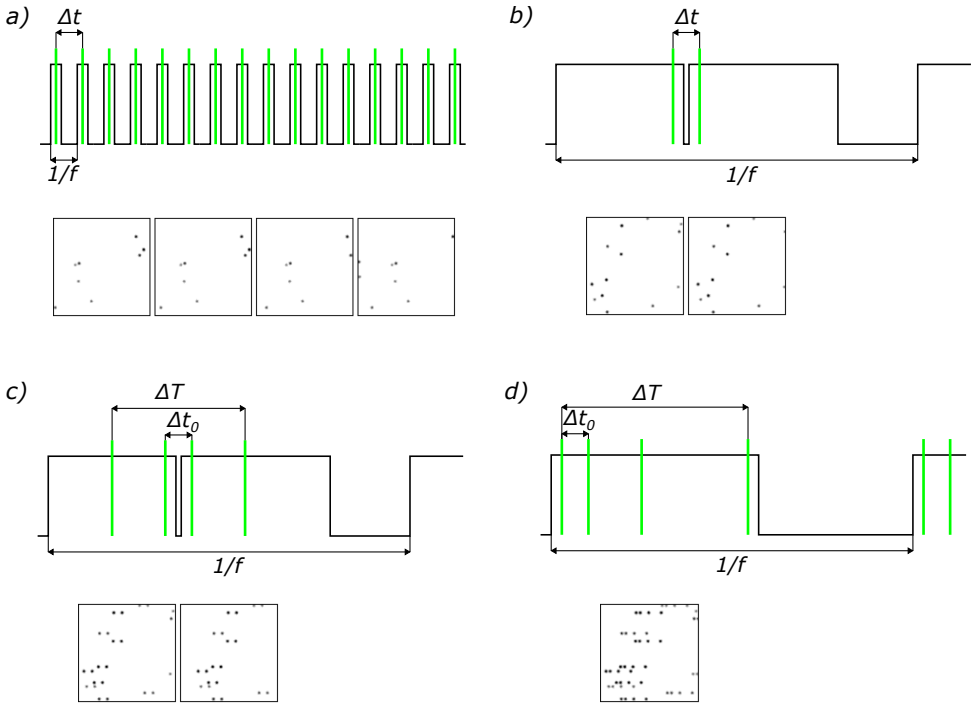

Figure 2.12: Template of illumination pulses and camera exposure, with corresponding image details, for: time-resolved mode (a), double frame with two (b) and four-pulses (c); single frame with four-pulses (d).

signal-to-noise ratio (SNR) of cross-correlation analysis. The compromise is mitigated by adding more samples of the particle position along its trajectory, which is practiced with multi-exposure (ME) techniques, as already introduced in figure 2.9 and discussed in the following.

Multi-exposure (ME) timing strategies with 3 or more illumination pulses offer the possibility of increasing the dynamic range of the measurement over two-pulse double-frame systems, while providing acceleration estimation, relevant for data-assimilation strategies (Godbersen *et al.*, 2024; Schneiders & Scarano, 2016) involving pressure estimation. The analysis of ME recordings stood long as a challenging problem especially for single-frame systems, due to the directional ambiguity of the particle traces (Adrian & Westerweel, 2011; Adrian, 1991). For double-frame recordings, as shown in figure 2.12(c), a four-pulse strategy has been proposed by Novara *et al.* (2019) within the STB framework, using the time information across the two frames to solve said ambiguity. Multiple exposed single-frame recordings would further simplify the hardware requirements and system synchronization (figure 2.9). In the context of 3D-PTV, a recent solution has been proposed that makes use of asymmetric timing templates, as shown in figure 2.12(d), which disambiguate the direction of motion using

kinematic similarity as detection criterion (Scarano *et al.*, 2025).

2.5. Data reduction techniques

From the scattered particle trajectories measured in a volumetric PIV experiment, as for example the ones shown in figure 2.13(left) for the case of a wall-mounted cube (A. Schröder *et al.*, 2020), Cartesian grid reduction (CGR) is a convenient operation to support data inspection as well as for evaluating derivatives (e.g. vorticity, shear rate) or integrals, like velocity circulation and pressure (Van Oudheusden, 2013). While ensemble-averaging of pointwise properties can be achieved at the desired spatial resolution by increasing the length of the measurement series (Agüera et al., 2016, among others), as shown in figure 2.13(right) for the measurements given in figure 2.13(left), the evaluation of the instantaneous flow structures as well as the turbulent vorticity fluctuations are strongly dependent upon the tracers concentration.

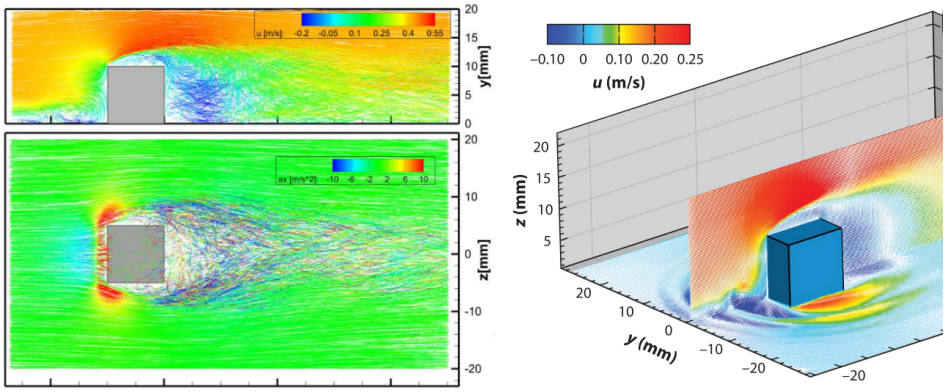

Figure 2.13: Particle trajectories around a wall-mounted cube (left), reproduced from A. Schröder *et al.* (2020), and ensemble-averaged result displayed on a Cartesian grid (right), adapted from A. Schröder and Schanz (2023).

For instantaneous measurements, averaging tracks over small regions leads to gappy velocity fields, requiring refill operations like interpolation or Kriging regression (De Baar *et al.*, 2014). More complex data assimilation methods have been proposed, namely the VIC+ (Schneiders & Scarano, 2016) and FlowFit (Gesemann *et al.*, 2016) techniques, which reduce the constraint imposed on particle concentration. Such methods fit the experimental data and enforce the governing equations of fluid motion. Exploiting the temporal information contained in the particle tracks, in the form of the velocity material derivative, an increased spatial resolution can be attained, and the approach is therefore referred to as *pouring time into space*. An example of a VIC+ application, adapted from the jet flow measurements of Schneiders and Scarano (2016), is given in figure 2.14. From a subset of particle tracks in the jet (figure 2.14-middle), heavily downsampled from the original seeding concentration in the measurement (figure 2.14-left), the data assimilation scheme is able to recover the dominant ring vortices (figure 2.14-right)

present in the flow field.

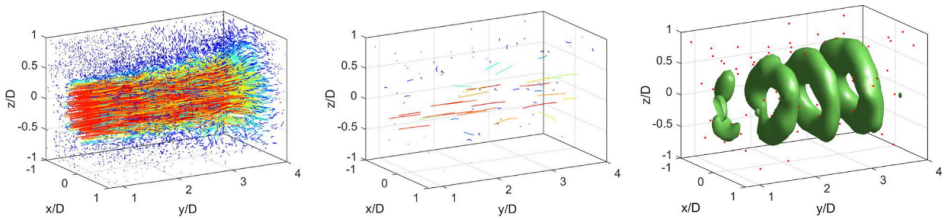

Figure 2.14: Particle trajectories in a jet flow, for full seeding concentration (left) and subsampled by a factor 100 (middle). Visualization of vortical structures from the VIC+ reconstruction of the subsampled tracks (right). Figures adapted from Schneiders and Scarano (2016).

While most of the data assimilation approaches employ solely the instantaneous velocity and acceleration for CGR purposes, recent works are proposing the use of a finite temporal segment (i.e. 4D data assimilation). Within the framework of the vortex-in-cell (VIC) technique (Schneiders *et al.*, 2014), time-segment assimilation, using advection-based models (Jeon *et al.*, 2019) or vorticity transport (Scarano *et al.*, 2022) have proven effective.

Beyond the use of time segments for CGR, Cortina-Fernández *et al.* (2021) approached the problem invoking the proper orthogonal decomposition (POD) method. The data-enhanced particle tracking velocimetry (DEPTV) exploits the statistical properties of full sequence of measured snapshots. In an analogy to the VIC+ methodology, this type of approach will be referred to as *pouring statistics into space*. Borrowing ideas from gappy POD approaches (Raben *et al.*, 2012; Venturi & Karniadakis, 2004) that aim at filling the gaps of cross-correlation PIV measurements, the DEPTV method combines a modal decomposition of gridded data (from cross-correlation analysis of PIV images) and particle tracking information (from the same set of images) to provide a CGR of the particle tracks at increased spatial resolution. The modal decomposition obtained from cross-correlation data is employed to generate a temporal basis on which to project the particle tracks, thus providing a representation of the spatial POD modes at increased resolution. A schematic representation of the method is reproduced in figure 2.15. While initially developed for planar 2D PIV data, the approach has been recently extended to 3D tomographic-PIV experimental data (Tirelli *et al.*, 2023).

The inherent limitation of DEPTV stems from the representation of the temporal coefficients, which arise from the low-resolution cross-correlation analysis. These can be updated with the use of a predictor-corrector iterative approach, where the particle trajectories are reprojected onto the high-resolution spatial basis. The process may be repeated until convergence of the decomposition, providing a better estimate of the temporal information together with enhancing the signal of the spatial structures. Following this rationale, a new method is discussed in chapter 6.

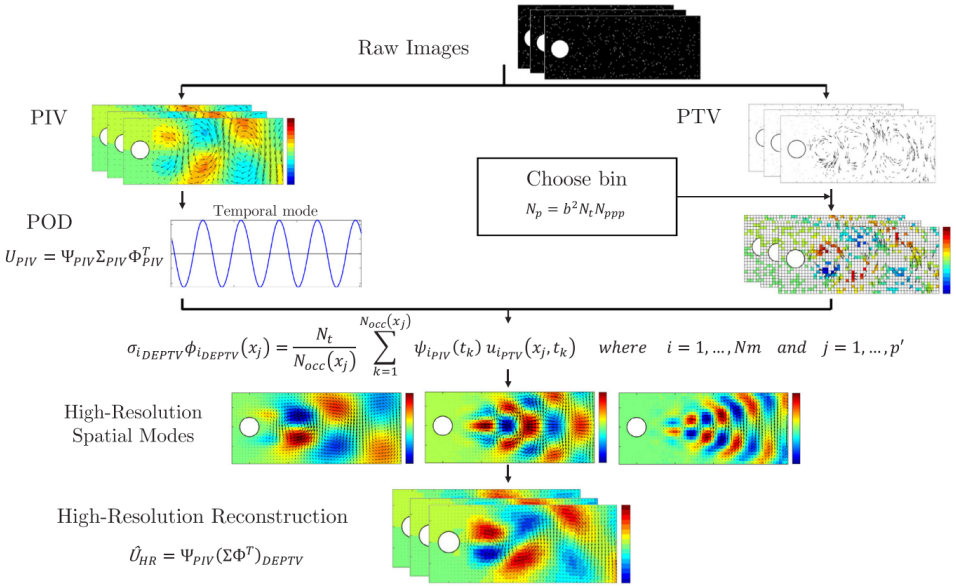

Figure 2.15: Schematic representation of the DEPTV method. Reproduced from Cortina-Fernández *et al.* (2021).

2.6. Research objectives

The main goal of the PhD dissertation is to promote the dissemination of volumetric PIV capabilities at large-scale industrial wind tunnels. For that purpose, a series of challenges currently preventing this possibility are tackled in the different research activities included in the document. The general framework is that of a static volumetric PIV system, composed of a redundant number of cameras and illuminators, such that optical access is achieved throughout the region of interest around the test object. This is opposed to existing solutions such as robotic volumetric PIV, whereby optical access is obtained by traversing the velocimeter, at the cost of measurement accuracy, severity of light reflections or measurement time, among others.

The first research objective is to explore the scalability of HFSB tracers, to enable volumetric PIV measurements at different scales. While the use of HFSB as flow tracers has already allowed experiments in the cubic meter range, slightly bigger bubbles could provide the extra light scattering efficiency necessary to compensate for the large distances between the PIV instrumentation and the region of interest associated with large-scale industrial facilities. On the other hand, smaller bubbles may boost the use of HFSB in research facilities for improved spatial resolution of the measurements, or even enable their use in the compressible flow regime.

The second objective is to develop a robust approach for the treatment of light reflections corrupting the PIV images. For industrial applications, treating the surface of wind tunnel models to prevent the appearance of light reflections might not always be possible. This means that light will reflect back to the cameras, thus corrupting part of

the image, in turn blinding the affected camera along its line of sight. The goal is to develop a method to detect such regions of light reflections and only use unaffected cameras for the particle triangulation step across the measurement volume, thus minimizing the appearance of erroneous particle trajectories and the computational cost.

The third research objective is to evaluate the feasibility of multi-exposure recording strategies for large-scale volumetric PIV measurements. For industrial applications, a system composed of several cameras and illuminators is envisioned. The latter can be fulfilled by distributed LED arrays capable of providing light pulses at a high repetition rate. For the imagers, the cost and simplicity of low repetition rate hardware may be preferred instead. The goal is to verify the tracking accuracy of multi-exposure timing strategies recorded onto a single- or double-frame, confirm the additional dynamic range when compared to the traditional double-frame single-exposure approach, and also explore the estimation of related quantities such as instantaneous pressure from PIV.

The fourth objective is to develop a data assimilation method suited for volumetric particle tracking data, and based on modal analysis of the velocity field. The expected input is a sequence of particle trajectories at low spatial resolution, as for instance measured with a multi-exposure recording strategy on a large-scale volumetric PIV experiment. The goal is twofold: on the one hand, aid the interpretability of complex flow dynamics by inspection of spatial modes at sufficient resolution, and on the other hand, allow for an instantaneous reconstruction of the velocity field at a spatial resolution beyond the one measured, by building a reduced-order model from the dominant modes.

References

Adatrao, S., & Sciacchitano, A. (2019). Elimination of unsteady background reflections in PIV images by anisotropic diffusion. *Measurement Science and Technology*, *30*(3). https://doi.org/10.1088/1361-6501/aafca9

Adrian, R. J. (1997). Dynamic ranges of velocity and spatial resolution of particle image velocimetry. *Measurement Science and Technology*, *8*(12), 1393–1398. https://doi.org/10.1088/0957-0233/8/12/003

Adrian, R. J., & Westerweel, J. (2011). *Particle Image Velocimetry*. Cambridge University Press. https://books.google.nl/books?id=jbDl2-yHbooC

Adrian, R. J. (1984). Scattering particle characteristics and their effect on pulsed laser measurements of fluid flow: speckle velocimetry vs particle image velocimetry. *Applied Optics*, *23*(11), 1690. https://doi.org/10.1364/AO.23.001690

Adrian, R. J. (1986). Image shifting technique to resolve directional ambiguity in double-pulsed velocimetry. *Applied Optics*, *25*(21), 3855. https://doi.org/10.1364/ao.25.003855

Adrian, R. J. (1991). Particle-imaging techniques for experimental fluid mechanics. *Annual Review of Fluid Mechanics*, *23*(1), 261–304. https://doi.org/10.1146/annurev.fl.23.010191.001401

Agüí, J. C., & Jiménez, J. (1987). On the performance of particle tracking. *Journal of Fluid Mechanics*, *185*(5), 447–468. https://doi.org/10.1017/S0022112087003252

Atkinson, C., Coudert, S., Foucaut, J. M., Stanislas, M., & Soria, J. (2011). The accuracy of tomographic particle image velocimetry for measurements

of a turbulent boundary layer. *Experiments in Fluids*, *50*(4), 1031–1056. https://doi.org/10.1007/s00348-010-1004-z

Bai, K., & Katz, J. (2014). On the refractive index of sodium iodide solutions for index matching in PIV. *Experiments in Fluids*, *55*(4). https://doi.org/10.1007/s00348-014-1704-x

Barros, D. C., Duan, Y., Troolin, D. R., & Longmire, E. K. (2021). Air-filled soap bubbles for volumetric velocity measurements. *Experiments in Fluids*, *62*(2), 1–12. https://doi.org/10.1007/s00348-021-03134-6

Beresh, S., Kearney, S., Wagner, J., Guildenbecher, D., Henfling, J., Spillers, R., Pruett, B., Jiang, N., Slipchenko, M., Mance, J., & Roy, S. (2015). Pulse-burst PIV in a high-speed wind tunnel. *Measurement Science and Technology*, *26*(9). https://doi.org/10.1088/0957-0233/26/9/095305

Bluyssen, P. M., Ortiz, M., & Zhang, D. (2021). The effect of a mobile HEPA filter system on 'infectious' aerosols, sound and air velocity in the SenseLab. *Building and Environment*, *188*(December 2020), 107475. https://doi.org/10.1016/j.buildenv.2020.107475

Boillot, A., & Prasad, A. K. (1996). Optimization procedure for pulse separation in cross-correlation PIV. *Experiments in Fluids*, *21*(2), 87–93. https://doi.org/10.1007/BF00193911

Bomphrey, R. J., Henningsson, P., Michaelis, D., & Hollis, D. (2012). Tomographic particle image velocimetry of desert locust wakes: instantaneous volumes combine to reveal hidden vortex elements and rapid wake deformation. *Journal of The Royal Society Interface*, *9*(77), 3378–3386. https://doi.org/10.1098/rsif.2012.0418

Bosbach, J., Kühn, M., & Wagner, C. (2009). Large scale particle image velocimetry with helium filled soap bubbles. *Experiments in Fluids*, *46*(3), 539–547. https://doi.org/10.1007/s00348-008-0579-0

Bross, M., Schanz, D., Novara, M., Eich, F., Schröder, A., & Kähler, C. J. (2023). Turbulent superstructure statistics in a turbulent boundary layer with pressure gradients. *European Journal of Mechanics, B/Fluids*, *101*, 209–218. https://doi.org/10.1016/j.euromechflu.2023.05.010

Caridi, G. C. A. (2018). *Development and application of helium-filled soap bubbles for large-scale PIV experiments in aerodynamics* [Doctoral dissertation, Delft University of Technology]. https://doi.org/10.4233/uuid:effc65f6-34df-4eac-8ad9-3fdb22a294dc

Caridi, G. C. A., Ragni, D., Sciacchitano, A., & Scarano, F. (2016). HFSB-seeding for large-scale tomographic PIV in wind tunnels. *Experiments in Fluids*, *57*(12), 1–13. https://doi.org/10.1007/s00348-016-2277-7

Cortina-Fernández, J., Sanmiguel Vila, C., Ianiro, A., & Discetti, S. (2021). From sparse data to high-resolution fields: ensemble particle modes as a basis for high-resolution flow characterization. *Experimental Thermal and Fluid Science*, *120*(May 2020), 110178. https://doi.org/10.1016/j.expthermflusci.2020.110178

De Baar, J. H., Percin, M., Dwight, R. P., Van Oudheusden, B. W., & Bijl, H. (2014). Kriging regression of PIV data using a local error estimate. *Experiments in Fluids*, *55*(1). https://doi.org/10.1007/s00348-013-1650-z

Depardon, S., Lasserre, J. J., Boueilh, J. C., Brizzi, L. E., & Borée, J. (2005). Skin friction pattern analysis using near-wall PIV. *Experiments in Fluids*, *39*(5), 805–818. https://doi.org/10.1007/s00348-005-0014-8

Elsinga, G. E., Scarano, F., Wieneke, B., & Van Oudheusden, B. W. (2006). Tomographic particle image velocimetry. *Experiments in Fluids*, *41*(6), 933–947. https://doi.org/10.1007/s00348-006-0212-z

Elsinga, G. E., Westerweel, J., Scarano, F., & Novara, M. (2011). On the velocity of ghost particles and the bias errors in Tomographic-PIV. *Experiments in Fluids*, *50*(4), 825–838. https://doi.org/10.1007/s00348-010-0930-0

Faleiros, D. E. (2021). *Soap bubbles for large-scale PIV Generation, control and tracing accuracy* [Doctoral dissertation, Delft University of Technology]. https://doi.org/10.4233/uuid:c579128f-9e96-4e9e-9997-6ce9486e1e25

Faleiros, D. E., Tuinstra, M., Sciacchitano, A., & Scarano, F. (2018). Helium-filled soap bubbles tracing fidelity in wall-bounded turbulence. *Experiments in Fluids*, *59*(3), 1–13. https://doi.org/10.1007/s00348-018-2502-7

Faleiros, D. E., Tuinstra, M., Sciacchitano, A., & Scarano, F. (2019). Generation and control of helium-filled soap bubbles for PIV. *Experiments in Fluids*, *60*(3). https://doi.org/10.1007/s00348-019-2687-4

Flammang, B. E., Lauder, G. V., Troolin, D. R., & Strand, T. E. (2011). Volumetric imaging of fish locomotion. *Biology Letters*, *7*(5), 695–698. https://doi.org/10.1098/rsbl.2011.0282

Friedhoff, B., Roettig, F., Wennemar, K., Hoyer, K., Beslac, R., Hesseling, C., & Beck, T. (2021). Comparison of stereoscopic particle image velocimetry and volumetric particle tracking velocimetry in the wake of a ducted propeller. *Ocean Engineering*, *234*(January 2020). https://doi.org/10.1016/j.oceaneng.2021.109291

Gesemann, S., Huhn, F., Schanz, D., & Schröder, A. (2016). From Particle Tracks to Velocity, Acceleration and Pressure Fields Using B-Splines and Penalties. *18th International Symposium on the Application of Laser and Imaging Techniques to Fluid Mechanics*. http://arxiv.org/abs/1510.09034

Gibeau, B., Gingras, D., & Ghaemi, S. (2020). Evaluation of a full-scale helium-filled soap bubble generator. *Experiments in Fluids*, *61*(2), 1–18. https://doi.org/10.1007/s00348-019-2853-8

Godbersen, P., Bosbach, J., Schanz, D., & Schröder, A. (2021). Beauty of turbulent convection: A particle tracking endeavor. *Physical Review Fluids*, *6*(11), 4–7. https://doi.org/10.1103/PhysRevFluids.6.110509

Godbersen, P., Gesemann, S., Schanz, D., & Schröder, A. (2024). FlowFit3: Efficient Data Assimilation Of LPT Measurements. *Proceedings of the International Symposium on the Application of Laser and Imaging Techniques to Fluid Mechanics*, *21*(1), 1–14. https://doi.org/10.55037/lxlaser.21st.216

Grant, I., & Liu, A. (1990). Directional ambiguity resolution in particle image velocimetry by pulse tagging. *Experiments in Fluids*, *10*(2-3), 71–76. https://doi.org/10.1007/BF00215013

Hale, R. W., Tan, P., Stowell, R. C., & Ordway, D. E. (1971). *Development of an integrated system for flow visualization in air using neutrally- buoyant bubbles* (tech. rep. No. SAI-RR 7107). Sage Action, Inc. Ithaca, New York.

Hendriksen, L. A., Sciacchitano, A., & Scarano, F. (2024). Object registration techniques for 3D particle tracking. *Measurement Science and Technology*, *35*(12). https://doi.org/10.1088/1361-6501/ad715c

Herman, G. T., & Lent, A. (1976). Iterative reconstruction algorithms. *Computers in Biology and Medicine*, *6*(4), 273–294. https://doi.org/10.1016/0010-4825(76)90066-4

Hou, J., Kaiser, F., Sciacchitano, A., & Rival, D. E. (2021). A novel single-camera approach to large-scale, three-dimensional particle tracking based on glare-point spacing. *Experiments in Fluids*, *62*(5). https://doi.org/10.1007/s00348-021-03178-8

Huhn, F., Schanz, D., Manovski, P., Gesemann, S., & Schröder, A. (2018). Time-resolved large-scale volumetric pressure fields of an impinging jet from dense Lagrangian particle tracking. *Experiments in Fluids*, *59*(5), 1–16. https://doi.org/10.1007/s00348-018-2533-0

Humble, R. A., Elsinga, G. E., Scarano, F., & van Oudheusden, B. W. (2009). Three-dimensional instantaneous structure of a shock wave/turbulent boundary layer interaction. *Journal of Fluid Mechanics*, *622*, 33–62. https://doi.org/10.1017/S0022112008005090

Hüttig, S., Gericke, T., Sciacchitano, A., & Akkermans, R. (2023). Automotive on-road flow quantification with a large scale Stereo-PIV setup. *Proceedings of the 15th International Symposium on Particle Image Velocimetry*.

Hysa, I., Tuinstra, M., Sciacchitano, A., Scarano, F., van der Meulen, M. J., Rockstroh, T., & Roosenboom, E. W. (2024). A multi-directional redundant 3D-LPT system for ship–flight–deck wind interactions. *Experiments in Fluids*, *65*(8), 1–15. https://doi.org/10.1007/s00348-024-03867-0

Jahn, T., Schanz, D., & Schröder, A. (2021). Advanced iterative particle reconstruction for Lagrangian particle tracking. *Experiments in Fluids*, *62*(8), 1–24. https://doi.org/10.1007/s00348-021-03276-7

Jeon, Y. J., Müller, M., Michaelis, D., & Wieneke, B. (2019). Data assimilation-based flow field reconstruction from particle tracks over multiple time steps. *13th International Symposium on Particle Image Velocimetry*, 1–8.

Jux, C., Sciacchitano, A., & Scarano, F. (2020). Flow pressure evaluation on generic surfaces by robotic volumetric PTV. *Measurement Science and Technology*, *31*(10). https://doi.org/10.1088/1361-6501/ab8f46

Jux, C., Sciacchitano, A., Schneiders, J. F., & Scarano, F. (2018). Robotic volumetric PIV of a full-scale cyclist. *Experiments in Fluids*, *59*(4), 1–15. https://doi.org/10.1007/s00348-018-2524-1

Kähler, C. J., Scholz, U., & Ortmanns, J. (2006). Wall-shear-stress and near-wall turbulence measurements up to single pixel resolution by means of long-distance micro-PIV. *Experiments in Fluids*, *41*(2), 327–341. https://doi.org/10.1007/s00348-006-0167-0

Kerho, M. F., & Bragg, M. B. (1994). Neutrally buoyant bubbles used as flow tracers in air. *Experiments in Fluids*, *16*(6), 393–400. https://doi.org/10.1007/BF00202064

Kühn, M., Ehrenfried, K., Bosbach, J., & Wagner, C. (2011). Large-scale tomographic particle image velocimetry using helium-filled soap bubbles. *Experiments in Fluids*, *50*(4), 929–948. https://doi.org/10.1007/s00348-010-0947-4

Maas, H. G., Gruen, A., & Papantoniou, D. (1993). Particle tracking velocimetry in three-dimensional flows - Part 1. Photogrammetric determination of particle coordinates. *Experiments in Fluids*, *15*(2), 133–146. https://doi.org/10.1007/BF00190953

Malik, N. A., Dracos, T., & Papantoniou, D. A. (1993). Particle tracking velocimetry in three-dimensional flows - Part II: Particle tracking. *Experiments in Fluids*, *15*(4-5), 279–294. https://doi.org/10.1007/BF00223406

Masullo, A., & Theunissen, R. (2017). Automated mask generation for PIV image analysis based on pixel intensity statistics. *Experiments in Fluids*, *58*(6), 1–11. https://doi.org/10.1007/s00348-017-2357-3

Mendez, M. A., Raiola, M., Masullo, A., Discetti, S., Ianiro, A., Theunissen, R., & Buchlin, J. M. (2017). POD-based background removal for particle image velocimetry. *Experimental Thermal and Fluid Science*, *80*, 181–192. https://doi.org/10.1016/j.expthermflusci.2016.08.021

Mertens, C., Costa Fernández, J. L., Sodja, J., Sciacchitano, A., & van Oudheusden, B. W. (2023). Nonintrusive Experimental Aeroelastic Analysis of a Highly Flexible Wing. *AIAA Journal*, *61*(7), 1–16. https://doi.org/10.2514/1.j062476

Meynart, R. (1983). Instantaneous velocity field measurements in unsteady gas flow by speckle velocimetry. *Applied Optics*, *22*(4), 535. https://doi.org/10.1364/ao.22.000535

Mitrotta, F., Sodja, J., & Sciacchitano, A. (2022). On the combined flow and structural measurements via robotic volumetric PTV. *Measurement Science and Technology*, *33*(4). https://doi.org/10.1088/1361-6501/ac41dd

Nishino, K., Kasagi, N., & Hirata, M. (1989). Three-dimensional particle tracking velocimetry based on automated digital image processing. *Journal of Fluids Engineering, Transactions of the ASME*, *111*(4), 384–391. https://doi.org/10.1115/1.3243657

Novara, M., Schanz, D., & Schröder, A. (2023). Two-Pulse 3D particle tracking with Shake-The-Box. *Experiments in Fluids*, *64*(5), 1–21. https://doi.org/10.1007/s00348-023-03634-7

Novara, M., Schanz, D., Geisler, R., Gesemann, S., Voss, C., & Schröder, A. (2019). Multi-exposed recordings for 3D Lagrangian particle tracking with Multi-Pulse Shake-The-Box. *Experiments in Fluids*, *60*(3), 1–19. https://doi.org/10.1007/s00348-019-2692-7

Novara, M., Schanz, D., Reuther, N., Kähler, C. J., & Schröder, A. (2016). Lagrangian 3D particle tracking in high-speed flows: Shake-The-Box for multi-pulse systems. *Experiments in Fluids*, *57*(8), 1–20. https://doi.org/10.1007/s00348-016-2216-7

Paterna, E., Moonen, P., Dorer, V., & Carmeliet, J. (2013). Mitigation of surface reflection in PIV measurements. *Measurement Science and Technology*, *24*(5). https://doi.org/10.1088/0957-0233/24/5/057003

Percin, M., & van Oudheusden, B. W. (2015). Three-dimensional flow structures and unsteady forces on pitching and surging revolving flat plates. *Experiments in Fluids*, *56*(2), 1–19. https://doi.org/10.1007/s00348-015-1915-9

Porcar Galan, L., Grille Guerra, A., Sciacchitano, A., & Scarano, F. (2024). Light Reflections Detection And Correction For Robotic Volumetric PIV. *Proceedings of the International Symposium on the Application of Laser and Imaging Techniques to Fluid Mechanics*, *21*, 1–19. https://doi.org/10.55037/lxlaser.21st.59

Raben, S. G., Charonko, J. J., & Vlachos, P. P. (2012). Adaptive gappy proper orthogonal decomposition for particle image velocimetry data reconstruction. *Measurement Science and Technology*, *23*(2). https://doi.org/10.1088/0957-0233/23/2/025303

Raffel, M., Willert, C. E., Scarano, F., Kähler, C. J., Wereley, S. T., & Kompenhans, J. (2018). *Particle Image Velocimetry: A Practical Guide*. Springer International Publishing. https://doi.org/10.1007/978-3-319-68852-7

Rosi, G. A., Sherry, M., Kinzel, M., & Rival, D. E. (2014). Characterizing the lower log region of the atmospheric surface layer via large-scale particle tracking velocimetry. *Experiments in Fluids*, *55*(5). https://doi.org/10.1007/s00348-014-1736-2

Saredi, E., Sciacchitano, A., & Scarano, F. (2020). Multi-Δt 3D-PTV based on Reynolds decomposition. *Measurement Science and Technology*, *31*(8), 084005. https://doi.org/10.1088/1361-6501/ab803d

Scarano, F. (2013). Tomographic PIV: Principles and practice. *Measurement Science and Technology*, *24*(1). https://doi.org/10.1088/0957-0233/24/1/012001

Scarano, F., Ghaemi, S., Caridi, G. C. A., Bosbach, J., Dierksheide, U., & Sciacchitano, A. (2015). On the use of helium-filled soap bubbles for large-scale tomographic PIV in wind tunnel experiments. *Experiments in Fluids*, *56*(2). https://doi.org/10.1007/s00348-015-1909-7

Scarano, F., Hysa, I., Grille Guerra, A., Tuinstra, M., & Sciacchitano, A. (2025). Asymmetric time sequence for multiple-exposure 3D PTV. *Experiments in Fluids*, *66*(4), 74. https://doi.org/10.1007/s00348-025-03993-3

Scarano, F., & Poelma, C. (2009). Three-dimensional vorticity patterns of cylinder wakes. *Experiments in Fluids*, *47*(1), 69–83. https://doi.org/10.1007/s00348-009-0629-2

Scarano, F., Schneiders, J. F. G., Saiz, G. G., & Sciacchitano, A. (2022). Dense velocity reconstruction with VIC-based time-segment assimilation. *Experiments in Fluids*, *63*(6), 96. https://doi.org/10.1007/s00348-022-03437-2

Schanz, D., Gesemann, S., & Schröder, A. (2016). Shake-The-Box: Lagrangian particle tracking at high particle image densities. *Experiments in Fluids*, *57*(5), 70. https://doi.org/10.1007/s00348-016-2157-1

Schanz, D., Novara, M., Geisler, R., Agocs, J., Eich, F., Bross, M., Kähler, C. J., & Schröder, A. (2019). Large-scale volumetric characterization of a turbulent boundary layer flow. *13th International Symposium on Particle Image Velocimetry – ISPIV 2019*, (July).

Schneiders, J. F., Dwight, R. P., & Scarano, F. (2014). Time-supersampling of 3D-PIV measurements with vortex-in-cell simulation. *Experiments in Fluids*, *55*(3). https://doi.org/10.1007/s00348-014-1692-x

Schneiders, J. F., & Scarano, F. (2016). Dense velocity reconstruction from tomographic PTV with material derivatives. *Experiments in Fluids*, *57*(9), 1–22. https://doi.org/10.1007/s00348-016-2225-6

Schneiders, J. F., Scarano, F., Jux, C., & Sciacchitano, A. (2018). Coaxial volumetric velocimetry. *Measurement Science and Technology*, *29*(6). https://doi.org/10.1088/1361-6501/aab07d

Schröder, A., Geisler, R., Staack, K., Elsinga, G. E., Scarano, F., Wieneke, B., Henning, A., Poelma, C., & Westerweel, J. (2011). Eulerian and Lagrangian views of a turbulent boundary layer flow using time-resolved tomographic PIV. *Experiments in Fluids*, *50*(4), 1071–1091. https://doi.org/10.1007/s00348-010-1014-x

Schröder, A., Schanz, D., Bosbach, J., Novara, M., Geisler, R., Agocs, J., & Kohl, A. (2022). Large-scale volumetric flow studies on transport of aerosol particles using a breathing human model with and without face protections. *Physics of Fluids*, *34*(3). https://doi.org/10.1063/5.0086383

Schröder, A., Willert, C., Schanz, D., Geisler, R., Jahn, T., Gallas, Q., & Leclaire, B. (2020). The flow around a surface mounted cube: a characterization by time-resolved PIV, 3D Shake-The-Box and LBM simulation. *Experiments in Fluids*, *61*(9). https://doi.org/10.1007/s00348-020-03014-5

Schröder, A., Geisler, R., Elsinga, G. E., Scarano, F., & Dierksheide, U. (2008). Investigation of a turbulent spot and a tripped turbulent boundary layer flow using time-resolved tomographic PIV. *Experiments in Fluids*, *44*(2), 305–316. https://doi.org/10.1007/s00348-007-0403-2

Schröder, A., & Schanz, D. (2023). 3D Lagrangian Particle Tracking in Fluid Mechanics. *Annual Review of Fluid Mechanics*, *55*(1), 511–540. https://doi.org/10.1146/annurev-fluid-031822-041721

Schröder, D., Leweke, T., & Stumpf, E. (2023). High-speed volumetric particle tracking measurements of unstable helical vortex pairs. *Experiments in Fluids*, *64*(8), 1–14. https://doi.org/10.1007/s00348-023-03679-8

Sciacchitano, A., & Scarano, F. (2014). Elimination of PIV light reflections via a temporal high pass filter. *Measurement Science and Technology*, *25*(8), 084009. https://doi.org/10.1088/0957-0233/25/8/084009

Spoelstra, A., de Martino Norante, L., Terra, W., Sciacchitano, A., & Scarano, F. (2019). On-site cycling drag analysis with the Ring of Fire. *Experiments in Fluids*, *60*(6), 90. https://doi.org/10.1007/s00348-019-2737-y

Thurow, B., Jiang, N., & Lempert, W. (2013). Review of ultra-high repetition rate laser diagnostics for fluid dynamic measurements. *Measurement Science and Technology*, *24*(1). https://doi.org/10.1088/0957-0233/24/1/012002

Tirelli, I., Solera-Rico, A., Guemes, A., Sanmiguel Vila, C., Ianiro, A., & Discetti, S. (2023). Assessment of data-driven 3D PTV techniques. *15th International Symposium on Particle Image Velocimetry – ISPIV 2023 June 19–21, 2023, San Diego, California, USA*.

Tokgoz, S., Elsinga, G. E., Delfos, R., & Westerweel, J. (2020). Large-scale structure transitions in turbulent Taylor–Couette flow. *Journal of Fluid Mechanics*, *903*. https://doi.org/10.1017/jfm.2020.679

Usherwood, J. R., Cheney, J. A., Song, J., Windsor, S. P., Stevenson, J. P., Dierksheide, U., Nila, A., & Bomphrey, R. J. (2020). High aerodynamic lift from the tail reduces drag in gliding raptors. *Journal of Experimental Biology*, *223*(3). https://doi.org/10.1242/jeb.214809

van Hout, R., Hershkovitz, A., Elsinga, G. E., & Westerweel, J. (2022). Combined three-dimensional flow field measurements and motion tracking of freely moving spheres in a turbulent boundary layer. *Journal of Fluid Mechanics*, *944*, 1–39. https://doi.org/10.1017/jfm.2022.477

van der Hoek, D., Frederik, J., Huang, M., Scarano, F., Simao Ferreira, C., & Van Wingerden, J. W. (2022). Experimental analysis of the effect of dynamic induction control on a wind turbine wake. *Wind Energy Science*, *7*(3), 1305–1320. https://doi.org/10.5194/wes-7-1305-2022

Van Oudheusden, B. W. (2013). PIV-based pressure measurement. *Measurement Science and Technology*, *24*(3). https://doi.org/10.1088/0957-0233/24/3/032001

Venturi, D., & Karniadakis, G. E. (2004). Gappy data and reconstruction procedures for flow past a cylinder. *Journal of Fluid Mechanics*, *519*, 315–336. https://doi.org/10.1017/S0022112004001338

Violato, D., & Scarano, F. (2011). Three-dimensional evolution of flow structures in transitional circular and chevron jets. *Physics of Fluids*, *23*(12). https://doi.org/10.1063/1.3665141

Wei, N. J., Brownstein, I. D., Cardona, J. L., Howland, M. F., & Dabiri, J. O. (2021). Near-wake structure of full-scale vertical-axis wind turbines. *Journal of Fluid Mechanics*, *914*, 1–40. https://doi.org/10.1017/jfm.2020.578

Westerweel, J. (1993). *Digital particle image velocimetry: Theory and application* [Doctoral dissertation, Delft University of Technology].

Westerweel, J., Elsinga, G. E., & Adrian, R. J. (2013). Particle image velocimetry for complex and turbulent flows. *Annual Review of Fluid Mechanics*, *45*, 409–436. https://doi.org/10.1146/annurev-fluid-120710-101204

Wieneke, B., & Rockstroh, T. (2024). Lagrangian particle tracking in the presence of obstructing objects. *Measurement Science and Technology*, *35*(5), 055303. https://doi.org/10.1088/1361-6501/ad289d

Wieneke, B. (2013). Iterative reconstruction of volumetric particle distribution. *Measurement Science and Technology*, *24*(2). https://doi.org/10.1088/0957-0233/24/2/024008

Willert, C. E., & Gharib, M. (1991). Digital particle image velocimetry. *Experiments in Fluids*, *10*(4), 181–193. https://doi.org/10.1007/BF00190388

Willert, C. (1997). Stereoscopic digital particle image velocimetry for application in wind tunnel flows. *Measurement Science and Technology*, *8*(12), 1465–1479. https://doi.org/10.1088/0957-0233/8/12/010

Wolf, C. C., Schanz, D., Schwarz, C., Heintz, A., Bosbach, J., Strübing, T., & Schröder, A. (2024). Volumetric wake investigation of a free-flying quadcopter using Shake-The-Box Lagrangian particle tracking. *Experiments in Fluids*, *65*(10), 152. https://doi.org/10.1007/s00348-024-03880-3

Zhang, D., Tropea, C., Zhou, W., Cai, T., Huang, H., Dong, X., Gao, L., & Cai, X. (2024). Particle streak velocimetry: a review. *Experiments in Fluids*, *65*(9). https://doi.org/10.1007/s00348-024-03857-2

3

On the scalability of helium-filled soap bubbles flow tracers

The development of sub-millimetre helium-filled soap bubbles (HFSB) has enabled a significant upscale in the achievable measurement volume for volumetric PIV in air flows. The first part of this chapter reviews the working principle of the HFSB generator, based on the supply of helium, bubble fluid solution (BFS) and air, to complete the description of the bubble generation process (section 3.1). Furthermore, the scaling behaviour based on gas flow rates and on exit orifice variation is discussed, both using a developed theoretical model and also bubble visualization experiments (section 3.3). It is shown that production of neutrally-buoyant HFSB is possible in the range of diameters 0.16 mm – 2.7 mm (section 3.4).

The second part of the chapter focuses on the impact of the tracer size to the image properties. A theoretical model is proposed and discussed first, followed by light scattering experiments to confirm the validity of the hypothesis considered (section 3.2). It is shown that increasing the bubble diameter allows increasing both the measurement domain as well as the working distance of the imagers to 10 m and beyond (section 3.4). Finally, a best-practice criterion is proposed for the selection of the adequate tracer size for a given volumetric PIV experiment.

Parts of this chapter have been published in: Grille Guerra, A., Scarano, F., & Sciacchitano, A. (2024). On the scalability of helium-filled soap bubbles for volumetric PIV. *Experiments in Fluids*, *65*(2), 23. https://doi.org/10.1007/s00348-024-03760-w

3.1. Working principle of HFSB generation

The working principle of a generic HFSB generator is sketched in figure 3.1(left). Helium (light blue) exits from the inner duct, surrounded by a ring-shaped duct supplying the bubble fluid solution (BFS, in pink). On the outer ring, the air flow has two main functions: 1) the air flow act as a buffer (avoiding contact) between the soap film and the outer surface of the duct. As a result, it becomes possible to converge the streamlines and reduce the size of the bubbles; 2) the air flow, similar to that of helium acts on the outer side of the BFS flow and the shear force results in its acceleration and thinning. This effect is important to obtain a thin BFS film such to attain neutral buoyancy of the bubble. A fluid supply unit (FSU) provides the desired helium, BFS and air volume flow rates (Q_{He}, Q_{BFS} and Q_{air} respectively), while the conditions at the exit are dictated by the orifice diameter, d_o.

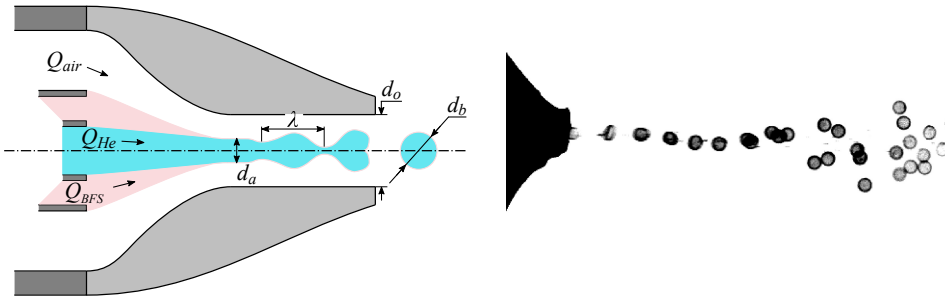

Figure 3.1: Schematic illustration of an HFSB generator exit region (left) and shadow visualization of HFSB production (right).

From the visualization studies of Faleiros *et al.* (2019), it emerges that HFSB achieve a spherical shape a few diameters after release from the orifice, which is corroborated by the shadow image shown in figure 3.1(right). This allows expressing the bubble volume V_b simply as:

$$V_b = \frac{\pi}{6} d_b^3, \tag{3.1}$$

where d_b is the bubble diameter. The bubble volume is composed of helium and a thin layer (less than a micrometre, Kerho and Bragg, 1994) of BFS. In the hypothesis that the helium gas is not lost during the production of bubbles, a simple estimate of the HFSB production frequency f_p is obtained on the basis of the helium flow rate and the bubble volume V_b as:

$$f_p = \frac{Q_{He}}{V_b}. \tag{3.2}$$

The production mechanism is explained here in the following hypotheses: air, helium and BFS reach the same velocity at the exit orifice (Mu *et al.*, 2020); air and helium maintain approximately equal pressure (except for the pressure difference caused by the soap film tension) along the contraction; BFS is released at the lip of the inner tubes

continuously at a negligible velocity compared to that of the gases. The released BFS is extruded under the shearing action of the helium and air flows. The work done by the shear stresses at the helium-BFS and air-BFS interfaces accelerates the BFS film. As a result of mass conservation, its thickness is reduced and the surface area is increased. At the end of the nozzle contraction, the BFS flow features a thin annular shape of diameter d_a. In the above hypotheses, d_a can be derived from the air-to-helium ratio of flow rates and the orifice diameter:

$$d_a = d_o \left(1 + \frac{Q_{air}}{Q_{He}}\right)^{-1/2} . \tag{3.3}$$

The annular BFS film is subject to Plateau-Rayleigh instability (Rayleigh, 1878), whereby disturbances of varicose mode are amplified eventually leading to the breakdown of the BFS filament into bubbles. The most amplified wavelength, λ, dictates the final bubble diameter as well as the production rate. Rayleigh (1878) derived theoretically the value of such wavelength for a cylindrical liquid jet in air, obtaining $\lambda \approx 4.5 d_a$. In absence of a theoretical value of λ for a hollow liquid film, we will use the latter value as first estimate for the most amplified wavelength. At the nozzle exit, due to the conservation of the helium mass, the cylinder of length λ and diameter d_a transforms into a spherical bubble of diameter d_b:

$$\frac{\pi}{4}\lambda d_a^2 = \frac{\pi}{6} d_b^3 . \tag{3.4}$$

Introducing this relation and the estimate for λ in equation (3.3) finally yields a theoretical estimate of the bubble diameter as:

$$d_b \approx 1.9 d_o \left(1 + \frac{Q_{air}}{Q_{He}}\right)^{-1/2} . \tag{3.5}$$

The above equation shows that the bubble diameter depends linearly upon the orifice diameter and in a milder way (0.5 exponent) upon the ratio of gases flow rates. The latter has been practiced and reported in several past experiments (Faleiros *et al.*, 2019; Gibeau & Ghaemi, 2018). However, it was also observed that controlled production of HFSB only occurs in a limited range of values for such ratio. For instance, Faleiros *et al.* (2019) showed that at too low air flow rate, the generator produces irregular bubbles of disperse diameter. Furthermore, at too high values of Q_{air}, the annular BFS film breaks up downstream of the orifice (*jetting* regime), leading to a polydisperse bubble generation. As a result, the ratio Q_{air}/Q_{He} for controlled production of monodispersed bubbles needs to be limited approximately between 5 and 15. Using equation (3.5), this would result in a max-min ratio of bubble diameter of 1.6, with bubble diameters typically between 0.45 and 0.8 times the orifice diameter. Current experiments, along with those reported by Faleiros *et al.* (2019) or Gibeau and Ghaemi (2018) confirm such range limitations.

3.1.1. Scalable HFSB generation

The present work explores the control of HFSB size by altering the orifice diameter d_o and the flow rates of the supply fluids, while maintaining unaltered the geometry

upstream of the contraction (see figure 3.2). In the simplifying hypothesis of equal pressure and velocity of the helium and air streams at the exit of the coaxial duct, the soap film contracts from the initial diameter d_{BFS} to d_a following the geometrical contraction of d_{air}/d_o. It can be concluded that small bubbles can be obtained by miniaturising the coaxial tube or by reducing the exit orifice. The former option is technically challenging, considering that current systems already feature a coaxial duct in the order of 1 mm and a wall thickness of the coaxial ducts in the order of 0.2 mm, at the limit of manufacturing accuracy or 3D-printing. The latter option, instead, only requires a modification of the orifice diameter, currently in the order of 1 mm.

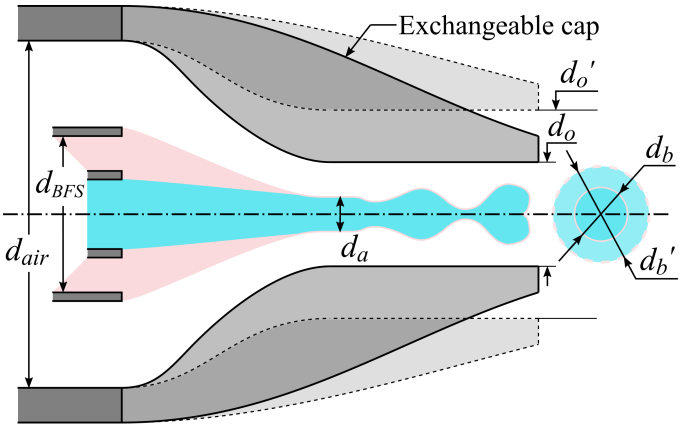

Figure 3.2: Schematic illustration of a scalable HFSB generator, where an exchangeable cap is used to change the orifice diameter from d_o to d_o', thus yielding a variation of the bubbles diameters from d_b to d_b'.

3.2. Light scattering behaviour of HFSB

HFSB have been introduced for their increased light scattering capabilities compared to conventional fog droplets. While it is clear that bigger particles scatter more light due to the larger cross section, the light reflecting region spreads over an area larger than the wavelength of the incident light and therefore entering the geometrical reflection regime. When such region is also resolved geometrically in the image, the particle image peak intensity reaches a plateau. This principle has been discussed in the early work of Adrian and Yao (1985), who, however, extrapolated their conclusions from conditions of high magnification, ultimately leading to the misconception of an upper bound for the tracers size. The main point of discussion is whether increasing the size of tracers, HFSB in particular, experiments at larger scale and/or at larger illumination and imaging distance can be performed. A discussion is developed hereafter that aims at determining the governing parameters of this optical problem and identifying the regimes for PIV experiments at different scales. Let us consider a measurement volume V (a cube of length L for simplicity), seeded with HFSB tracers illuminated and imaged with a 3D

PIV system. The illumination, light reflection and imaging situation is schematically represented in figure 3.3. The light scattered by the bubble is collected at a distance z_o by a lens of focal length f and numerical aperture $f_\#$, whereas z_i is the lens-sensor distance. As discussed by Adrian (1991) for planar PIV, the energy collected over the area of a particle image, $\bar{\varepsilon}$, is given by:

$$\bar{\varepsilon} \sim \underbrace{\frac{I_0}{L^2}}_{\text{Illumination}} \cdot \underbrace{\lambda_0^2 \left(\frac{d_b}{\lambda_0}\right)^n}_{\text{Light scattering}} \cdot \underbrace{\frac{(f/f_\#)^2}{z_o^2 d_\tau^2}}_{\text{Imaging}}, \tag{3.6}$$

where I_0 and λ_0 are the pulse energy and wavelength of the incident light, n is the power-law exponent describing the scattered light energy and d_τ is the particle image diameter. The right-hand-side of equation (3.6) has been rearranged into three different factors that account for the contribution of illumination, light scattering and imaging respectively.

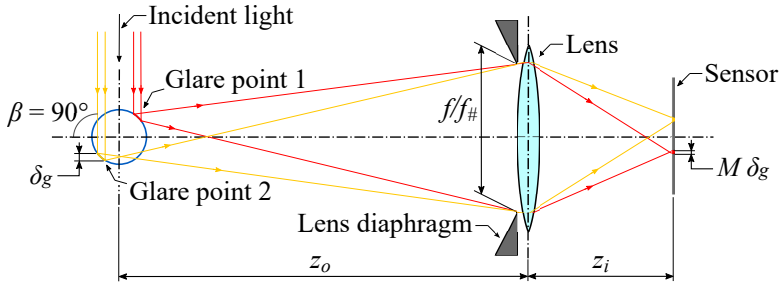

Figure 3.3: Sketch of the illumination and imaging of a HFSB.

3.2.1. Illumination

The original derivation of equation (3.6) is based on laser illumination (monochromatic, collimated and coherent) as commonly employed for PIV. For volumetric illumination, the energy of the light pulse needs to be spread over the width and height of the laser sheet, thus scaling as $1/L^2$. For uncollimated light sources, such as LEDs, the energy flux depends on the relative distance between the light source and the tracer. In general, LED illuminators are placed at a distance from the measurement volume that is comparable to the size of this volume itself. This is done to achieve to best compromise between light intensity evenness across the volume and total energy flux. In this situation, the same scaling as for collimated light sources applies. In the present discussion, collimated illumination from a single direction is considered, for sake of simplicity.

3.2.2. Light scattering

The light scattered from a spherical particle as a function of the particle diameter is described by Mie's theory (Hergert & Wriedt, 2012). The relative diameter of the

particle (d_p) to the wavelength of the illumination demarcates the range of Rayleigh ($d_p \ll \lambda_0$), Mie ($d_p \sim \lambda_0$) and geometric scattering ($d_p \gg \lambda_0$) respectively. Conventional PIV seeding (liquid droplets around 1 µm) lie in the intermediate Mie region. For Rayleigh scattering, the power-law exponent tends to $n = 6$, while this drops to $n = 2$ for geometric scattering (Tropea, 2011), which is the case for HFSB.

For particles in the Mie region, the scattered light intensity strongly depends on the angle between the illuminator and the camera (Raffel *et al.*, 2018), β, which is therefore of utter importance for PIV experiments. Conversely, previous results from Caridi (2018) have demonstrated only minor variations for the case of HFSB, which is a direct consequence of these pertaining to the geometric scattering regime. For the sake of simplicity, side scattering ($\beta = 90°$) is considered in the remainder of the document.

In the geometric scattering regime, the various scattering orders (e.g., reflection and refraction) can be visualized through simple ray-tracing models. Since the difference in refractive index between helium and air is negligible, and given the small thickness of the soap film, refraction is neglected in the present discussion.

3.2.3. Imaging

For volumetric PIV, two visible regions (the so-called glare points) are imaged per tracer, oriented along the illumination direction. A first visible region is caused by the light rays reflected at the bubble's outer surface that are captured by the lens aperture. For HFSB, a second glare point appears from the light rays that initially go through the bubble before being reflected at the inner surface (see figure 3.3). The projection of these regions onto a plane parallel to the sensor indicates an elliptical shape of eccentricity $e = 1/\sqrt{2}$, as sketched in figure 3.4. To simplify the discussion, the size of the glare points is defined here based on an equivalent diameter (δ_g), obtained as the average between the axes of the ellipse. The glare point diameter in the object space depends not only on the bubble size but also on the imaging conditions, since these affect the subtended angle of light captured by the lens. As discussed by Faleiros *et al.* (2021), this may be approximated as:

$$\delta_g \approx \frac{2+\sqrt{2}}{16} \frac{f}{f_\#} \frac{d_b}{z_o}. \tag{3.7}$$

The geometrical image of the glare points does further depend on the imaging configuration through the optical magnification, $M = z_i/z_o$, such that the imaged size becomes $M\delta_g$ (see figure 3.3). Another contribution to the glare point size in the image plane is due to diffraction, whereby a point source is imaged over a finite spot of diameter d_{diff} (Goodman, 1996):

$$d_{diff} = 2.44\lambda_0 f_\# (1+M). \tag{3.8}$$

Assuming both the geometric image and the point response function behave as a Gaussian distribution (Adrian & Yao, 1985), the glare point image diameter (d_τ) can be approximated as:

$$d_\tau = \sqrt{\left(M\delta_g\right)^2 + d_{diff}^2}. \tag{3.9}$$

In the above expression the effects of optical aberrations are neglected and the glare points are assumed to be imaged in focus. Furthermore, it is assumed that d_τ is larger than the sensor pixel, which allows neglecting the discretisation effects due to pixels. As the relative importance of geometric imaging and diffraction is still subject to the imaging conditions, a further relation can be obtained from the depth of focus. For volumetric PIV, it is crucial for the focal depth δZ to be larger or equal than the depth of the measurement volume L, leading to (Schuth & Buerakov, 2017):

$$\delta Z = 2 f_\# d_{diff} \frac{1+M}{M^2} \geq L\,. \tag{3.10}$$

Considering $\delta Z = L$, equation (3.10) can be used to compare the geometric glare point image to the diffraction spot. A non-dimensional parameter R_{GD} (ratio of geometric to diffraction diameters) is introduced:

$$R_{GD} = \frac{M\delta_g}{d_{diff}} = \frac{2+\sqrt{2}}{8}(1+M)\frac{f}{Mz_o}\frac{d_b}{L}\,. \tag{3.11}$$

The physical interpretation of R_{GD} is that it indicates the optical regimes governed by diffraction ($R_{GD} \ll 1$) from those where the tracer image (or the reflecting region thereof) is resolved in its geometry ($R_{GD} \gg 1$). When $R_{GD} = \mathcal{O}(1)$, both effects need to be contemplated and a possible combination is given by equation (3.9).

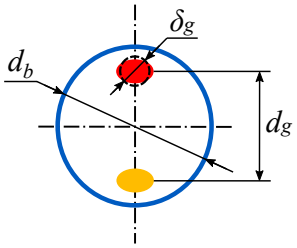

Figure 3.4: Sketch of the glare points of a HFSB in the object space.

Large-scale PIV applications typically entail large distance from the object and $M \ll 1$. From the thin-lens equation, this implies $f \approx Mz_o$ and equation (3.11) simplifies into:

$$R_{GD} \approx 0.4 \frac{d_b}{L}\,. \tag{3.12}$$

For any meaningful large-scale volumetric PIV experiment the ratio $d_b/L \ll 1$ (typically $[10^{-2} - 10^{-4}]$, see table 3.1), in turn, indicating that $R_{GD} \ll 1$. It can be concluded that also for HFSB tracers the imaging process is governed by diffraction [equation (3.9)], contrary to what is stated on reference literature and textbooks (Adrian, 1991; Raffel *et al.*, 2018), where an upper limit (around 10 – 100 µm) is postulated for the tracer size before the geometric optics imaging regime needs to be accounted for.

Another relevant parameter for the imaging of HFSB is the distance between the two glare points, d_g in object space, as sketched in figure 3.4. This distance depends on the

Research group	Measurement volume, V (Reference length scale, $L = \sqrt[3]{V}$)	Tracers (d_b)	d_b/L	$R_{GD} = \frac{M\delta_g}{d_{diff}}$	$R_{DD} = \frac{Md_g}{d_{diff}}$
Rosi *et al.* (2014), atmospheric boundary layer	16 m^3 (2.5 m)	Fog-filled soap bubbles (25 mm)	10^{-2}	$4 \cdot 10^{-3}$	Not applicable
Scarano *et al.* (2015), cylinder wake	$4.8 \cdot 10^{-3}$ m^3 (0.17 m)	HFSB (0.4 mm)	$2 \cdot 10^{-3}$	10^{-3}	0.6
Caridi *et al.* (2016), vertical axis wind turbine	$1.2 \cdot 10^{-2}$ m^3 (0.23 m)	HFSB (0.3 mm)	10^{-3}	$6 \cdot 10^{-4}$	0.7
Jux *et al.* (2018), full-scale cyclist	$3 \cdot 10^{-2}$ m^3 (0.31 m)	HFSB (0.4 mm)	10^{-3}	$6 \cdot 10^{-4}$	0.06
Schanz *et al.* (2019), turbulent boundary layer	$5.8 \cdot 10^{-1}$ m^3 (0.83 m)	HFSB (0.37 mm)	$4 \cdot 10^{-4}$	$2 \cdot 10^{-4}$	0.3
Godbersen *et al.* (2021), Rayleigh-Bénard convection	2 m^3 (1.2 m)	HFSB (0.37 mm)	$3 \cdot 10^{-4}$	10^{-4}	0.2
Wei *et al.* (2021), vertical axis wind turbine	490 m^3 (7.9 m)	Artificial snow (11 mm)	10^{-3}	$6 \cdot 10^{-4}$	Not applicable
Hou *et al.* (2021), tractor-trailer model	9 m^3 (2.1 m)	Air-filled soap bubbles (20 mm)	10^{-2}	$4 \cdot 10^{-3}$	15
van der Hoek *et al.* (2022), horizontal axis wind turbine	$2.8 \cdot 10^{-1}$ m^3 (0.65 m)	HFSB (0.37 mm)	$6 \cdot 10^{-4}$	$2 \cdot 10^{-4}$	0.8
Schröder *et al.* (2022), breathing human model	12 m^3 (2.3 m)	HFSB (0.37 mm)	$2 \cdot 10^{-4}$	$7 \cdot 10^{-5}$	0.2

Table 3.1: Survey of large-scale experiments performed with tracers in the mm-cm range. Size of tracers, corresponding measurement volume and their ratio. Non-dimensional parameter R_{GD} indicating ratio of glare to diffraction diameters. R_{DD} ratio of glare points distance to diffraction diameter.

tracer size and the illumination-imaging relative angle (β) as (Dehaeck *et al.*, 2005):

$$d_g = \cos\left(\frac{\pi - \beta}{2}\right) d_b \,, \tag{3.13}$$

which, for $\beta = 90°$, reduces to $d_g = \frac{\sqrt{2}}{2} d_b$. In the image plane, this distance transforms into $M d_g$. This can be further compared with the diffraction spot [equation (3.8)], thus defining a new non-dimensional parameter, R_{DD} (ratio of glare point distance and diffraction diameter), as:

$$R_{DD} = \frac{M d_g}{d_{diff}} \approx 0.3 \frac{M}{f_\#} \frac{d_b}{\lambda_0} \,. \tag{3.14}$$

The physical interpretation of R_{DD} is that it indicates if the two glare points will be imaged separately ($R_{DD} \gg 1$) or will fall into the same diffraction spot ($R_{DD} \ll 1$). The former poses additional challenges to the triangulation and tracking of the tracers, as discussed by Faleiros *et al.* (2021). While the condition for diffraction-governed imaging is easily satisfied in volumetric PIV experiments [equation (3.12)], that for glare point merging is more restrictive and will further depend upon the imaging configuration [equation (3.14)]. Still, for large-scale experiments, where $M \ll 1$, this condition is easily satisfied as well.

The ratio R_{DD} is given in table 3.1 for a series of relevant large-scale volumetric PIV experiments. In general, $R_{DD} < 1$ is observed. The condition $R_{DD} \ll 1$ (glare point merging) is more easily achieved when considering low values of β, as set when using the coaxial volumetric velocimeter (Jux *et al.*, 2018; Schneiders *et al.*, 2018). On the other hand, $R_{DD} \gg 1$ (separate glare points) brings the opportunity of triangulating tracers from single-camera approaches (Hou *et al.*, 2021; Kaiser & Rival, 2023).

3.2.4. HFSB sizing rules for large-scale PIV

As a result of the above discussion, the scattered light by HFSB tracers scales with the square of the bubble diameter. Furthermore, glare points imaging remains governed by diffraction and, when imaged at small magnification, both glare points fall within the diffraction spot. Introducing these results in equation (3.6), together with the depth of focus condition from equation (3.10) in the assumption of large-scale experiment the mean exposure $\bar{\varepsilon}$ reads as:

$$\bar{\varepsilon} \sim \frac{I_0 d_b^2}{L^4 M^2} \,. \tag{3.15}$$

When the optical magnification is expressed as the ratio between the image and the object size ($M = s/L$), equation (3.15) can be rearranged to express the measurement size as a function of the other parameters:

$$L \sim \sqrt{\frac{I_0}{\bar{\varepsilon}}} \frac{d_b}{s} \,. \tag{3.16}$$

Equation (3.16) implies that, for a given level of illumination and sensor size and for a required exposure, the achievable volumetric measurement size scales linearly with the bubble diameter. This strong dependence motivates the exploration of the scalability

of the tracers, such to match the needs of aerodynamics experiments for different purposes and scales. Furthermore, equation (3.16) is consistent with the slope of the linear trend in figure 2.6 for tracers scattering in the Mie regime (tracers larger than 1 µm), and sets a benchmark for future large-scale volumetric PIV experiments.

3.3. Experimental setup and procedures

3.3.1. HFSB generator

The bubble generator employed is based on a 3D printed HFSB-GEN-V11 model, developed at TU Delft. The generator is modified to feature a variable orifice diameter, while the geometry of the tri-axial duct and the contraction are left unaltered. The orifice diameter is changed by installing an adapted cap. Experiments cover a wide range of $d_o = \{0.35, 0.4, 0.5, 0.6, 0.75, 1, 1.5, 2, 2.5, 3\}$ mm. The lower limit of this interval is set by the achievable resolution of the 3D printer used (Anycubic *Photon Mono X 6K*), while the upper one is approaching the outer size of the generator itself, such that $d_{air}/d_o \sim 1$.

The generator is supplied with pressurized air and helium. *SAI 1035* fluid, from Sage Action, Inc. is used as BFS, with a surface tension of 27.5 mN/m. The air flow rate is set using a Festo *SFAH* mass flow controller, while the helium and BFS flow rates are set by imposing a known pressure ahead of previously calibrated flow resistors. At all flow rates, the neutrally-buoyant nominal condition in ambient air is maintained by controlling $Q_{He}/Q_{BFS} \simeq 1080$ (Faleiros *et al.*, 2019). The flow rates vary from $Q_{He} = 2.2$ l/h, $Q_{BFS} = 2$ ml/h and $Q_{air} = 15$ l/h for the smallest orifice to $Q_{He} = 30$ l/h, $Q_{BFS} = 28$ ml/h and $Q_{air} = 230$ l/h for the largest one.

3.3.2. Bubble diameter and production rate

Shadow visualisation is used to observe the production mechanism and infer bubble diameter and production rate, as sketched in figure 3.5. Continuous white light is provided by a LED (Scangrip *Nova R*, 2000 lumen) along the region of interest (~ 20 mm at the exit of the generator), placed behind a light diffuser. Images of the HFSB shadows are taken with a high-speed CMOS camera (Photron *FASTCAM SA1.1*, 1024×1024 px, 12 bits, 20 µm pixel pitch), placed perpendicular to the bubble stream and opposite to the illumination source, using a camera lens with $f = 105$ mm and setting $f_\# = 5.6$.

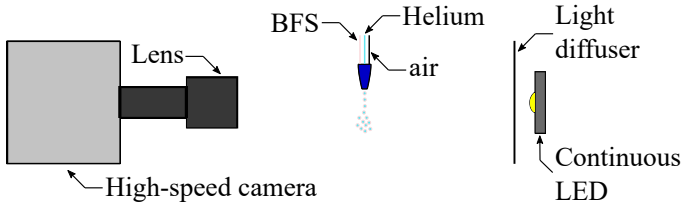

Figure 3.5: Sketch of the experimental setup for shadow visualization of the HFSB production.

The production mechanism is inspected from a visualization with a digital imaging

resolution of approximately 50 px/mm, cropping the sensor down to 320×128 px to achieve an acquisition frequency of 100 kHz. The imager is operated with a shutter of 8 µs to avoid motion blur. As discussed by Faleiros *et al.* (2019) and Gibeau *et al.* (2020), only specific combinations of the fluids flow rates result in a stable production of HFSB in the so-called *bubbling* regime. An in-house algorithm detects the bubbles of circular shape and counts the number of bubbles produced during an acquisition of 10 ms (1000 frames). Statistics on the diameter and production rate are based on a typical ensemble size of 300 bubbles.

3.3.3. Light scattering behaviour and glare points

Illumination and imaging directions are placed perpendicularly as shown in figure 3.6. The LED source is placed at a distance of approximately 10 cm from the generator's exit and the light scattered by the HSFB is captured with the CMOS camera at a distance varying from 0.2 m up to 10 m. The goal of this experiment is to verify the power two scaling of scattered light with the bubble diameter and confirm the hypothesis of diffraction-dominated regime [$R_{GD} \ll 1$, equation (3.11)].

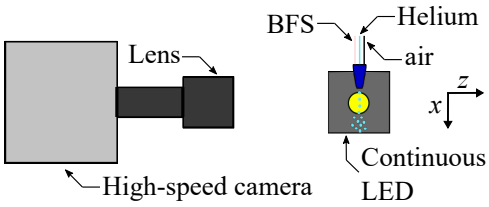

Figure 3.6: Sketch of the experimental setup for the light scattering investigation of scaled HFSB, using a viewing angle of 90° between the camera and the illumination source.

The experiments are conducted by varying both the bubble diameter and the optical magnification (see table 3.2). The bubble diameter is varied by changing the generator orifice and controlling the fluids flow rates. The imaging distance is adjusted by moving the camera away from the generator. Furthermore, the aperture is varied through the f-number. The optical magnification is varied from $M = 0.01$, representative of large-scale applications, up to $M = 0.25$, more aligned with experiments at smaller laboratory scale. In these cases, the f-number is set to $f_\# = 8$ (commonly employed for volumetric PIV) and the camera exposure time to 10.5 µs. Some recordings are performed at high-magnification ($M = 1.1$), large aperture ($f_\# = 2.8$) and short exposure time (3 µs), to attain the condition $R_{GD} > 1$. The latter resembles more closely the study of Adrian and Yao (1985), conducted at $M = 1$ with varying $f_\#$. For HFSB, raising the f-number has a major impact on the relative importance of geometric imaging, as it not only increases the diffraction spot [equation (3.8)], but also decreases the perceived glare point size [equation (3.7)]. The list of imaging configurations explored is given in table 3.2.

The condition $R_{DD} > 1$ [equation (3.14)], indicating that the glare points are imaged separately, is obtained for high magnifications and/or large bubbles. From these, the

Object distance [m]	0.2	0.53	1.16	2.21	55.36	10.61
Magnification	1.1	0.25	0.1	0.05	0.02	0.01
Pixel image size [µm]	18	80	200	400	1000	2000
f-number	2.8	8	8	8	8	8
Exposure [µs]	3	10.5	10.5	10.5	10.5	10.5

Table 3.2: Imaging parameters for the light scattering experiment.

bubble diameter is estimated to be $\sqrt{2}$ times larger than the distance between them (Scarano *et al.*, 2015), given the 90° viewing angle. An in-house algorithm matches neighbouring glare points corresponding to the same bubble and extracts the individual particle image diameters, peak intensity (indicative of particle detectability) and also integrates the intensity over the particle image region to obtain the total scattered light energy. Instead, for low magnifications and/or small bubbles, the two glare points merge in the image plane, and the algorithm is simply a peak finder that still computes the aforementioned properties for each bubble. Representative images of the regimes $R_{DD} > 1$ and $R_{DD} < 1$ are given in figure 3.7, obtained by decreasing the optical magnification from $M = 0.1$ to $M = 0.02$ for bubbles with a diameter of $d_b = 1.3$ mm.

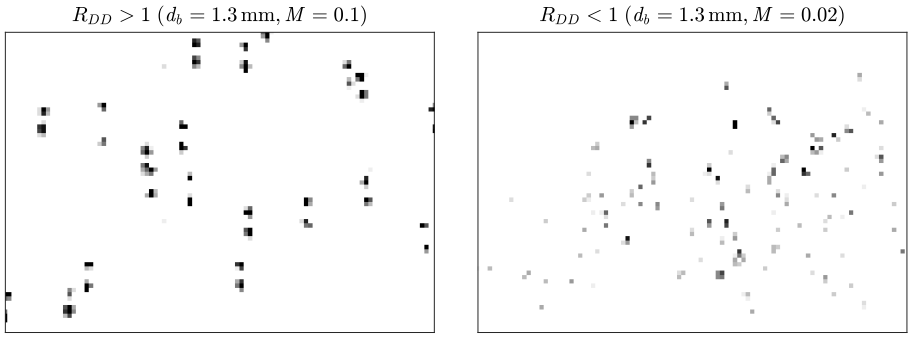

Figure 3.7: Recordings of the light scattered by HFSB with a diameter of $d_b = 1.3$ mm. Left: high optical magnification ($M = 0.1$), where the glare points are resolved separately ($R_{DD} > 1$). Right: typical optical magnification of PIV experiments ($M = 0.02$), where the glare points merge onto a single pixel or within the diffraction diameter ($R_{DD} < 1$).

For every imaging configuration listed in table 3.2 and every bubble diameter considered, a total of 1000 snapshots are recorded. The particle image properties are obtained as the mean of all detected bubbles, after removing outliers using a third-order median filter. For the case of separate glare points, the intensity information from the two is added together, for a better comparison with the merged glare points situation. Uncertainty in the reported quantities is estimated as two times the standard deviation divided by the square-root of the number of bubbles detected (Moffat, 1988), which

represents 95% confidence assuming a Gaussian distribution.

3.4. Results

3.4.1. Bubble production visualization

Changing the orifice diameter of the HFSB generator has a major impact on the size of the bubbles produced. Examples of the bubbles generated are given in figure 3.8 for six different orifice diameters. The shadow images are accompanied by a 1 mm grid to give a clear indication of the bubble size. Besides, the diameter of a specific bubble is also indicated for each case. For every orifice, the fluids flow rates are kept constant at Q_{He} = 10 l/h, Q_{BFS} = 9.3 ml/h and Q_{air} = 100 l/h. From the visualizations, it is apparent that HFSB can be produced within a range of diameters $d_b \in [0.5, 2.6]$ mm simply by changing the orifice diameter.

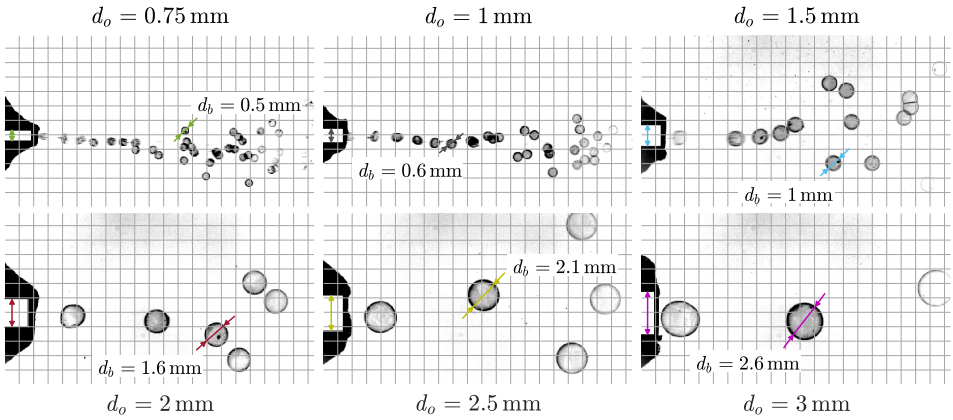

Figure 3.8: Shadow visualization of HFSB produced varying the orifice diameter of the nozzle. Fluids flow rates are kept constant at Q_{He} = 10 l/h, Q_{BFS} = 9.3 ml/h and Q_{air} = 100 l/h. Reference grid with 1 mm pitch.

The complete set of bubble diameters measured from the shadow visualizations are given in figure 3.9 in terms of the orifice diameter, ranging from d_b = 160 µm for d_o = 0.35 mm to d_b = 2.7 mm for d_o = 3 mm. For a chosen orifice, different bubbles can be generated by changing the air and helium relative flow rates, obtaining diameters roughly from $d_b = 0.5 d_o$ up to $d_b = d_o$. While the upper limit is set by the orifice itself, it is argued that the lower limit is set by the maximum shear tolerated during the extrusion of the BFS film. The fluids flow rates combination employed to generate the HFSB diameters numbered in figure 3.9, which correspond to the minimum and maximum bubble diameters achieved for d_o = 0.35 mm, d_o = 1 mm and d_o = 3 mm are listed in table 3.3. The error bars next to the symbols in figure 3.9 indicate the mean of the bubble diameter standard deviation measured for every fluid flow rates combination during the full acquisition. The obtained values are below 5% of the mean bubble

diameter, in agreement with the results discussed by Faleiros *et al.* (2019) for stable production in the *bubbling* regime. The size dispersion is further illustrated in figure 3.10 by showing histograms of the measured bubble diameter distribution for three different situations: d_b = 0.2 mm, d_b = 0.5 mm and d_b = 2 mm.

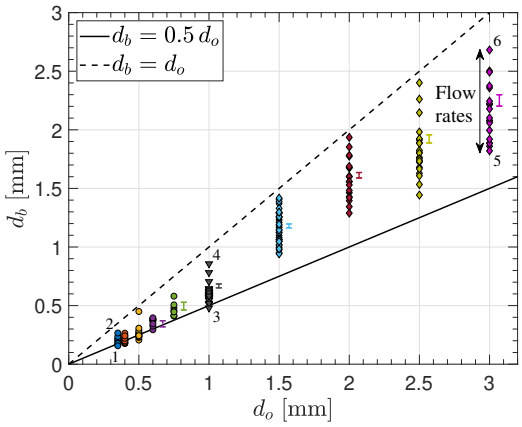

Figure 3.9: HFSB diameter as a function of the orifice diameter, for every fluids flow rates combination.

Orifice diameter, d_o [mm]	0.35		1		3	
Number label (see figure 3.9)	1	2	3	4	5	6
Mean bubble diameter, d_b [mm]	0.16	0.27	0.48	0.86	1.82	2.68
Standard deviation of bubble diameter [mm]	0.01	0.01	0.01	0.02	0.11	0.15
Q_{He} [l/h]	2.2	2.8	9.4	9.9	22.0	30.0
Q_{BFS} [ml/h]	2.0	2.6	8.7	9.2	20.4	27.8
Q_{air} [l/h]	40	15	145	50	230	90

Table 3.3: Fluids flow rates employed to obtain the HFSB diameters numbered in figure 3.9.

The experimental measurements of the bubble diameter are further compared with the theoretical prediction derived in equation (3.5). The comparison is given in figure 3.11, where the theoretical trend is represented by a dashed line that goes through the origin with a slope equal to m = 1.9. This value results from assuming that the bubble production dominant wavelength is the same as the one derived by Rayleigh (1878) for a cylindrical liquid jet in air. The experimental measurements are indicated by the scattered dots coloured by the orifice diameter, and in general are in good agreement with the theory. For $d_o \geq 1.5$ mm and low values of both Q_{He} and Q_{air}, an alternative regime is also observed, that results in bigger bubbles than those predicted by equation

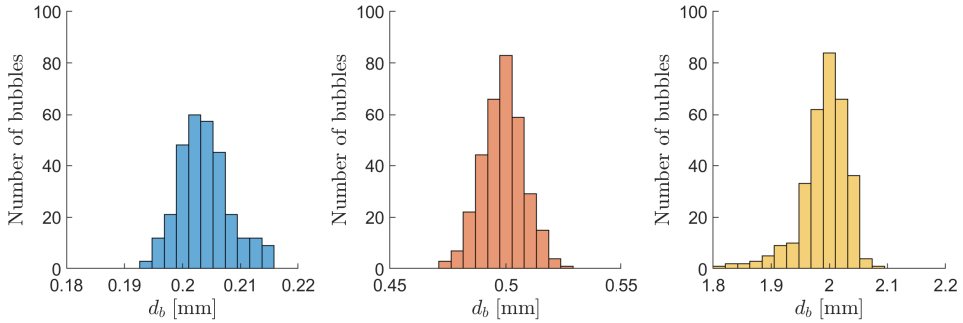

Figure 3.10: Distribution of bubble diameter. Left: for a mean bubble diameter of 0.2 mm (obtained from d_o = 0.5 mm). Middle: for a mean bubble diameter of 0.5 mm (obtained from d_o = 0.75 mm). Right: for a mean bubble diameter of 2 mm (obtained from d_o = 3 mm).

(3.5) for the fluids flow rates imposed. Arguably, this is caused by the merging of two bubbles just ahead of the orifice, forming a bigger bubble downstream of the generator.

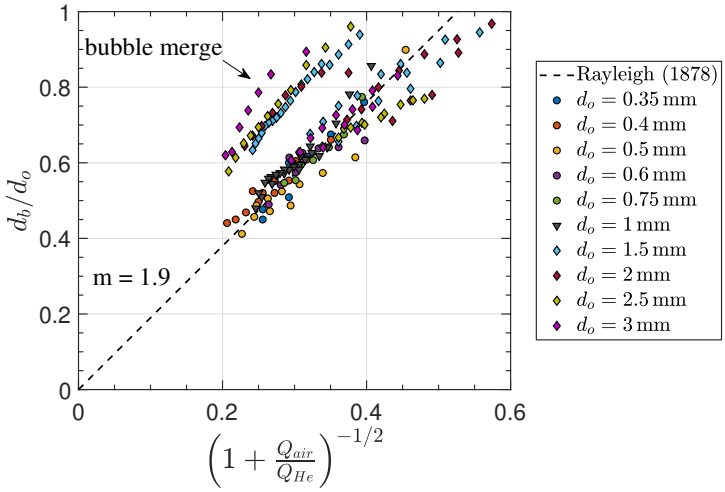

Figure 3.11: Comparison between the experimental measurements of HFSB diameter and the theoretical prediction derived in equation (3.5).

The high-speed shadow visualizations allow estimating the bubble production rate. Counting the number of bubbles crossing a line at a chosen distance from the exit delivers the results shown in figure 3.12. The data is compared with the prediction from equation (3.2), which imposes helium mass conservation. The production rate is plotted as a function of Q_{He} normalised with the bubble volume. The data exhibit linearity over a wide range, spanning from 250 Hz, obtained for the largest bubbles of approximately 3

mm, to 50 kHz for bubbles of 0.3 mm. Extrapolation of this behaviour to the smallest bubbles of 160 µm predicts a production rate in excess of 300 kHz. The latter could not be measured with the current apparatus, leaving the point open for further verifications. The measured production rate, in excess of f_p = 10 kHz for d_o = 1 mm, is in agreement with both Gibeau *et al.* (2020) and Faleiros *et al.* (2019).

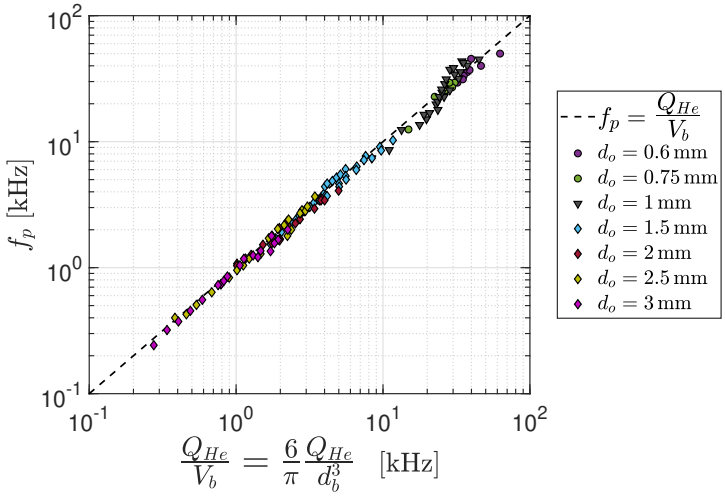

Figure 3.12: HFSB production rate as a function of bubble diameter and helium flow rate imposed.

3.4.2. Light scattering and HFSB imaging

The imaging regime of HFSB depends upon their size, the optical magnification and to a lesser extent it is affected by the relative angle between illumination and imaging direction. Figure 3.13 illustrates the images of HFSB obtained at relatively high magnification, (M = 1.1), for bubbles with diameter ranging from d_b = 0.27 mm to d_b = 2.13 mm. In this condition, the glare points are always imaged with two maxima separated by a distance (vertical, given the top-to-bottom illumination, figure 3.6), which suggests R_{DD} > 1. A third glare point, of weaker intensity is observed for the larger bubbles, caused by a higher order internal light reflection. Given its low intensity, the contribution of this glare point to the total scattered energy is neglected.

Reducing the optical magnification (see table 3.2) to M = 0.1 and for bubble size ranging from d_b = 0.25 mm up to d_b = 2 mm (inferred from the glare points distance), figure 3.14 shows that the glare points merge into a single peak for the smaller bubbles (R_{DD} < 1), causing either an elongated particle image (for d_b = 0.4 mm), or a single pixel being activated (for d_b = 0.25 mm). In this case both the geometric and diffraction contributions are smaller than the pixel pitch of 20 µm. Introducing the appropriate values into the theoretical estimations given in equation (3.7) and equation (3.8), returns

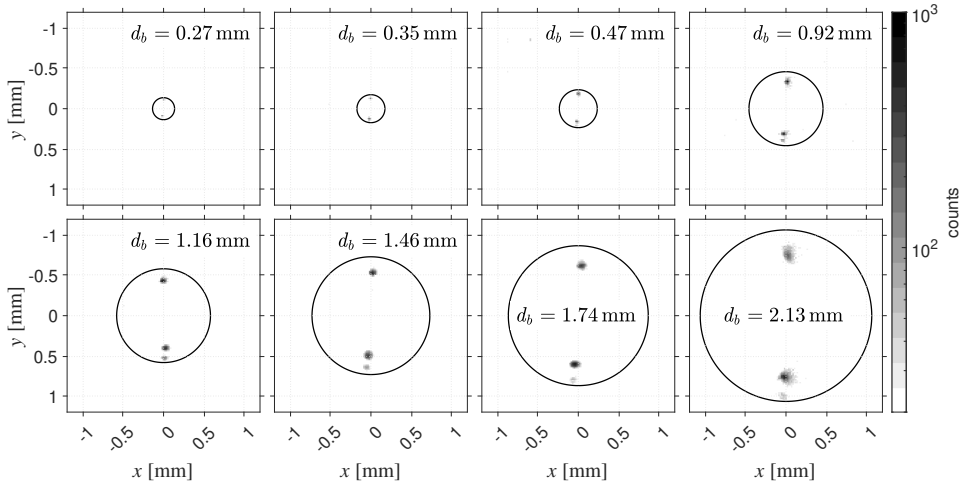

Figure 3.13: High-magnification recordings (M = 1.1) of the light scattered by HFSB of different diameter. The black circles indicate the estimated positions of the bubbles.

a geometric glare point image size ($M\delta_g$) of only 0.05 µm. Comparatively, the diffraction spot is larger (approximately 12 µm), thus in agreement with the experimental evidence.

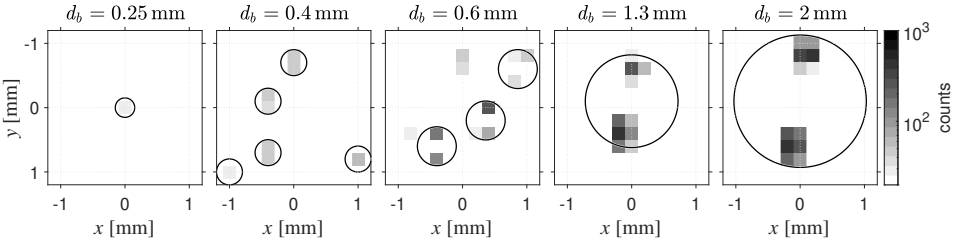

Figure 3.14: Low-magnification recordings (M = 0.1) of the light scattered by HFSB tracers. The black circles indicate the estimated positions of the bubbles.

The information about the particle image size is further used to integrate the detected intensity level in this region, thus providing an estimate of the total light energy scattered by the HFSB. The results obtained for every bubble diameter considered are shown in figure 3.15 for the imaging configurations at M = 1.1 and M = 0.1. The experimental measurements, displayed in logarithmic scale, are further compared with linear trends with a slope of m = 2. This value responds to the power-law exponent of the geometric light scattering regime (Tropea, 2011). It can be seen that this exponent matches well for both imaging situations, as the light scattered is a function of the particle diameter (relative to the incoming light wavelength) only.

The influence of the imaging configuration arises when looking at the particle image

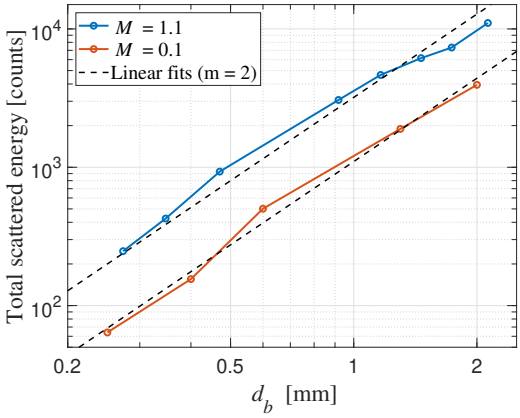

Figure 3.15: Total scattered energy, integrated over the particle image diameter, for various HFSB diameters and two optical magnifications: M = 1.1 and M = 0.1.

diameter and peak intensity, the latter being representative of particle detectability and therefore of great importance for PIV experiments. Starting with the high magnification situation, M = 1.1, the obtained particle image diameter and peak intensity are given in figure 3.16 for the eight different HFSB diameters considered. As the bubble size increases, the peak intensity initially does also increase, before reaching a constant value for bubbles bigger than 1 mm. This is caused by the role of geometric optics on the particle image diameter of the glare points. While $R_{GD} = \mathcal{O}(1)$, the contribution of diffraction and geometric imaging are comparable, and thus both peak intensity and particle image diameter increase. As $R_{GD} \gg 1$ for the bigger bubbles tested, diffraction becomes negligible and the particle image size increases linearly with that of the bubble. This situation, originally discussed by Adrian (1991) to postulate an upper limit for the usable tracer size for PIV, has no implication for volumetric experiments, as can only be achieved for low f-numbers (decreasing the depth of focus) combined with big tracers and high optical magnifications.

Instead, for an imaging situation more representative of a large-scale volumetric PIV experiment, such as the one discussed above for M = 0.1, the evolution of peak intensity and particle image diameter as the tracer size is increased follows the pattern given in figure 3.17. Here, even if diffraction dominates over the geometric size ($R_{GD} \ll 1$), the particle image diameter is limited by the pixel pitch of the sensor. Only for bigger bubbles the high intensity peak makes the distribution spread slightly to neighbouring pixels, as can be seen in figure 3.14. According to equation (3.7), the HFSB would need to be bigger than 3 cm for its glare point to spread over more than a pixel in this configuration. As the particle image diameter remains nearly constant throughout the entire range, the peak intensity follows a quadratic relation with the bubble diameter, which maintains the quadratic relation for the total scattered energy discussed in figure 3.15. This means that, for practical applications, the tracer size can be increased to improve particle

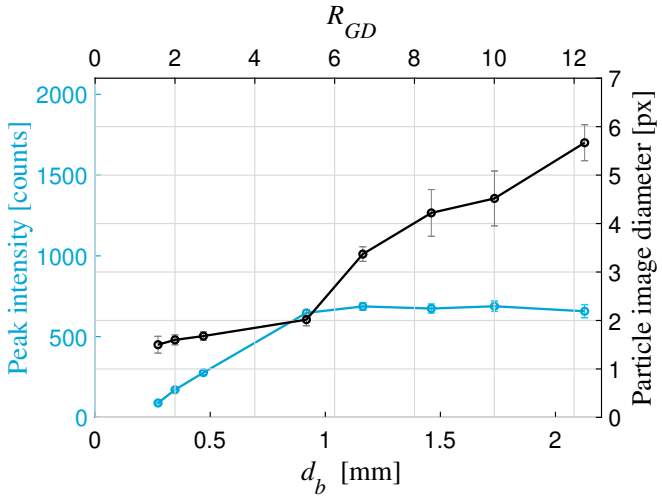

Figure 3.16: Peak intensity and particle image diameter for various HFSB diameters imaged at M = 1.1 ($R_{GD} \geq 1$).

detectability. This may be used to better distinguish tracers over reflecting backgrounds or simply to scale the measurement size, as summarized in equation (3.16).

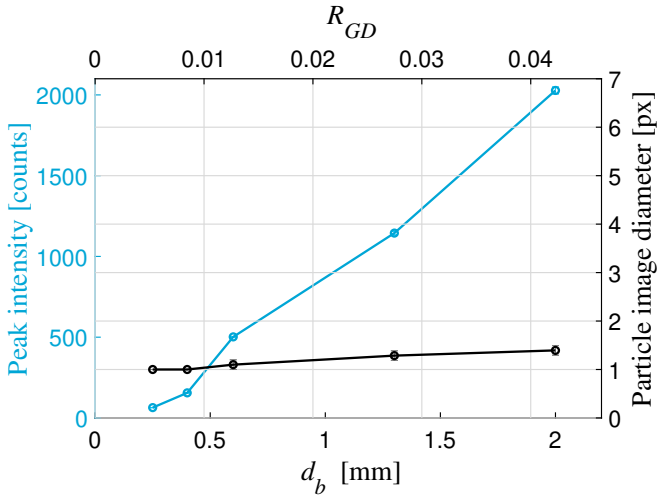

Figure 3.17: Peak intensity and particle image diameter for various HFSB diameters imaged at M = 0.1 ($R_{GD} \ll 1$).

The peak intensity analysis is extended to other optical magnifications, as reported in

table 3.2. The measured intensity is shown in figure 3.18 for every combination of bubble diameter and measurement size ($L = s/M$) tested. The observed trend agrees well with the theoretical scaling derived in equation (3.16), which suggests an intensity increase for bigger bubbles and smaller measurement domains. The actual intensity values reported in figure 3.18 depend not only on the quantum efficiency of the sensor but also on the illumination and recording characteristics. For more general purposes, they could be scaled with respect to the 2000 lumen illumination source placed at 10 cm from the tracers and exposed during 10.5 µs.

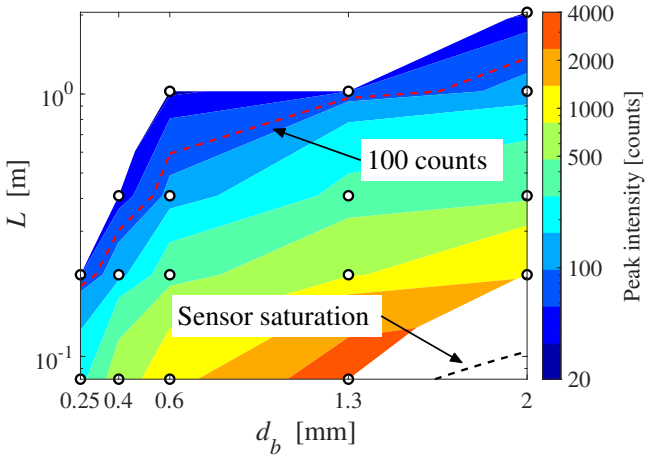

Figure 3.18: Peak intensity (in logarithmic scale) for various HFSB diameters and measurement sizes. Values of L are based on the current choice of illumination and scale with the pulse energy of the source.

3.5. Conclusions

The scalability of HFSB as tracers for volumetric PIV applications is explored by changing the orifice of the bubble generator and fluids flow rates. While keeping the nominal neutral buoyancy condition, bubble diameters between 160 µm and 2.7 mm have been produced. For every situation, the diameter dispersion is below 5% of the mean. As the bubble production frequency is inversely proportional to the bubble volume, production rates range from 250 Hz for the bigger bubbles to more than 300 kHz for the smaller ones. For a given geometry and fluids flow rates, the bubble diameter could be accurately predicted by imposing mass conservation and estimating the dominant wavelength of the bubble production instability mechanism.

The light scattering behaviour of the scaled HFSB has been investigated both from a theoretical and experimental perspective. While the size of HFSB translates into the geometric light scattering regime, it is demonstrated that, for large-scale volumetric

PIV applications, the imaging conditions are such that the particle images are still well represented by the diffraction spot. This means that the bubble diameter can be further increased to produce brighter particle images thus allowing for larger measurement volumes imaged from longer distances. It is postulated that $L \sim d_b$, which supports wide range scalability for volumetric PIV experiments.

References

Adrian, R. J. (1991). Particle-imaging techniques for experimental fluid mechanics. *Annual Review of Fluid Mechanics*, *23*(1), 261–304. https://doi.org/10.1146/annurev.fl.23.010191.001401

Adrian, R. J., & Yao, C.-S. (1985). Pulsed laser technique application to liquid and gaseous flows and the scattering power of seed materials. *Applied Optics*, *24*(1), 44. https://doi.org/10.1364/ao.24.000044

Caridi, G. C. A. (2018). *Development and application of helium-filled soap bubbles for large-scale PIV experiments in aerodynamics* [Doctoral dissertation, Delft University of Technology]. https://doi.org/10.4233/uuid:effc65f6-34df-4eac-8ad9-3fdb22a294dc

Caridi, G. C. A., Ragni, D., Sciacchitano, A., & Scarano, F. (2016). HFSB-seeding for large-scale tomographic PIV in wind tunnels. *Experiments in Fluids*, *57*(12), 1–13. https://doi.org/10.1007/s00348-016-2277-7

Dehaeck, S., Van Beeck, J. P., & Riethmuller, M. L. (2005). Extended glare point velocimetry and sizing for bubbly flows. *Experiments in Fluids*, *39*(2), 407–419. https://doi.org/10.1007/s00348-005-1004-6

Faleiros, D. E., Tuinstra, M., Sciacchitano, A., & Scarano, F. (2019). Generation and control of helium-filled soap bubbles for PIV. *Experiments in Fluids*, *60*(3). https://doi.org/10.1007/s00348-019-2687-4

Faleiros, D. E., Tuinstra, M., Sciacchitano, A., & Scarano, F. (2021). The slip velocity of nearly neutrally buoyant tracers for large-scale PIV. *Experiments in Fluids*, *62*(9), 1–24. https://doi.org/10.1007/s00348-021-03274-9

Gibeau, B., & Ghaemi, S. (2018). A modular, 3D-printed helium-filled soap bubble generator for large-scale volumetric flow measurements. *Experiments in Fluids*, *59*(12), 1–11. https://doi.org/10.1007/s00348-018-2634-9

Gibeau, B., Gingras, D., & Ghaemi, S. (2020). Evaluation of a full-scale helium-filled soap bubble generator. *Experiments in Fluids*, *61*(2), 1–18. https://doi.org/10.1007/s00348-019-2853-8

Godbersen, P., Bosbach, J., Schanz, D., & Schröder, A. (2021). Beauty of turbulent convection: A particle tracking endeavor. *Physical Review Fluids*, *6*(11), 4–7. https://doi.org/10.1103/PhysRevFluids.6.110509

Goodman, J. W. (1996). *Introduction to Fourier Optics* (2nd ed.). McGraw-Hill Book Company.

Grille Guerra, A., Scarano, F., & Sciacchitano, A. (2024). On the scalability of helium-filled soap bubbles for volumetric PIV. *Experiments in Fluids*, *65*(2), 23. https://doi.org/10.1007/s00348-024-03760-w

Hergert, W., & Wriedt, T. (2012). *The Mie Theory* (W. Hergert & T. Wriedt, Eds.; Vol. 169). Springer Berlin Heidelberg. https://doi.org/10.1007/978-3-642-28738-1

Hou, J., Kaiser, F., Sciacchitano, A., & Rival, D. E. (2021). A novel single-camera approach to large-scale, three-dimensional particle tracking based on glare-point spacing. *Experiments in Fluids*, *62*(5). https://doi.org/10.1007/s00348-021-03178-8

Jux, C., Sciacchitano, A., Schneiders, J. F., & Scarano, F. (2018). Robotic volumetric PIV of a full-scale cyclist. *Experiments in Fluids*, *59*(4), 1–15. https://doi.org/10.1007/s00348-018-2524-1

Kaiser, F., & Rival, D. E. (2023). Large-scale volumetric particle tracking using a single camera: analysis of the scalability and accuracy of glare-point particle tracking. *Experiments in Fluids*, *64*(9), 149. https://doi.org/10.1007/s00348-023-03682-z

Kerho, M. F., & Bragg, M. B. (1994). Neutrally buoyant bubbles used as flow tracers in air. *Experiments in Fluids*, *16*(6), 393–400. https://doi.org/10.1007/BF00202064

Moffat, R. J. (1988). Describing the uncertainties in experimental results. *Experimental Thermal and Fluid Science*, *1*(1), 3–17. https://doi.org/10.1016/0894-1777(88)90043-X

Mu, K., Ding, H., & Si, T. (2020). Experimental and numerical investigations on interface coupling of coaxial liquid jets in co-flow focusing. *Physics of Fluids*, *32*(4). https://doi.org/10.1063/5.0002102

Raffel, M., Willert, C. E., Scarano, F., Kähler, C. J., Wereley, S. T., & Kompenhans, J. (2018). *Particle Image Velocimetry: A Practical Guide*. Springer International Publishing. https://doi.org/10.1007/978-3-319-68852-7

Rayleigh, L. (1878). On the Instability of Jets. *Proceedings of the London Mathematical Society*.

Rosi, G. A., Sherry, M., Kinzel, M., & Rival, D. E. (2014). Characterizing the lower log region of the atmospheric surface layer via large-scale particle tracking velocimetry. *Experiments in Fluids*, *55*(5). https://doi.org/10.1007/s00348-014-1736-2

Scarano, F., Ghaemi, S., Caridi, G. C. A., Bosbach, J., Dierksheide, U., & Sciacchitano, A. (2015). On the use of helium-filled soap bubbles for large-scale tomographic PIV in wind tunnel experiments. *Experiments in Fluids*, *56*(2). https://doi.org/10.1007/s00348-015-1909-7

Schanz, D., Novara, M., Geisler, R., Agocs, J., Eich, F., Bross, M., Kähler, C. J., & Schröder, A. (2019). Large-scale volumetric characterization of a turbulent boundary layer flow. *13th International Symposium on Particle Image Velocimetry – ISPIV 2019*, (July).

Schneiders, J. F., Scarano, F., Jux, C., & Sciacchitano, A. (2018). Coaxial volumetric velocimetry. *Measurement Science and Technology*, *29*(6). https://doi.org/10.1088/1361-6501/aab07d

Schröder, A., Schanz, D., Bosbach, J., Novara, M., Geisler, R., Agocs, J., & Kohl, A. (2022). Large-scale volumetric flow studies on transport of aerosol particles using a breathing human model with and without face protections. *Physics of Fluids*, *34*(3). https://doi.org/10.1063/5.0086383

Schuth, M., & Buerakov, W. (2017, September). *Handbuch Optische Messtechnik* (3rd ed.). Carl Hanser Verlag GmbH & Co. KG. https://doi.org/10.3139/9783446436619

Tropea, C. (2011). Optical particle characterization in flows. *Annual Review of Fluid Mechanics*, *43*, 399–426. https://doi.org/10.1146/annurev-fluid-122109-160721

van der Hoek, D., Frederik, J., Huang, M., Scarano, F., Simao Ferreira, C., & Van Wingerden, J. W. (2022). Experimental analysis of the effect of dynamic induction control on a wind turbine wake. *Wind Energy Science*, *7*(3), 1305–1320. https://doi.org/10.5194/wes-7-1305-2022

Wei, N. J., Brownstein, I. D., Cardona, J. L., Howland, M. F., & Dabiri, J. O. (2021). Near-wake structure of full-scale vertical-axis wind turbines. *Journal of Fluid Mechanics*, *914*, 1–40. https://doi.org/10.1017/jfm.2020.578

4

3D treatment of light reflections

In this chapter, a generalized procedure for the mitigation of light reflections in volumetric PIV measurements is introduced, within the framework of object-aware Lagrangian particle tracking (OA-LPT). The approach proposes an automated reflection detection method based on the separation between particles and background signal in the spatio-temporal frequency domain. The method follows with an adaptive masking procedure and involves logics similar to OA-LPT, in this case for the blinded viewing directions. Therefore, regions of the cameras affected by light reflections are treated as optically blocked, such that the particle triangulation and tracking processes are informed accordingly.

The mechanisms of optical blinding from light reflections are first discussed in section 4.1, followed by the proposed deactivation procedure in section 4.2. The automated reflection detection algorithm is presented in section 4.3. The assessment in section 4.4 considers two experimental conditions: the flow around a wall-mounted cube, measured in a wind tunnel; the flow in the wake of a running athlete measured using the Ring-of-Fire apparatus.

Parts of this chapter have been published in: Grille Guerra, A., Porcar Galan, L., Sciacchitano, A., & Scarano, F. (2025). Treatment of light reflections in 3D PIV systems. *Measurement Science and Technology*, *36*(11), 115301. https://doi.org/10.1088/1361-6501/ae1993

4.1. Ghost formation in blinded bundles

Volumetric particle tracking algorithms involve both triangulation and tracking steps. In the triangulation process (e.g. Iterative Particle Reconstruction, IPR, Wieneke, 2013), epipolar lines are intersected to find the three-dimensional location of a particle. While in principle two viewing directions are sufficient for triangulation, typically more cameras are employed to reduce the probability of triangulating ghost particles. The region produced by the intersection of all N cameras is denoted as the domain of interest (DOI), where all camera views contribute to the triangulation of particles. Within the DOI, some regions may be covered by $N - M$ cameras only. This circumstance does not necessarily prevent the measurement, as long as the triangulation algorithm is aware of the camera coverage (the region covered by each camera). For the remainder, we recall the concept of camera coverage rank R_c from Hendriksen *et al.* (2024) as the integer representing the number of independent views participating the triangulation at each point of the measurement domain. The coverage rank must be at least 2 to enable particle triangulation.

From Elsinga *et al.* (2006), a system of N cameras will generate N_g^0 ghost particles in the measurement volume as:

$$N_g^0 = \left(\mathrm{ppp} \cdot A_p\right)^N \cdot l_x \cdot l_y \cdot l_z , \tag{4.1}$$

where ppp (particles per pixel) is the particle density in the recordings and A_p is the particle image area. The volume is imaged onto $l_x \cdot l_y$ pixels and l_z represents the depth in voxel units.

Let us assume that in a region of the object surface in the domain of interest light is scattered towards the imagers, as illustrated in figure 4.1 (left) for a system of $N = 3$ cameras. A portion of the sensor A_r^i, with the superscript i indicating the camera index, in each of the three cameras will receive light from the particle tracers superimposed to the direct scattering/reflection from the surface referred to as blinded areas. In this context, the term blinding is intended as the condition of a significantly increased light intensity compared to the remaining of the image. Such intensity does not necessarily need to exceed the saturation level to blind the view. The blinded viewing directions (i.e. blinded bundle $A_r^1 \cdot l_z$) from camera 1 is prone to produce ghost particles (G), at any intersection of epipolar lines from cameras 2 and 3. The equation proposed by Elsinga *et al.* (2006) is modified here for the purpose of estimating the number of ghost particles produced inside a blinded bundle, N_g^1, which reads as:

$$N_g^1 = \left(\mathrm{ppp} \cdot A_p\right)^{N-1} \cdot A_r^1 \cdot l_z , \tag{4.2}$$

with the lower exponent ($N - 1$ instead of N) suggesting that N_g^1 will quickly exceed N_g^0.

The problem of ghost formation is exacerbated in the regions where blinded bundles intersect. For instance, in the intersection between cameras 1 and 2 ($A_r^1 \cdot l_z \cap A_r^2 \cdot l_z$), $N_g^{1,2}$ ghost particles will be formed, as:

$$N_g^{1,2} = \left(\mathrm{ppp} \cdot A_p\right)^{N-2} \cdot \left(A_r^1 \cdot l_z \cap A_r^2 \cdot l_z\right) . \tag{4.3}$$

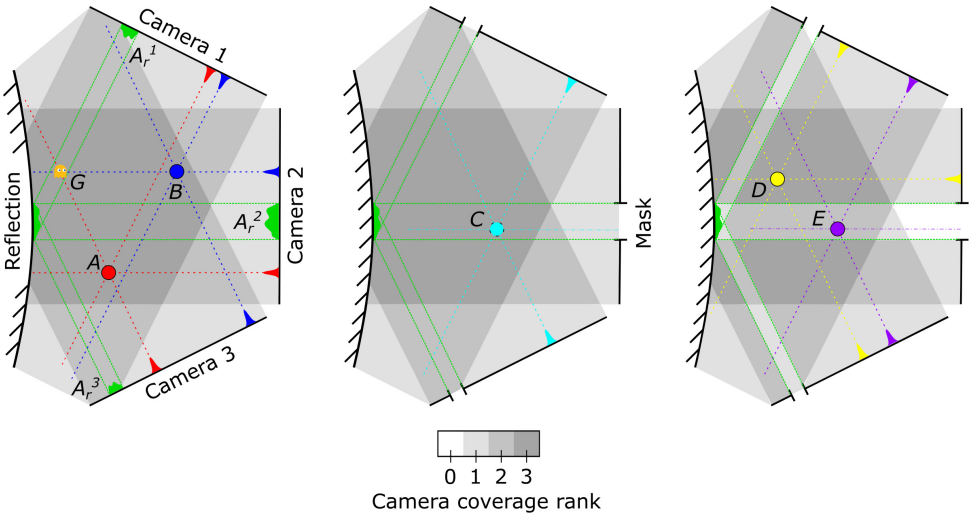

Figure 4.1: Camera coverage rank R_c and particle triangulation for a 3-camera system in presence of a finite region of light reflection. Left: two particles (A and B) are triangulated and a ghost (G) is formed in the blinded bundle of camera 1. Middle: blinded bundles are masked (value set to zero). A single particle (C) is triangulated by cameras 1 and 3 and falls within the masked region of camera 2, hence it is not reconstructed. Right: the blinded bundles are excluded by the triangulation process (object aware) and the two particles (D and E) are reconstructed even when one (E) falls inside a single blinded bundle.

A generalized formulation for a N-camera system yields an estimate of N_g ghost following the equation below:

$$\begin{aligned} N_g &= N_g^0 + \sum_{i=1}^{N} N_g^i + \sum_{i=1}^{N-1}\sum_{j=i+1}^{N} N_g^{i,j} + \cdots + N_g^{1,\ldots,N} = \\ &= \left(\mathrm{ppp}\cdot A_p\right)^N \cdot l_x \cdot l_y \cdot l_z + \sum_{i=1}^{N} \left(\mathrm{ppp}\cdot A_p\right)^{N-1} \cdot A_r^i \cdot l_z + \\ &+ \sum_{i=1}^{N-1}\sum_{j=i+1}^{N} \left(\mathrm{ppp}\cdot A_p\right)^{N-2} \cdot \left(A_r^i \cdot l_z \cap A_r^j \cdot l_z\right) + \cdots + \left(A_r^1 \cdot l_z \cap A_r^2 \cdot l_z \cap \cdots \cap A_r^N \cdot l_z\right). \end{aligned} \tag{4.4}$$

The ratio between ghost and actual particles is often taken as a measure of reconstruction accuracy. Equations 4.1 and 4.4 are evaluated below under typical conditions of seeding density ppp = [0.001 – 0.02], particle diameter d_τ = 2 px and fraction of area affected by light reflections A_r^*= [0 – 0.1]. Furthermore, the evaluation considers a varying number of cameras N.

An accurate particle field reconstruction is characterised by $N_g/N_p < 0.1$. Figure 4.2

(left) indicates that in absence of reflections, a system of four cameras is sufficient to reconstruct faithfully a particle field at ppp = 0.01. To incorporate light reflections into the discussion, a simplified situation is considered. It is assumed that reflections affect all cameras equally, and that the imagers observe the DOI with a constant angular separation between them (tomographic aperture angle, θ) of $\theta = \pi/4$, such that the intersection bundle of k cameras can be simply estimated as:

$$A_r^1 \cdot l_z \cap A_r^2 \cdot l_z \cap \cdots \cap A_r^k \cdot l_z = \frac{(A_r)^{3/2}}{2^{k-1} \tan\theta}. \tag{4.5}$$

For such conditions, the ratio N_g/N_p is given in figure 4.2 (right). Overall, a reduction in the particle reconstruction quality is observed. More importantly, increasing the number of cameras is a less effective measure to reduce spurious triangulations. Therefore, for an experiment affected by blinded bundles, adding new cameras does not provide further information, and ghost particles will still be formed in the affected areas.

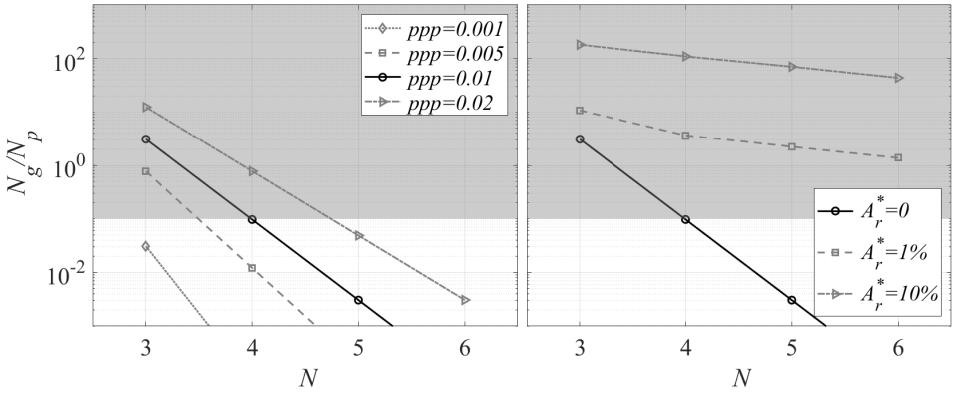

Figure 4.2: Ratio of ghost to real particles (N_g/N_p) as a function of the number of cameras N. Left: in the absence of light reflections, for varying ppp levels (equation 4.1). Right: for images affected by light reflections (equation 4.4), for varying reflection areas and ppp=0.01. Acceptable range is considered below 0.1 (N_g/N_p < 10%) and the region above such level is shaded to indicate conditions of overly corrupted reconstruction.

4.2. Deactivation of blinded bundles

A possible solution to the problem of ghost formation modelled by equation 4.4 is that the regions of the measurement domain that correspond to the reflections (blinded bundles) are excluded from the process of particle image triangulation. As a consequence, the coverage rank decrease in blinded bundle and the triangulation makes use of the remaining, not blinded, views. Bundle deactivation is a procedure similar to that devised by Wieneke and Rockstroh (2024) to deactivate regions of the DOI obscured by the

object presence. In that case, the position of the delimiting surface requires knowledge of the object position. Instead, for a blinded bundle, such information is not needed being the bundle deactivated along its entire depth. However, the identification of such bundle requires identification of the blinded area A_r on the sensor, in turn opening the problem of reflection detection.

Sample views from the 3D measurements around a scaled cyclist from Hendriksen *et al.* (2024), shown in figure 4.3, render the complexity of imaging the seeding tracers in the regime of volumetric illumination and imaging. The recording features regions where the tracers are clearly distinct from the background. In other regions, some background light is visible (e.g. ground floor, see the annotation in figure 4.3-left) and it can be often removed by time-average or time-minimum intensity subtraction. Finally, some bright regions emanate from the points where the light impinging onto the surface is reflected directly towards the imager. Such regions often feature a high intensity, and the image corruption is not recoverable by a simple subtraction. These regions are therefore considered as "blinded" and their back projection in three-dimensional space are the blinded bundles. An example of such blinded bundles for the images given in figure 4.3 are illustrated in figure 4.4. The blinded bundles from the three camera views shown in figure 4.3-left, middle and right are indicated in red, green and blue respectively. The complexity of the geometry causes the appearance of multiple blinded bundles, with some of them intersecting in small regions of the DOI.

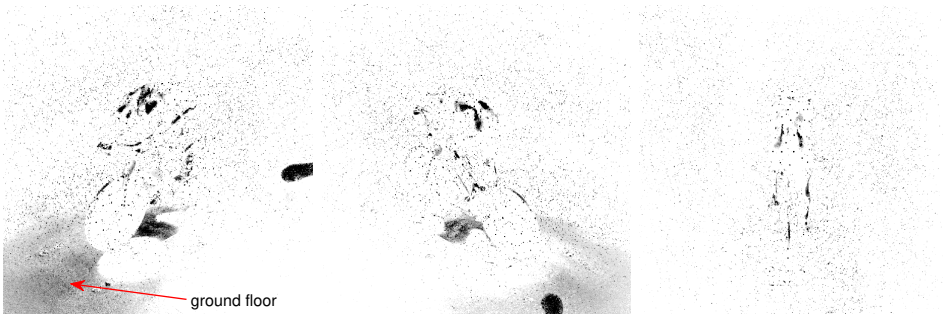

Figure 4.3: Raw PIV images as seen from three cameras from measurements around a scaled cyclist (Hendriksen *et al.*, 2024), including the presence of light reflections emanating from the object's surface.

A straightforward approach for blinded bundle deactivation consists in setting the intensity level to zero within A_r (figure 4.1-middle), provided such area has been detected. However, the shortcoming of such approach is that all particles in the blinded bundle will be neglected (C), leading to significant gaps in the measurement domain. Recalling the nomenclature introduced by Hysa *et al.* (2024), a volumetric loss V_{loss} of the DOI is formed, considering the union of the blinded bundles as:

$$V_{loss} = \mathrm{DOI} \cap \left(A_r^1 \cdot l_z \cup A_r^2 \cdot l_z \cup \cdots \cup A_r^N \cdot l_z \right) . \tag{4.6}$$

The above corresponds to the condition that a particle can be reconstructed if and only if it is triangulated by all the available N viewing directions. It can be easily demonstrated

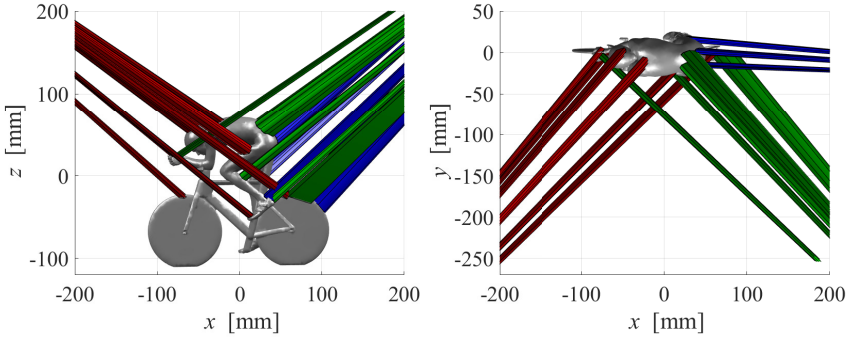

Figure 4.4: Side (left) and top (right) view of the blinded bundles affecting three cameras from the experiments of Hendriksen *et al.* (2024) on the flow around a scaled cyclist.

that by the above approach, further adding cameras paradoxically leads to an increased volumetric loss of the measurement.

A less invasive solution is that of masking (viz. disabling) the reflected regions, while adopting the object aware particle reconstruction technique (OA-LPT, Wieneke and Rockstroh, 2024) to the blinded bundles. In the reflection-aware context (RA-LPT), the requirement for particle reconstruction is relaxed to triangulation from a subset of $N - M$ cameras (in this context $N - M$ corresponds to the camera rank R_c), which does not include the M cameras blinded at the specific location of reconstruction. By the latter approach (figure 4.1-right), the formation of ghost particles can be mitigated and the measurement domain erosion only includes the regions where more than $N - 2$ blinded bundles intersect. In this example, particles can be reconstructed in regions unaffected by reflections (D) and also inside single blinded bundles (E).

Figure 4.5 exemplifies the above discussion by illustrating the distribution of coverage rank based on the principle of blinded bundles intersection (equation 4.5). The example consists of four cameras observing a sphere, representative of the measurements from Jux *et al.* (2020). In the original experiments, the use of a coaxial volumetric velocimeter (CVV, Schneiders *et al.*, 2018) for illumination and imaging produced the situation illustrated in figure 4.5 (left), where the blinded bundles intersect over a relatively large volume. Considering a minimum coverage rank of $R_{min} = 3$ for particle triangulation (instead of the default 2), a loss of approximately $V_{loss} = 6\%$ of the DOI is formed. The scenario is improved employing a more conventional camera arrangement with higher tomographic aperture, of $\theta = 30°$, as illustrated in figure 4.5 (right), where $V_{loss} = 3\%$ of the DOI and the missing region is kept closer to the object surface.

4.3. Reflection identification and masking

From the above it is clear that any method that requires blinded bundle deactivation requires knowledge of the blinded region in the domain, in turn asking for identification

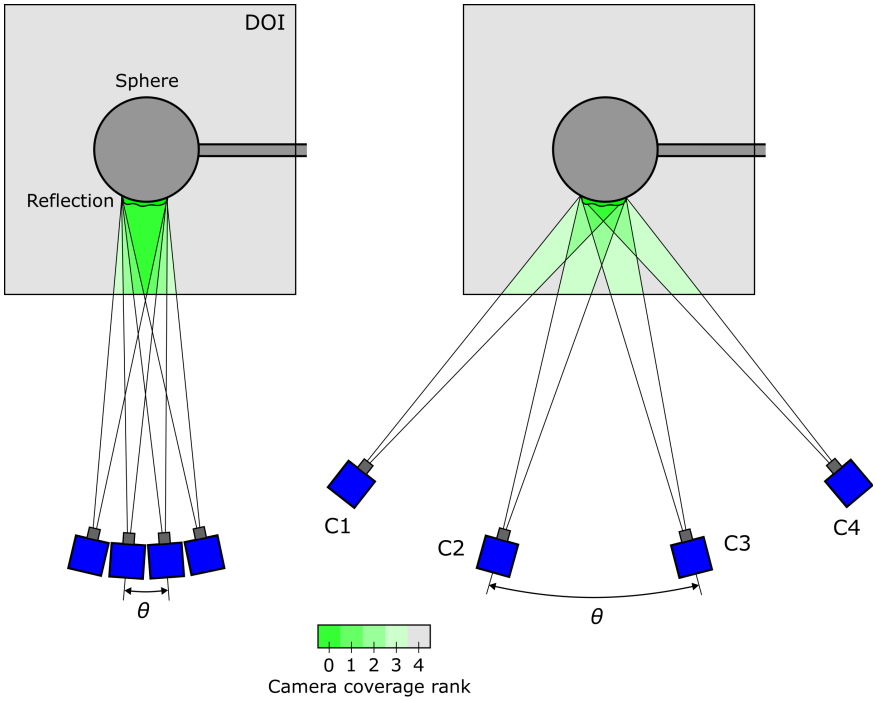

Figure 4.5: Camera coverage rank for a 4-camera system looking at a sphere under volumetric illumination. Left: for a low tomographic aperture system (θ = 4°). Right: for a higher tomographic aperture (θ = 30°).

of the image region overexposed by light reflections. Volumetric PIV light reflections tend to be more diffuse compared to the typical bright stripe encountered in planar PIV. Often such reflections do not saturate the sensor, however their shape and intensity can largely vary which complexifies their identification.

A raw image from the volumetric PIV experiment around a sphere of Jux *et al.* (2020) is shown in figure 4.6 (left). Particle images appear as tiny dots; the sphere surface is not visible, but indicated by a dashed green line; the region of reflection is a rather circular blob with maximum intensity at the middle and decaying radially.

In this example, the reflection is stationary, and therefore image pre-processing by subtracting the (sliding) time-minimum along the recording sequence is a proven approach (Gui *et al.*, 1997). The result is shown in figure 4.6 (middle), where the reflection intensity is attenuated. Yet some time variations due to model-camera vibrations and illumination jitter prevent full elimination of the reflected light. A spatial high-pass filter (Willert, 1997) yields similar results (figure 4.6-right). In general, separating particles image intensity from the background remains a challenging problem lacking a universal solution. The problem becomes particularly intricate when dealing with reflections that vary in space and time. In this respect, image masking is considered a more viable approach.

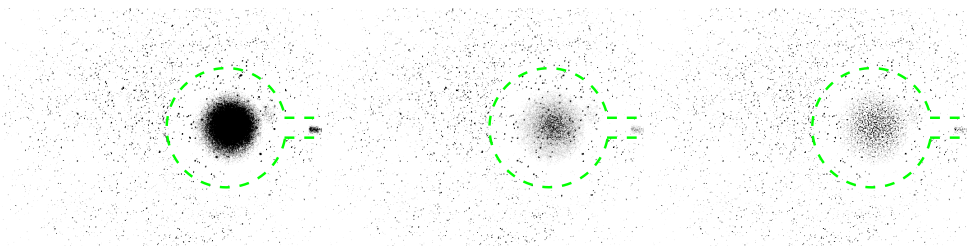

Figure 4.6: Images of the flow around a sphere (inverted greyscale), indicated by the green dashed line, obtained from a 3D PIV system. Left: raw image. Middle: pre-processed image after subtraction of the minimum intensity in time. Right: pre-processed image obtained via high-pass filtering in space.

Here, we consider the reduction of the reflection intensity level associated with the image pre-processing methods as shown in figure 4.6; by a comparison with the raw image, the region of largest disparity can be identified to form a processing mask (Porcar Galan *et al.*, 2024). While any method available in the literature could be used for this purpose, the approach discussed here aims at generalizing the procedure such to be suited for both stationary as well as fast-moving reflections.

The method combines time-based and spatial-based filters. In the time domain, a third-order Butterworth high-pass filter is considered (Sciacchitano & Scarano, 2014), that tackles the contribution of stationary or slow-moving reflections. The filter is defined by the cut-off frequency f, expressed in terms of the Nyquist acquisition frequency. In the spatial domain, a high-pass filter with a Gaussian isotropic kernel is considered, to tackle reflection areas bigger than the particle images. When implemented in the frequency domain (Porcar Galan *et al.*, 2024), the filter is defined by a cut-off wavenumber κ. The resulting operator can be considered acting in the frequency-wavenumber space as a high-pass filter. In the remainder, the combined method will be referred to as spatio-temporal high-pass filter. For computational efficiency both approaches are implemented in the frequency domain. Applying this methodology, with $f = 0.1$ and $\kappa = 0.01$ 1/px (please refer to Sciacchitano and Scarano, 2014 and Porcar Galan *et al.*, 2024 for the choice of appropriate spatio-temporal cut-offs respectively) to the raw image in figure 4.6 (left) returns the image shown in figure 4.7 (left). Due to the combination of time and space information, the analysis outperforms that of previously discussed methods, but still fails to fully separate the particle images from the background for its complete elimination.

Therefore, the approach aims at a producing a mask from the normalized comparison between raw (i) and pre-processed (j) images. The operation follows the concept of the structural similarity index measure (SSIM, introduced by Wang *et al.*, 2004), which reads as:

$$\mathrm{SSIM}(i,j) = \frac{\left(2\mu_i\mu_j + c_1\right)\left(2\sigma_{ij} + c_2\right)}{\left(\mu_i^2 + \mu_j^2 + c_1\right)\left(\sigma_i^2 + \sigma_j^2 + c_2\right)}, \tag{4.7}$$

where μ_i, μ_j, σ_i, σ_j and $\sigma_i j$ are the local (over a Gaussian window) mean, standard

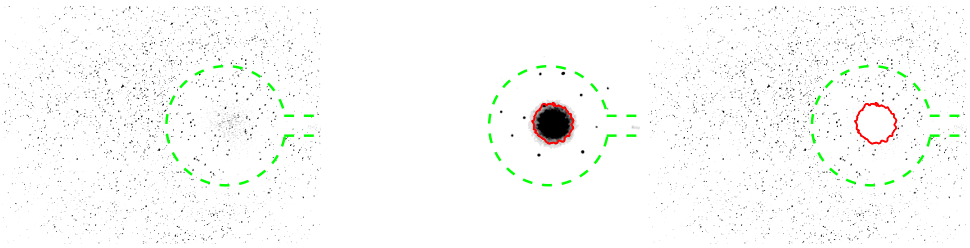

Figure 4.7: Image pre-processing approach applied to an image of the flow around a sphere, indicated by the green dashed line, obtained from a 3D PIV system. Left: image pre-processed via spatio-temporal high-pass filtering. Middle: SSIM between raw and pre-processed images, with SSIM=0.5 indicated by a red line; dark indicates low values of SSIM, whereas white represents SSIM=1. Right: masking applied to the pre-processed image for SSIM<0.5.

deviation and covariance of the images, and c_1 and c_2 are small regularization constants. This metric is frequently adopted in machine vision to assess the quality of image compression. The operator yields unity for identical images, and tends to zero when changes in intensity and contrast are significant. The SSIM between the raw image in figure 4.6 (left) and the pre-processed image in figure 4.7 (left) is illustrated in figure 4.7 (middle). Lower values in the reflection area can be used as indicator of reflection. A few dots are visible too, due to the object markers painted on the surface of the sphere. A reflection detection criterion is chosen as SSIM<0.5, which is indicated in figure 4.7 (middle) by a red line. The region inside this boundary is then considered blinded and the corresponding blinded bundle is evaluated by ray tracing and deactivated from the process of particles reconstruction. Masking this region in the pre-processed image finally returns the image shown in figure 4.7 (right), where the blinded region intensity level is set to zero for readability.

The computational cost of the additional masking step is comparable to that of the pre-processing stages. For the images of the test case presented in section 4.4.1 (100 snapshots and 10 cameras in double-frame mode), the involved CPU times for the Butterworth temporal high-pass filter, the spatial high-pass filter and the masking step were approximately 300 s, 100 s and 150 s respectively, with all methods implemented on *Matlab 2024b* running on an Intel(R) *Xeon(R) W-2223* processor. This means that the image masking added an extra 37.5 % of computational time.

4.4. Experimental assessment

Two experiments are presented that demonstrate the viability and the performance of the method. The first is conducted in a low-speed wind tunnel facility, and consists of measurements around a wall-mounted cube (Hendriksen *et al.*, 2025). The region of interest is illuminated from four different directions, and the particles are imaged from ten directions. The low acquisition frequency of the cameras limits the measurements to double-frame mode, and the particle tracking is done using the so-called two-pulse

Shake-the-Box algorithm (Novara *et al.*, 2023).

In the second experiment, the velocity field around and past a running athlete (D'Angelo *et al.*, 2026) is measured using the Ring-of-Fire system (Spoelstra *et al.*, 2019). Light is provided from a single illumination direction in form of a 30 cm thick slab. The light scattered by the tracers is collected with only three high-speed cameras and time-resolved particle tracking makes use of the Shake-the-Box algorithm (Schanz *et al.*, 2016). The athlete crossing the illuminated region produces strong and fast-varying reflection regions in all cameras.

Both experiments make use of sub-millimetre helium-filled soap bubbles (Scarano *et al.*, 2015) as tracers, resulting in good image quality thanks to their excellent light scattering characteristics. The most relevant experimental parameters are summarized in table 4.1.

	Wall-mounted cube (wind tunnel)	Running athlete (Ring-of-Fire)
Tracer particles	HFSB	HFSB
Illumination	4 x *LED Flashlight 300* (300 W)	4 x *LED Flashlight 300* (300 W)
Imaging	10 x LaVision *Imager LX* (CCD, 2 MPx, 4.4 µm, 14 bit)	3 x Photron *Mini AX100* (CMOS, 1 MPx, 20 µm, 12 bit)
Reference velocity [m/s]	10 (free stream)	8 (running speed)
Measurement volume [L]	125	2200
Acquisition frequency [Hz]	8 (double-frame)	400
Pulse duration [µs]	25	250
Pulse separation [µs]	250	2500
Objective focal length [mm]	25	50
Digital image resolution [px/mm]	4.4	0.4
f-number $f_\#$	8	5.6
Particles per pixel (ppp)	0.01	0.03

Table 4.1: Measurement parameters of the two experiments.

4.4.1. Wall-mounted cube

The flow around a wall-mounted cube with a side length of 10 cm is measured in the W-Tunnel of the Faculty of Aerospace Engineering of TU Delft, an open jet facility with a cross section of 60 x 60 cm^2. The cube is mounted at zero incidence, i.e. its faces are parallel and perpendicular to the freestream direction. The freestream speed is set to U_∞ = 10 m/s (Re = 70,000). The flow is seeded with neutrally-buoyant HFSB, released by an in-house 200-generator seeding rake installed in the settling chamber of the wind tunnel (Saiz *et al.*, 2022). To avoid optical blockage due to shadow regions, a measurement volume of approximately 50 x 50 x 50 cm^3 is illuminated from various directions using four LaVision *LED-Flashlight 300* modules. Similarly, a total of ten

LaVision *Imager LX* cameras (2 MPx, 4.4 µm pitch, 14 bit) are placed around the object to compensate for optical blockage due to camera occlusions. The cameras are mounted on two arrays, containing five cameras each, referred to as *antennas*. The camera arrangement of such antennas is shown in figure 4.8 (left). The cameras are equipped with 25 mm focal length objectives and the f-number is set to $f_{\#}$ = 8 in order to achieve the desired depth of field. For the given configuration, this results in a digital image resolution of 4.4 px/mm. A top-view of the experimental setup is given in figure 4.8 (right).

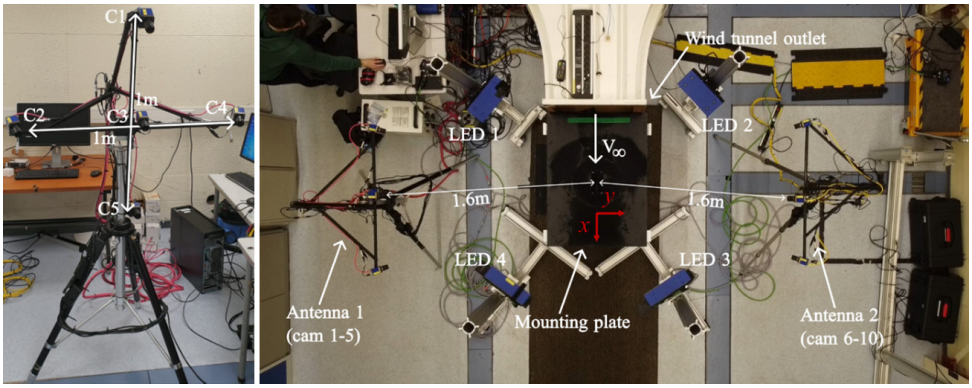

Figure 4.8: Experimental setup of the wind tunnel measurements of the flow around a wall-mounted cube. Left: arrangement of five cameras in an antenna array. Right: top-view of the setup, containing the wind tunnel outlet, illumination, imaging and mounting plate for the object of interest.

The maximum acquisition frequency of the chosen cameras is insufficient for time-resolved particle tracking, and thus the measurements are conducted in double-frame mode, at a frequency of 8 Hz, and velocity information is obtained via TP-STB. To maximize illumination, the LED modules are operated in overdrive mode, using a pulse width of 25 µs, which results in a pulse energy of 7.25 mJ. The pulse separation is therefore set to 250 µs, respecting the duty cycle of the hardware, which corresponds to a typical particle displacement of around 10 px in the images.

Each antenna is calibrated independently using a planar calibration plate that is shifted and rotated in the measurement volume, and the two arrays are coupled together using a wand-based approach (Nutta *et al.*, 2023). A pinhole camera model is considered, and refined based on a volume self-calibration (Wieneke, 2008) performed on the particle images. Calibration, particle tracking and data postprocessing operations are performed in the DaVis 11.2 software, which incorporates object-aware capabilities (Wieneke & Rockstroh, 2024).

The relative location of illumination and imaging within the experimental setup causes the appearance of light reflection regions in some cameras. For instance, camera 1 (top camera in antenna 1, see figure 4.8) is mostly unaffected, as shown in figure 4.9 (left). While the location of the cube can be recognized in the raw image, the pixel intensity in this area is weaker than that of the particle images and it can be filtered out effectively.

Instead, camera 2 (downstream camera in antenna 1) is affected by the position of the upstream illuminator on the opposite side of the cube, whose light reflects from the mounting plate corrupting part of the image, as shown in figure 4.9 (middle). Using the automated masking approach discussed in section 4.3, with $f = 0.1$ and $\kappa = 0.01$ 1/px, transforms the image into the one shown in figure 4.9 (right). The pre-processed image contains a mask in the light reflection region coming from the mounting plate and two smaller masks at the mounting points of the cube, indicated by red lines in the figure.

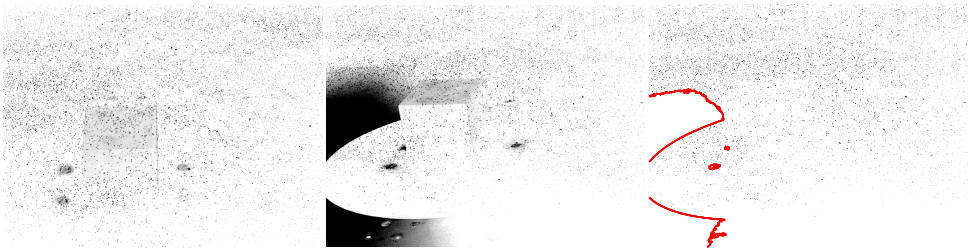

Figure 4.9: Experimental images of the flow around a wall-mounted cube. Left: raw image in camera 1, looking at the cube from above. Middle: raw image from camera 2, looking at the cube from downstream. Right: pre-processed image (spatio-temporal high-pass filter) from camera 2, with generated mask indicated by red lines.

The spatial location of the generated masks can be incorporated into the OA-LPT framework as another source of optical blockage. Without it, all contributions in the present experiment arise from camera occlusions due to the presence of the cube in the measurement domain. This is illustrated in figure 4.10 (left), by showing a slice of the camera coverage rank R_c at a height of $z = 75$ mm from the mounting plate. R_c is extracted directly from the TP-STB analysis, by reducing the particle-based results onto a Cartesian grid using an ensemble-averaging approach, collecting samples from 100 snapshots and averaging over bins with a side length of 1 cm and 75% overlap. In the wake of the cube, all ten cameras have optical access, while this number reduces closer to the object, with only five cameras seeing each side of the cube close to the surface.

Including the optical blockage arising from the presence of light reflections in the downstream imagers results in the coverage rank shown in figure 4.10 (right). At this height, the reflections coming from the mounting plate have an effect on the front part of the cube, with the rank reducing from ten to eight due to two cameras being affected.

The impact of the masking approach and the inclusion of masks in the OA-LPT framework is discussed in the following, both in terms of the particle tracking analysis and Cartesian grid reduction results. A benchmark is established employing images that have been pre-processed using the approach introduced in section 4.3, but without the masking step, so that reflections are attenuated and not removed completely. This represents a typical scenario of image pre-processing for volumetric PIV, and resembles the situation sketched in figure 4.1 (left). Particle tracks extracted from the TP-STB analysis are shown in figure 4.11 (left), coloured by streamwise velocity. For improved visualization, only a small region around the cube is included, and up to a height of

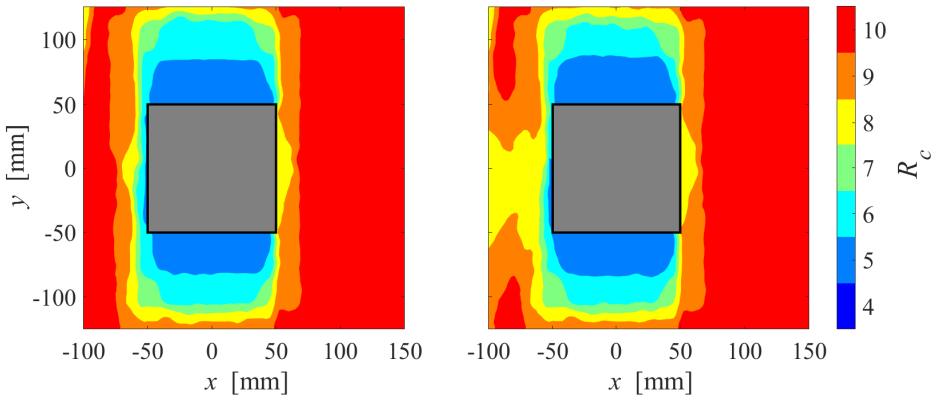

Figure 4.10: Camera coverage rank R_c around the cube in a slice at a height of z = 75 mm from the wall. Left: where only optical blockage due to camera occlusion has been considered. Right: where both camera occlusion and light reflection have been considered.

z = 100 mm from the wall, from an ensemble of 5 snapshots. Notably, the remaining intensity in the regions of reflection causes the appearance of an agglomeration of ghost particles at the mounting points of the cube (z = 0), indicated by purple circles in the figure. These locations can be already observed in the raw images, as for example the one shown in figure 4.9 (middle). Besides, ghost particles are triangulated in regions where fewer cameras have optical access, this is, close to the sides (see figure 4.10-left). The region next to the lateral face at positive y is particularly clear, with particles of high velocity being tracked in a region where flow separation is expected. The asymmetric behaviour between the two sides of the cube is attributed to a slightly different location and orientation of the LED illuminators, which produced a more severe reflection in the positive y side. This behaviour is in line with the discussion introduced in section 4.1, as reflections cause the appearance of ghost particles (false positives) throughout the domain.

The appearance of ghost particles can be attenuated by masking the regions affected by light reflections, as sketched in figure 4.1 (middle). Without further modifications to the particle tracking algorithm, this solution introduces the problematic of false negatives (regions void of particles), since particles travelling over masked areas cannot be found in all cameras that have optical access. The situation is illustrated in figure 4.11 (right), which shows particle tracks extracted from masked images (see figure 4.9-right), while requiring R_c to follow the behaviour given in figure 4.10 (left). For visualization purposes, only a region for $y > 0$ is included in the figure, from an ensemble of 100 snapshots. The results show the appearance of a bundle void of particles in the domain, indicated in purple, which belongs to the propagation of a mask along the line of sight of the affected camera. The comparison between the two situations given in figure 4.11 reveals that, without image masking, the ratio of ghost to real particles is approximately $N_g/N_p = 0.35$. On the other hand, a volumetric loss of $V_{loss} = 8\%$ of the

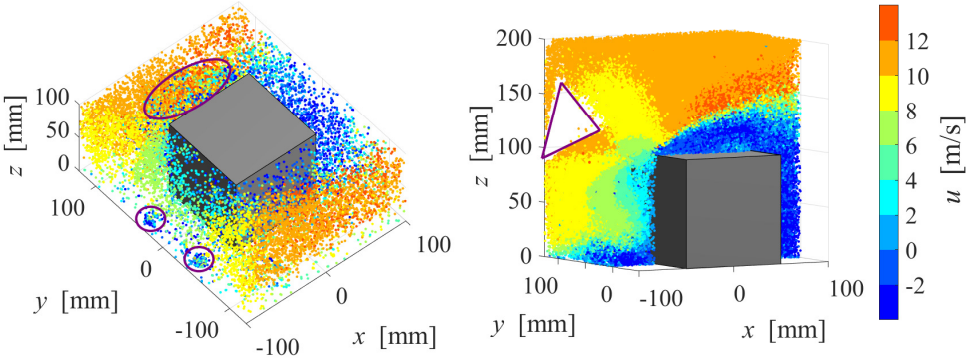

Figure 4.11: Particle tracks in the surroundings of the wall-mounted cube, coloured by streamwise velocity. Left: images have been pre-processed with the spatio-temporal high-pass filter but not masked, and regions dominated by ghost particles are indicated in purple. Right: images have been masked, but optical blockage has not been accounted for. Region void of particles indicated in purple.

DOI is introduced by masking the reflection areas.

Both situations (false positives and false negatives) affect the time-averaged velocity field once reduced onto a Cartesian grid (using the same ensemble-averaging parameters as discussed earlier for R_c). Contours of the time-averaged streamwise velocity and the standard deviation of streamwise velocity, extracted at a slice at a height of z = 75 mm from the wall are shown in figure 4.12 (top) and figure 4.12 (bottom) respectively. The results shown in figure 4.12 (left) are obtained without the masking step. Here, ghost particles corrupt the solution close to the surface on the sides, as anticipated in figure 4.11 (left). This behaviour is more noticeable for $y > 0$, where no flow separation can be observed and high velocity fluctuations are measured in potential flow areas upstream and to the side of the cube.

The solution shown in figure 4.12 (middle) is the one obtained when masking the images but not modifying the required R_c, extracted from the particle tracks shown in figure 4.11 (right). This case is affected by false negatives, and no time-averaged solution can be obtained in a region upstream of the cube. Both false positives and false negatives can be avoided employing the approach introduced in this article, resembling the situation sketched in figure 4.1 (right). Masking the images and modifying the required camera coverage rank to match the one shown in figure 4.10 (right) returns the velocity field shown in figure 4.12 (right). This solution does not contain any data gaps and no significant effect of ghost particles can be appreciated. The flow field agrees well with results in the literature (Schröder *et al.*, 2020), including flow separation on the sides and a recirculation region in the wake extending more than a side length downstream of the back face.

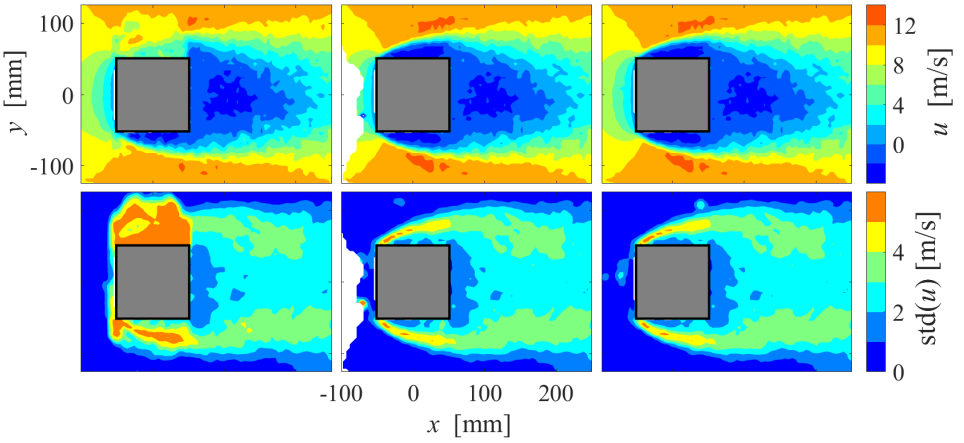

Figure 4.12: Contours of time-averaged streamwise velocity (top) and standard deviation of streamwise velocity (bottom) at a height of z = 75 mm from the wall. Left: images have been pre-processed with the spatio-temporal high-pass filter but not masked. Middle: images have been masked, but optical blockage has not been accounted for. Right: images have been masked and optical blockage has been accounted for.

4.4.2. Running athlete

The flow field around a running athlete has been measured experimentally in an indoor sprint hall at the Omnisport sport facility, located in Apeldoorn, The Netherlands. Prior to the experiments, the participant signed an informed consent form. The approximate running speed is 8 m/s (Re ~ 200,000 based on a shoulder width of 0.4 m), measured using a laser Doppler device (Jenoptik *Laveg LDM 300C*, Ashton and Jones, 2019). The flow is seeded using HFSB, generated by the same seeding rake discussed earlier for the wall-mounted cube experiment. A region of 0.3 x 2.7 x 2.7 m^3 (x x y x z) is illuminated using four LaVision *LED-Flashlight 300* modules, and imaged using three Photron *Mini AX100* high-speed cameras (CMOS, 1 MPx, 20 µm pitch, 12 bit) equipped with 50 mm focal length objectives set to $f_\#$ = 5.6. For the chosen configuration, the resulting digital image resolution is equal to 0.4 px/mm. A picture of the experimental setup is given in figure 4.13.

The recording sequence, triggered by a photoelectric sensor, consists of a series of 1000 images acquired at 400 Hz, using an illumination pulse duration of 250 µs (pulse energy of 72.5 mJ). This results in a covered distance of approximately 20 m, of which 14 m correspond to the athlete's wake. Camera calibration is performed using a custom two-level calibration plate, employing a pinhole camera model later refined via VSC (Wieneke, 2008) from the particle images.

The present analysis focuses on the near wake of the athlete. While passing through the illuminated region, light reflects from the skin and clothing causing the appearance of a strong reflection in the cameras. This changes rapidly from frame to frame posing

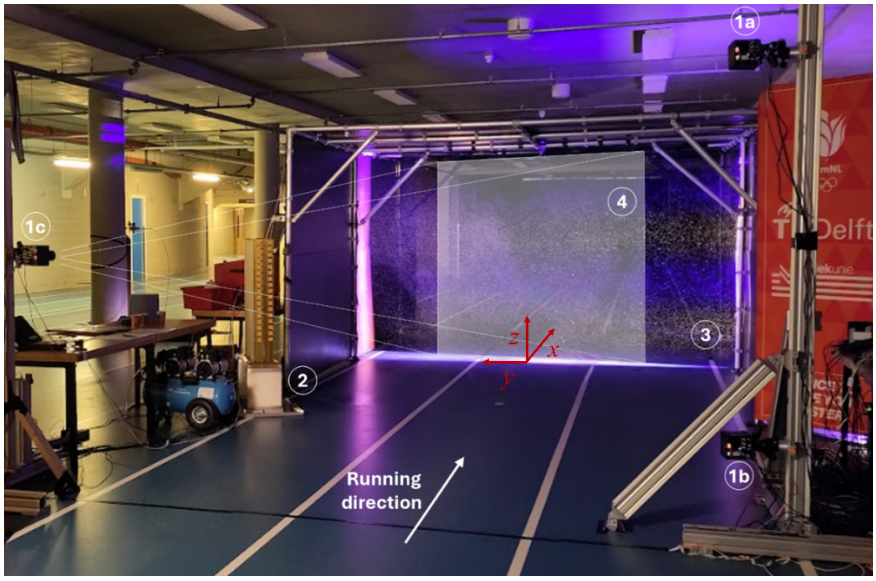

Figure 4.13: Picture of the experimental arrangement of the on-site measurements of the flow in the wake of a running athlete. High-speed cameras (1), seeding rake (2), LED modules (3) and region of interest (4).

additional challenges to the image pre-processing stage. Raw and pre-processed images are shown in figure 4.14 (top) and figure 4.14 (bottom) respectively, for a frame when the athlete has almost made it through the illuminated slab. The images have been dewarped to the plane $x = 0$ for a better representation of the perspective angle.

In Ring-of-Fire experiments, slow-moving particles are present away from the measurement target. A time-based high-pass filter applied to the images, as the one discussed in section 4.3, may cancel these out. To avoid it, the normalized frequency of the filter is set to $f = 0$ for the current test case, effectively acting like an average subtraction applied to the sequence. Further using $\kappa = 0.01$ 1/px and the automated masking step returns the image shown in figure 4.14 (bottom). The current method is able to mask both the stationary reflections (floor) as well as the moving athlete, as indicated in red in the figure.

In the wake of the runner, it can be assumed that the only source of optical blockage is that induced by the light reflections. Without this consideration, it is required that all-three cameras detect a tracer particle, such that $R_{min} = R_c = 3$. In this scenario, and pre-processing the images without the masking step, particle tracks obtained from the STB algorithm are shown in figure 4.15 (left). These are coloured by streamwise velocity and represent the trajectories measured in a time interval of eleven snapshots around the frame depicted in figure 4.14. The residual intensity in the regions of reflections causes the triangulation and tracking of the athlete's foot, which is still travelling through the illuminated domain in the time interval considered here. Apart from that, ghost particles are reconstructed around the silhouette of the runner, mostly on the positive y

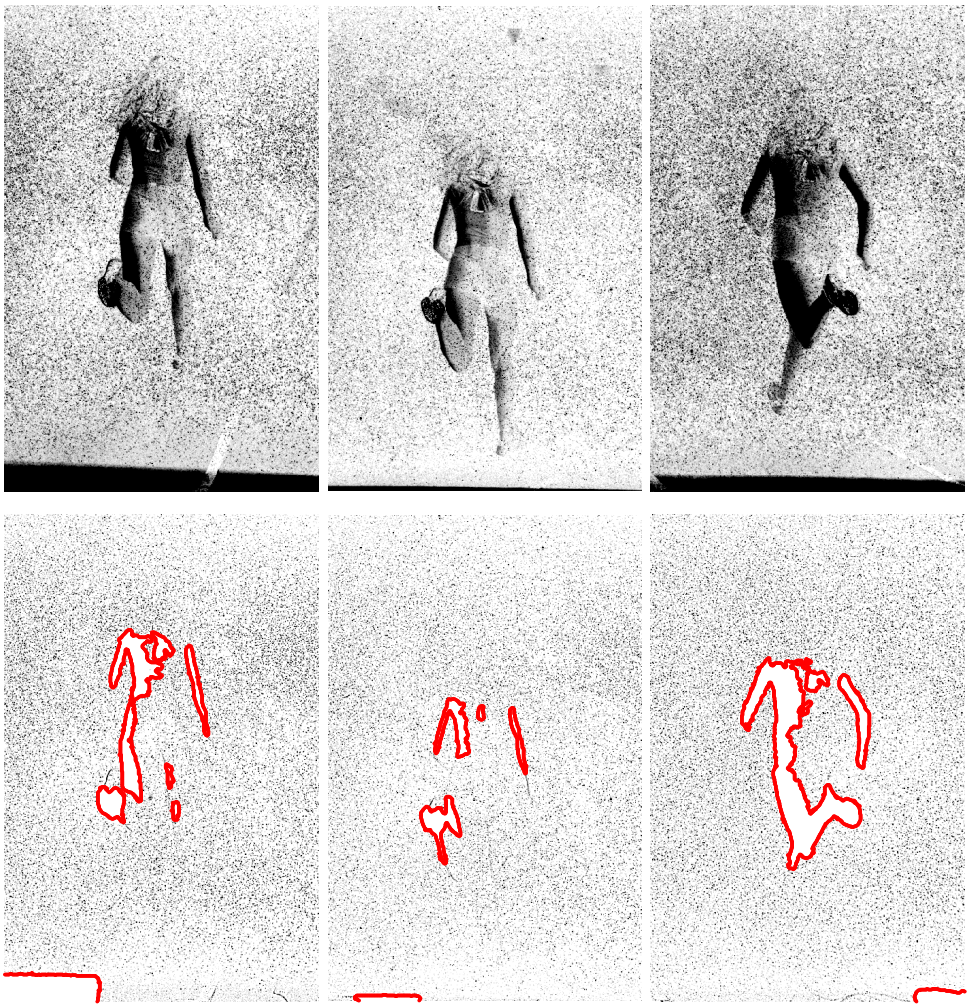

Figure 4.14: Experimental images of the flow in the near wake of a running athlete. Images from cameras 1a to 1c (see figure 4.13) given from left to right. Top: raw images. Bottom: pre-processed images (spatio-temporal high-pass filter), with masked regions indicated in red.

side since this is the region most severely affected by reflections (see figure 4.14). These are visible as scattered tracks with unphysically high velocity for their region, and represent approximately 7% of the total number of particles tracked ($N_g/N_p \approx 0.07$).

The proposed approach is to mask the images, as shown in figure 4.14 (bottom), and modify the camera coverage rank for every frame independently, such that regions where only two cameras are not blocked ($R_c = 2$) can still be recovered. This approach is more robust than setting $R_{min} = 2$ everywhere, which would cause the excessive

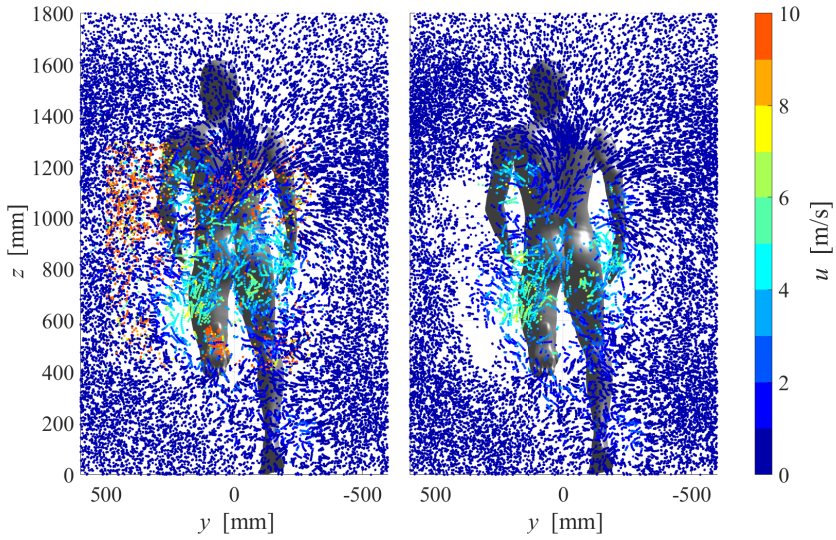

Figure 4.15: Particle tracks measured in the near wake of a running athlete, from a sequence of 11 snapshots. Left: images have been pre-processed using the spatio-temporal high-pass filter without the masking step. Right: images have been masked and the camera coverage rank has been modified accordingly.

formation of ghost particles due to the low number of viewing directions involved in the triangulation process (Elsinga *et al.*, 2006). The trajectories obtained by such procedure can be found in figure 4.15 (right). Ghost particles are not visible in the result, and the regions void of particles (V_{loss}, estimated as those where no particles are reconstructed at double the average inter-particle distance in the domain) are kept to approximately 4% of the DOI.

The resulting flow field reveals a significant streamwise velocity deficit in the near wake, and may be further used for inspection of dominant flow features such as the vortical structures released by the arms and shoulder of the athlete, typically only accessible through numerical simulations (Schickhofer & Hanson, 2021).

4.5. Conclusions

A framework for the treatment of light reflections in volumetric PIV measurements has been introduced. It makes use of the recent development of object-aware particle tracking strategies (Wieneke & Rockstroh, 2024) that account for optical blockage in the measurement volume arising from camera occlusion. Regions of the images affected by light reflections are treated as optically occluded, such that the particle tracking operation is not hampered by the formation of ghost particles (false positives) or data gaps due to cancelled particles (false negatives). The RA-LPT method exploits

the concept of camera redundancy to employ the ideal number of cameras in the reconstruction process of every tracer particle.

A masking procedure for volumetric PIV images is introduced as a means of detecting the blinded regions. The method is based on the comparison between the raw image and its high-pass filtered version in the space-time domain, used to generate a mask which, applied to the pre-processed version, creates an image unaffected by reflections. The extracted mask is used to define a region in space not accessible by the affected camera.

The method has been assessed considering two different experimental conditions, representative of large-scale volumetric PIV applications. First, a wind tunnel experiment is explored, where stationary reflections around the object of interest are formed, adding sources of optical blockage to the camera occlusion problematic. Secondly, a more challenging Ring-of-Fire (Spoelstra *et al.*, 2019) situation has also been tackled, where the measurement target, a running athlete, creates strong reflections that change significantly in shape and intensity between successive snapshots. In both situations, the method has been shown able of reducing the appearance of ghost particles while maximizing the achievable measurement domain, as summarized in table 4.2.

	Wall-mounted cube		Running athlete	
	N_g/N_p [%]	V_{loss}	N_g/N_p [%]	V_{loss}
Without masking	35	-	7	-
Only masking	<1	8	<1	20
RA-LPT	<1	0	<1	4

Table 4.2: Ratio of ghost to real particles (N_g/N_p) and volumetric loss (V_{loss}) relative to the two experiments.

References

Ashton, J., & Jones, P. A. (2019). The reliability of using a laser device to assess deceleration ability. *Sports*, *7*(8), 1–9. https://doi.org/10.3390/sports7080191

D'Angelo, C., Buszek, M., Terra, W., & Sciacchitano, A. (2026). On-site investigation of sprinter aerodynamics. *Accepted for publication in Experiments in Fluids*, 1–16.

Elsinga, G. E., Van Oudheusden, B. W., & Scarano, F. (2006). Experimental assessment of Tomographic-PIV accuracy. *13th Int Symp on Applications of Laser Techniques to Fluid Mechanics Lisbon, Portugal, 26-29 June, 2006*.

Grille Guerra, A., Porcar Galan, L., Sciacchitano, A., & Scarano, F. (2025). Treatment of light reflections in 3D PIV systems. *Measurement Science and Technology*, *36*(11), 115301. https://doi.org/10.1088/1361-6501/ae1993

Gui, L., Merzkirch, W., & Shu, J.-Z. (1997). Evaluation of Low Image Density PIV recordings with the MQD method and application to the flow in a liquid bridge. *Journal of Flow Visualization and Image Processing*, *4*(4), 333–343. https://www.scopus.com/inward/record.uri?eid=2-s2.0-0005985485%7B%5C&%

7DpartnerID=40%7B%5C&%7Dmd5=2936ec23f021b29fd60f5a8fd27a5bb5
Export Date: 28 January 2025; Cited By: 20.

Hendriksen, L. A., Grille Guerra, A., Sciacchitano, A., & Scarano, F. (2025). Omnidirectional Particle Image Velocimetry. *Proceedings of the 16th International Symposium on Particle Image Velocimetry*.

Hendriksen, L. A., Sciacchitano, A., & Scarano, F. (2024). Object registration techniques for 3D particle tracking. *Measurement Science and Technology*, *35*(12). https://doi.org/10.1088/1361-6501/ad715c

Hysa, I., Tuinstra, M., Sciacchitano, A., Scarano, F., van der Meulen, M. J., Rockstroh, T., & Roosenboom, E. W. (2024). A multi-directional redundant 3D-LPT system for ship–flight–deck wind interactions. *Experiments in Fluids*, *65*(8), 1–15. https://doi.org/10.1007/s00348-024-03867-0

Jux, C., Sciacchitano, A., & Scarano, F. (2020). Flow pressure evaluation on generic surfaces by robotic volumetric PTV. *Measurement Science and Technology*, *31*(10). https://doi.org/10.1088/1361-6501/ab8f46

Novara, M., Schanz, D., & Schröder, A. (2023). Two-Pulse 3D particle tracking with Shake-The-Box. *Experiments in Fluids*, *64*(5), 1–21. https://doi.org/10.1007/s00348-023-03634-7

Nutta, T., Sciacchitano, A., & Scarano, F. (2023). Wand-based calibration technique for 3D LPT. *15th International Symposium on Particle Image Velocimetry*.

Porcar Galan, L., Grille Guerra, A., Sciacchitano, A., & Scarano, F. (2024). Light Reflections Detection And Correction For Robotic Volumetric PIV. *Proceedings of the International Symposium on the Application of Laser and Imaging Techniques to Fluid Mechanics*, *21*, 1–19. https://doi.org/10.55037/lxlaser.21st.59

Saiz, G. G., Sciacchitano, A., & Scarano, F. (2022). On the closure of Collar's triangle by optical diagnostics. *Experiments in Fluids*, *63*(8), 128. https://doi.org/10.1007/s00348-022-03468-9

Scarano, F., Ghaemi, S., Caridi, G. C. A., Bosbach, J., Dierksheide, U., & Sciacchitano, A. (2015). On the use of helium-filled soap bubbles for large-scale tomographic PIV in wind tunnel experiments. *Experiments in Fluids*, *56*(2). https://doi.org/10.1007/s00348-015-1909-7

Schanz, D., Gesemann, S., & Schröder, A. (2016). Shake-The-Box: Lagrangian particle tracking at high particle image densities. *Experiments in Fluids*, *57*(5), 70. https://doi.org/10.1007/s00348-016-2157-1

Schickhofer, L., & Hanson, H. (2021). Aerodynamic effects and performance improvements of running in drafting formations. *Journal of Biomechanics*, *122*, 110457. https://doi.org/10.1016/j.jbiomech.2021.110457

Schneiders, J. F., Scarano, F., Jux, C., & Sciacchitano, A. (2018). Coaxial volumetric velocimetry. *Measurement Science and Technology*, *29*(6). https://doi.org/10.1088/1361-6501/aab07d

Schröder, A., Willert, C., Schanz, D., Geisler, R., Jahn, T., Gallas, Q., & Leclaire, B. (2020). The flow around a surface mounted cube: a characterization by time-resolved PIV, 3D Shake-The-Box and LBM simulation. *Experiments in Fluids*, *61*(9). https://doi.org/10.1007/s00348-020-03014-5

Sciacchitano, A., & Scarano, F. (2014). Elimination of PIV light reflections via a temporal high pass filter. *Measurement Science and Technology*, *25*(8), 084009. https://doi.org/10.1088/0957-0233/25/8/084009

Spoelstra, A., de Martino Norante, L., Terra, W., Sciacchitano, A., & Scarano, F. (2019). On-site cycling drag analysis with the Ring of Fire. *Experiments in Fluids*, *60*(6), 90. https://doi.org/10.1007/s00348-019-2737-y

Wang, Z., Bovik, A., Sheikh, H., & Simoncelli, E. (2004). Image Quality Assessment: From Error Visibility to Structural Similarity. *IEEE Transactions on Image Processing*, *13*(4), 600–612. https://doi.org/10.1109/TIP.2003.819861

Wieneke, B. (2008). Volume self-calibration for 3D particle image velocimetry. *Experiments in Fluids*, *45*(4), 549–556. https://doi.org/10.1007/s00348-008-0521-5

Wieneke, B., & Rockstroh, T. (2024). Lagrangian particle tracking in the presence of obstructing objects. *Measurement Science and Technology*, *35*(5), 055303. https://doi.org/10.1088/1361-6501/ad289d

Wieneke, B. (2013). Iterative reconstruction of volumetric particle distribution. *Measurement Science and Technology*, *24*(2). https://doi.org/10.1088/0957-0233/24/2/024008

Willert, C. (1997). Stereoscopic digital particle image velocimetry for application in wind tunnel flows. *Measurement Science and Technology*, *8*(12), 1465–1479. https://doi.org/10.1088/0957-0233/8/12/010

5

Multi-exposure particle tracking

In this chapter, the viability of multi-exposure (ME) recordings for volumetric particle tracking (3D-PTV) is explored. A tracking algorithm is described in section 5.1, that deals with arbitrary timing templates both for single- and double-frame recordings. The working principle is first illustrated in section 5.2 using numerically generated images from imposed particle motion. The effect of parameters such as seeding density, sequence timing and its length is evaluated.

The principles are verified in section 5.3, on ME 3D-PTV data simulated from an experiment conducted in time-resolved mode, which yields a quantitative analysis of performance under more realistic conditions. Finally, an experimental demonstration is conducted, for completeness, that illustrates the viability of 3D pressure from ME 3D-PTV (section 5.4).

Parts of this chapter have been published in:

- Grille Guerra, A., Scarano, F., & Wieneke, B. (2025). On the accuracy of multi-exposure 3D-PTV. *Proceedings of the 16th International Symposium on Particle Image Velocimetry*
- Scarano, F., Grille Guerra, A., & Wieneke, B. (2025). Detection of low-velocity traces in ME-PTV. *Proceedings of the 16th International Symposium on Particle Image Velocimetry*

5.1. Generalized ME tracking algorithm

A multi-exposure (ME) sequence consists of particles illuminated by N pulses. The discussion is generalized here to the case where such N pulses are captured onto a single frame or a double frame recording. The pulses are taken at times $t_1, t_2, ..., t_N$, with corresponding time separation $\Delta t_1, ..., \Delta t_{N-1}$. For simplicity, the time separation is normalized with respect to the smallest time separation, Δt_0, in the shape $\Delta t^* = \frac{\Delta t_1}{\Delta t_0}, ..., \frac{\Delta t_{N-1}}{\Delta t_0}$, where Δt_0 typically corresponds to a displacement of 5-10 pixels in the camera images. For every particle trajectory, a trace of N dots is formed, at the corresponding particle locations $x_1, x_2, ..., x_N$. The sequence is characterized by the number of pulses in each frame and the chosen timing template. A specific notation is introduced for compactness in the remainder, whereby the number of frames, exposures and relative time intervals are indicated. For example, ME(1 + 2, Δt^* = 1 – 2) refers to a double-frame recording (denoted by the + symbol) with one pulse in the first frame and two in the second (1 + 2), with non-uniform time separation ($\Delta t_1 = \Delta t_0$ and $\Delta t_2 = 2\Delta t_0$, thus Δt^* = 1 – 2). Similarly, ME(4, Δt^* = 1 – 2 – 3) corresponds to a single-frame recording that captures four pulses with non-uniform separation in proportion to 1, 2 and 3. Such asymmetric distribution is necessary to resolve the directional ambiguity, as discussed in Scarano, Hysa *et al.* (2025).

A sketch of the particle tracking process is shown in figure 5.1, based on a double-iterative 3D particle reconstruction approach. The inner loop is based on the IPR algorithm (Jahn *et al.*, 2021; Wieneke, 2013). Once the first 3D distribution of particle samples is obtained, particle samples need to be associated with a trajectory (tracking step) yielding the traces ascribing a time tag and a trajectory tag to each sample. Such process may differ depending on whether the single- or double-frame recording approach is taken. However, many aspects of the method remain similar, and the remainder describes the general aspects of it.

Trace detection in time resolved particle tracking (e.g. Shake-the-Box) is based on the (marching) process that extrapolates an existing trajectory towards the expected occurrence of the next particle sample. For double frame single exposure analysis trace detection reduces to the problem of particle pairing, often based on nearest neighbour principle. The latter can be stabilised imposing a condition based on spatial regularity of the velocity. The criterion of minimum dispersion of the velocity from a group of pairs has been widely used in 3D-PTV in various ways as also proven effective in a recent work (Le Bris *et al.*, 2025).

In the present approach, ME recordings are used to generate candidate traces (section 5.1.1) followed by a selection procedure that identifies the most likely, based on minimization of a cost function (section 5.1.2). The following sections detail such process of trace detection.

5.1.1. Trace candidates generation

From the volumetric particle distributions obtained with 3D particle reconstruction, the search for candidate traces is performed in a chosen neighbourhood of a selected sample. The procedure is exemplified considering a ME(3, Δt^* = 1 – 2) recording. The neighbourhood comprises three (not yet detected) traces, each made of three

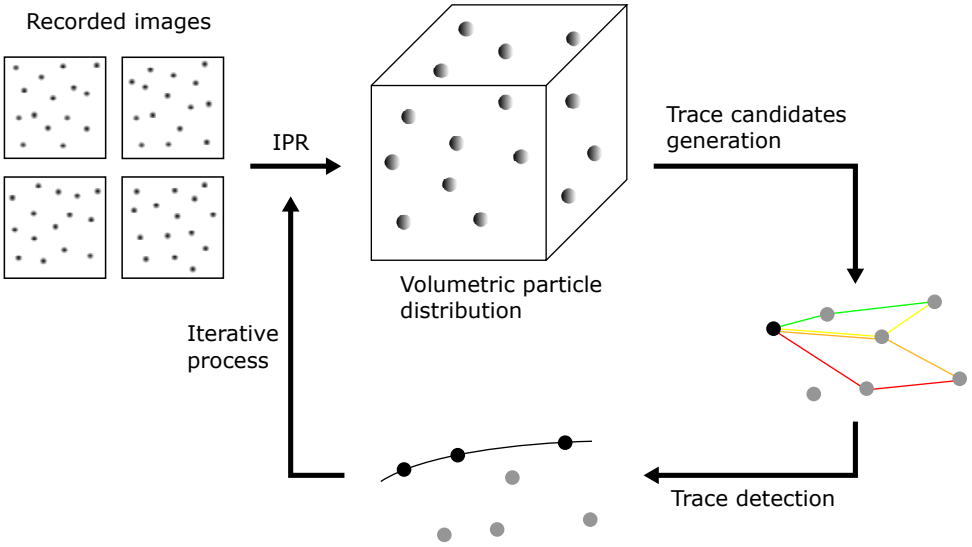

Figure 5.1: Schematic description of the iterative particle detection and tracking for ME-STB. Single-frame images are recorded from a 4-camera system; 3D particle position is obtained with IPR; groups of particles complying with kinematic likelihood are candidate traces; cost function minimization identifies the physical traces. The latter are iteratively fed into IPR to confirm or discard particles from the previous distribution.

exposures (figure 5.2(a)).

The search for the trace including the selected sample P_i (in green in figure 5.2) requires assuming the reference time t_{ref} of the sample. Without lack of generality, one can assume $t_{ref} = t_1$ in the present example. For a specified velocity range, $\mathbf{v}_{range}$ (figure 5.2(b)), particle matches are searched in the neighbourhood of P_i. In general, the search region may be a sphere or a cuboid, but the use of a velocity predictor (Novara *et al.*, 2023) may significantly accelerate the search by reducing the spatial extent where candidate matches are sought for.

For every matched pair, the search continues forward, collecting samples until the trace includes N samples (3 in the present case). After the first match, further branching is informed by the velocity estimated from the initial pair, assuming constant velocity (dashed lines in figure 5.2(c)). Correspondences are established allowing a departure from the linear extrapolation assuming an acceleration-related range, a_{range}, to establish the search radius (figure 5.2(c)). This process is repeated for every particle in the neighbourhood, forming a collection of candidate traces (figure 5.2(d)). Since the time correspondences of the particles are unknown, particles not belonging to t_{ref} may result in the generation of wrong traces, as the one depicted in figure 5.2(d).

For double-frame recordings, it is advisable to design the sequence with the shortest time separation across the two frames. Thus, t_{ref} pertains to the last pulse of the first frame, and t_{ref+1} the first in the second frame, which reduces the number of possible

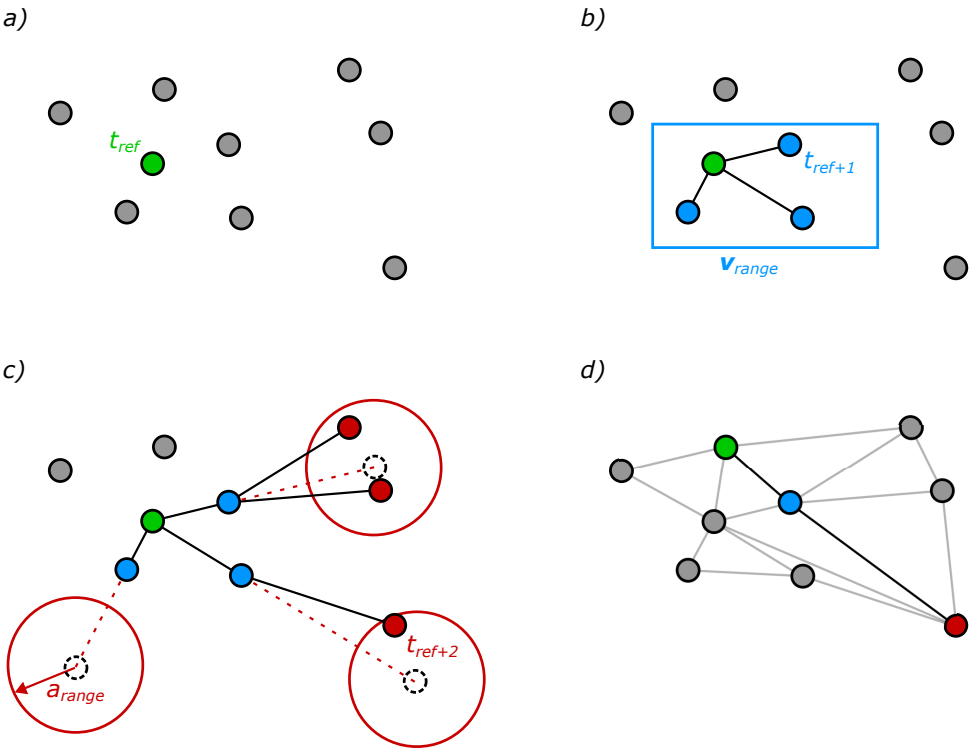

Figure 5.2: Generation of candidate traces for a ME(3, Δt^* = 1 – 2) recording. Neighbourhood around a selected particle sample (green) at $t_{ref} = t_1$ (a); matching pairs based at t_{ref+1} within the allowed velocity range, $\boldsymbol{v}_{range}$ (b); extrapolated trajectories based on estimated velocity and bounded acceleration, a_{range} (c). Formation of a wrong trace from a particle not belonging to t_{ref} (d), together with all candidate traces formed.

matches and accelerates the detection. For single-frame recordings, instead, the algorithm should begin with the largest Δt_i. Although this option produces a larger amount of pairs, the probability of overlapping particle images (at low velocity) is minimized.

5.1.2. Trace detection

For each candidate trace a score is assigned based on the kinematic similarity criterion (Ouellette *et al.*, 2006; Scarano, Hysa *et al.*, 2025). Furthermore, neighborhood consistency is quantified, according to Wieneke and Rockstroh (2024). A final cost function, *w*, is assigned as the product of both elements, and the best option (lowest *w*) is extracted as the valid trace for the particle. The procedure is exemplified in figure 5.3 for the set of trace candidates generated in figure 5.2.

The kinematic similarity criterion is evaluated along the trace. For each of the $N - 1$

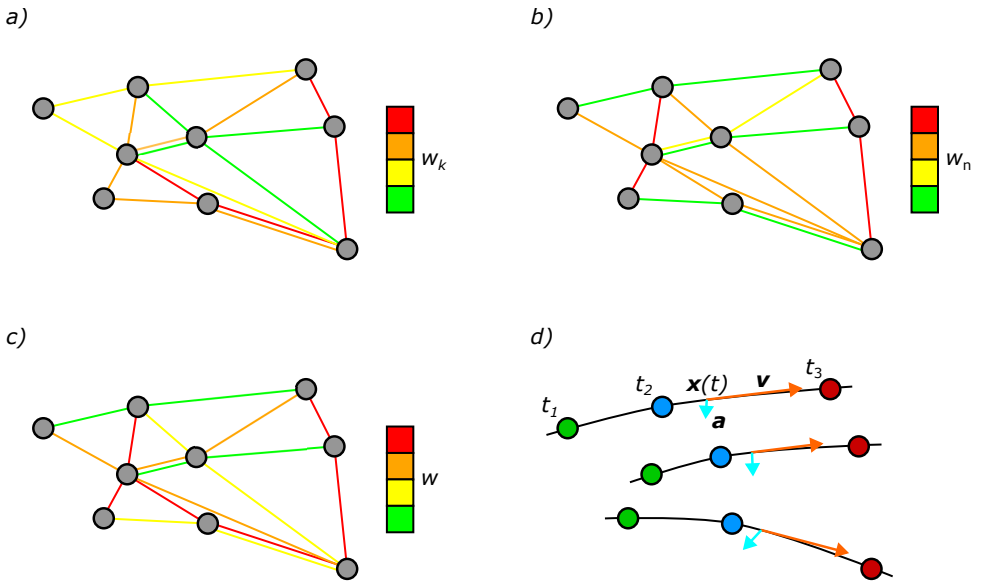

Figure 5.3: Trace detection for a ME(3, $\Delta t^* = 1-2$) situation. Each candidate trace is assigned a score based on kinematic similarity (w_k) (a) and neighbourhood consistency (w_n) (b), yielding the final cost function (w) (c). Traces with the lowest values of w are accepted. A polynomial function models position, velocity and acceleration at time $t = (t_1 + t_3)/2$ for valid traces (d).

segments forming a trace of N pulses, a velocity vector $v = (v_x, v_y, v_z)$ is obtained from the two particles forming the segment and the time separation between them. Then, a kinematic cost function w_k is constructed for the trace by adding up the standard deviations of the three velocity components, evaluated over the $N-1$ segments:

$$w_k = \sigma(v_x) + \sigma(v_y) + \sigma(v_z)\,. \tag{5.1}$$

The neighborhood consistency expresses the velocity similarity among candidate traces in a limited region of space. For every trace candidate T_i, the velocity difference with respect to neighboring traces T_k, $\delta_{i,k}$, is evaluated taking the average over all segments of the trace:

$$\delta_{i,k} = \overline{||\boldsymbol{v}(T_i) - \boldsymbol{v}(T_k)||}\,. \tag{5.2}$$

Neighbor traces involving particles shared with T_i are not considered, since most likely either T_i or those neighbors are ghost traces. For every particle P_j in the neighborhood of T_i, the best matching trace involving that particle is taken as the most likely correspondence, i.e., $\delta^*_{i,j} = \min(\delta_{i,k})$ between the k traces passing through P_j. Finally, a neighborhood cost function w_n (figure 5.3(b)) is constructed as the average of a few (M, e.g. 5) best fitting correspondences:

$$w_n(T_i) = \frac{\sum_{j=1}^{M} \delta^*_{i,j}}{M}\,. \tag{5.3}$$

The likelihood of a candidate trace to correspond to a physical trajectory is expressed as the product of the above criteria, $w = w_k \cdot w_n$. Among the set of candidate traces, that exhibiting the lowest value of w is selected as a valid trace for the particle, as shown in figure 5.3(c).

In the work of Scarano, Hysa *et al.* (2025) the particle samples in a given neighborhood are interrogated according to a combinatorial algorithm that varies the time index of the candidate sequence. The kinematic similarity criterion and trace regularity criterion produce respective residuals and their product is considered as a composite criterion for trace detection. Although effective, the approach has two shortcomings: the amount of computations in the combinatorial approach increases rapidly with the number of particles considered in the neighborhood; and the kinematic similarity penalizes tangential acceleration and trace regularity the acceleration magnitude along the trace.

The present approach advances the above by pre-selecting traces candidates based on regularity, which largely reduces the combinatorial basis for kinematic similarity evaluation, as illustrated in figure 5.2. The second advancement replaces the trace regularity criterion (individual regularity) with that of neighborhood consistency (group regularity), whereby the absolute value of acceleration is not penalized, but rather the spatial variation thereof. Such concept is illustrated in figure 5.3 using the set of trace candidates generated in figure 5.2.

The assignment of particles to traces follows a hierarchical approach: particles samples ascribed to more than one candidate trace are assigned to the trace with the lowest cost function. After a trace has been accepted, the particle samples are included as initial distribution for the iterative particle reconstruction (IPR) process (figure 5.1), with the objective of improving the accuracy of particles detection and reduce the amount of spurious detections (ghost particles).

Upon convergence, a second-order polynomial is used to fit the final set of traces. Position, velocity and acceleration are estimated at the intermediate time $t = (t_1 + t_N)/2$ (figure 5.3(d)).

5.2. Performance analysis

A data set is produced from an analytical flow field and a synthetically generated particle distribution is considered here with a flow field described by a steady Taylor-Green vortex lattice, as shown below:

$$\begin{cases} u = u_0 \cos\left(\frac{2\pi x}{\lambda}\right) \sin\left(\frac{2\pi y}{\lambda}\right) \\ v = -u_0 \sin\left(\frac{2\pi x}{\lambda}\right) \cos\left(\frac{2\pi y}{\lambda}\right) \\ w = u_0 \end{cases} \tag{5.4}$$

where x, y and z are the Cartesian coordinates, $u_0 = 5$ m/s is the velocity amplitude of the waves and $\lambda = 800$ mm is their wavelength. Sine-based velocity distributions are a popular choice for numerical assessments (Kähler *et al.*, 2016), focusing the attention on the modulation of the peak value. The present analysis considers a simulated domain of 800x800x200 mm^3. The spatial distribution of the horizontal velocity component is shown in figure 5.4(left).

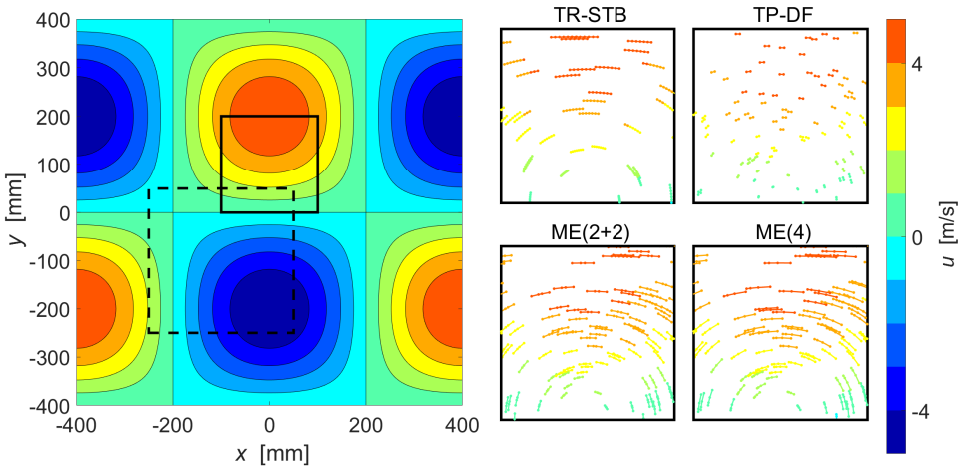

Figure 5.4: Horizontal component of the velocity field (left) and particle traces collected inside the solid black box using various 3D-PTV strategies (right). The dashed black box represents the domain studied in section 5.2.5 for the vanishing velocity scenario.

The *w*-component is set here to a constant value, such that all particles feature a non-zero velocity and the condition of overlapping particle images is avoided for the case of multiple exposures in a single frame. The topic of how to deal with small-to-vanishing velocities – and thus overlapping particle images – remains an open challenge in ME particle tracking, as also discussed in Scarano, Hysa *et al.* (2025). Some strategies to overcome this situation are explored in section 5.2.5.

5.2.1. Image generation

The domain of interest is imaged by four cameras with 800x800 px resolution under simplified conditions of parallel viewing, in-focus imaging and absence of optical distortions. The angle between cameras is 30°. Tracer particles are rendered with a constant diameter of 2 px and a peak intensity of 700 ± 300 counts. The seeding density is described in terms of particles-per-pixel (ppp), referring to that obtained from a single exposure. The relation between the single-exposure seeding density and the cumulative value from N exposures is cppp = $N \cdot$ ppp. The reference time separation between exposures, Δt_0, corresponds to particle displacement of 5 px.

Various pulse sequencing strategies have been considered to explore the effect of relevant experimental parameters such as the cumulative seeding density cppp, timing template Δt_i and number of exposures N. State-of-the-art 3D-PTV methods are considered for reference, namely: time resolved Shake-the-Box (TR-STB), two-pulse double-frame STB (TP-DF, Novara *et al.*, 2023), and four-pulse double-frame STB (ME(2 + 2), with $\Delta t^* = 2 - 1 - 2$, Novara *et al.*, 2019). Particle traces obtained with the aforementioned methods are shown in figure 5.4(right) alongside the case of four-pulses

single-frame recording with an asymmetric time sequence.

5.2.2. Seeding density

The accuracy and reliability of ME-STB is examined by varying the concentration of tracer particles (ppp). A correct trace detection is considered when all particle samples comprised in the trace correspond to their exact locations within 1 voxel deviation. To study the influence of seeding density, a recording of type ME(3, Δt^* = 1 – 2) is considered. The correct detection rate is given in figure 5.5(left) when the seeding density is varied from sparse (ppp < 0.01) to dense (ppp = 0.05). It should be retained in mind that the corresponding cumulative seeding density cppp approaches 0.15 for the dense conditions. The fraction of correctly detected traces is relatively flat at a level above 90% up to ppp = 0.03. In the same range the error rate remains below 2%. Beyond ppp = 0.04 a large drop of detected traces and an explosive increase of erroneous traces is observed. This behaviour is ascribed to the increased number of faulty particle detections during the particle reconstruction process (IPR), consistent with what has been reported by Wieneke (2013) in the original study about the IPR algorithm.

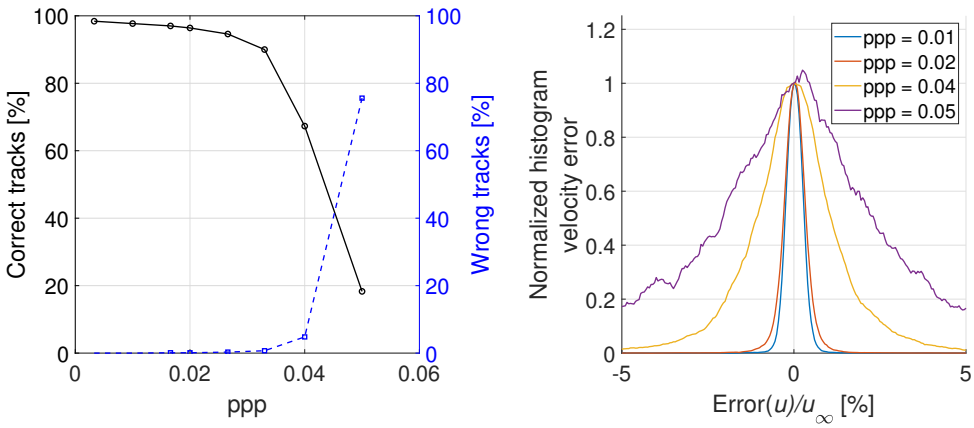

Figure 5.5: Robustness and accuracy of ME-STB, for N = 3. Percentage of correct and incorrect traces as a function of seeding density (left) and normalized histogram of velocity error (right).

For the correctly detected traces, the positional accuracy of the detected particles will in turn determine that of the velocity measurement. The normalized histogram of the velocity error – setting the histogram curve to 1 at zero error – is shown in figure 5.5(right) at four selected values of ppp. For mild density (ppp < 0.02) the error stays below 0.5%. Again, the rapid increase around ppp ~ 0.04 (cppp ~ 0.12) is ascribed to the phenomenon of ghost particles formation.

5.2.3. Timing template

While an asymmetric timing template is a must for single-frame ME-STB, the temporal separation between exposures can be considered as an additional variable to optimize the design of the template, to maximize the tracking robustness or the dynamic range of the measurement. This is explored for ME(3) sequences by solely increasing the time separation between the second and third exposure. For all cases, the seeding density is set at ppp = 0.01 (cppp = 0.03). The tracking performance is shown in figure 5.6(left) in terms of detection and error rates. As the time separation increases, only a minor decrease of detection rate is observed and the error rate remains below significant levels. These results confirm the adequacy of the chosen trace detectability criteria (section 5.1.2) as being able to recover correct traces even with a relatively long particle displacement.

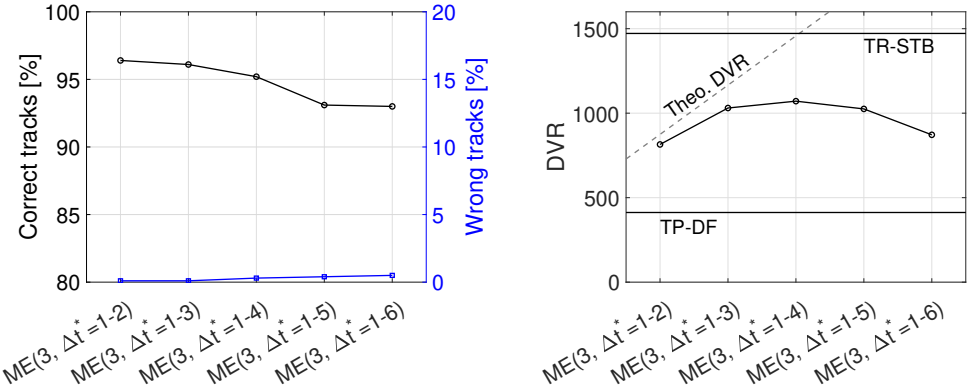

Figure 5.6: Detection rate and erroneous traces as a function of the second time interval (left) and dynamic velocity range (right).

The accuracy of the measured velocity is expressed in terms of velocity dynamic range (DVR, Adrian, 1997). The DVR is defined as the ratio between the maximum and minimum measurable velocity and computed here as it follows:

$$\mathrm{DVR} = \frac{u_{max}}{u_{min}} = \frac{u_0}{\sigma_u}, \tag{5.5}$$

where the minimum velocity is dictated by the measurement uncertainty σ_u, which may be decreased when using more exposures. For a two-pulse double-frame acquisition, velocity is obtained as:

$$\boldsymbol{u} = \frac{\boldsymbol{x}_2 - \boldsymbol{x}_1}{t_2 - t_1} = \frac{\Delta \boldsymbol{x}_1}{\Delta t_1}, \tag{5.6}$$

and via error propagation, the uncertainty can be estimated as:

$$\sigma_{\boldsymbol{u}} = \frac{\sqrt{2}}{\Delta t_1}\sigma_{\boldsymbol{x}}, \tag{5.7}$$

where $\sigma_{\boldsymbol{x}}$ represents the uncertainty of the particle location.

For ME(3), estimating the velocity at the intermediate time using a second-order polynomial reads:

$$\boldsymbol{u} = \frac{\Delta \boldsymbol{x}_1 + \Delta \boldsymbol{x}_2}{\Delta t_1 + \Delta t_2}\,, \tag{5.8}$$

thus returning an uncertainty of:

$$\sigma_{\boldsymbol{u}} = \frac{2}{\Delta t_1 + \Delta t_2}\sigma_{\boldsymbol{x}}\,. \tag{5.9}$$

For the sequence ME(3, $\Delta t^* = 1 - 2$), the dynamic range approximately doubles that of TP-DF. It further increases as the second time separation is elongated and then it reduces again, as ascribed to the growth of truncation errors. The DVR obtained for the current analysis is shown in figure 5.6(right), using the rms of the velocity error to estimate the minimum velocity. The values obtained for TR-STB and TP-DF measurements at ppp = 0.01 are also included for reference. A theoretical estimate of the attainable DVR is constructed from equation (5.9), where the positional uncertainty has been extracted from the TP-DF system. For the shorter ME(3) sequences considered, the measured DVR is only slightly below the theoretical estimate due to the increased positional error at the higher ppp of 0.03. Instead, the values start decreasing for the higher temporal separation as a result of the increasing role of truncation errors, which underestimate the curvature of particle paths in the Taylor-Green vortex flow field. Overall, a significant DVR increase can be obtained with respect to TP-DF, despite the higher cppp level, at an intermediate level of that obtained using TR-STB.

5.2.4. Number of pulses

While maintaining the cppp level in the appropriate range (section 5.2.2), more than three pulses offer the potential to further increase the measurement dynamic range although at lower spatial resolution. A higher number of pulses positively impacts the estimation of velocity based on polynomial regression of the discrete particle samples. Sequences of up to five exposures have been considered, both for single and double-frame systems. For a single exposure seeding density of ppp = 0.01, tracking results are given in figure 5.7(left). The percentage of correct tracks decreases slightly when using more pulses as a result of the increased cppp. However, no noticeable increase of the error rate is observed. Figure 5.7(right) illustrates the error of the material derivative (i.e. Lagrangian acceleration). When normalized, the error is below 2% for TR-STB and about 2% for a double-frame 5-pulses measurement. Other options yield significantly larger errors, with 4-pulse methods yielding approximately 4% error irrespective of whether the pulses are equally distributed or not across the two frames. Finally, the 3-pulse sequence yields the largest uncertainty exceeding 10%.

Table 5.1 summarizes the findings from figure 5.7. The accuracy of the velocity and acceleration are expressed in terms of the DVR and dynamic acceleration range (DAR, Schanz *et al.*, 2016) respectively. TR-STB offers the highest accuracy, with DVR of 1500 and DAR exceeding 100. In contrast, the double-frame single-exposure approach yields a DVR of 400. Multi-exposure strategies with three and four pulses clearly outperform TP-DF (DVR ~ 1000), but offer a very modest DAR with three exposures (DAR <

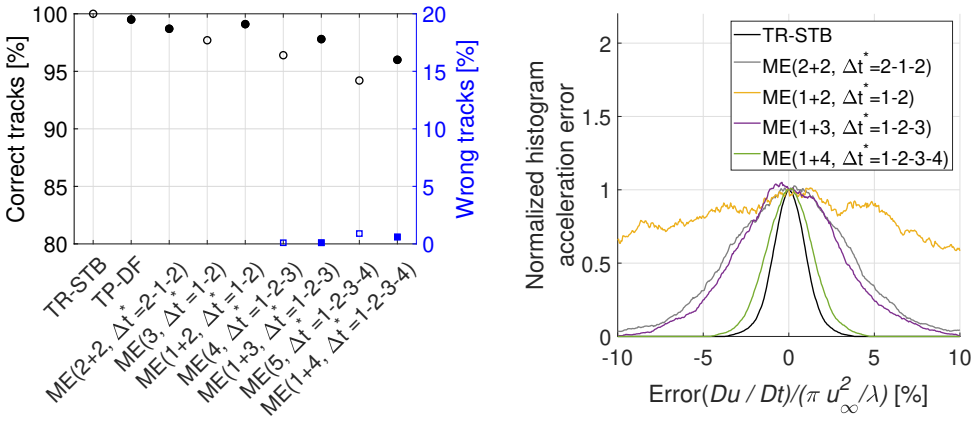

Figure 5.7: Percentage of correct and wrong tracks (left) and normalized histogram of horizontal acceleration error (right), for various timing strategies at ppp=0.01. Double-frame options are represented by filled symbols.

10). The latter improves with the number of exposures, but it remains in the range of 30-60. A five exposures recording deteriorates already the DVR, presumably as a result of higher positional errors (higher cppp) and truncation effects (longer traces). In summary, double-frame options (indicated by filled symbols in figure 5.7(left)), such as the ME(2 + 2, Δt^* = 2 − 1 − 2) system, offer optimal performance nearing that of TR-STB, and are suited for maximizing seeding density (and therefore the dynamic spatial range, DSR) together with the velocity dynamic range. Regarding the acceleration, the use of more exposures is beneficial as random errors tend to dominate the acceleration uncertainty. This trend is however valid only at very low levels of the seeding density (ppp < 0.01) where the additional exposures do not bring cppp at levels where the reconstruction error becomes dominated by ghost particles.

	TR-STB	TP-DF	ME	ME	ME
Exposures	1	1+1	2+2	3	1+2
Δt^*	-	1	2-1-2	1-2	1-2
DVR	1500	400	1300	800	1100
DAR	110	-	30	6	8
	ME	ME	ME	ME	
Exposures	4	1+3	5	1+4	
Δt^*	1-2-3	1-2-3	1-2-3-4	1-2-3-4	
DVR	1000	1200	600	650	
DAR	25	30	60	80	

Table 5.1: DVR and DAR of various ME 3D-PTV strategies at ppp=0.01.

5.2.5. Detection of low-velocity traces

The generation of trace candidates discussed in section 5.1.1 requires the successful reconstruction of the N particles composing an ME trace. In regions of low velocity, particle images overlap and therefore less than N particles might be reconstructed by the IPR algorithm. This is illustrated in figure 5.8 for a single-frame recording measuring a linear velocity profile. A sequence of three pulses with an asymmetric template is considered, in the shape ME(3, $\Delta t^* = 1 - 3$), as illustrated in figure 5.8(left).

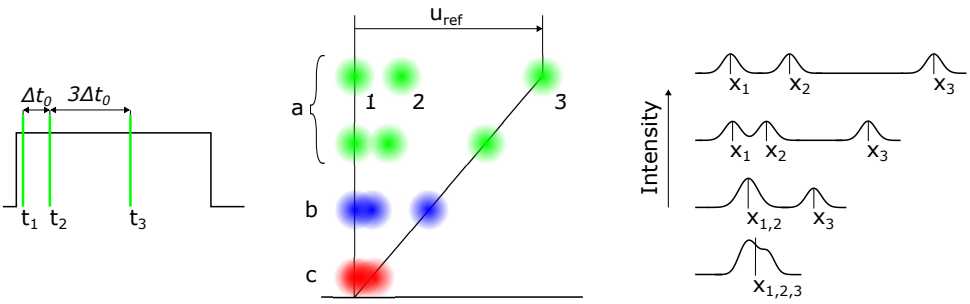

Figure 5.8: Traces generated by a 3-pulse sequence (left) for a linear velocity profile (middle). Particle image intensity (right) indicating the appearance of three regimes: (a) formation of a *dotted trace*; (b) two collapsed dots and a separate one (*streak-dot*); (c) all dots are indistinguishable (*streak*).

In the portions of the flow with higher velocity (figure 5.8-middle), the multiple exposures produce a trace with spacing analogous to the temporal template of light pulses. Below a certain velocity, the two particle images corresponding to the shortest time separation start to overlap (figure 5.8-right), posing a challenge to the particle reconstruction step. For IPR, the limit condition to detect separate particles is reported to be approximately that of 50% overlap among particle images. As long as the overlap is below this threshold, all N dots of the trace will be reconstructed (*dotted trace*, or regime *a*, indicated in green in figure 5.8) and no modifications of the candidates generation step are necessary.

For higher overlap, a merged particle will be reconstructed at $x_{1,2} = (x_1 + x_2)/2$, forming a *streak-dot* pattern for the trace (regime *b*, indicated in blue in figure 5.8). This possibility can be accounted for in the trace candidate generation step by allowing traces with less than N entries. The velocity associated with *streak-dot* traces of only two elements suffers from directional ambiguity. However, the first dot (blob) is produced by two overlapping exposures and will feature a higher overall energy and a measurable higher peak intensity (see figure 5.8-right). Similar to the pulse-tagging approach (Grant & Liu, 1990) the velocity vector can be pointed in the direction from relative high to low intensity dots. For a more accurate estimation of the velocity, the time separation between $x_{1,2}$ and x_3 is considered to be $\Delta t_1/2 + \Delta t_2$, while the acceleration cannot be estimated and is set to zero.

In regions of very low velocity, all particle images composing the trace will merge into a single blob or *streak* (regime *c*, indicated in red in figure 5.8), of skewed intensity for

asymmetric timing templates. In this regime, no velocity can be extracted directly from single-frame recordings. However, the trace might be continued in the subsequent frame of the recording given the low velocity, as recently explored by Scarano, Grille Guerra and Wieneke (2025). This interframe analysis to tackle regime *c* has not been considered in the present work and is subject to further research. For double-frame recordings, the situation is simpler and restricted to the analysis of regimes *a* and *b* only.

The proposed approach is explored for the synthetic test case already introduced in section 5.2, but now imposing a zero out-of-plane velocity component ($w = 0$) to introduce regions of low velocity in the domain. A single-frame recording, ME(3, $\Delta t^* = 1 - 3$), at a base seeding density of ppp = 0.01 is considered. Particles reconstructed by IPR are shown in figure 5.9(left) in a subdomain described by the dashed black square in figure 5.4(left).

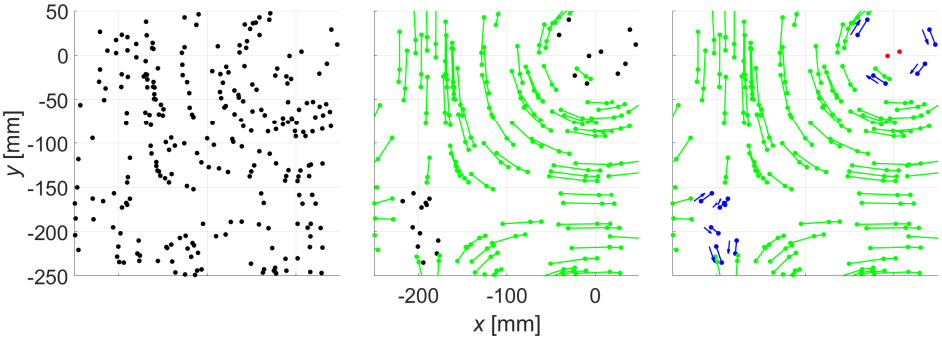

Figure 5.9: Reconstructed particles (left), detected traces in the *dotted-trace* regime only (middle) and including the *streak-dot* regime (right) for a single-frame recording, ME(3, $\Delta t^* = 1 - 3$), at ppp=0.01.

Without accounting for possible traces outside the *dotted-trace* regime (regime *a* in figure 5.8), the detected traces are the ones shown in figure 5.9(middle), each composed of three particles. It can be seen that some particles are left unmatched in regions of low velocity, i.e. the vortex core and saddle point. Allowing for traces in the *streak-dot* regime (regime *b* in figure 5.8) makes it possible to recover traces composed of two particles only (figure 5.9-right, indicated in blue), where flow directionality is indicated by an arrow placed on the left of the respective trace. Still, a few particles very close to the vortex core (indicated in red), belonging to the *streak* regime (regime *c* in figure 5.8), cannot be tracked with the current algorithm.

5.3. Experimental verification

5.3.1. Instrumentation and layout

Volumetric measurements of the flow around a wall-mounted cube discussed by Hendriksen *et al.* (2024) are considered. The experiments, conducted in the W-tunnel facility (low-speed, open jet) at the aerodynamics laboratories of the Aerospace

Engineering Department of TU Delft, feature a 12 cm side length cube installed on a flat plate immersed in a stream at u_∞ = 10 m/s. Sub-millimeter (d ~ 0.4 mm) helium-filled soap bubbles are used as flow tracers, illuminated by two *LED-Flashlight 300* arrays from LaVision GmbH and imaged by seven high-speed cameras (Photron *FastCam*, 1 Mpx, 12-bit) at a rate of 3 kHz. The whole volumetric dataset encompasses a domain of 40x40x30 cm^3. The cameras are positioned such that their view covers the entire domain of interest from various directions, and the flowfield is reconstructed using the object-aware STB algorithm (Wieneke & Rockstroh, 2024). The seeding density in a single exposure image is approximately ppp = 0.01, and 10,000 particles are tracked on average every frame.

Multi-exposure images are simulated by summing up the intensity of frames selected from the originally recorded time-resolved (single-exposure) sequence. The time separation between light pulses is used as the base separation for ME, with Δt_0 = 0.33 ms. The traces obtained from TR-STB are used as reference to benchmark the results from the simulated ME recordings. An indication of image quality and seeding concentration is given in figure 5.10(left), where an original single-exposure image is shown, together with the computed multi-exposure images simulating the condition ME(3, Δt^* = 1 – 2), in figure 5.10(middle), and ME(5, Δt^* = 1 – 2 – 3 – 4), in figure 5.10(right).

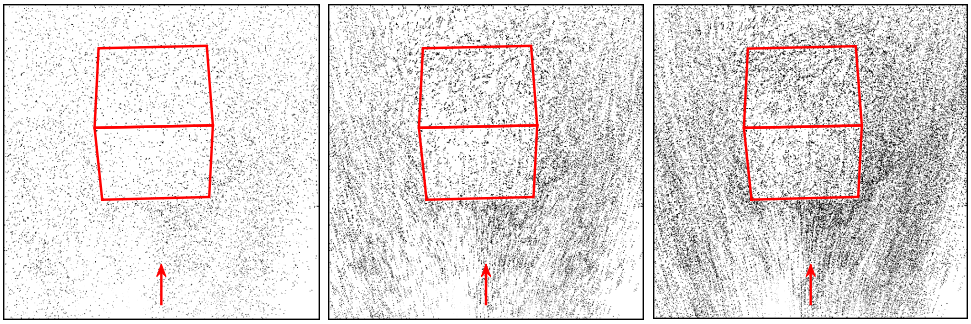

Figure 5.10: Particle images and their sequences around a wall-mounted cube. Left: single-exposure image. Middle: generated multi-exposure, ME(3, Δt^* = 1 – 2). Right: generated multi-exposure, ME(5, Δt^* = 1 – 2 – 3 – 4).

5.3.2. Benchmark

The same multi-exposure strategies presented in the synthetic test case (section 5.2.4) are considered here. Correct traces are those where particles deviate less than 1 voxel from the reference (i.e. TR-STB analysis). Tracking results are shown in figure 5.11. As expected for the moderate seeding density (ppp ~ 0.01 and cppp < 0.05), excellent detectability is found, with more than 90% of correct detection. The error rate is higher, at around 5%, and comparable to that of TP-DF. This can be ascribed to imperfections associated with the experimental conditions. Furthermore, any erroneous measurement in the TR-STB analysis (experimental ground truth) will be considered as additional error.

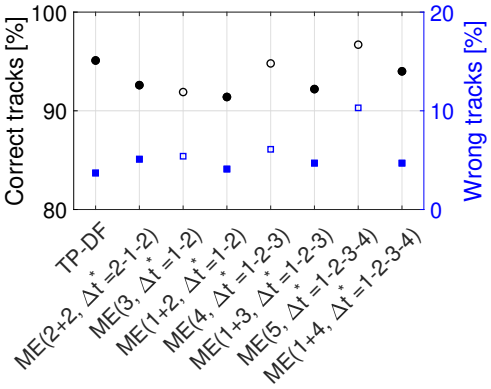

Figure 5.11: Percentage of correct and spurious traces for various 3D-PTV strategies. TR-STB is taken as reference. Double-frame options are represented by filled symbols.

The measurement obtained with ME-STB is further scrutinized by direct inspection of the time-averaged flow properties (ensemble-averaging of 100 snapshots). The data is reduced on a Cartesian grid collecting the scattered vectors into cubic bins of 24 mm side length with 75% overlap. A second-order polynomial fits the spatial distribution inside the bin, following Agüera *et al.* (2016). The flow field is displayed at the symmetry plane (figure 5.12) for TR-STB, TP-DF, a double-frame ME sequence (ME(2 + 2, Δt^* = 2 – 1 – 2)) and also a single frame ME sequence, ME(4, Δt^* = 1 – 2 – 3). The time-averaged streamwise velocity component exhibits no appreciable differences, except for the single-frame ME analysis, differing by some small details.

The map of turbulent fluctuations follows a similar trend, with the single exposure method being affected by a slight underestimation of peak value at the horse-shoe vortex and at the front of the cube. Finally, the material acceleration obtained with ME(2 + 2, Δt^* = 2 – 1 – 2) shows a remarkable agreement with TR-STB indicating the potential to serve as basis for pressure evaluation. The single-frame ME analysis does capture the acceleration at the leading edge, but again, the details of the horse-shoe vortex are not captured, arguably due to particle images overlapping in the low-speed regions, which pose a fundamental limit to the single-frame ME trace detectability (Scarano, Hysa *et al.*, 2025).

5.4. Demonstration on ME recordings

5.4.1. Experimental set-up and measurement conditions

The wake of a cylinder is measured using the volumetric PIV setup discussed in detail by Grille Guerra, Porcar Galan *et al.* (2025). A 60 cm long cylinder with a diameter of D = 6 cm is installed vertically at the outlet of the W-tunnel facility (section 5.3.1), immersed in the free-stream flow of u_∞ = 5 m/s. This results in a diameter-based Reynolds number of Re_D = 20,000. Sub-millimeter helium-filled soap bubbles are used as flow

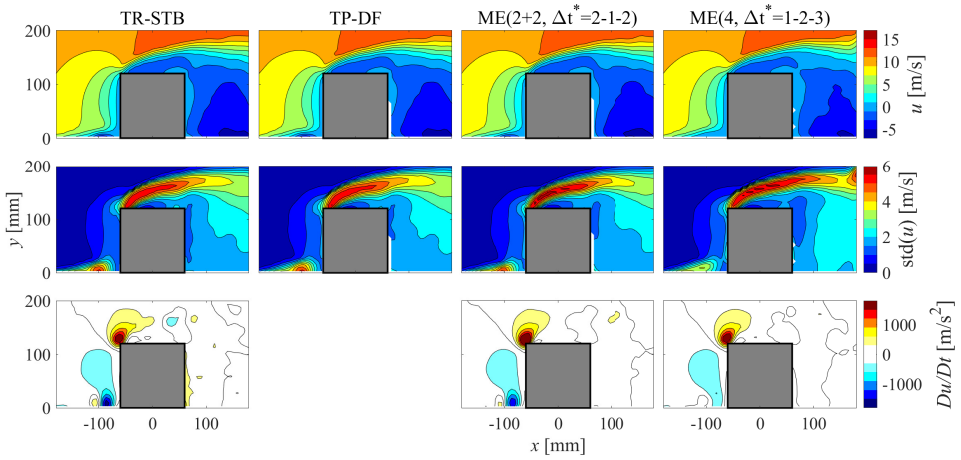

Figure 5.12: Time-averaged streamwise velocity (top), standard deviation of streamwise velocity (middle) and streamwise material acceleration (bottom), for TR-STB, TP-DF, ME(2 + 2, Δt^* = 2 – 1 – 2) and ME(4, Δt^* = 1 – 2 – 3).

tracers, illuminated by four *LED-Flashlight 300* arrays, providing the pulsed high-speed illumination needed for ME 3D-PTV, and imaged by ten LaVision *Imager LX* cameras (2 MPx, 4.4 µm pitch, 14 bit). The cameras are mounted on two arrays, containing five cameras each, referred to as *antennas* (Hendriksen *et al.*, 2025), that observe the cylinder wake from each side of the wind tunnel. The cameras are equipped with 25 mm focal length objectives and the f-number is set to $f_\# = 8$ in order to achieve the desired depth of field. For the given configuration, this results in a digital image resolution of 4.4 px/mm. A measurement volume of approximately 7D (x),5D (y) and 5D (z) is obtained.

At full resolution, the maximum acquisition frequency of the cameras (16 Hz) is insufficient for TR-STB purposes, setting up a relevant condition to justify ME alternatives. Based on the results from previous sections, two ME strategies are explored: ME(2 + 2, Δt^* = 2 – 1 – 2) and ME(4, Δt^* = 1 – 2 – 3). The smallest time separation between pulses, Δt_0, is set equal to 0.25 ms, corresponding to a particle displacement of approximately 5 px at the freestream velocity. Raw images from both recordings are shown in figure 5.13. The flow direction and cylinder trailing edge are indicated by a red arrow and line respectively. The timing template is revealed by following a single tracer in the bottom-left region of the images, and the illumination pulses are also indicated for further clarity. The baseline seeding density (for a single exposure) is ppp = 0.02. In the double-frame scenario, the cumulative seeding density cppp ~ 0.04 and it increases to 0.08 when recording onto a single frame.

5.4.2. Velocity and pressure distribution

Approximately 40,000 traces are extracted for each ME recording, corresponding to a particle concentration of approximately 1 particles/cm^3. An instantaneous visualization

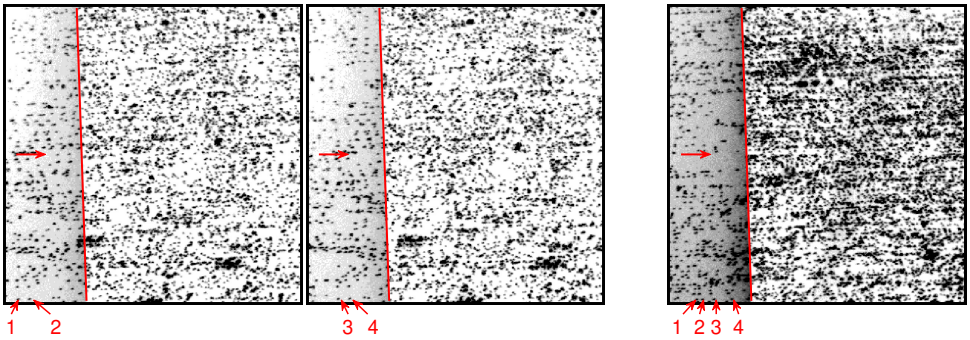

Figure 5.13: ME images of the flow in the wake of a cylinder, with the flow direction and cylinder trailing edge indicated by a red arrow and line respectively. Left: first frame of a ME(2 + 2, $\Delta t^* = 2 - 1 - 2$) recording. Middle: second frame of a ME(2 + 2, $\Delta t^* = 2 - 1 - 2$) recording. Right: ME(4, $\Delta t^* = 1 - 2 - 3$) recording. The four illumination pulses are indicated for a single tracer in the bottom-left region of the images.

of traces, colored by the associated streamwise velocity is given in figure 5.14. For improved visualization, only a slab of 5 cm in the spanwise direction is depicted. The particle trajectories already reveal the main features of the cylinder wake flow, i.e., the shedding of vortices (Kármán street) from the shear layers on both sides of the cylinder. The tracking method proves effective also in the recirculation region close to the back of the cylinder, despite the limited particle displacement.

The availability of acceleration information from the ME traces makes it possible to employ advanced data assimilation schemes to represent the instantaneous flow field on a Cartesian grid. The VIC# method, implemented in the DaVis 11 software (Jeon *et al.*, 2022), has been applied on a grid of 1 cm pitch. An instantaneous representation of the three-dimensional flow field is shown in figure 5.15 using isosurfaces of vorticity, color coded by their sign and component.

For both ME recordings, the illustration reveals the presence of spanwise-coherent vortices (Williamson, 1996), shed with an alternating sign, visualized through isosurfaces of spanwise vorticity (ω_y = ±150 Hz, red and blue respectively). These main rollers feature an oblique orientation with respect to the cylinder axis (Szepessy & Bearman, 1992) and undulations of wavelength larger than the cylinder diameter (Prasad & Williamson, 1997). The illustrations also reveal the presence of thinner, streamwise-oriented vortical structures interconnecting the main rollers, as reported in literature for measurements at comparable Reynolds numbers (Grille Guerra *et al.*, 2024; Scarano & Poelma, 2009). These structures are visualized through iso-surfaces of streamwise vorticity (ω_x = ±150 Hz, yellow and green respectively).

From ME 3D-PTV, not only the velocity-vorticity flow field may be obtained, but also an instantaneous representation of the pressure field thanks to the direct estimation of Lagrangian acceleration. The static pressure is obtained here via solving a Poisson equation (Van Oudheusden, 2013) with Neumann boundary conditions. Contours of the

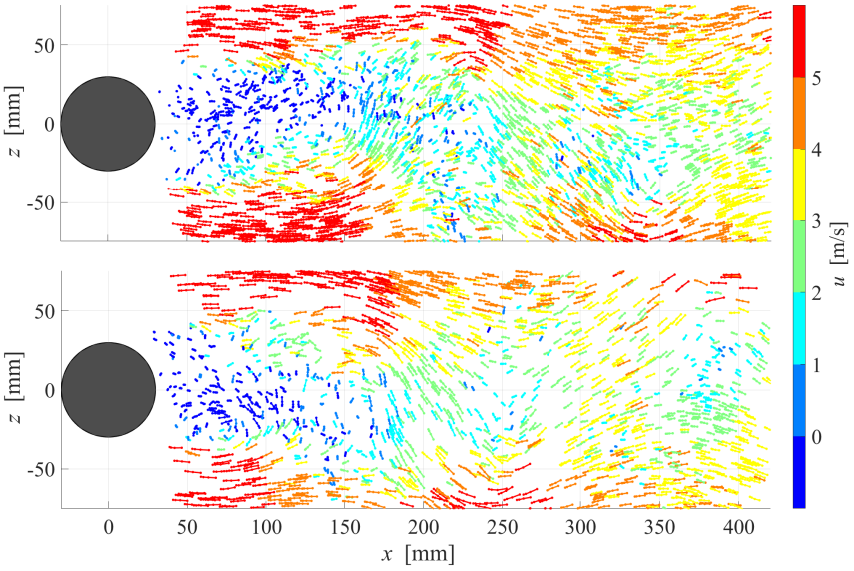

Figure 5.14: Instantaneous visualization of ME traces in the wake of a cylinder, for a slab of 5 cm along the span, and colored by streamwise velocity. Top: belonging to ME(2 + 2, $\Delta t^* = 2 - 1 - 2$). Bottom: for ME(4, $\Delta t^* = 1 - 2 - 3$).

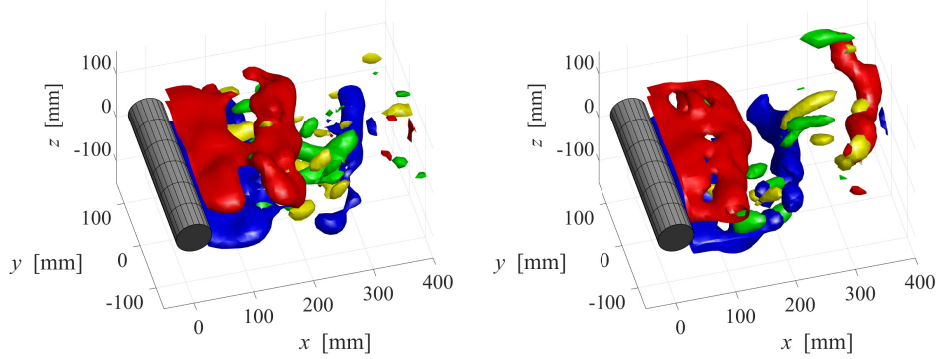

Figure 5.15: Instantaneous visualization of the three-dimensional flow field in the wake of a cylinder using isosurfaces of spanwise ($\omega_y = \pm 150$ Hz, red and blue respectively) and streamwise ($\omega_x = \pm 150$ Hz, yellow and green respectively) vorticity. Left: for ME(2 + 2, $\Delta t^* = 2 - 1 - 2$). Right: for ME(4, $\Delta t^* = 1 - 2 - 3$).

static pressure coefficient, c_p, at the plane $y = 0$ are shown in figure 5.16 for the two ME sequences explored. As expected, the pressure field is dominated by the low pressure in

the core of the main rollers (figure 5.15), thus confirming the suitability of the approach.

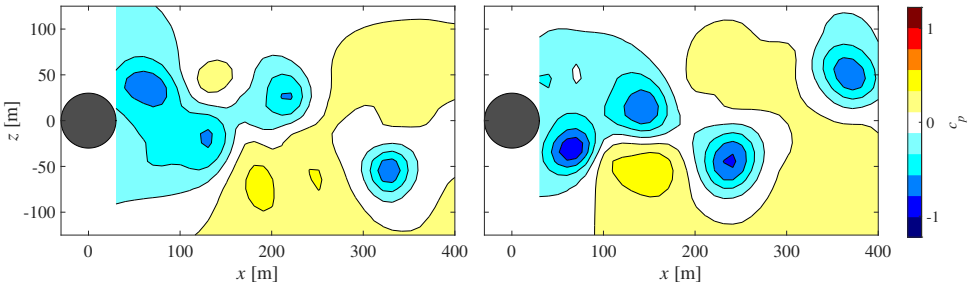

Figure 5.16: Contours of static pressure coefficient, c_p, at $y = 0$. Left: for ME(2 + 2, $\Delta t^* = 2 - 1 - 2$). Right: for ME(4, $\Delta t^* = 1 - 2 - 3$).

5.5. Conclusions

The accuracy of multi-exposure (ME) 3D-PTV has been explored, as a means of increasing the dynamic ranges of volumetric PIV measurements involving low frame rate hardware, together with adding information about Lagrangian acceleration and instantaneous pressure. An ME-STB tracking algorithm has been introduced, which can deal with arbitrary timing sequences for both single- and double-frame ME recordings. For single-frame systems, which alleviate the hardware and synchronization requirements, tracking is made possible by making use of asymmetric timing templates (Scarano, Hysa *et al.*, 2025).

A synthetic test case, based on a Taylor-Green vortex lattice, is initially considered to explore the effects of particle seeding density and timing strategy, which is later complemented using images from an experimental database of the flow around a wall-mounted cube. For both synthetic and experimental images, the proposed ME-STB algorithm shows excellent tracking performance (detection rate above 90%) for cumulative seeding densities below cppp = 0.1, found to be limited by the particle triangulation step. The results appear to be almost independent of the timing template selected and the dynamic velocity range (DVR) doubles that of single-exposure double-frame systems, approaching the values attainable by TR-STB. Besides, acceleration can be accurately estimated when using several exposures, with dynamic acceleration range (DAR) values in the order of 100 for the synthetic test case.

The method is demonstrated using experimental ME images from the flow in the wake of a cylinder, measured using a large-scale volumetric PIV set-up (measurement volume of approximately 40 litres) involving low frame rate cameras and LED modules for pulsed illumination. Around 40,000 particle traces could be extracted every instant both for single- and double-frame ME recordings at a base seeding density of ppp = 0.02. The information from the traces (position, velocity and acceleration) is used to obtain a representation of the three-dimensional flow field on a Cartesian grid of 1 cm pitch using the VIC# data assimilation scheme. This allows visualizing not only the spanwise-coherent vortices in the wake (Kármán street) but also smaller vortical

structures interconnecting the main rollers in the streamwise direction. Finally, the instantaneous pressure field could be estimated using the Lagrangian acceleration obtained from the ME traces, highlighting the potential of ME 3D-PTV in this regard.

The main limitation of ME recording strategies remains the difficulty of dealing with low-velocity regions and the associated overlapping particle images. The problematic can be mitigated employing double-frame timing strategies and modifications to the tracking algorithm to treat these special situations, as recently explored by Scarano, Grille Guerra and Wieneke (2025).

References

Adrian, R. J. (1997). Dynamic ranges of velocity and spatial resolution of particle image velocimetry. *Measurement Science and Technology*, *8*(12), 1393–1398. https://doi.org/10.1088/0957-0233/8/12/003

Agüera, N., Cafiero, G., Astarita, T., & Discetti, S. (2016). Ensemble 3D PTV for high resolution turbulent statistics. *Measurement Science and Technology*, *27*(12). https://doi.org/10.1088/0957-0233/27/12/124011

Grant, I., & Liu, A. (1990). Directional ambiguity resolution in particle image velocimetry by pulse tagging. *Experiments in Fluids*, *10*(2-3), 71–76. https://doi.org/10.1007/BF00215013

Grille Guerra, A., Porcar Galan, L., Sciacchitano, A., & Scarano, F. (2025). Treatment of light reflections in 3D PIV systems. *Measurement Science and Technology*, *36*(11), 115301. https://doi.org/10.1088/1361-6501/ae1993

Grille Guerra, A., Scarano, F., & Wieneke, B. (2025). On the accuracy of multi-exposure 3D-PTV. *Proceedings of the 16th International Symposium on Particle Image Velocimetry*.

Grille Guerra, A., Sciacchitano, A., & Scarano, F. (2024). Iterative modal reconstruction for sparse particle tracking data. *Physics of Fluids*, *36*(7). https://doi.org/10.1063/5.0209527

Hendriksen, L. A., Grille Guerra, A., Sciacchitano, A., & Scarano, F. (2025). Omnidirectional Particle Image Velocimetry. *Proceedings of the 16th International Symposium on Particle Image Velocimetry*.

Hendriksen, L. A., Sciacchitano, A., & Scarano, F. (2024). Object registration techniques for 3D particle tracking. *Measurement Science and Technology*, *35*(12). https://doi.org/10.1088/1361-6501/ad715c

Jahn, T., Schanz, D., & Schröder, A. (2021). Advanced iterative particle reconstruction for Lagrangian particle tracking. *Experiments in Fluids*, *62*(8), 1–24. https://doi.org/10.1007/s00348-021-03276-7

Jeon, Y. J., Müller, M., & Michaelis, D. (2022). Fine scale reconstruction (VIC#) by implementing additional constraints and coarse-grid approximation into VIC+. *Experiments in Fluids*, *63*(4), 1–24. https://doi.org/10.1007/s00348-022-03422-9

Kähler, C. J., Astarita, T., Vlachos, P. P., Sakakibara, J., Hain, R., Discetti, S., La Foy, R., & Cierpka, C. (2016). Main results of the 4th International PIV Challenge. *Experiments in Fluids*, *57*(6), 1–71. https://doi.org/10.1007/s00348-016-2173-1

Le Bris, J., Leclaire, B., Cornic, P., Champagnat, F., Musci, B., & Cheminet, A. (2025). Consensus-based tracking for 3D PTV at high seeding densities. *Experiments in Fluids*, *66*(10), 1–24. https://doi.org/10.1007/s00348-025-04109-7

Novara, M., Schanz, D., & Schröder, A. (2023). Two-Pulse 3D particle tracking with Shake-The-Box. *Experiments in Fluids*, *64*(5), 1–21. https://doi.org/10.1007/s00348-023-03634-7

Novara, M., Schanz, D., Geisler, R., Gesemann, S., Voss, C., & Schröder, A. (2019). Multi-exposed recordings for 3D Lagrangian particle tracking with Multi-Pulse Shake-The-Box. *Experiments in Fluids*, *60*(3), 1–19. https://doi.org/10.1007/s00348-019-2692-7

Ouellette, N. T., Xu, H., & Bodenschatz, E. (2006). A quantitative study of three-dimensional Lagrangian particle tracking algorithms. *Experiments in Fluids*, *40*(2), 301–313.

Prasad, A., & Williamson, C. H. K. (1997). Three-dimensional effects in turbulent bluff-body wakes. *Journal of Fluid Mechanics*, *343*, 235–265. https://doi.org/10.1017/S002211209700579X

Scarano, F., Grille Guerra, A., & Wieneke, B. (2025). Detection of low-velocity traces in ME-PTV. *Proceedings of the 16th International Symposium on Particle Image Velocimetry*.

Scarano, F., Hysa, I., Grille Guerra, A., Tuinstra, M., & Sciacchitano, A. (2025). Asymmetric time sequence for multiple-exposure 3D PTV. *Experiments in Fluids*, *66*(4), 74. https://doi.org/10.1007/s00348-025-03993-3

Scarano, F., & Poelma, C. (2009). Three-dimensional vorticity patterns of cylinder wakes. *Experiments in Fluids*, *47*(1), 69–83. https://doi.org/10.1007/s00348-009-0629-2

Schanz, D., Gesemann, S., & Schröder, A. (2016). Shake-The-Box: Lagrangian particle tracking at high particle image densities. *Experiments in Fluids*, *57*(5), 70. https://doi.org/10.1007/s00348-016-2157-1

Szepessy, S., & Bearman, P. W. (1992). Aspect ratio and end plate effects on vortex shedding from a circular cylinder. *Journal of Fluid Mechanics*, *234*(-1), 191. https://doi.org/10.1017/S0022112092000752

Van Oudheusden, B. W. (2013). PIV-based pressure measurement. *Measurement Science and Technology*, *24*(3). https://doi.org/10.1088/0957-0233/24/3/032001

Wieneke, B., & Rockstroh, T. (2024). Lagrangian particle tracking in the presence of obstructing objects. *Measurement Science and Technology*, *35*(5), 055303. https://doi.org/10.1088/1361-6501/ad289d

Wieneke, B. (2013). Iterative reconstruction of volumetric particle distribution. *Measurement Science and Technology*, *24*(2). https://doi.org/10.1088/0957-0233/24/2/024008

Williamson, C. H. (1996). Vortex dynamics in the cylinder wake. *Annual Review of Fluid Mechanics*, *28*, 477–539. https://doi.org/10.1146/annurev.fl.28.010196.002401

6

Pouring statistics into space by modal reconstruction

In this chapter, a method to reconstruct the dense velocity field from relatively sparse particle tracks is introduced. The approach leverages the properties of proper orthogonal decomposition (POD), and it iteratively reconstructs the detailed spatial modes from a first, coarse estimation thereof. Finally, the enhanced velocity field is represented at high-resolution with a reduced order model using the dominant POD modes. The method is referred to as iterative modal reconstruction (IMR), and its algorithm is presented in section 6.1.

The performance of the method is evaluated from the analysis of experimental volumetric data obtained with large-scale PIV measurements in the wake of a cylinder at Re_D = 27,000 (section 6.2). In section 6.3, the obtained results are compared to other data-assimilation algorithms and the statistical convergence of the IMR method is also assessed.

Parts of this chapter have been published in: Grille Guerra, A., Sciacchitano, A., & Scarano, F. (2024). Iterative modal reconstruction for sparse particle tracking data. *Physics of Fluids*, *36*(7). https://doi.org/10.1063/5.0209527

6.1. The IMR method

The input to the iterative modal reconstruction (IMR) method is a relatively long (such that the velocity variance is converged) sequence of Lagrangian particle tracking (LPT) data (or alternatively particle traces obtained from multiple exposure recordings, as discussed in chapter 5) obtained with a coarse resolution, that is initially transformed onto a Cartesian grid (Cartesian grid reduction, CGR) as discussed in section 6.1.1. The gridded data undergoes an iterative modal decomposition procedure, as described in section 6.1.2, which is used to provide a low-order representation, referred to as reduced order model (ROM), of the instantaneous velocity field at high spatial resolution, as discussed in section 6.1.3. The computational complexity of the method is presented in section 6.1.4, together with an overview of the algorithm.

6.1.1. CGR of LPT data

Consider the set of particle trajectories obtained by LPT measurements, as sketched in the left part of figure 6.1, and represented by scattered velocity vectors at the particles' locations. In the time domain, n_{time} snapshots are acquired at a sampling frequency f_{acq}. The sparse velocity vectors are initially projected onto a coarse Cartesian grid (see figure 6.1) of spacing h_{LR} through window-based averaging (i.e. binning), to avoid data gaps (bins without velocity information) and prevent biasing the modal decomposition towards regions of higher seeding concentration. This is relevant, but not restricted to, for large-scale PIV experiments involving the use of helium-filled soap bubbles (HFSB) as tracers (Bosbach *et al.*, 2009). As a rule of thumb, for an average inter-particle distance $\bar{r}$, the bin size may be conservatively chosen one order of magnitude larger than $\bar{r}$. This choice ensures that bins include at least a few datapoints in regions of lower seeding concentration.

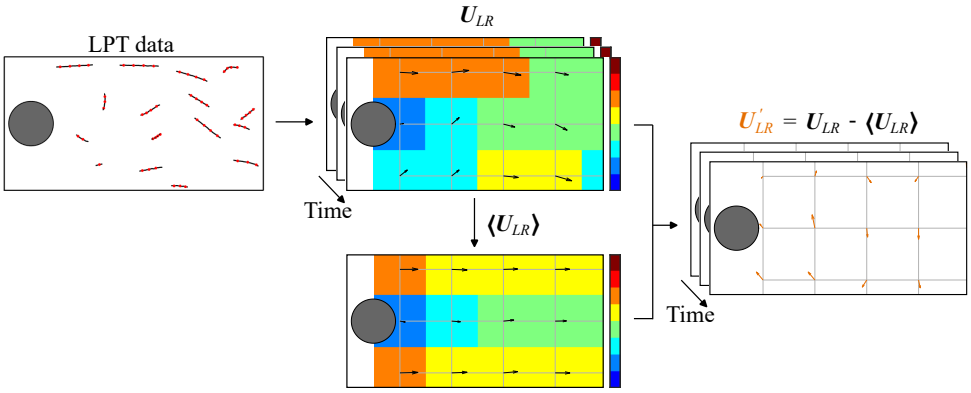

Figure 6.1: Sketch of the low-resolution velocity field, $\boldsymbol{U}_{LR}$, obtained from the LPT data, and the corresponding fluctuating component, $\boldsymbol{U}'_{LR}$, obtained via Reynolds decomposition.

Each snapshot of the binned data may be reshaped into a row vector $\boldsymbol{u}_{LR_k} \in \mathbb{R}^{1 \times n_s^{LR}}$,

with n_s^{LR} representing the total number of spatial elements, this is, $n_s^{LR} = 3n_x n_y n_z$ after accounting for the three velocity components. Appending all vectors returns the low-resolution velocity data matrix $\boldsymbol{U}_{LR} \in \mathbb{R}^{n_{time} \times n_s^{LR}}$. IMR is intended for statistically stationary processes, with the modal analysis targeting the fluctuating component of the velocity field only, $\boldsymbol{u}'_{LR_k} \in \mathbb{R}^{1 \times n_s^{LR}}$, obtained via Reynolds decomposition as $\boldsymbol{u}'_{LR_k} = \boldsymbol{u}_{LR_k} - \bar{\boldsymbol{u}}_{LR}$, where $\bar{\boldsymbol{u}}_{LR} \in \mathbb{R}^{1 \times n_s^{LR}}$ is the time-averaged velocity field. The extension of the method to non-stationary processes is out of the scope of the current work. The vectors of velocity fluctuations are reshaped into a low-resolution fluctuating velocity data matrix $\boldsymbol{U}'_{LR} \in \mathbb{R}^{n_{time} \times n_s^{LR}}$.

In parallel, the scattered velocity vectors at the particles' locations are projected onto a finer Cartesian grid, as sketched in figure 6.2, of spacing h_{HR} (and n_s^{HR} spatial elements), with $h_{HR} < h_{LR}$, through a similar binning process. The value of h_{HR} is chosen according to the statistical convergence of the ensemble of snapshots, as will be discussed in the remainder of the document. Because of the relatively small size of the bins used in the high-resolution Cartesian grid, the resulting velocity field, rearranged as $\boldsymbol{U}_{HR} \in \mathbb{R}^{n_{time} \times n_s^{HR}}$, will contain gaps that do not contribute to the modal reconstruction process. The time-averaged velocity field at this spatial resolution, $\bar{\boldsymbol{u}}_{HR} \in \mathbb{R}^{1 \times n_s^{HR}}$, can be obtained from an ensemble particle tracking approach (Cowen & Monismith, 1997; Kähler *et al.*, 2012) instead of Reynolds decomposition for improved accuracy (Tirelli *et al.*, 2023). The row vector $\bar{\boldsymbol{u}}_{HR}$ can be stacked to form a data matrix $\bar{\boldsymbol{U}}_{HR} \in \mathbb{R}^{n_{time} \times n_s^{HR}}$ and obtain the high resolution fluctuating velocity matrix $\boldsymbol{U}'_{HR} \in \mathbb{R}^{n_{time} \times n_s^{HR}}$ as $\boldsymbol{U}'_{HR} = \boldsymbol{U}_{HR} - \bar{\boldsymbol{U}}_{HR}$.

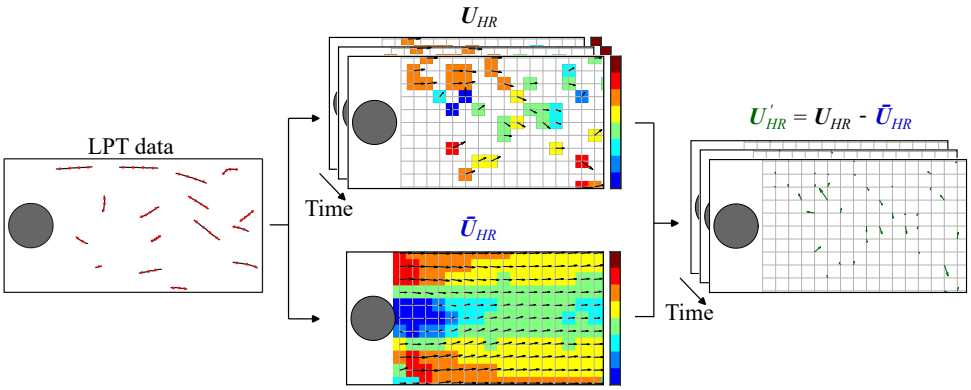

Figure 6.2: Sketch of the high-resolution (gappy) velocity field, $\boldsymbol{U}_{HR}$, the time-averaged flow field obtained from ensemble-averaging of the particle tracks, $\bar{\boldsymbol{U}}_{HR}$, and the fluctuating part $\boldsymbol{U}'_{HR}$.

6.1.2. Iterative modal decomposition

The low resolution CGR operation is employed to construct an initial guess of the modal decomposition of the dataset, as illustrated in figure 6.3, unaffected by the presence of gaps in the binned velocity representation. As in the original implementation of the data-enhanced particle tracking velocimetry (DEPTV, Cortina-Fernández *et al.*, 2021) method, the spatio-temporal bases are obtained from proper orthogonal decomposition (POD), but other decomposition choices are also possible (see for instance the work of Mendez *et al.*, 2019). The POD decomposition of $\boldsymbol{U}'_{LR}$, which can be implemented via the singular value decomposition (SVD) of the data matrix, reads:

$$\boldsymbol{U}'_{LR} = \boldsymbol{\Psi}_0 \boldsymbol{\Sigma}_0 \boldsymbol{\Phi}_0^T, \tag{6.1}$$

where $\boldsymbol{\Psi}_0 = [\boldsymbol{\psi}_1, ..., \boldsymbol{\psi}_{rk(\boldsymbol{U}'_{LR})}] \in \mathbb{R}^{n_{time} \times rk(\boldsymbol{U}'_{LR})}$ and $\boldsymbol{\Phi}_0 = [\boldsymbol{\phi}_1, ..., \boldsymbol{\phi}_{rk(\boldsymbol{U}'_{LR})}] \in \mathbb{R}^{n_s^{LR} \times rk(\boldsymbol{U}'_{LR})}$ are the orthonormal matrices that contain the so-called temporal (chronos) and spatial (topos) modes respectively. $\boldsymbol{\Sigma}_0 = \mathrm{diag}[\sigma_1, ..., \sigma_{rk(\boldsymbol{U}'_{LR})}] \in \mathbb{R}^{rk(\boldsymbol{U}'_{LR}) \times rk(\boldsymbol{U}'_{LR})}$ is the diagonal matrix containing the energy contribution of each mode, which for the case of velocity fluctuations represents the turbulent kinetic energy content. The total number of modes is dictated by the rank of the data matrix, $rk(\boldsymbol{U}'_{LR}) = \min(n_{time}, n_s^{LR})$. The common choice of POD is a result of the optimality of the decomposition from an energy perspective (using the L^2 error), as guaranteed by the Eckart- Young-Mirsky theorem (Eckart & Young, 1936).

The initial guess of the temporal basis is employed to increase the spatial resolution of the spatial modes (see figure 6.3), from the grid spacing h_{LR} to h_{HR} in an iterative manner, denoted by the subscript n. This is achieved by projecting $\boldsymbol{\Psi}_0$ (represented as $\boldsymbol{\Psi}_{n-1}$ in the iterative process) onto the high resolution fluctuating velocity data matrix, thus creating an updated representation of the spatial modes in a similar fashion to the extended POD modes discussed by Borée (2003). To account for the sparsity of $\boldsymbol{U}'_{HR}$, the projection step must be normalized to compensate for changes in seeding concentration across the measurement volume. For every spatial bin (or column of $\boldsymbol{U}'_{HR}$), counting the number of velocity entries is used to construct a vector of temporal occurrences, $\boldsymbol{n}_t \in \mathbb{R}^{1 \times n_s^{LR}}$. After normalizing by the total number of snapshots n_{time}, as $\hat{\boldsymbol{n}}_t = \boldsymbol{n}_t / n_{time}$, this information can be stacked to generate the matrix of temporal occurrences $\hat{\boldsymbol{N}}_t \in \mathbb{R}^{rk(\boldsymbol{U}'_{LR}) \times n_s^{LR}}$, which leverages the projection operator. Taking this into account, the projection of the temporal basis onto $\boldsymbol{U}'_{HR}$ returns:

$$\boldsymbol{\Sigma}_n \boldsymbol{\Phi}_n^T = \left(\boldsymbol{\Psi}_{n-1}^T \boldsymbol{U}'_{HR}\right) \oslash \hat{\boldsymbol{N}}_t, \tag{6.2}$$

where $\oslash$ denotes the Hadamard (element-wise) division operator. Inspection of equation (6.2) reveals that the spatial resolution of $\boldsymbol{\Phi}_n \in \mathbb{R}^{n_s^{HR} \times rk(\boldsymbol{U}'_{LR})}$ has been increased according to the grid spacing h_{HR}. The updated POD modes may be sorted according to their new energy contribution, $\boldsymbol{\Sigma}_n \in \mathbb{R}^{rk(\boldsymbol{U}'_{LR}) \times rk(\boldsymbol{U}'_{LR})}$, and the minor loss of orthogonality introduced in the projection step is corrected via reduced QR factorization of $\boldsymbol{\Phi}_n$.

While in the DEPTV method the high-resolution spatial modes are combined with the initial guess of the temporal coefficients to reconstruct the instantaneous velocity field, IMR uses $\boldsymbol{\Phi}_n$ to further update the temporal modes, and the process is repeated until

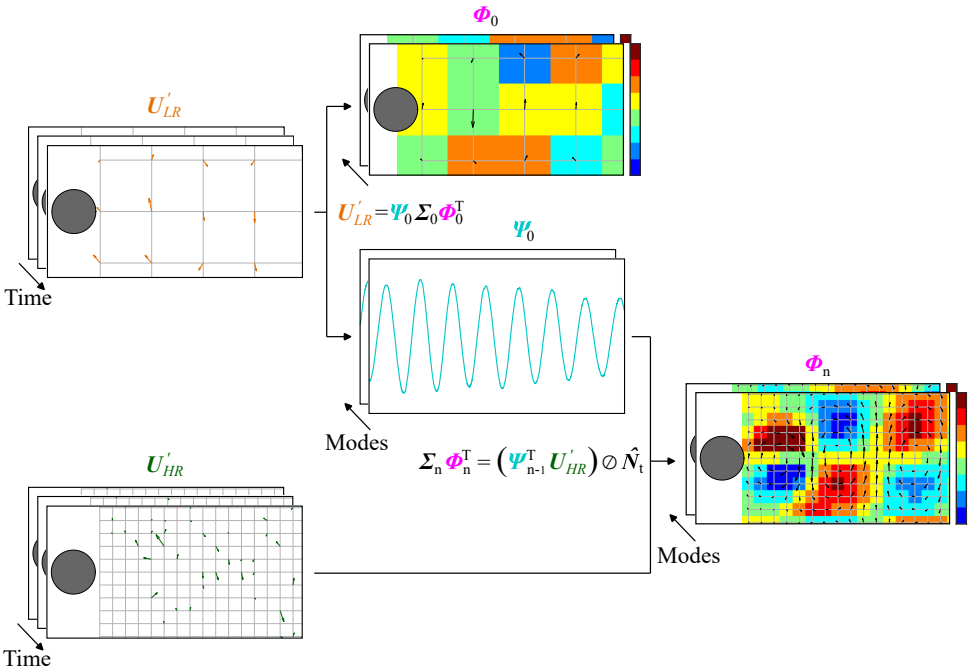

Figure 6.3: Sketch of the initial POD decomposition from the coarse binning data $\boldsymbol{U}'_{LR}$, and projection of the temporal coefficients $\boldsymbol{\Psi}$ onto the high resolution (gappy) velocity field $\boldsymbol{U}'_{HR}$ to increase the spatial resolution of the spatial modes $\boldsymbol{\Phi}$.

convergence of the decomposition (Venturi & Karniadakis, 2004). This is achieved by reprojecting $\boldsymbol{\Phi}_n$ onto $\boldsymbol{U}'_{HR}$, after accounting for the spatial sparsity of the snapshots. In an analogous fashion, for every snapshot (or row of $\boldsymbol{U}'_{HR}$), counting the number of velocity entries is used to construct a vector of spatial occurrences, $\boldsymbol{n}_s \in \mathbb{R}^{n_{time}\times 1}$. After normalizing by the total number of spatial elements, as $\hat{\boldsymbol{n}}_s = \boldsymbol{n}_s / n_s^{HR}$, this information can be stacked to generate the matrix of spatial occurrences $\hat{\boldsymbol{N}}_s \in \mathbb{R}^{n_{time}\times rk(\boldsymbol{U}'_{LR})}$. This matrix accounts for the changes in particles' concentration along time, which is usually rather minor compared to the changes across space. Including this contribution, the reprojection step reads:

$$\boldsymbol{\Psi}_n = \left(\boldsymbol{U}'_{HR}\boldsymbol{\Phi}_n\boldsymbol{\Sigma}_n^{-1}\right) \oslash \hat{\boldsymbol{N}}_s \,. \tag{6.3}$$

The process is completed by restoring the orthogonality of $\boldsymbol{\Psi}_n$ via reduced QR factorization and by checking the convergence of the process. The latter is implemented by requiring a relative change of $\boldsymbol{\Sigma}_n$ with respect to the previous iteration of less than 1%, considering the L^∞ norm (max vector norm).

6.1.3. High resolution instantaneous reconstruction

The result of the iterative modal decomposition is a set of $rk(\boldsymbol{U}'_{LR})$ orthogonal modes, ranked by their energy contribution, that provide a statistical representation of $\boldsymbol{U}'_{HR}$

after accounting for its sparsity. A representation of the instantaneous velocity field on a Cartesian grid of spacing h_{HR}, $\boldsymbol{U}_{HR}$, may be obtained by combination of the time-averaged flow field obtained via ensemble-averaging of the particle tracks, $\bar{\boldsymbol{U}}_{HR}$, and the contribution of r dominant modes, as illustrated in figure 6.4, which may be written as:

$$\boldsymbol{U}_{HR} = \bar{\boldsymbol{U}}_{HR} + \sum_{i=1}^{r} \boldsymbol{\psi}_i \sigma_i \boldsymbol{\phi}_i \,. \tag{6.4}$$

The resulting flow field is void of gaps irrespective of the choice of h_{HR} and r, but the means for setting both coefficients will be discussed in the remainder of the document.

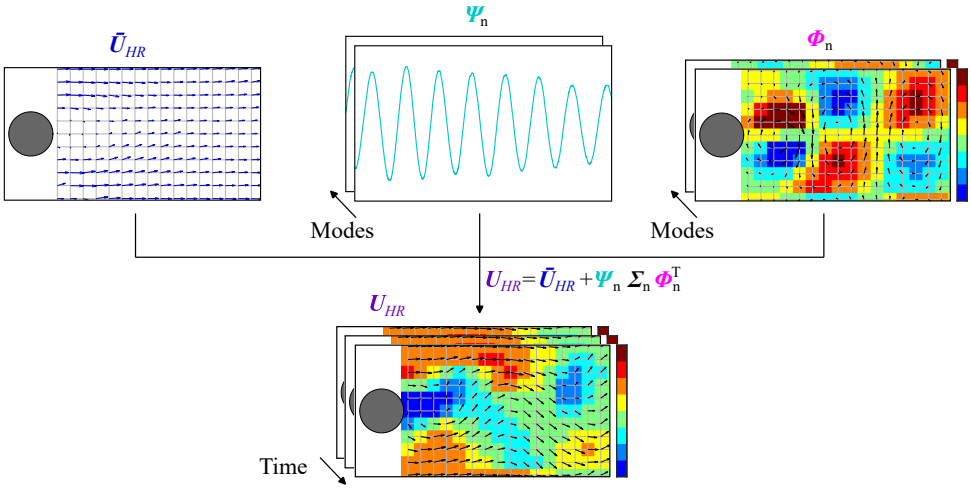

Figure 6.4: Sketch of the high resolution instantaneous reconstruction. The velocity field $\boldsymbol{U}_{HR}$ is obtained by combination of the time-averaged flow field $\bar{\boldsymbol{U}}_{HR}$ and dominant IMR modes.

6.1.4. Computational complexity

The current implementation of IMR is memory demanding. While for 3D fluid mechanics problems, where the number of spatial elements is usually much bigger than the number of time realizations, the current norm for POD implementation is the so-called snapshot POD strategy (Sirovich, 1987), IMR requires storing the entire $\boldsymbol{U}'_{HR}$ data matrix for minimal overhead, to be used in the projection steps. However, for very sparse matrices, the requirements can be simplified using sparse indexing. Alternative implementations of the method could load batches of the data matrix on demand at the cost of computational time.

On the other hand, the evaluation of the computational cost is relatively simple. The dominant term is the projection (and reprojection) step, a matrix multiplication. For equation (6.2), a standard implementation of the operation would have a cost $\mathcal{O}\left(rk(\boldsymbol{U}'_{LR}) \cdot n_{time} \cdot n_s^{HR}\right)$, although more advanced algorithms do exist. Since the

process is repeated during n iterations until convergence, the total cost reads $\mathcal{O}\left(rk(\boldsymbol{U}'_{LR}) \cdot n_{time} \cdot n_s^{HR} \cdot n\right)$. A simple trick for further time reduction is to compute only a subset of modes, n_m, with $n_m < rk(\boldsymbol{U}'_{LR})$, thus reducing the cost to $\mathcal{O}\left(n_m \cdot n_{time} \cdot n_s^{HR} \cdot n\right)$.

The requirements of IMR for the experimental assessment case presented in section 6.2 are summarized in table 6.1, and compared to linear interpolation and the VIC# method for reference. All computations are performed in a workstation with 64 GB of installed RAM and Intel Xeon E5-1620 CPU. The proposed algorithm is summarized by the flowchart shown in figure 6.5.

	Memory (RAM)	CPU time
Linear interpolation	<1 GB	40 min
VIC#	2 GB	5 days
IMR	50 GB	1 hour

Table 6.1: Memory and CPU time requirements for the evaluation of the cylinder wake data (20,000 snapshots) using linear interpolation, VIC# and the proposed IMR method (with nine iterations until convergence).

6.2. Experimental assessment: cylinder wake

The experimental case considered for the evaluation of the IMR algorithm is the Kármán-Benard wake behind a circular cylinder discussed by Scarano *et al.* (2022). The experimental setup is described in section 6.2.1. The LPT analysis is discussed in section 6.2.2, followed by a description of the assessment method in section 6.2.3. The flow field under study is presented in detail in section 6.2.4, both in terms of instantaneous reconstruction and modal analysis.

6.2.1. Experimental apparatus and procedures

Experiments are conducted in the OJF (open jet facility), a large-scale low-speed wind tunnel at the laboratories of the aerospace engineering faculty of TU Delft. The OJF features an exit cross section of 2.85 × 2.85 m^2. A 2-m-long cylinder of diameter D = 10 cm is installed vertically and immersed in the free-stream flow at U_∞ = 4 m/s. The resulting value of the diameter-based Reynolds number is 27,000. The domain of interest is the near wake of the cylinder. The measurement covers a domain of $5D(x) \times 6D(y) \times 3D(z)$.

Neutrally buoyant, sub-millimeter helium-filled soap bubbles (HFSB) are used as tracers, produced by a seeding rake comprising 204 bubble generators, and installed ahead of the wind tunnel contraction. With the seeding rake installed, turbulence intensity in the test section is reported to increase from the nominal 0.5% of the freestream (Lignarolo *et al.*, 2014) to approximately 0.8% (Giaquinta, 2018). After the contraction, a seeded streamtube of an approximate diameter of 60 cm is obtained. Tracers are illuminated by two LaVision *LED-Flashlight 300* directed along the span of

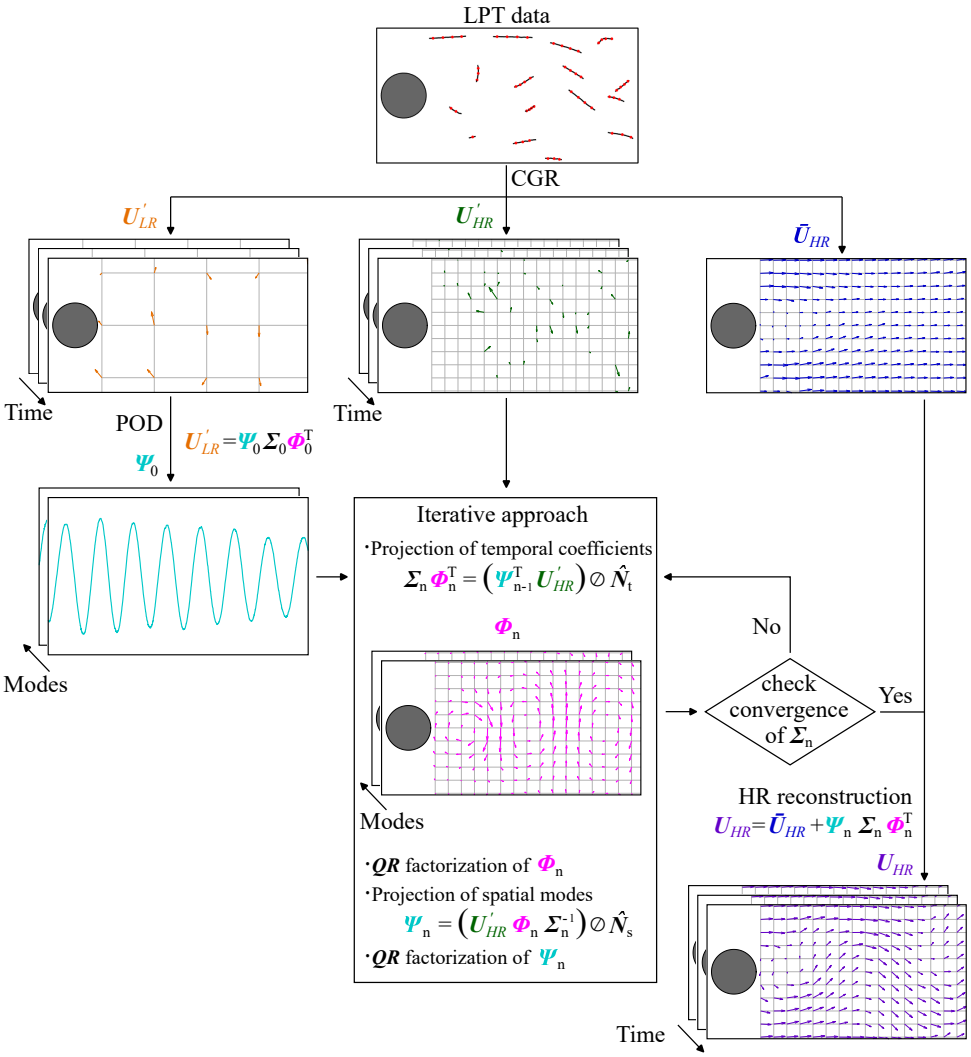

Figure 6.5: Flowchart of the proposed IMR algorithm. The LPT data initially undergoes two CGR procedures at different spatial resolutions. The fluctuating component of the low-resolution version, $\boldsymbol{U}'_{LR}$, is used to construct an initial modal decomposition using POD. The temporal modes, $\boldsymbol{\Psi}_0$, are projected onto the sparse high resolution fluctuating velocity, $\boldsymbol{U}'_{HR}$, to obtain a representation of the spatial modes, $\boldsymbol{\Phi}_n$, at high spatial resolution. This process is repeated until convergence of the decomposition. Finally, an instantaneous representation of the velocity field at high resolution, $\boldsymbol{U}_{HR}$, is extracted from the time-averaged flow field $\bar{\boldsymbol{U}}_{HR}$ combined with the dominant modes.

the cylinder. The light scattered by the tracers is recorded using three Photron *Fastcam SA 1.1* CMOS cameras (1024×1024 pixel, 12-bit, 20 µm pixel pitch) equipped with Nikon 50 mm focal length objectives, set at numerical aperture $f_\# = 22$. The experimental setup is illustrated in figure 6.6.

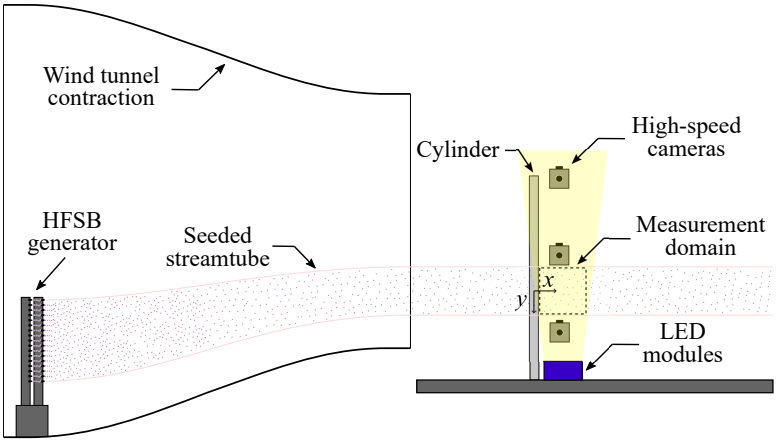

Figure 6.6: Schematic side-view of the experimental setup in the OJF.

A sequence of $n_{time} = 2,000$ frames is obtained at $f_{acq} = 2$ kHz. Approximately eight shedding cycles are observed during the experiment, corresponding to a Strouhal number of $St = (fD)/U_\infty = 0.2$, in agreement with the literature (Williamson, 1996). Data recording and LPT processing operations are performed in the DaVis 10 software.

6.2.2. Particle tracking analysis

The images are pre-processed with a Butterworth high-pass filter in the time domain (Sciacchitano & Scarano, 2014) to reduce background illumination. A raw-to-world mapping function is obtained by calibration with a translating target and refined with the volume self-calibration technique (Wieneke, 2008). An optical transfer function (Schanz *et al.*, 2013) is computed prior to the evaluation of the particle images using the LPT Shake-the-Box algorithm (Schanz *et al.*, 2016). Accepting only tracks comprising at least four consecutive samples results in an average concentration of tracks across the volume of $C = 0.12$ tracks/cm^3, corresponding to an average inter-particle distance of $\bar{r} = \sqrt[3]{3/(4\pi C)} = 1.25$ cm. An illustration of particle tracks captured during ten snapshots, color-coded by streamwise velocity, is shown in figure 6.7 (left).

6.2.3. IMR assessment method

In order to evaluate the ability of the IMR method to accurately reconstruct the instantaneous flow field from sparse data, a downsampling-resampling approach has been adopted. Since the exact velocity field is unknown, a common approach in experimental research consists of generating a reference solution from another

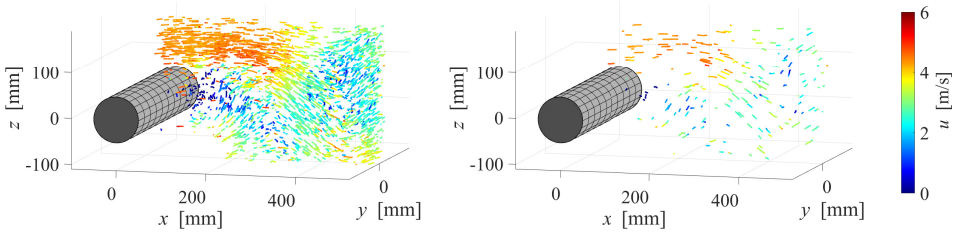

Figure 6.7: Visualization of particle tracks reconstructed with Shake-the-Box (left) and coarsened measurement (right, where only 10% of the data is retained). Tracks including 10 frames are color-coded by streamwise velocity. Only a slab of 10 cm depth is shown for clarity.

experiment. This may be done employing another experimental measurement technique (Boomsma *et al.*, 2016), the same one but at higher resolution (Sciacchitano *et al.*, 2015) or using more accurate evaluation methods (Sciacchitano *et al.*, 2013). Similarly, one may artificially downsample the data in time (Schneiders *et al.*, 2014) or space (Cai *et al.*, 2024; Schneiders & Scarano, 2016) and construct the reference solution with the full dataset. This way, a ground truth can be constructed for evaluation of a proposed methodology, while at the same time the dataset preserves the nature of the experimental measurements, including a certain level of noise or presence of outliers, for example. In the current study, the latter approach is taken for the assessment of the IMR method. The LPT dataset is artificially coarsened by downsampling it to 1:10 of the total number of tracks. The remaining tracks are appended to the dataset, thus creating a sequence of $n_{time} = 20,000$ snapshots at one tenth of the original concentration, this is, $C = 0.012$ tracks/cm^3, corresponding to an average inter-particle distance of $\bar{r} = 2.7$ cm. An illustration of particle tracks at this concentration is given in figure 6.7 (right).

From the full concentration of tracks, the reference instantaneous velocity field is obtained using the VIC# algorithm (Jeon *et al.*, 2022) on a Cartesian grid with spacing of $h = 7.3$ mm, following the criterion suggested by Schneiders and Scarano (2016), $h = \frac{1}{4}C^{-1/3}$. The resulting grid contains $n_x = 69$, $n_y = 82$ and $n_z = 41$ elements respectively, and therefore $n_s = 695,934$.

From the downsampled dataset, a coarse representation of the instantaneous flow field ($\boldsymbol{U}_{LR}$) is obtained through a binning procedure, whose parameters are summarized in table 6.2. Please note that $rk(\boldsymbol{U}'_{LR}) = \min(n_{time}, n_s^{LR}) = n_s^{LR}$ and therefore the total number of available IMR modes is dictated by the number of spatial elements. Since the goal is to obtain a high-resolution representation of the flow field, comparable to the reference situation discussed in section 6.2.4 for the original LPT dataset, the target resolution for IMR is set equal to that of the reference. This represents an eight-times increase with respect to the coarse binning operation. At this resolution, a gappy representation of the flow field ($\boldsymbol{U}_{HR}$) is obtained through a binning process summarized in table 6.2. The time-averaged velocity field at this spatial resolution ($\bar{\boldsymbol{U}}_{HR}$) is obtained from the ensemble-average of particle tracks by fitting a second-order polynomial inside each bin (Agüera *et al.*, 2016).

	Bin size [mm]	Overlap factor	h [mm]	n_s
Low resolution	233.6	75%	58.4	2,079
High resolution	29.2	75%	7.3	695,934

Table 6.2: Main parameters of the binning procedures for the cylinder-wake dataset.

6.2.4. Reference instantaneous reconstruction and modal decomposition

As discussed in section 6.2.3, the reference solution is obtained from the full concentration of trajectories using the VIC# data assimilation algorithm. An instantaneous representation of the three-dimensional flow field is shown in figure 6.8 using isosurfaces of vorticity, color coded by their sign and component. The illustration reveals the dominant spanwise-coherent vortices (Kármán street), visualized through isosurfaces of spanwise vorticity ω_y (red and blue), that are shed with alternating sign. The two-dimensional homogeneity of the flow is altered in several ways, as abundantly reported in the literature (Williamson, 1996). The main rollers may feature locally and occasionally an oblique orientation to the cylinder axis (oblique shedding, Prasad and Williamson, 1997; Szepessy and Bearman, 1992). Furthermore, the rollers may exhibit undulations of wavelength several times larger than the cylinder diameter, similar to the reported *mode A* exhibited in the laminar shedding regime (Williamson, 1996). Finally, thin, elongated structures interconnecting the main rollers are often observed and visualized through the dominant vorticity component ω_x (green and yellow). These structures, usually referred to as *fingers* or *ribs*, have been mostly visualized at Reynolds number in the order of $Re = 10^2 - 10^3$ (*Mode B*, Kanaris *et al.*, 2011; Prasad and Williamson, 1997; Williamson, 1996), while their coherence is reported to decrease with increasing Reynolds number (Parnaudeau *et al.*, 2008), although still present up to $Re = 5,000$ (Scarano & Poelma, 2009).

The instantaneous flow visualization is provided for two different time instants to illustrate the changes in spanwise coherence of the main vortices. Inspection of figure 6.8 (right) reveals a condition whereby the main rollers are shed at an angle with respect to the cylinder. Figure 6.8 (left) instead, shows evident undulation of the rollers. In both examples, the rollers feature strong local distortions from the inception of the fingers.

The interpretation of the flow field is further elucidated by the analysis of the POD decomposition of the reference velocity field, which will later also serve as reference evaluating the results obtained with the IMR technique. The decomposition is summarized by the spectrum of energy captured in each mode given in figure 6.9, alongside the cumulative energy; the three-dimensional representation of the eight most dominant spatial modes shown in figure 6.10, and the corresponding temporal coefficients, given in figure 6.11 together with their frequency spectra. To the authors' best knowledge, only a handful of publications (namely the simulations of Ma and Karniadakis, 2002, for $Re_D = 185$, and Wang *et al.*, 2012, for $Re_D = 1,000$) provide a three-dimensional representation and interpretation of cylinder wake modes. In the

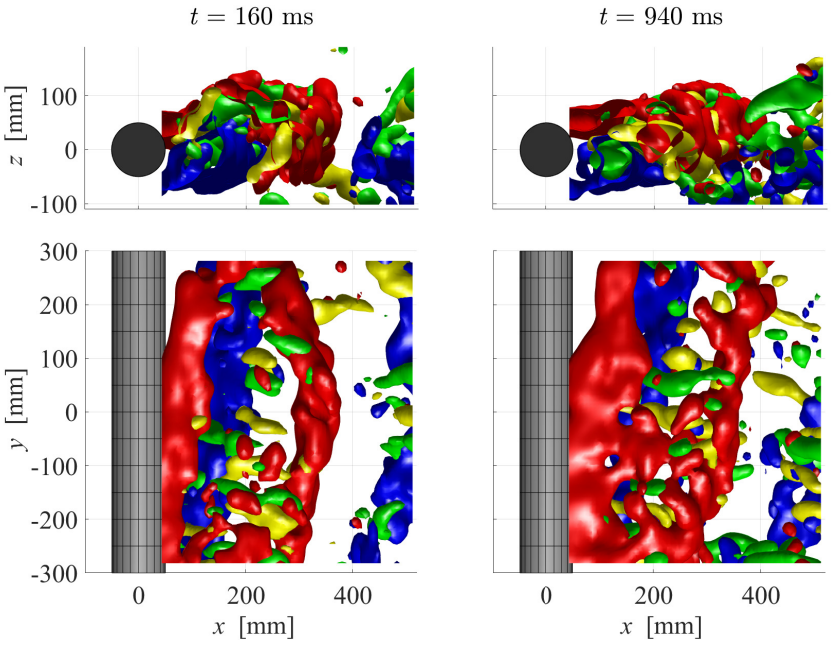

Figure 6.8: Instantaneous visualization of the three-dimensional flow field using isosurfaces of spanwise (red and blue, ω_y = ±70 s^{-1}) and streamwise (green and yellow, ω_x = ±70 s^{-1}) vorticity, obtained using the VIC# algorithm. Represented both using side (upper row) and top (bottom row) views, for two different time instants: t = 160 ms (left) and t = 940 ms (right).

following, we tackle the fully turbulent regime (Re_D = 27,000) and extensively discuss not only the dominant Kármán wake modes (namely modes 1 and 2), representing the advection of spanwise-coherent vortical structures, but also higher-order ones (spanwise distributed, like mode-A and with the introduction of streamwise-binormal vorticity, like mode-B), inherently three-dimensional.

The modal energy distribution returns the first two modes accounting for approximately 60% of the total turbulent kinetic energy, in agreement with existing two-dimensional experiments performed at comparable Reynolds number (Zhang *et al.*, 2014). These two modes capture the most global feature of the Kármán wake. Because the vortex street is convected, such as a travelling wave homogeneously along the span, this first fluid dynamic mode requires two POD entries phase-shifted of a quarter wavelength ($\pi/4$). The spatial arrangement of the modes corroborates the oblique shedding discussed above, and the frequency spectra of the temporal coefficients confirms that the vortices are shed at St = 0.2.

POD entries 3 and 4 also exhibit a similar level of energy. Furthermore, their pattern is very similar and shifted of $\pi/4$, which is a strong indication that these two entries form an additional convective mode. In this case, the spatial distribution is not homogeneous

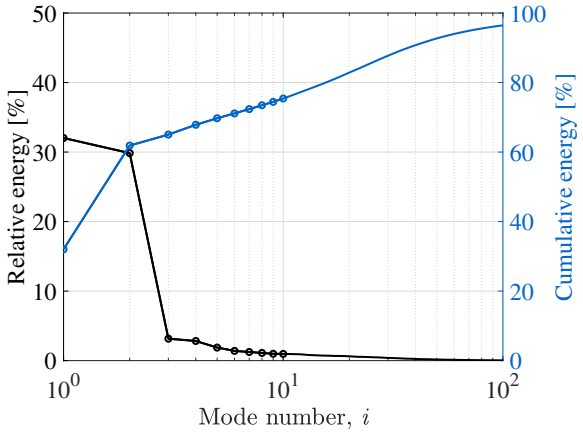

Figure 6.9: Relative and cumulative modal energy contribution of the hundred most dominant modes obtained from the POD decomposition of the reference velocity field.

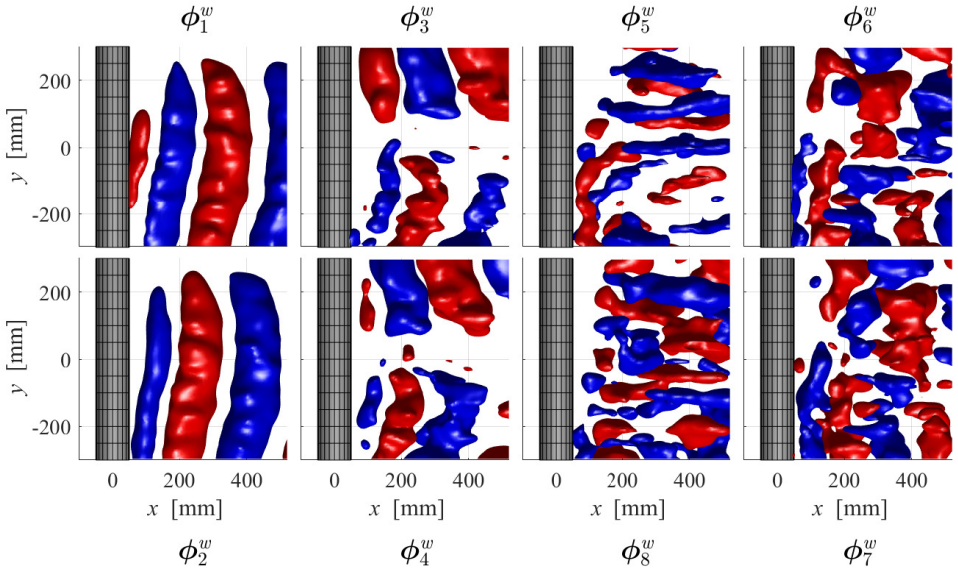

Figure 6.10: Top view of the eight most dominant spatial POD modes obtained from the reference velocity field, represented using isosurfaces of $\boldsymbol{\phi}^w$ (positive and negative, red and blue respectively).

along the span. Instead, a phase jump is exhibited, whereby the transverse motions invert their sign. The spatial arrangement of these modes suggests the presence of a spanwise wavelength, λ_y, that exceeds the measurement domain, such that $\lambda_y/D > 6$.

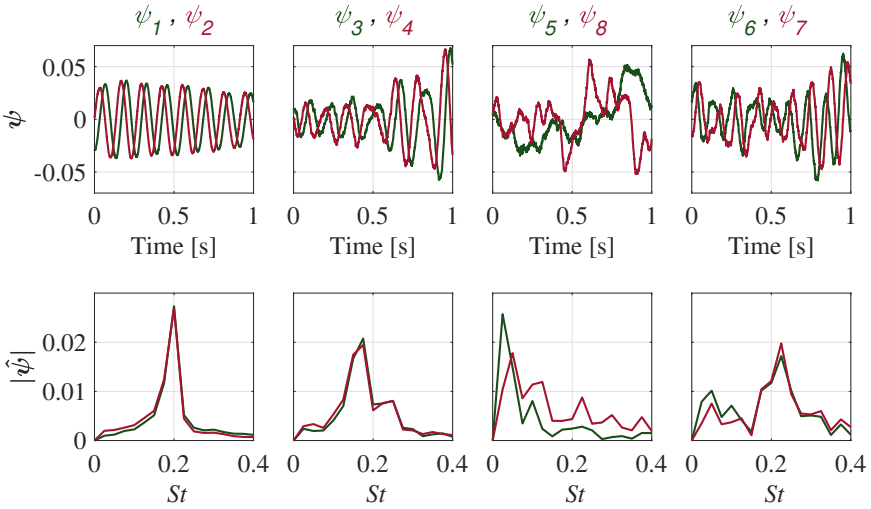

Figure 6.11: Representation of the eight most dominant temporal POD modes obtained from the reference velocity field, together with their frequency spectra.

Besides, the spectra of the associated temporal coefficients also reveal a peak around $St = 0.2$, indicating that these entries are still related to the Kármán street.

Mode 5 represents that part of flow motions where spanwise vorticity has been largely tilted along the streamwise direction and stretched under the action of the two counter-rotating rollers. These structures are frequently observed in Kármán wakes at higher values of the Reynolds number and feature a pattern and wavelength resembling *mode B* of the transitional cylinder wake, characterized by $\lambda_y/D \approx 1$ (Williamson, 1996), which is in agreement with the current observations. Also this mode is expected to convect alongside the main rollers and it is expected that two POD entries, with similar phase shift to the above, compose this fluid-dynamic motion. However, the energy captured by this mode is similar to that of modes 6 and 7, and the mode ranking by energy becomes no guarantee that subsequently ranked POD entries pertain to the same fluid dynamic mode. Instead, mode 5 shows a stronger resemblance with mode 8, both in terms of spatial arrangement and spectra of temporal coefficients, and are therefore represented together. These entries do not show a clear phase correlation with a shift of $\pi/4$, arguably due to the fact that in the turbulent regime, the *ribs* occurrence is less regular and they may require more POD entries to fully capture their motions. Furthermore, their spectra is dominated by lower frequencies, requiring a longer time sequence for further evaluation of this phenomenon.

Instead, modes 6 and 7 form another convective pair associated to the main rollers, in this case introducing a non-homogeneity along the span governed by $\lambda_y/D \approx 4$, similar to what is reported in the literature for *mode A* (Williamson, 1996). As for previous entries, the peak of the spectra around $St = 0.2$ links them to the main rollers.

6.3. Results

The proposed IMR method is applied to the downsampled LPT dataset. The role of the number of spatio-temporal occurrences is illustrated in section 6.3.1. The resulting decomposition, compared to that obtained from the reference dataset and the DEPTV method, is discussed in section 6.3.2. Section 6.3.3 covers the instantaneous high-resolution reconstruction of the flow field and finally section 6.3.4 discusses the statistical convergence of the proposed methodology.

6.3.1. Number of spatio-temporal occurrences

One of the key aspects of the IMR algorithm is the normalization introduced in the projection (and reprojection) step, that accounts for the changes in seeding concentration in time and space, inherent to experimental LPT approaches. For the current dataset, changes across the measurement volume are significant. The normalized vector of temporal occurrences, $\hat{\boldsymbol{n}}_t$, is shown in figure 6.12 (left) at the mid-span of the domain (y = 0 mm), indicating a higher concentration of trajectories closer to the cameras (positive z).

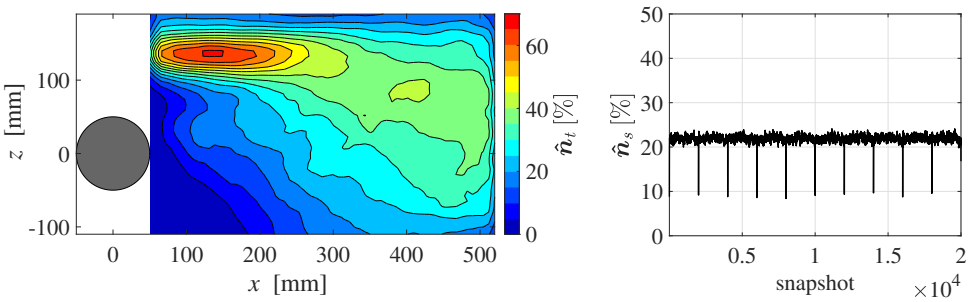

Figure 6.12: Number of normalized temporal occurrences, $\hat{\boldsymbol{n}}_t$, at the mid-span of the domain (left) and number of normalized spatial occurrences, $\hat{\boldsymbol{n}}_s$ (right).

On the other hand, only minor changes in the number of spatial occurrences are observed (continuous seeding), as shown in figure 6.12 (right). Significant drops in $\hat{\boldsymbol{n}}_s$ are only present in the initialization step of the Shake-the-Box algorithm, which propagates through the ten stacked sequencies of the downsampled dataset. On average, almost 80% of the spatial bins contain no velocity information, an unprecedented value when making use of modal analysis for flow reconstruction (Raben *et al.*, 2012; Venturi & Karniadakis, 2004).

6.3.2. Modal decomposition

The modal decomposition obtained with IMR is compared to that obtained from the coarse binning operation summarized in table 6.2 and the reconstruction from DEPTV. Furthermore the results are benchmarked against the reference (section 6.2.4). The modal energy contribution (squared elements of $\boldsymbol{\Sigma}$ normalized by $n_{time}n_s$ to provide a grid-independent estimation), is shown in figure 6.13 for the first hundred modes. The

spatial modulation introduced in the binning operation causes an overall energy drop with respect to the reference data. The energy is largely recovered by DEPTV for the first twenty modes. After that, the lack of statistical convergence and the presence of experimental noise contaminates the modal distribution and the DEPTV solution shows a flatter decay (Cortina-Fernández *et al.*, 2021), unable to reproduce the filtering effect introduced by the VIC# methodology. The iterative approach of IMR yields an energy distribution in agreement with the reference data for the first four modes. After that it progressively overestimates the contribution of high-order ones. As discussed in the following, this results from the appearance of high-frequency noise in the DEPTV and IMR spatial modes. For DEPTV, the added energy arising from noise is compensated by the poor reconstruction of the temporal coefficients, thus yielding an energy distribution that agrees better with the reference.

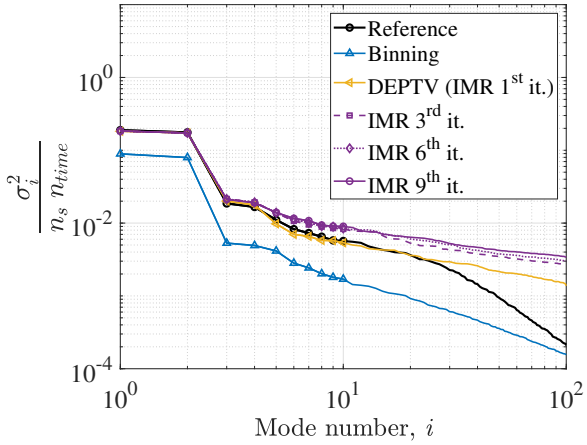

Figure 6.13: Comparison of the grid-independent modal energy contribution of the hundred most dominant modes obtained from the reference POD decomposition, the coarse binning operation, DEPTV and IMR.

The high-resolution spatial modes obtained with the proposed methodology are compared to the other methods as shown in figure 6.14. The visualization represents one entry of the four most dominant mode pairs discussed in section 6.2.4, drawn using isosurfaces (positive and negative, in red and blue respectively) of the vertical (z) component of the spatial modes, $\boldsymbol{\phi}^w$. The spatial averaging introduced by the binning process is now evident when looking at modes 1 and 3. For modes 5 and 6 the output of the binning method falls below the threshold chosen for representation. The DEPTV and IMR show similar patterns, both in good agreement with the reference data. A degree of granularity (high-frequency noise) is observed for all modes. While Cortina-Fernández *et al.* (2021) suggest the use of a low-pass filter to counter this effect for DEPTV, the approach has not been pursued, in absence of a theoretical justification for it.

Regarding the modal decomposition, the main upgrade of IMR consists of providing an updated representation of the temporal modes after the computation of spatial modes at higher resolution. The effect is illustrated in figure 6.15 by comparing four

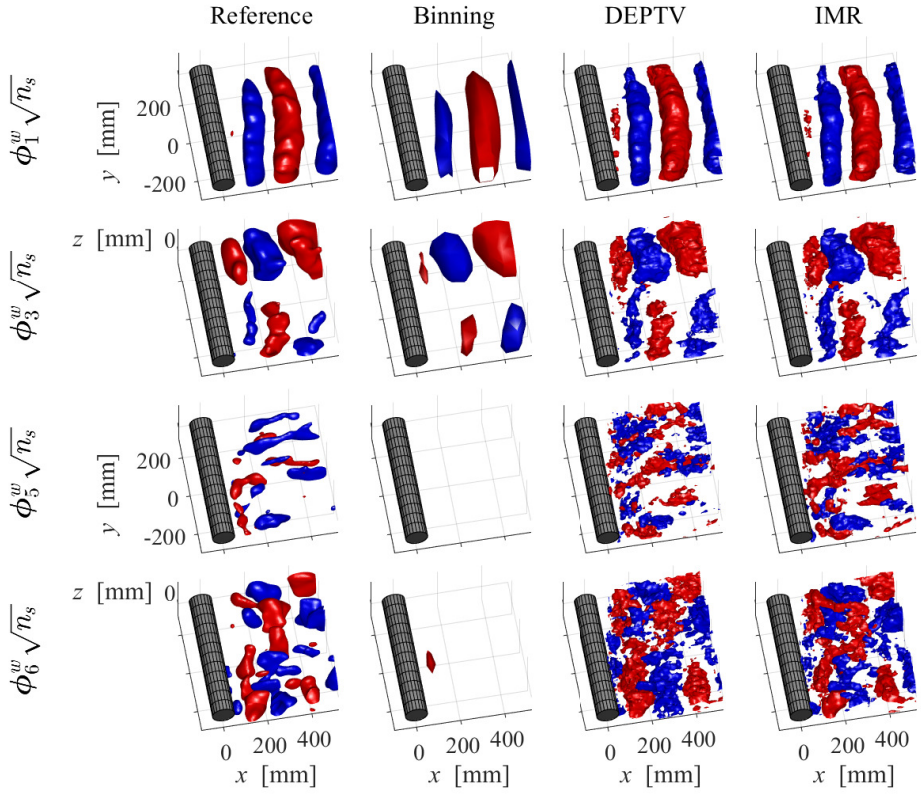

Figure 6.14: Comparison of grid-independent four dominant spatial modes obtained from the reference POD decomposition, the coarse binning operation, DEPTV and IMR. Three-dimensional visualization drawn using isosurfaces of $\boldsymbol{\phi}^w$ (positive and negative, red and blue respectively).

dominant temporal modes with those extracted from the other methods. As expected, no significant differences are observed for modes 1 and 3, since these are well represented by the binning procedure already. However, higher-order modes are not resolved with binning and therefore depart from the reference ones. Instead, the iterative procedure of IMR is able to recover the main shape of the temporal coefficients, thus providing a significant upgrade for the use of modal decomposition as a tool for instantaneous high-resolution reconstruction. The good agreement of the temporal coefficients, combined with the granularity of the spatial modes discussed above, is argued to be responsible for the overestimate in modal energy contribution observed in figure 6.13 for IMR.

The comparison of temporal coefficients is extended to higher-order ones by computing the zero-lag cross-correlation coefficient with respect to the reference modes, as a means to indicate the degree of correlation that IMR can recover. The results are

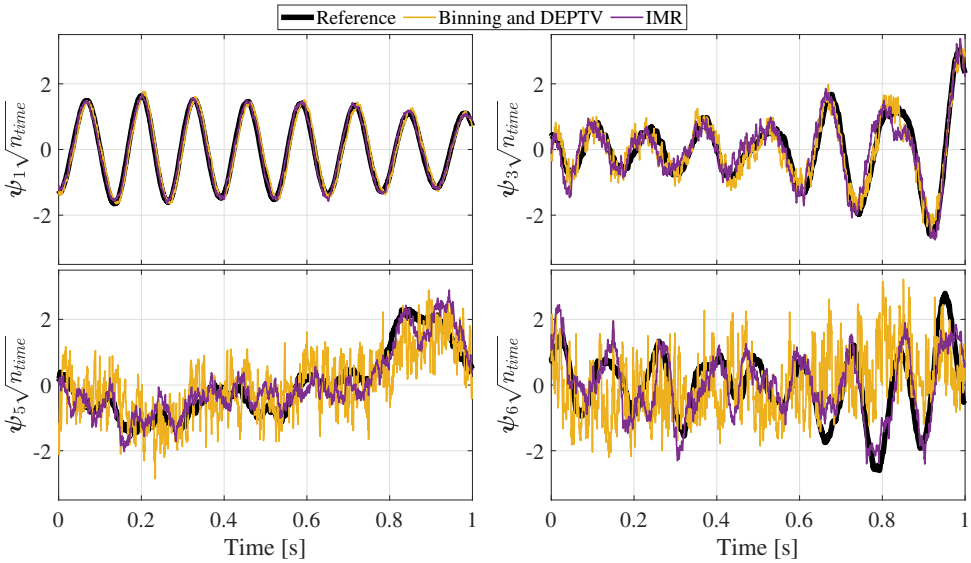

Figure 6.15: Comparison of grid-independent four dominant temporal modes obtained from the reference POD decomposition, the coarse binning operation, DEPTV and IMR.

given in figure 6.16 for the hundred most dominant modes. For DEPTV, the trend decays sharply after the first four modes, which could already be observed in figure 6.15. The iterative process allows to recover agreement with the reference for modes that were not resolved by the coarse binning procedure, thus suggesting the possibility of building a more accurate reduced order model by involving more modes in the reconstruction.

6.3.3. High-resolution instantaneous reconstruction

An instantaneous high-resolution reconstruction of the flow field can be built using the IMR decomposition, as discussed in equation (6.4), by choosing a number of dominant modes r. The obtained velocity field is compared, relative to the reference dataset, to that obtained using linear interpolation from the scattered trajectories, the physics-based VIC# approach (also obtained from the downsampled set of tracks, not to be confused with the reference solution) and the DEPTV method. In every case, the target spatial resolution is set to h = 7.3 mm. For VIC#, the criterion $h = \frac{1}{4}C^{-1/3}$ is no longer verified. For every situation, a mean reconstruction error, ε, is built from the difference between the reconstructed velocity field, $\boldsymbol{U}(x,t)$, and the reference solution, $\boldsymbol{U}_{ref}(x,t)$, as:

$$\varepsilon = \frac{1}{U_\infty}\sqrt{\frac{1}{n_{time}n_s^{HR}}\sum_{i=1}^{n_t}\sum_{j=1}^{n_s^{HR}}\|\boldsymbol{U}(\boldsymbol{x}_j,t_i)-\boldsymbol{U}_{ref}(\boldsymbol{x}_j,t_i)\|_2}\,. \tag{6.5}$$

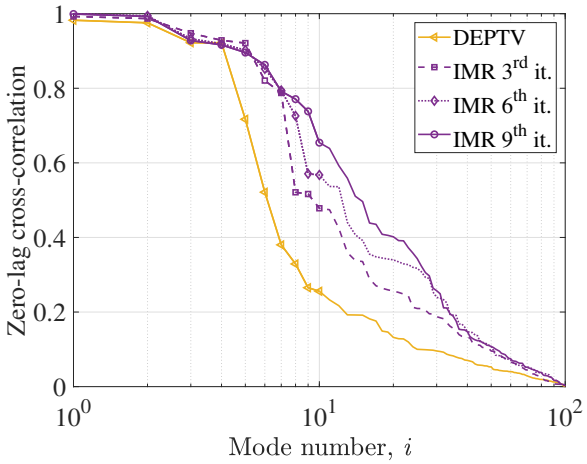

Figure 6.16: Zero-lag cross-correlation coefficient of the hundred most dominant DEPTV and IMR temporal modes with respect to the reference ones.

For the sake of simplicity, only the first sequence of $n_{time} = 2,000$ snapshots is considered in the remainder. The mean reconstruction error obtained with every data assimilation approach is shown in figure 6.17, in terms of the number of modes considered for the DEPTV and IMR algorithms. While the modal-based methods show an error decrease when compared to linear interpolation and VIC#, the relative differences are minor with respect to the error relative to the reference. For both methods, the reconstruction error initially decreases when considering more modes in the reconstruction, since this involves a more detailed representation of the flow field. At a certain point, a minimum error is reached, after which the error increases due to the excessive presence of noise in higher-order modes. For IMR, the minimum is achieved when considering more modes than for DEPTV, a direct consequence of the better representation of the temporal modes achieved with the proposed methodology, as discussed in section 6.3.2.

To provide further insight into the reconstruction process, the streamwise spectra of vertical velocity, E_x^{ww}, is obtained for every method. The spectra, represented in terms of the streamwise wavenumber $\kappa_x = 2\pi/\lambda_x$, where λ_x represents a streamwise wavelength, is averaged over the span and time for convergence. The results, shown in figure 6.18 (left), have been compensated using the square of the wavenumber to magnify the behavior of the medium and small scales. For DEPTV and IMR, the number of dominant modes used for the reconstruction are chosen from the minimum mean error shown in figure 6.17 (five and twenty modes respectively). The reference spectrum is dominated by the streamwise spacing between spanwise-coherent rollers and harmonics. While the linear interpolation solution underestimates the content of the dominant large scales, the VIC# one shows the opposite trend. For both situations, the poor representation of dominant scales may be responsible for the higher mean reconstruction error. The DEPTV method captures the first peak of the spectrum at $\kappa_x = 27$ m^{-1} rather accurately

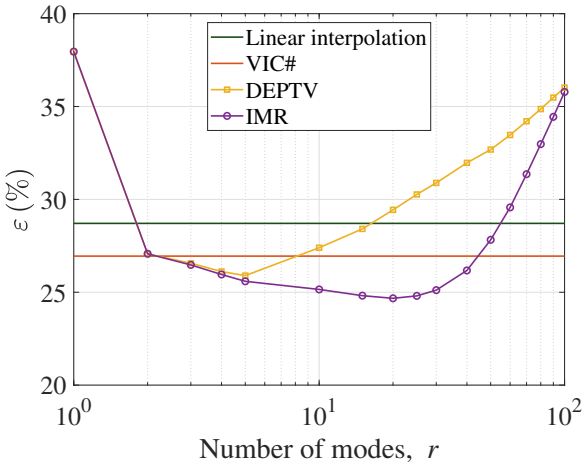

Figure 6.17: Mean reconstruction error with respect to the reference velocity field, obtained using linear interpolation, VIC#, DEPTV and IMR. For the modal-based approaches, the result is given in terms of the number of dominant modes used in the reconstruction.

since the main rollers are mostly described by the first two modes (see figure 6.14). Beyond that point, the spectrum shows a strong decay, arguably due to the fact that medium scales are contained in higher-order modes. By including more modes in the reconstruction, the IMR solution shows a much better agreement with the reference up to $\kappa_x \sim 100$ m^{-1}. However, the high-frequency noise that could already be observed in the shape of the spatial modes introduces an overestimation of the small-scale content.

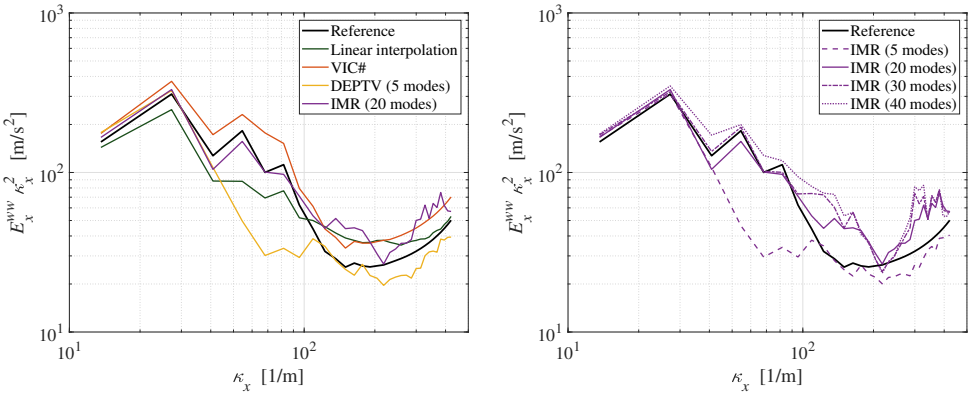

Figure 6.18: Compensated streamwise spectra of vertical velocity, averaged in time and over the span, for different data assimilation methods (left) and obtained with IMR changing the number of dominant modes used in the reconstruction (right).

The role of the number of dominant modes used in the IMR reconstruction is further illustrated in figure 6.18 (right), by showing the spectra obtained changing this parameter. As expected, choosing a small number of modes causes an underestimation of the medium-scale content. While the best agreement with the reference, up to $\kappa_x \sim 100$ m^{-1}, is obtained when considering thirty modes, the added small-scale contribution results in a slightly weaker reconstruction in terms of the mean error (see figure 6.17).

The possibility of having a reference dataset to select the dominant number of modes for the reconstruction is typically not available for experimental measurements. The appropriate choice of this parameter has been a topic of research since the introduction of modal analysis for building reduced order models, and dates back to the classic *scree test plot* (Cattell, 1966) method of finding an elbow in the modal energy distribution (as the ones showed in figure 6.13). More accurate methods have been also proposed (Gavish & Donoho, 2014), even some tailored to experimental PIV data (Epps & Krivitzky, 2019; Raiola *et al.*, 2015), but cannot be directly applied to IMR since the method does not involve a canonical POD decomposition of the experimental data. A more robust approach, purely based on the topology of the spatial modes, has been proposed by Brindise and Vlachos (2017) and is suggested as suitable for the implementation of IMR. The method targets the spatial differences between modes containing relevant flow structures and those corrupted by random noise. It is implemented via calculation of the Shannon entropy of the spatial modes, after a change of basis using the discrete cosine transform. Extending the procedure described by Brindise and Vlachos (2017) to a three-dimensional situation returns an optimum threshold of nineteen modes, in excellent agreement with the error-based minimization with respect to the reference dataset discussed in figure 6.17.

The topology of the reconstructed flow field may be inspected in figure 6.19. A comparison is made between the reference solution, linear interpolation, the VIC# algorithm and a reconstruction using IMR with $r = 19$. The visualization shows isosurfaces of spanwise vorticity, $\omega_y = \pm 70$ s^{-1} (red and blue), and also isosurfaces of streamwise vorticity, $\omega_x = \pm 70$ s^{-1} (green and yellow). The interpretation of the instantaneous organization of the flow field, from the reference solution, has already been discussed in section 6.2.4. Linear interpolation fails to represent the shear layers and most of the streamwise-oriented vortical structures. In general, the solution is strongly affected by the spatial differentiation operator required for the visualization of the vorticity field. The VIC# algorithm produces a solution that appears contaminated by the presence of small structures, arguably due to the fact that the grid resolution has been chosen beyond the presence of particle trajectories, causing an ill-posed minimization problem. The IMR reconstruction shows better agreement with the reference, but certain features are worth being discussed. While the vorticity in the shear layers and the main rollers are accurately reconstructed, some of the *ribs* (green and yellow structures) do not appear in the reconstructed flow field (especially for $x > 400$ mm), likely because their representation involves higher-order modes. On the other hand, some structures are introduced that do not find a correspondence in the reference case (around $x = 300$ mm and $y = 200$ mm), arguably because they do appear in other shedding cycles of the full acquisition. In general, this situation highlights the capabilities of IMR in reconstructing instantaneous vortical structures that are not accurately sampled by the

particle trajectories but at the same time the difficulty of dealing with certain turbulent events for which providing a statistical description is challenging.

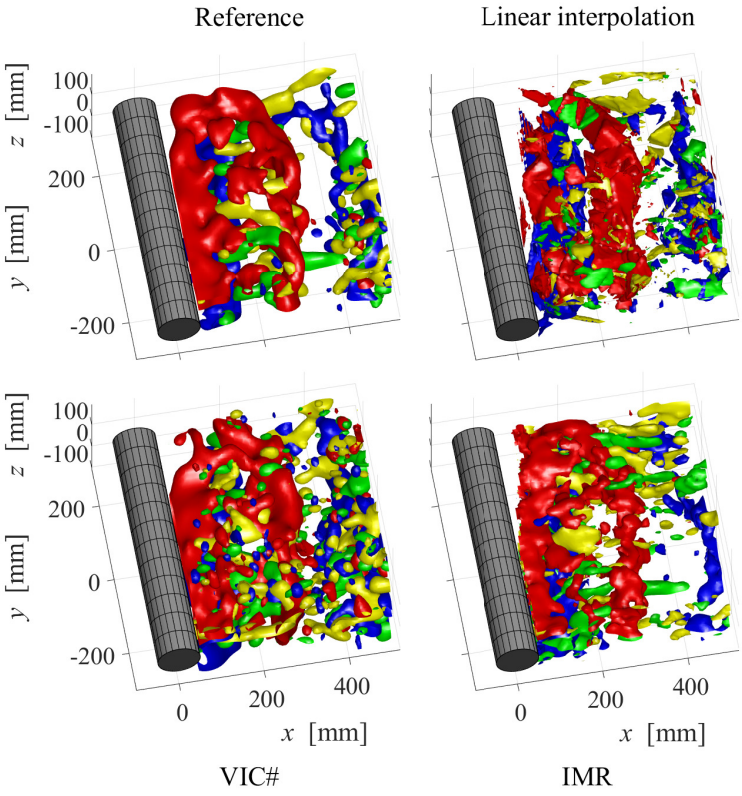

Figure 6.19: Instantaneous visualization of the three-dimensional flow field using isosurfaces of spanwise (red and blue, ω_y = ±70 s^{-1}) and streamwise (green and yellow, ω_x = ±70 s^{-1}) vorticity, for the reference solution (top-left), linear interpolation (top-right), the VIC# algorithm (bottom-left) and IMR with r = 19 (bottom-right).

6.3.4. Statistical convergence of the IMR method

As for any modal-based reconstruction method, IMR relies on the statistical convergence of a series of flow events, represented by modes, with high-energy modes typically requiring less instantaneous realizations to converge. As discussed in section 6.2.3, the IMR method has been applied to a downsampled version of the LPT dataset, producing ten stacked sequences of n_{time} = 2,000 snapshots each. The obtained modal decomposition and instantaneous reconstruction are compared here to those extracted from considering only a subset of the total number of snapshots available.

The modal energy distributions are shown in figure 6.20, obtained from the POD decomposition of the reference flow field and the IMR method applied to $n_{time} = 2,000$, $n_{time} = 10,000$ and $n_{time} = 20,000$ snapshots. As expected, using more snapshots reduces the discrepancy with respect to the reference. The first two modes converge rather well, while the discrepancy increases for higher-order ones. After approximately mode number ten, the three IMR curves show a parallel trend, as dictated by the noise level of the experimental dataset (Cortina-Fernández *et al.*, 2021).

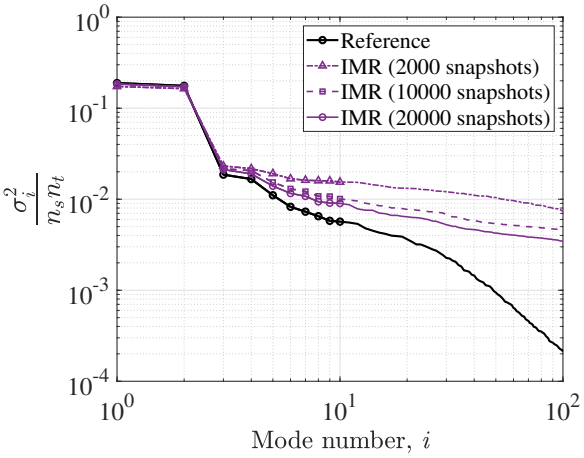

Figure 6.20: Comparison of the grid-independent modal energy contribution of the first 100 POD modes obtained from the reference POD decomposition and the IMR method applied to $n_{time} = 2,000$, $n_{time} = 10,000$ and $n_{time} = 20,000$ snapshots.

The effect of the number of snapshots in the reconstructed velocity field is studied by comparing the mean reconstruction error with respect to the reference, shown in figure 6.21 (left), and the time- and spanwise-averaged streamwise spectra of vertical velocity, shown in figure 6.21 (right). The mean error trends demonstrate that improving the statistical convergence of the decomposition allows not only reducing the global error but also makes it possible to include more modes in the reconstruction before they become too much affected by random noise. The latter is confirmed by looking at the spectra, obtained using $r = 20$ for every situation. For the case $n_{time} = 2,000$ snapshots, a strong overestimation of the medium and small-scale contributions is observed, direct consequence of the presence of noise in some of the modes employed for the reconstruction.

The analysis of the statistical convergence of IMR highlights one of the main limitations of the proposed methodology, which is inherent to experimental time-resolved measurements. The sequence of $n_{time} = 2,000$ snapshots considered in this study does only capture approximately eight shedding cycles (see figure 6.15). While the high acquisition frequency is necessary for particle tracking, the resulting snapshots are strongly correlated (Sciacchitano & Wieneke, 2016). For modal-based reconstruction

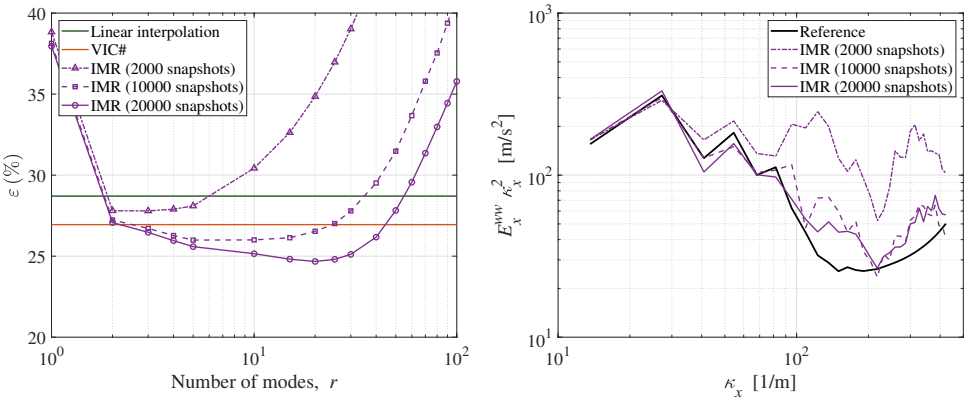

Figure 6.21: Comparison of the grid-independent modal energy contribution of the first 100 POD modes obtained from the reference POD decomposition and the IMR method applied to $n_{time} = 2,000$, $n_{time} = 10,000$ and $n_{time} = 20,000$ snapshots.

methods, it is advisable to collect more than one sequence of time-resolved information for improved statistical convergence. This will especially affect higher-order modes and would make possible extending the IMR method to spectrally richer flows.

6.4. Conclusions

A method has been proposed for the dense reconstruction of the three-dimensional velocity field from sparse measurements obtained with LPT. The IMR technique leverages upon the principle of proper orthogonal decomposition in a similar way as introduced recently with DEPTV. However, attention is placed on the consistency of the temporal coefficients, alongside that of the spatial modes. This result is obtained by iteratively projecting the initial temporal and spatial POD modes onto the measured particles velocity field. The higher level of spatial resolution is used to build a reduced order model from the dataset.

The IMR method is evaluated on experimental data obtained in the turbulent wake of a circular cylinder and a comparison is afforded with existing approaches, based on linear interpolation, local averaging (binning) and data assimilation (VIC#). Furthermore, the method is compared to the existing modal-based DEPTV method. The data is artificially coarsened by sub-sampling the particle tracers, such to yield a low-concentration measurement, to compare all methods, whereas the data at the original higher resolution is used to provide a reference.

The spatial modes obtained using IMR follow with good fidelity the reference data for the first 8 entries and cumulative energy of 75%. Furthermore, the phase relations between pairs contributing to the same fluid dynamic mode are more clearly restored with the IMR algorithm, compared to DEPTV. This condition entitles to a robust interpretation of the modes and their combination into pairs, when dealing with

convective instabilities. Besides, the iterative approach allows recovering the shape of the temporal coefficients that were not captured by the initial window-based averaging approach. This shows that IMR has potential to recover information at spatial scales comparable to the inter-particle distance of the LPT dataset.

A reduced order model is built using the first 20 modes, yielding with clarity the main motions exhibited in the unsteady flow and in good agreement with the reference high-resolution data. The obtained flow field shows that IMR can correctly model the shear layers on both sides of the cylinder, the main spanwise-coherent shed vortices and also the smaller streamwise-oriented structures interconnecting those. In general, the method outperforms the state-of-the-art data assimilation methodologies in terms of reconstruction error, spatial spectra, and coherence of the reconstruction. Future works will explore the applicability of the method to other flow problems featuring a broader distribution of the modal energy.

References

Agüera, N., Cafiero, G., Astarita, T., & Discetti, S. (2016). Ensemble 3D PTV for high resolution turbulent statistics. *Measurement Science and Technology*, *27*(12). https://doi.org/10.1088/0957-0233/27/12/124011

Boomsma, A., Bhattacharya, S., Troolin, D., Pothos, S., & Vlachos, P. (2016). A comparative experimental evaluation of uncertainty estimation methods for two-component PIV. *Measurement Science and Technology*, *27*(9). https://doi.org/10.1088/0957-0233/27/9/094006

Borée, J. (2003). Extended proper orthogonal decomposition: A tool to analyse correlated events in turbulent flows. *Experiments in Fluids*, *35*(2), 188–192. https://doi.org/10.1007/s00348-003-0656-3

Bosbach, J., Kühn, M., & Wagner, C. (2009). Large scale particle image velocimetry with helium filled soap bubbles. *Experiments in Fluids*, *46*(3), 539–547. https://doi.org/10.1007/s00348-008-0579-0

Brindise, M. C., & Vlachos, P. P. (2017). Proper orthogonal decomposition truncation method for data denoising and order reduction. *Experiments in Fluids*, *58*(4), 1–18. https://doi.org/10.1007/s00348-017-2320-3

Cai, S., Gray, C., & Karniadakis, G. E. (2024). Physics-Informed Neural Networks Enhanced Particle Tracking Velocimetry: An Example for Turbulent Jet Flow. *IEEE Transactions on Instrumentation and Measurement*, *73*, 1–9. https://doi.org/10.1109/TIM.2024.3398068

Cattell, R. B. (1966). The Scree Test for the number of factors. *Multivariate Behavioral Research*, *1*(2), 245–276. https://doi.org/10.1207/s15327906mbr0102

Cortina-Fernández, J., Sanmiguel Vila, C., Ianiro, A., & Discetti, S. (2021). From sparse data to high-resolution fields: ensemble particle modes as a basis for high-resolution flow characterization. *Experimental Thermal and Fluid Science*, *120*(May 2020), 110178. https://doi.org/10.1016/j.expthermflusci.2020.110178

Cowen, E. A., & Monismith, S. G. (1997). A hybrid digital particle tracking velocimetry technique. *Experiments in Fluids*, *22*(3), 199–211. https://doi.org/10.1007/s003480050038

Eckart, C., & Young, G. (1936). The approximation of one matrix by another of lower rank. *Psychometrika*, *1*(3), 211–218. https://doi.org/10.1007/BF02288367

Epps, B. P., & Krivitzky, E. M. (2019). Singular value decomposition of noisy data: noise filtering. *Experiments in Fluids*, *60*(8), 1–23. https://doi.org/10.1007/s00348-019-2768-4

Gavish, M., & Donoho, D. L. (2014). The optimal hard threshold for singular values is $4/\sqrt{3}$. *IEEE Transactions on Information Theory*, *60*(8), 5040–5053. https://doi.org/10.1109/TIT.2014.2323359

Giaquinta, D. (2018). *The Flow Topology of the Ahmed Body in Cross-Wind* [Doctoral dissertation, TU Delft].

Grille Guerra, A., Sciacchitano, A., & Scarano, F. (2024). Iterative modal reconstruction for sparse particle tracking data. *Physics of Fluids*, *36*(7). https://doi.org/10.1063/5.0209527

Jeon, Y. J., Müller, M., & Michaelis, D. (2022). Fine scale reconstruction (VIC#) by implementing additional constraints and coarse-grid approximation into VIC+. *Experiments in Fluids*, *63*(4), 1–24. https://doi.org/10.1007/s00348-022-03422-9

Kähler, C. J., Scharnowski, S., & Cierpka, C. (2012). On the resolution limit of digital particle image velocimetry. *Experiments in Fluids*, *52*(6), 1629–1639. https://doi.org/10.1007/s00348-012-1280-x

Kanaris, N., Grigoriadis, D., & Kassinos, S. (2011). Three dimensional flow around a circular cylinder confined in a plane channel. *Physics of Fluids*, *23*(6). https://doi.org/10.1063/1.3599703

Lignarolo, L. E., Ragni, D., Krishnaswami, C., Chen, Q., Simão Ferreira, C. J., & van Bussel, G. J. (2014). Experimental analysis of the wake of a horizontal-axis wind-turbine model. *Renewable Energy*, *70*, 31–46. https://doi.org/10.1016/j.renene.2014.01.020

Ma, X., & Karniadakis, G. E. (2002). A low-dimensional model for simulating three-dimensional cylinder flow. *Journal of Fluid Mechanics*, *458*, 181–190. https://doi.org/10.1017/S0022112002007991

Mendez, M. A., Balabane, M., & Buchlin, J.-M. (2019). Multi-scale proper orthogonal decomposition of complex fluid flows. *Journal of Fluid Mechanics*, *870*, 988–1036. https://doi.org/10.1017/jfm.2019.212

Parnaudeau, P., Carlier, J., Heitz, D., & Lamballais, E. (2008). Experimental and numerical studies of the flow over a circular cylinder at Reynolds number 3900. *Physics of Fluids*, *20*(8). https://doi.org/10.1063/1.2957018

Prasad, A., & Williamson, C. H. K. (1997). Three-dimensional effects in turbulent bluff-body wakes. *Journal of Fluid Mechanics*, *343*, 235–265. https://doi.org/10.1017/S002211209700579X

Raben, S. G., Charonko, J. J., & Vlachos, P. P. (2012). Adaptive gappy proper orthogonal decomposition for particle image velocimetry data reconstruction. *Measurement Science and Technology*, *23*(2). https://doi.org/10.1088/0957-0233/23/2/025303

Raiola, M., Discetti, S., & Ianiro, A. (2015). On PIV random error minimization with optimal POD-based low-order reconstruction. *Experiments in Fluids*, *56*(4). https://doi.org/10.1007/s00348-015-1940-8

Scarano, F., & Poelma, C. (2009). Three-dimensional vorticity patterns of cylinder wakes. *Experiments in Fluids*, *47*(1), 69–83. https://doi.org/10.1007/s00348-009-0629-2

Scarano, F., Schneiders, J. F. G., Saiz, G. G., & Sciacchitano, A. (2022). Dense velocity reconstruction with VIC-based time-segment assimilation. *Experiments in Fluids*, *63*(6), 96. https://doi.org/10.1007/s00348-022-03437-2

Schanz, D., Gesemann, S., & Schröder, A. (2016). Shake-The-Box: Lagrangian particle tracking at high particle image densities. *Experiments in Fluids*, *57*(5), 70. https://doi.org/10.1007/s00348-016-2157-1

Schanz, D., Gesemann, S., Schröder, A., Wieneke, B., & Novara, M. (2013). Non-uniform optical transfer functions in particle imaging: Calibration and application to tomographic reconstruction. *Measurement Science and Technology*, *24*(2). https://doi.org/10.1088/0957-0233/24/2/024009

Schneiders, J. F., Dwight, R. P., & Scarano, F. (2014). Time-supersampling of 3D-PIV measurements with vortex-in-cell simulation. *Experiments in Fluids*, *55*(3). https://doi.org/10.1007/s00348-014-1692-x

Schneiders, J. F., & Scarano, F. (2016). Dense velocity reconstruction from tomographic PTV with material derivatives. *Experiments in Fluids*, *57*(9), 1–22. https://doi.org/10.1007/s00348-016-2225-6

Sciacchitano, A., Neal, D. R., Smith, B. L., Warner, S. O., Vlachos, P. P., Wieneke, B., & Scarano, F. (2015). Collaborative framework for PIV uncertainty quantification: comparative assessment of methods. *Measurement Science and Technology*, *26*(7), 074004. https://doi.org/10.1088/0957-0233/26/7/074004

Sciacchitano, A., & Scarano, F. (2014). Elimination of PIV light reflections via a temporal high pass filter. *Measurement Science and Technology*, *25*(8), 084009. https://doi.org/10.1088/0957-0233/25/8/084009

Sciacchitano, A., & Wieneke, B. (2016). PIV uncertainty propagation. *Measurement Science and Technology*, *27*(8). https://doi.org/10.1088/0957-0233/27/8/084006

Sciacchitano, A., Wieneke, B., & Scarano, F. (2013). PIV uncertainty quantification by image matching. *Measurement Science and Technology*, *24*(4). https://doi.org/10.1088/0957-0233/24/4/045302

Sirovich, L. (1987). Turbulence and the dynamics of coherent structures. III. Dynamics and scaling. *Quarterly of Applied Mathematics*, *45*(3), 583–590. https://doi.org/10.1090/qam/910464

Szepessy, S., & Bearman, P. W. (1992). Aspect ratio and end plate effects on vortex shedding from a circular cylinder. *Journal of Fluid Mechanics*, *234*(-1), 191. https://doi.org/10.1017/S0022112092000752

Tirelli, I., Ianiro, A., & Discetti, S. (2023). A simple trick to improve the accuracy of PIV/PTV data. *Experimental Thermal and Fluid Science*, *145*, 1–6. https://doi.org/10.1016/j.expthermflusci.2023.110872

Venturi, D., & Karniadakis, G. E. (2004). Gappy data and reconstruction procedures for flow past a cylinder. *Journal of Fluid Mechanics*, *519*, 315–336. https://doi.org/10.1017/S0022112004001338

Wang, Z., Akhtar, I., Borggaard, J., & Iliescu, T. (2012). Proper orthogonal decomposition closure models for turbulent flows: A numerical comparison.

Computer Methods in Applied Mechanics and Engineering, *237-240*, 10–26. https://doi.org/10.1016/j.cma.2012.04.015

Wieneke, B. (2008). Volume self-calibration for 3D particle image velocimetry. *Experiments in Fluids*, *45*(4), 549–556. https://doi.org/10.1007/s00348-008-0521-5

Williamson, C. H. (1996). Vortex dynamics in the cylinder wake. *Annual Review of Fluid Mechanics*, *28*, 477–539. https://doi.org/10.1146/annurev.fl.28.010196.002401

Zhang, Q., Liu, Y., & Wang, S. (2014). The identification of coherent structures using proper orthogonal decomposition and dynamic mode decomposition. *Journal of Fluids and Structures*, *49*, 53–72. https://doi.org/10.1016/j.jfluidstructs.2014.04.002

7

Conclusions and perspectives

This chapter summarizes the key conclusions of the dissertation and provides indicative lines of future research to complement and expand the findings discussed in this document. The chapter is divided into different components of the typical PIV measurement chain, in analogy to the main body of the thesis. Tracer particles are discussed in section 7.1, focusing on the role of HFSB for volumetric applications in air flows. Section 7.2 covers the design of large-scale 3D PIV systems, which includes the choice of hardware, calibration procedures, recording strategy, treatment of light reflections and processing algorithm. Finally, the topic of data reduction techniques is included in section 7.3.

7.1. Tracer particles

The use of HFSB in large wind-tunnel facilities has now been reported for several applications. Arrays hosting hundreds of generators can be placed in the settling chamber of the wind tunnel facility, to uniformly seed the flow in relatively large areas with minimal intrusion. For instance, Terra *et al.* (2024) report the use of a 2 m^2 seeder hosting 400 generators, permanently installed in the settling chamber of the Open Jet Facility (OJF) at the Faculty of Aerospace Engineering of TU Delft. An even bigger array, of 9 m^2, and also encompassing 400 generators, was used by Faleiros (2021) at the Large Low-speed Facility (LLF) of the German-Dutch Wind Tunnels (DNW). In both cases, HFSB with a diameter of approximately 0.5 mm were considered, based on generators evolved from the one proposed by Bosbach *et al.* (2009). As demonstrated in chapter 3, minimal variations in the generator's geometry are sufficient to obtain bubbles with diameters ranging from approximately 100 µm to a few millimetres. A new generation of HFSB seeders can be envisioned where the bubble diameter is chosen to be tailored to the experimental facility. Smaller bubbles may be preferred at research facilities of moderate size and speeds for improved spatial resolution, whereas bigger bubbles are more suitable for industrial facilities, to alleviate the constraints imposed by the large distances between illumination, tracers and imaging.

For wind tunnels of the Göttingen type (closed-loop), as is typically the case for large-scale industrial ones, HFSB produced in the settling chamber of the facility will continue to travel downstream of the test section. Most will burst when hitting small mesh elements (in the heat exchanger or turbulence-reduction meshes), generating a residue from the bubble fluid solution. Countermeasures such as bubble capturing are to be explored to ensure a smooth and sustainable operation of the facility. To minimize the impact of large seeding generators, a partitioning of the array into independently operated subdomains would be beneficial. Seeding could be produced only in regions of interest for a given wind tunnel model, lowering the use of materials, simplifying the image processing and reducing the overall impact on the facility.

Aside from large seeding arrays inside low-speed wind tunnels, the light scattering capabilities of HFSB offer other possibilities for volumetric PIV applications in air flows. A single HFSB generator can be used as a flow visualization tool, producing a streakline similar to that commonly observed using smoke visualization (van Dyke, 1982). Compared to smoke, which may dissipate due to turbulence, reducing the observability, individual HFSB tracers are clearly visible when illuminated with common LED light sources from a short distance. A possible approach is the integration of an HFSB generator onto a hand-held aerodynamically-shaped device, as depicted in figure 7.1(left), for easy manipulation inside a wind tunnel facility. As discussed by Barcinski (2024), this approach allows for easy inspection of stagnation regions, flow separation, or vortical structures. When combined with the high-speed recording capabilities present in most of nowadays smartphones, the method has the potential to become a powerful tool for educational purposes.

The development of small HFSB, in the order of 100 µm diameter, makes them more suitable for the study of wall-bounded flows, of paramount relevance in aerodynamics. Existing HFSB arrays, placed in the settling chamber of the wind tunnel, are not ideal for this application, since they uniformly seed a big volume instead of just the region close

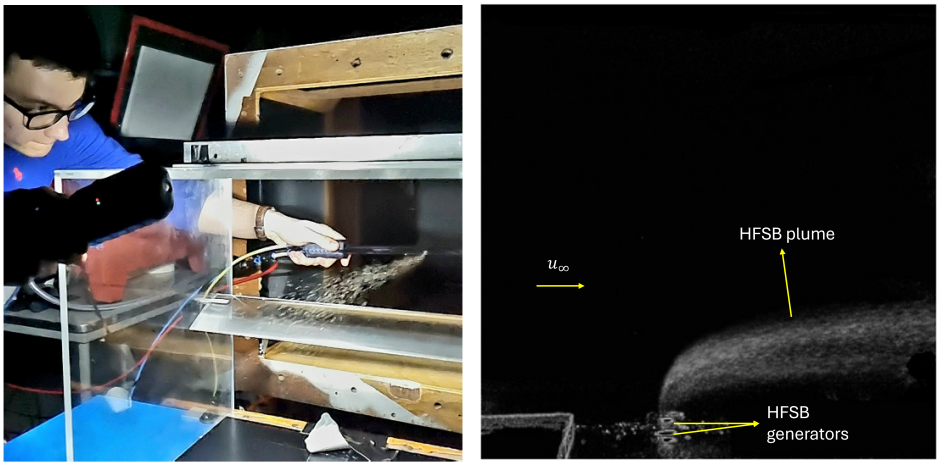

Figure 7.1: Alternative applications of HFSB. Left: hand-held bubble generator for flow visualization inside a wind tunnel facility, reproduced from Barcinski (2024). Right: wall-mounted bubble generators for near-wall inspection, adapted from Somlai (2025).

to the wall. Alternative configurations can be used for this purpose, as for instance, embedding the HFSB generators in the wall, to maximize the seeding concentration close to it. Following this approach, Somlai (2025) reported a concentration of approximately 25 bubbles/cm^3 in the near-wall region, for a freestream velocity of 10 m/s. A picture of the HFSB evolution close to the outlet of the generator is reproduced in figure 7.1(right). Smaller bubbles may also provide a higher level of tracing fidelity, offering a reduced slip velocity compared to what is reported in the literature for those in the millimetre range (Faleiros *et al.*, 2021). This is not only beneficial for low-speed applications requiring high levels of precision in the determination of velocity, but may also enable the use of HFSB in the compressible regime, thus opening a wide range of opportunities for volumetric PIV investigations.

7.2. Large-scale 3D PIV systems

The OA-LPT framework (Wieneke & Rockstroh, 2024) has enabled volumetric PIV investigations around complex objects using a redundant system of cameras with high tomographic aperture between them (Hendriksen *et al.*, 2024; Hysa *et al.*, 2024). Compared to robotic volumetric PIV (Jux *et al.*, 2018), where optical access around the model is obtained by traversing the velocimeter around it, OA-LPT allows for the use of a static system, where the redundancy in the number of imagers considered guarantees optical access throughout the domain of interest. This implies not only an improved triangulation and tracking accuracy from the higher tomographic aperture, but also depicts a PIV system that is more robust to the appearance of light reflections, as discussed in chapter 4. The efficiency of the system is also significantly improved

without the need for a scanning procedure.

For a large-scale wind tunnel facility, a possible implementation of such a system is the recently introduced Omnidirectional PIV (Omni-PIV, Hendriksen *et al.*, 2025). In Omni-PIV, groups of cameras are arranged together in so-called *antennas*. These have fixed optics (focal length and f-number) and can be calibrated independently, prior to the wind tunnel experiments. System calibration is typically performed by traversing a planar target throughout the domain of interest, using robust camera models such as the pinhole one, later refined by volume self-calibration (VSC, Wieneke, 2008). In Omni-PIV, independently calibrated *antennas* are coupled together once placed in their final position, by finding the transformation matrix linking their calibration from the triangulation of a series of points in space. This is particularly useful for situations where the wind tunnel model cannot be easily removed, and the PIV calibration must be performed with the object in place, complicating the simultaneous view of a calibration target from various directions. A recent example of an Omni-PIV experimental set-up inside the OJF wind tunnel of the TU Delft is shown in figure 7.2, for the case of a two-blade propeller mounted on a robotic arm.

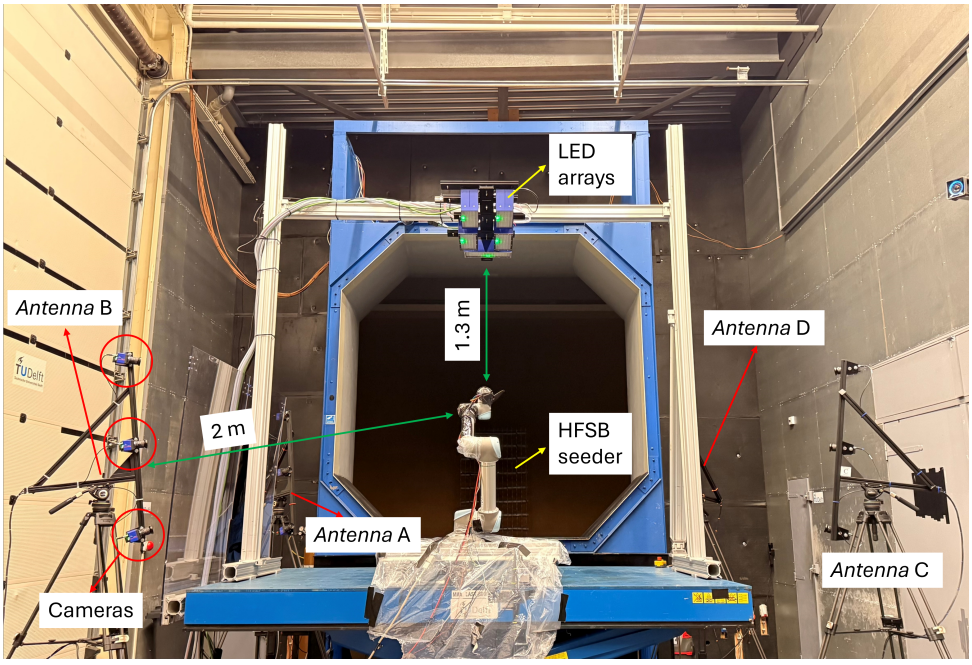

Figure 7.2: Omnidirectional PIV set-up inside the OJF of the TU Delft. Measurements around a two-blade propeller, mounted on a robotic arm. The PIV system consists of four *antennas* of three cameras each. Illumination is provided by LED arrays placed above the propeller, and the flow is seeded with HFSB. Picture courtesy of A. Garofano Soldado, from the Flow Physics and Technology department of the Faculty of Aerospace Engineering of TU Delft.

The experiment involves the use of a large HFSB seeding generator installed in the settling chamber of the wind tunnel, LED arrays for volumetric illumination around the propeller and four *antennas* hosting three cameras each. An *antenna* consists of a simple structure on which three cameras are mounted, separated by 50 cm between them, and resting on a camera tripod for easy manipulation. When placed at the correct distance from the domain of interest, each *antenna* will be looking at a region of approximately 1 m^3.

The degree of redundancy considered (a total of 12 cameras) is hardly conceivable if combined with high-speed imagers, heavy and expensive, as typically employed for LPT investigations (Schröder & Schanz, 2023). Instead, low repetition rate cameras are suggested, which implies a change in the recording strategy from the multi-frame single-exposure option to the alternatives discussed in chapter 5. Beyond the common double-frame single-exposure, it is shown that multi-exposure recording strategies offer a significant advantage in terms of velocity and acceleration dynamic ranges, and enable the estimation of instantaneous pressure in the domain of interest. These alternatives are ideal for large-scale scenarios involving the use of HFSB, since their concentration in the camera images is typically in the order of ppp ~ 0.01, thus allowing for placing several illumination pulses in a frame without compromising the triangulation accuracy.

The Omni-PIV system illustrated in figure 7.2 consists of LaVision *CX3*-5 CMOS cameras, with repetition rates in the range of 100 - 500 Hz, depending on bit-depth and resolution. While this is insufficient to perform time-resolved measurements at the typical speeds of operation of the OJF (10 - 20 m/s), the low optical magnification of the system (M < 0.01) means that a slight boost in the recording frequency would be able to close the gap. A multi-frame multi-exposure recording strategy, as the one illustrated in figure 7.3, could be envisioned to use the multi-exposure framework as a frequency boost for the imaging system, enabling time-resolved measurements with low repetition rate cameras. This would maximize the velocity and acceleration dynamic ranges, enable inspection of the flow dynamics and benefit from the tracking aid of the predictor-corrector scheme associated with the STB algorithm (Schanz *et al.*, 2016).

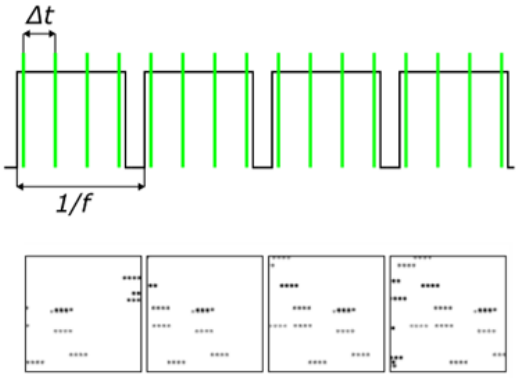

Figure 7.3: Template of illumination pulses and camera exposure, with corresponding image details, for a multi-frame multi-exposure recording strategy.

7.3. Data reduction

The scattered particle trajectories obtained from LPT measurements (or scattered velocity and acceleration vectors from double-frame or multiple-exposure recording strategies) provide a well-suited input basis for data assimilation techniques, aiming at providing a representation of the 3D flow field at high spatial resolution, which includes not only the velocity field but also vorticity or pressure. Adding to existing variational approaches (mostly adjoint CFD schemes), statistics-based methods (POD), or others like VIC+ (Schneiders & Scarano, 2016) or FlowFit (Gesemann *et al.*, 2016), a relevant appearance has been the recent application of Physics Informed Neural-Networks (PINNs) to fluid mechanics (Cai *et al.*, 2021). At a higher computational cost, PINNs have been shown to be superior to existing data assimilation schemes in terms of reconstruction error and spatial resolution (Zhou *et al.*, 2024).

While most of these methods are tailored to time-resolved data (long particle trajectories), enforcing the Navier-Stokes equations as constraints, a statistics-based approach has been discussed in chapter 6 that makes use of velocity information only, as obtained with a low repetition rate volumetric PIV system, envisioned for large-scale industrial applications. Recordings of statistically converged velocity information can be used to enhance the spatial resolution of the instantaneous representation of the flow field, aiding the interpretation of the flow dynamics. Future work may incorporate the Lagrangian acceleration information obtained from multi-exposure recordings, or even combine the statistical framework with other machine learning schemes to add the physical constraints as well, thus maximizing the use of available information from a recording set.

The relevance of data reduction techniques in the research community is evident from the appearance of data assimilation challenges (Leclaire *et al.*, 2021; Sciacchitano *et al.*, 2025; Sciacchitano *et al.*, 2021) as an evaluation tool. Currently, the 2nd data assimilation challenge is ongoing. Preliminary results were already presented in the summer of 2025 in conjunction with the ISFV and ISPIV symposiums in Tokyo, whereas the final output will be presented at the 22nd International Symposium on Applications of Laser and Imaging Techniques to Fluid Mechanics, to be held in the summer of 2026 in Lisbon. The first case of the challenge, provided by the TU Delft, consists of synthetic particle track data advected along a time-series of DNS of a turbulent flow in a square channel (Pirozzoli *et al.*, 2018). Not only is time-resolved information considered, but also cases for double-frame single-exposure recordings and even multi-exposure situations (double-frame, double-exposure, Novara *et al.*, 2019), for varying seeding densities. Several research groups participated in the challenge, as illustrated in figure 7.4.

Apart from the ground truth solution and the linear interpolation one, provided by the organizers, ten different participants contributed to the time-resolved situation of the first case. The approaches considered are quite different, although PINNs are already predominant, with four different research groups opting for that direction. The obtained results are also quite different, highlighting the complexity of the challenge. Figure 7.4(bottom) includes contours of vorticity magnitude in a plane close to the wall, for the highest seeding density condition provided (ppp = 0.2). Even with the aid of high particle concentrations, most contributions fail to represent the small-scale vortical

structures in the near-wall region. Resolving all scales of turbulent flow at high Reynolds numbers remains a challenge, certainly still beyond the state-of-the-art of volumetric PIV hardware and software.

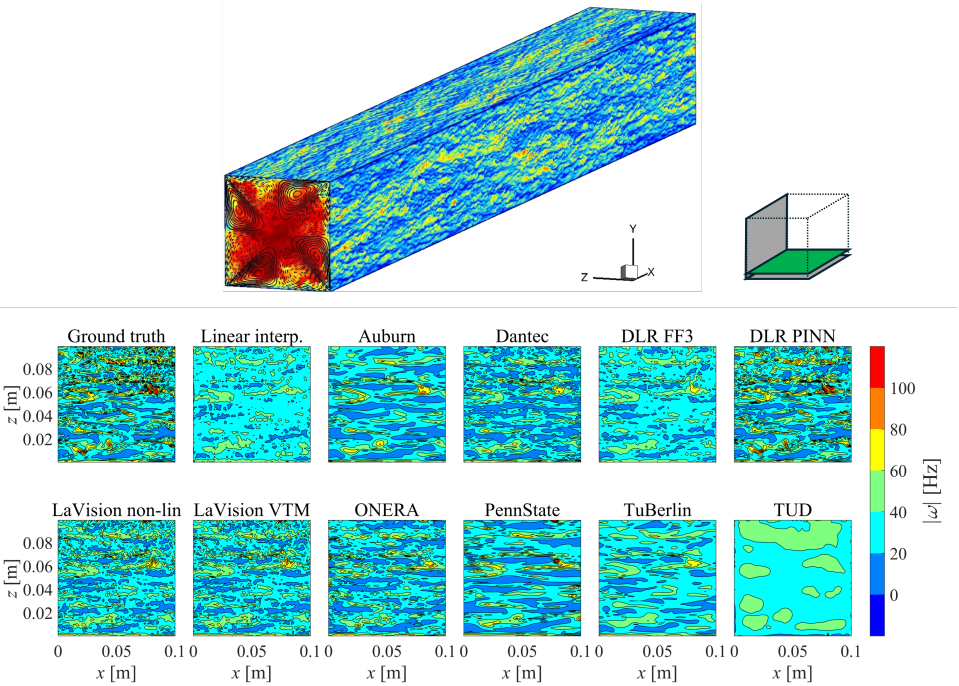

Figure 7.4: DNS simulation of a square duct turbulent flow considered for the first case of the 2nd data assimilation challenge (top), and contours of vorticity magnitude in a plane close to the wall, as submitted by the participants (bottom).

References

Barcinski, J. (2024). *A Novel Approach to Flow Visualization using HFSB* (tech. rep.). Delft University of Technology.

Bosbach, J., Kühn, M., & Wagner, C. (2009). Large scale particle image velocimetry with helium filled soap bubbles. *Experiments in Fluids*, *46*(3), 539–547. https://doi.org/10.1007/s00348-008-0579-0

Cai, S., Mao, Z., Wang, Z., Yin, M., & Karniadakis, G. E. (2021). Physics-informed neural networks (PINNs) for fluid mechanics: a review. *Acta Mechanica Sinica*, *37*(12), 1727–1738. https://doi.org/10.1007/s10409-021-01148-1

Faleiros, D. E. (2021). *Soap bubbles for large-scale PIV Generation, control and tracing accuracy* [Doctoral dissertation, Delft University of Technology]. https://doi.org/10.4233/uuid:c579128f-9e96-4e9e-9997-6ce9486e1e25

Faleiros, D. E., Tuinstra, M., Sciacchitano, A., & Scarano, F. (2021). The slip velocity of nearly neutrally buoyant tracers for large-scale PIV. *Experiments in Fluids*, *62*(9), 1–24. https://doi.org/10.1007/s00348-021-03274-9

Gesemann, S., Huhn, F., Schanz, D., & Schröder, A. (2016). From Particle Tracks to Velocity, Acceleration and Pressure Fields Using B-Splines and Penalties. *18th International Symposium on the Application of Laser and Imaging Techniques to Fluid Mechanics*. http://arxiv.org/abs/1510.09034

Hendriksen, L. A., Grille Guerra, A., Sciacchitano, A., & Scarano, F. (2025). Omnidirectional Particle Image Velocimetry. *Proceedings of the 16th International Symposium on Particle Image Velocimetry*.

Hendriksen, L. A., Sciacchitano, A., & Scarano, F. (2024). Object registration techniques for 3D particle tracking. *Measurement Science and Technology*, *35*(12). https://doi.org/10.1088/1361-6501/ad715c

Hysa, I., Tuinstra, M., Sciacchitano, A., Scarano, F., van der Meulen, M. J., Rockstroh, T., & Roosenboom, E. W. (2024). A multi-directional redundant 3D-LPT system for ship–flight–deck wind interactions. *Experiments in Fluids*, *65*(8), 1–15. https://doi.org/10.1007/s00348-024-03867-0

Jux, C., Sciacchitano, A., Schneiders, J. F., & Scarano, F. (2018). Robotic volumetric PIV of a full-scale cyclist. *Experiments in Fluids*, *59*(4), 1–15. https://doi.org/10.1007/s00348-018-2524-1

Leclaire, B., Mary, I., Liauzun, C., Péron, S., Sciacchitano, A., Schröder, A., Cornic, P., & Champagnat, F. (2021). First challenge on Lagrangian Particle Tracking and Data Assimilation: datasets description and planned evolution to an open online benchmark. *14th International Symposium on Particle Image Velocimetry*, *1*(1), 1–2. https://doi.org/10.18409/ispiv.v1i1.119

Novara, M., Schanz, D., Geisler, R., Gesemann, S., Voss, C., & Schröder, A. (2019). Multi-exposed recordings for 3D Lagrangian particle tracking with Multi-Pulse Shake-The-Box. *Experiments in Fluids*, *60*(3), 1–19. https://doi.org/10.1007/s00348-019-2692-7

Pirozzoli, S., Modesti, D., Orlandi, P., & Grasso, F. (2018). Turbulence and secondary motions in square duct flow. *Journal of Fluid Mechanics*, *840*, 631–655. https://doi.org/10.1017/jfm.2018.66

Schanz, D., Gesemann, S., & Schröder, A. (2016). Shake-The-Box: Lagrangian particle tracking at high particle image densities. *Experiments in Fluids*, *57*(5), 70. https://doi.org/10.1007/s00348-016-2157-1

Schneiders, J. F., & Scarano, F. (2016). Dense velocity reconstruction from tomographic PTV with material derivatives. *Experiments in Fluids*, *57*(9), 1–22. https://doi.org/10.1007/s00348-016-2225-6

Schröder, A., & Schanz, D. (2023). 3D Lagrangian Particle Tracking in Fluid Mechanics. *Annual Review of Fluid Mechanics*, *55*(1), 511–540. https://doi.org/10.1146/annurev-fluid-031822-041721

Sciacchitano, A., Leclaire, B., & Schröder, A. (2025). On the accuracy of data assimilation algorithms for dense flow field reconstructions. *Experiments in Fluids*, *66*(2), 1–28. https://doi.org/10.1007/s00348-025-03969-3

Sciacchitano, A., Leclaire, B., & Schroeder, A. (2021). Main results of the first Lagrangian Particle Tracking Challenge. *14th International Symposium on Particle Image Velocimetry*, *1*(1). https://doi.org/10.18409/ispiv.v1i1.197

Somlai, V. (2025). *Investigation of small-sized HFSB and AFSB generation for PTV & PIV measurements* (tech. rep.). Delft University of Technology.

Terra, W., Brown, C., Vloemans, S., van der Waals, M., Sciacchitano, A., Burton, D., Thompson, M. C., & Huysmans, T. (2024). A Generic Cyclist Model for aerodynamic investigation: Design, geometry & first aerodynamic analysis of a male time-trial and sprint model. *Journal of Wind Engineering and Industrial Aerodynamics*, *252*(July), 105829. https://doi.org/10.1016/j.jweia.2024.105829

van Dyke, M. (1982). *An Album of Fluid Motion* (Vol. 104). The Parabolic Press. https://doi.org/10.1115/1.3241909

Wieneke, B. (2008). Volume self-calibration for 3D particle image velocimetry. *Experiments in Fluids*, *45*(4), 549–556. https://doi.org/10.1007/s00348-008-0521-5

Wieneke, B., & Rockstroh, T. (2024). Lagrangian particle tracking in the presence of obstructing objects. *Measurement Science and Technology*, *35*(5), 055303. https://doi.org/10.1088/1361-6501/ad289d

Zhou, K., Grauer, S. J., Schanz, D., Godbersen, P., Schröder, A., Rockstroh, T., Jeon, Y. J., & Wieneke, B. (2024). Benchmarking Data Assimilation Algorithms For 3D Lagrangian Particle Tracking. *Proceedings of the International Symposium on the Application of Laser and Imaging Techniques to Fluid Mechanics*, *21*, 1–22. https://doi.org/10.55037/lxlaser.21st.229

Acknowledgements

After nearly 150 pages of modest contribution to the field of knowledge, the reader now encounters a section unrelated to PIV, but focused on something way more important: thanking all those who contributed to making this dissertation possible. Coming back to Delft after a few years abroad was an easy decision to make, I have always felt like at home surrounded by bicycles and a bit of rain. This book now closes a 4-year chapter of my life but, who knows how will the story continue?

I must start by thanking my promotor, prof. dr. *Fulvio Scarano*, the perfect example of academic inspiration. Your dedication and chase for perfection when it comes to writing, conducting experiments or coaching students has boosted my efforts during the PhD trajectory. Counting on your support has been very encouraging, and I loved our scientific disputes throughout this time. And what can I say about our brainstorming sessions? Initially a bit jealous about this incredible skill of yours, now just grateful I could have you by my side along this amazing path.

The research team could not be complete without my copromotor, dr. *Andrea Sciacchitano*. From the first day, we have shared crazy goals and ambitions. Your full support, patience and perseverance made my dream of conducting outdoor experiments on ground vehicles possible. Looking back, we started the journey with a toy RC-car, and ended up measuring a race car and a full-scale truck. Thank you as well for the opportunity of joining the organization of the DA-LPT challenge, where I could meet some of the top researchers in the field and learn from all of you.

To *Luuk Hendriksen*, for being a lot more than a colleague. I remember helping you out during your first experimental campaign, and now you have evolved to the point where our Omni-PIV baby, a.k.a. *"Luuk's system"*, is quickly gaining popularity within the faculty. You are now a PIV master, and I could not be any prouder about it. Thank you for the great moments we have shared during these years, from conducting experiments together to the road trips to a conference in Lisbon or a secret wind tunnel facility in the UK. I wish you the very best and would love to work with you again in the future.

To dr. *Edoardo Saredi*, whose persuasion made me accept this job. My biggest gratitude for solving the housing problem in Delft for me, and in general for your continuous support, positive attitude and insightful conversations throughout these years. I do not fully understand the faith you have deposited in me, and I also do not think I will ever be able to pay you back for all the favours, but be sure that I will try my best.

Thanks to the industrial partners supporting this project. Especially to *Paula García Ruiz* and *Joe Musson*, for your trust in our work and for being such good hosts. To dr. *Robbie Stevens*, for giving me my first opportunity. I wish you the best, although you will easily achieve it by yourselves.

To the great students I had the privilege of supervising during their MSc thesis project: *Josée Klappe*, *Andrea Battegazzore*, *Laura Porcar Galán*, *Coen Holland*, *Pablo Álvarez*

García and *Mark van der Klein*. Our experiments together give me the fondest memories of my PhD trajectory, and supervising your work has certainly been the most enjoyable activity of them all. Please feel this book as yours.

To the BSc students who bravely jumped into the development of HFSB technology as part of their honours programme: *Jakub Barciński*, *Valter Somlai* and *Slava Kovalyov*. I am still shocked by your determination and skills. I hope you enjoyed getting your hands 'dirty' in soap as much as I did. Feel proud of your effort and contribution. I will follow your career closely.

To all the scientific collaborators I had the honour of working with. To dr. *Daniel Schanz*, for giving me the chance of learning how to set up a STB experiment from the developer himself, during the early stages of my PhD in preparation for the 1st edition of the Masters of Flow Visualization. To dr. *Hyun Jin Park*, for making HFSB even more beautiful by adding colours to the experiments, and your valuable suggestions about Tokyo. To the colleagues from UC3M, dr. *Iacopo Tirelli*, dr. *Andrea Ianiro* and dr. *Stefano Discetti*, for sharing our same passion, providing great ideas to continue some lines of research, and making international symposiums a lot more enjoyable. To the organizers of the 2nd LPT and DA challenge, dr. *Andrea Sciacchitano*, dr. *Andreas Schröder*, dr. *Benjamin Leclaire*, dr. *Samuel Grauer*, dr. *Daniel Schanz* and *Philipp Godbersen*, for your warm welcome in the team, trust in my work and valuable scientific discussions. To dr. *Bernd Wieneke*, for your guidance and continuous feedback. It has been an absolute pleasure working with you during the last period of my PhD, and now I can proudly say there is a tiny bit of me inside *DaVis*.

None of the above would have been possible without the continuous support of those working at the FPT department and, in particular, at the HSL. To *Colette Russo*, *Peter Duyndam*, *Joost Clemens*, *Floris Blok*, dr. *Adam Head*, *Henk-Jan Siemer*, *Dennis Bruikman* and ir. *Frits Donker Duyvis*, for your work and availability. Special thanks to *Gert-Jan Berends*. I have learnt so much from you, always while having fun, and I hope I managed to teach you a few things about PIV as well.

My biggest gratitude to all my colleagues at the PhD office, and also those at the dark side of the moon, or LSL. Thank you for the spontaneous interactions during lunchtime, academic events or various celebrations. It has been an absolute pleasure walking this path together.

To my family, and especially my parents, *Rogelio* and *Emilia*, who have been my biggest support since I left home almost 12 years ago. Thank you for your understanding and love. Every time I visit, I keep wondering when to finally return. I hope you enjoy this book.

To *Luz*, for sharing life together. Thank you for joining me on this adventure in the Netherlands, and for your immense patience whilst listening to my PIV verbose. Above all, thank you for gifting me with our beloved *Manuela*, who joined us during the last stages of the PhD and has since contributed to the writing of this dissertation, by laying, sitting, crawling and finally standing by my side.

Adrián Grille Guerra
Delft, February 2026

Curriculum Vitæ

Adrian Grille Guerra

13-06-1996 Born in Santiago de Compostela, Spain

Education

2014–2018 Bachelor of Science, Aerospace Engineering
Universidad Politécnica de Madrid, Spain
Thesis: Plasma actuators for flow control

2018–2022 Master of Science, Aerospace Engineering, Aerodynamics
Delft University of Technology, The Netherlands
Thesis: Experimental investigation of a laminar separation bubble subjected to wing structural motion

2022–2026 PhD Aerospace Engineering
Delft University of Technology, The Netherlands

Professional experience

2019–2020 Internship, Aerodynamics Engineer
Renault Sport Racing F1 Team, United Kingdom

2021–2022 Research Technician
The University of Arizona, United States of America

List of Publications

Journal publications

11. **Grille Guerra, A.**, Battegazzore, A., Holland, C., Álvarez García, P. I., & Sciacchitano, A. Underbody ground-vehicle aerodynamics with the Ring-of-Fire. In preparation for *Experiments in Fluids*

10. Hendriksen, L. A., **Grille Guerra, A.**, Sciacchitano, A., & Scarano, F. Omnidirectional Particle Image Velocimetry. In preparation for *Measurement Science and Technology*

9. Park, H. J., **Grille Guerra, A.**, & Scarano, F. Color-based 3D particle tracking velocimetry using soap bubbles. Under review in *Experiments in Fluids*

8. Borgmann, D., **Grille Guerra, A.**, & Little, J. Physics and control of laminar separation bubbles subjected to unsteady structural motion. Under review in *AIAA Journal*

7. **Grille Guerra, A.**, Wieneke, B., & Scarano, F. On the accuracy of multi-exposure 3D-PTV. Accepted for publication in *Experiments in Fluids*

6. **Grille Guerra, A.**, Porcar Galán, L., Sciacchitano, A., & Scarano, F. (2025). Treatment of light reflections in 3D PIV systems. *Measurement Science and Technology, 36*(11), 115301

5. Tirelli, I., **Grille Guerra, A.**, Ianiro, A., Sciacchitano, A., Scarano, F., & Discetti, S. (2025). Full-domain POD modes from PIV asynchronous patches. *Experiments in Fluids, 66*(6), 105

4. Scarano, F., Hysa, I., **Grille Guerra, A.**, Tuinstra, M., & Sciacchitano, A. (2025). Asymmetric time sequence for multiple-exposure 3D PTV. *Experiments in Fluids, 66*(4), 74

3. **Grille Guerra, A.**, Sciacchitano, A., & Scarano, F. (2024). Iterative modal reconstruction for sparse particle tracking data. *Physics of Fluids, 36*(7), 075107

2. **Grille Guerra, A.**, Sciacchitano, A., & Scarano, F. (2024). On the scalability of helium-filled soap bubbles for volumetric PIV. *Experiments in Fluids, 65*(2), 23

1. **Grille Guerra, A.**, Mertens, C., Little, J., & van Oudheusden, B. W. (2023). Experimental characterization of an unsteady laminar separation bubble on a pitching wing. *Experiments in Fluids, 64*(1), 16

Conference proceedings and presentations

22. Álvarez García, P. I., **Grille Guerra, A.**, & Sciacchitano, A. On-site full-scale race car aerodynamics analysis using the Ring-of-Fire. *22nd International Symposium on Applications of Laser and Imaging Techniques to Fluid Mechanics*, Lisbon, Portugal, June 29 - July 2, 2026

21. Scarano, F., **Grille Guerra, A.**, & Wieneke, B. Time-resolved particle tracking using ME and low repetition-rate imagers. *22nd International Symposium on Applications of Laser and Imaging Techniques to Fluid Mechanics*, Lisbon, Portugal, June 29 - July 2, 2026

20. Sciacchitano, A., Godbersen, P., Grauer, S., **Grille Guerra, A.**, Leclaire, B., Schanz, D., & Schröder, A. Main results of the second LPT challenge. *22nd International Symposium on Applications of Laser and Imaging Techniques to Fluid Mechanics*, Lisbon, Portugal, June 29 - July 2, 2026

19. Schröder, A., Godbersen, P., Schanz, D., Sciacchitano, A., **Grille Guerra, A.**, Grauer, S., & Leclaire, B. Main results of the second DA challenge. *22nd International Symposium on Applications of Laser and Imaging Techniques to Fluid Mechanics*, Lisbon, Portugal, June 29 - July 2, 2026

18. **Grille Guerra, A.**, Porcar Galán, L., Sciacchitano, A., & Scarano, F. Treatment of light reflections in Omnidirectional PIV. *16th International Symposium on Particle Image Velocimetry*, Tokyo, Japan, June 26-28, 2025

17. **Grille Guerra, A.**, Wieneke, B., & Scarano, F. On the accuracy of multi-exposure 3D-PTV. *16th International Symposium on Particle Image Velocimetry*, Tokyo, Japan, June 26-28, 2025

16. Scarano, F., **Grille Guerra, A.**, & Wieneke, B. Detection of low-velocity traces in ME-PTV. *16th International Symposium on Particle Image Velocimetry*, Tokyo, Japan, June 26-28, 2025

15. Park, H. J., **Grille Guerra, A.**, & Scarano, F. Color 3D-PTV in air flows with HFSB. *16th International Symposium on Particle Image Velocimetry*, Tokyo, Japan, June 26-28, 2025

14. Hendriksen, L. A., **Grille Guerra, A.**, Sciacchitano, A., & Scarano, F. Omnidirectional Particle Image Velocimetry. *16th International Symposium on Particle Image Velocimetry*, Tokyo, Japan, June 26-28, 2025

13. Holland, C., **Grille Guerra, A.**, & Sciacchitano, A. On-site 3D LPT for automotive underbody aerodynamics. *16th International Symposium on Particle Image Velocimetry*, Tokyo, Japan, June 26-28, 2025

12. Porcar Galán, L., **Grille Guerra, A.**, Sciacchitano, A., & Scarano, F. Light reflections detection and correction for Robotic Volumetric PIV. *21st International Symposium on Applications of Laser and Imaging Techniques to Fluid Mechanics*, Lisbon, Portugal, July 8-11, 2024

11. Battegazzore, A., **Grille Guerra, A.**, & Sciacchitano, A. On-site characterization of automotive diffuser aeordynamics by 3D LPT. *21st International Symposium on Applications of Laser and Imaging Techniques to Fluid Mechanics*, Lisbon, Portugal, July 8-11, 2024

10. Scarano, F., Hysa, I., **Grille Guerra, A.**, Tuinstra, M., & Sciacchitano, A. Multiple-exposure PTV with variable time steps. *21st International Symposium on Applications of Laser and Imaging Techniques to Fluid Mechanics*, Lisbon, Portugal, July 8-11, 2024

9. Tirelli, I., **Grille Guerra, A.**, Ianiro, A., Sciacchitano, A., Scarano, F., & Discetti, S. Full-domain POD modes from PIV asynchronous patches. *21st International Symposium on Applications of Laser and Imaging Techniques to Fluid Mechanics*, Lisbon, Portugal, July 8-11, 2024

8. **Grille Guerra, A.**, Sciacchitano, A., & Scarano, F. On the scalability of helium-filled soap bubbles. *20th International Symposium on Flow Visualization*, Delft, The Netherlands, July 10-13, 2023

7. **Grille Guerra, A.**, Sciacchitano, A., & Scarano, F. Dense modal decomposition from sparse LPT data. *15th International Symposium on Particle Image Velocimetry*, San Diego, USA, June 19-21, 2023

6. **Grille Guerra, A.**, Scarano, F., & Sciacchitano, A. Generation of HFSB at scale and their optical behaviour. *15th International Symposium on Particle Image Velocimetry*, San Diego, USA, June 19-21, 2023

5. Mertens, C., **Grille Guerra, A.**, van Oudheusden, B. W., Fehrs, M., & Ritter, M. R. Analysis of the boundary layer on a highly flexible wing based on infrared thermography measurements. *23rd STAB/DGLR Symposium*, Berlin, Germany, November 9-10, 2022

4. **Grille Guerra, A.**, Mertens, C., Little, J., & van Oudheusden, B. W. Investigation of the unsteady behaviour of a laminar separation bubble using infrared thermography. *20th International Symposium on Applications of Laser and Imaging Techniques to Fluid Mechanics*, Lisbon, Portugal, July 11-14, 2022

3. **Grille Guerra, A.**, Hosseinverdi, S., Little, J., & Fasel, H. Unsteady behavior of a laminar separation bubble subjected to wing structural motion. *AIAA SciTech 2022 Forum*, San Diego, USA, January 3-7, 2022

2. Hosseinverdi, S., **Grille Guerra, A.**, Fasel, H., & Little, J. Investigation of transition and its active control in separation bubbles for a wing section at Re = 200k: DNS, theory, and experiments. *AIAA SciTech 2022 Forum*, San Diego, USA, January 3-7, 2022

1. **Grille Guerra, A.**, Hosseinverdi, S., Singh, A., Little, J., & Fasel, H. Unsteady evolution of a laminar separation bubble subjected to structural motion. *AIAA Aviation 2021 Forum*, virtual event, August 2-6, 2021

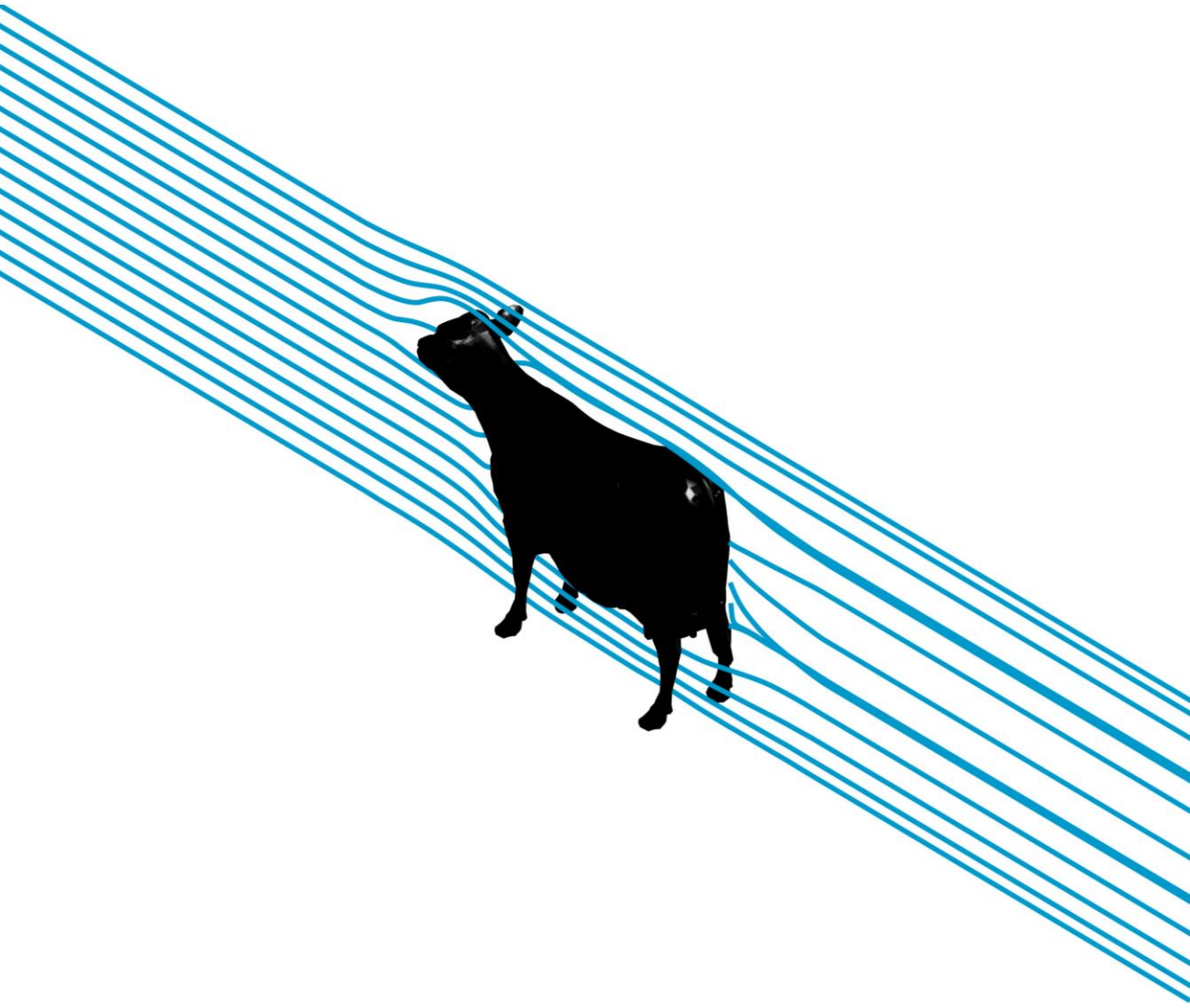

TU Delft

ISBN 978-94-6384-957-9